Downloaded from orbit.dtu.dk on: May 05, 2023

DTU Library

Negative Index Materials and Plasmonic Antennas Based Nanocouplers

Andryieuski, Andrei

Publication date:
2011

Document Version
Publisher's PDF, also known as Version of record

Link back to DTU Orbit

Citation (APA):
Andryieuski, A. (2011). *Negative Index Materials and Plasmonic Antennas Based Nanocouplers*. Technical University of Denmark.

General rights
Copyright and moral rights for the publications made accessible in the public portal are retained by the authors and/or other copyright owners and it is a condition of accessing publications that users recognise and abide by the legal requirements associated with these rights.

- Users may download and print one copy of any publication from the public portal for the purpose of private study or research.
- You may not further distribute the material or use it for any profit-making activity or commercial gain
- You may freely distribute the URL identifying the publication in the public portal

If you believe that this document breaches copyright please contact us providing details, and we will remove access to the work immediately and investigate your claim.

Andrei Andryieuski

Negative Index Materials and Plasmonic Antennas Based Nanocoupler

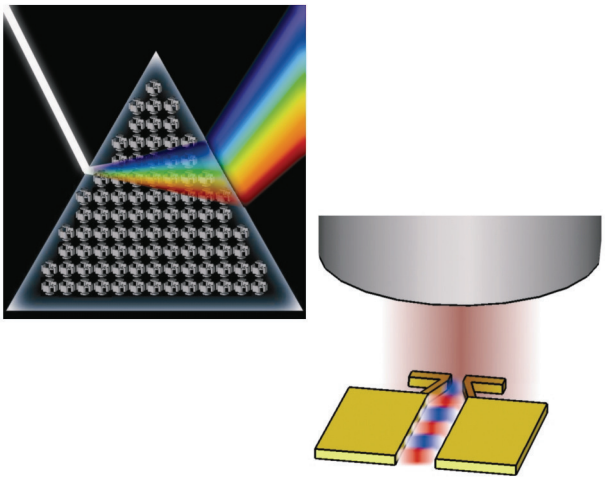

DTU Fotonik, Technical University of Denmark

2011

Abstract

This thesis describes the development, design and fabrication of the nanocoupler that is a device coupling light from conventional optical fiber to the nanosize plasmonic slot waveguide. This device can decrease the coupling region to several micrometers providing compact interface between an optical fiber and future optical integrated circuit. Multiple nanocoupler possibilities are analyzed. Two realizations are investigated: negative index metamaterial and plasmonic nanoantenna based.

The cubic symmetric negative index metamaterial Split cube in Cage and Split cube in Carcass designs for the telecom frequencies are proposed. It is shown that despite the exceptional bulkness (effective properties do not depend on the number of layers) and cubic symmetry the abovementioned designs exhibit strong spatial dispersion in the frequency range of interest. That prevents treating them as an isotropic negative index material.

The wave propagation retrieval method for metamaterials with linear and circular eigenpolarizations and the field averaging of the restored Bloch mode method are proposed for metamaterials effective properties characterization. The methods are based on observation of the wave propagation in the metamaterial slab. The methods are unambiguous, simple, can be applied to lossy and lossless metamaterials with negative and positive refractive index, permittivity and permeability.

The technology of silver nanometallization of complex $3D$ dielectric structures is developed. The metallization is based on silver reduction from the silver-ammonia complex with formaldehyde. Continuous and smooth silver layer can be deposited starting from $30\,nm$. The technology can be used for the complex photonic structures fabrication for the infrared frequencies.

The coupling effects between metamaterials monolayers are investigated. It is shown that some metamaterials can be treated as homogeneous in the resonant frequency region, but some cannot at any value of the metamaterials period. The quantitative homogenization condition is formulated.

Five types of the nanoantenna based couplers are developed: dipole antennas outside symmetric and asymmetric waveguide, antennas gratings, antennas inside waveguide and battle axe nanocoupler. It is shown that the usage of the side and top reflectors generally increases the power captured by the nanocoupler from the incident wave. The optimized geometrical parameters of the nanoantenna couplers are found out. The best performance is shown by the battle axe nanocoupler that has an antenna figure of merit equal to $1.8\ \mu m^2$ for five antenna periods. That is 90 times larger than antenna figure of merit for the waveguide without nanocoupler ($0.02\ \mu m^2$).

The antenna nanocoupler fabrication technology is optimized. Plasmonic antennas nanocouplers are fabricated. Coupling to the plasmonic slot waveguide is experimentally demonstrated.

Resumé

Denne afhandling beskriver udviklingen, designet og fabrikationen af en nanocoupler, der er en anordning der kobler lys fra konventionel optisk fibre til en nanostørrelse plasmonisk slot bølgeleder. Denne anordning kan reducere koblingsregionen til flere mikrometer, der giver et kompakt interface mellem optiske fibre og fremtidige optisk integrerede kredsløb. Flere nanocoupler muligheder er analyseret. To realiseringer, som er baseret på negativt indeks metamaterialer og plasmoniske nanoantenner, er undersøgt.

De kubisk symmetriske negative indeks metamaterialer designs, Split Cube in Cage og Split Cube in Carcass er foreslået for telecom frekvenserne. Det er vist, at trods den usædvanlige bulkness (effektive egenskaber afhænger ikke af antallet af lag) og kubiske symmetri udviser de ovennævnte design stærk spatial dispersion i frekvensområdet af interesse. Dette umuliggør at behandle dem som et isotropisk negativ indeks materiale.

Wave Propagation Retrieval metoden for metamaterialer med lineære og cirkulære eigenpolarizationer og Field Averaging of the Restored Bloch Mode metoden er foreslået til karakterisering af de effektive egenskaber. Metoderne er baseret på observation af bølgeudbredelse i metamaterial skive. Metoderne er entydige, simple, kan anvendes på absorberende og tabsfri metamaterialer med negative og positive brydningsindeks, permittivitet og permeabilitet.

Teknologien til sølv nanometallisering af komplekse $3D$ dielektriske strukturer er udviklet. Metalliseringen er baseret på sølvreduktion fra sølv-ammoniak komplekset med formaldehyd. Kontinuerte og glatte sølv lag kan deponeres startende fra $30\ nm$. Teknologien kan anvendes til fabrikation af komplekse fotoniske strukturer for infrarøde frekvenser.

Koblingseffekter mellem metamaterialer monolagene er undersøgt. Det er vist, at nogle metamaterialer kan behandles som homogene i resonansfrekvens regionen, men nogle kan ikke for nogen værdi af perioden i metamaterialet. Den kvantitative homogeniseringsbetingelse er formuleret.

Fem typer af den nanoantenne-baserede couplers er udviklet: dipol antenner udenfor symmetriske og asymmetriske bølgeleder, antenner gratings, antenner indenfor bølgeleder og battle axe nanocouplers. Det er vist, at

brugen af side og top reflektorer øger effekten optaget af nanocoupleren fra den indfaldende bølge. De optimerede geometriske parametre for nanoantenne coupleren er fundet. Den bedste præstation viser sig for battle axe nanocoupleren, der har et antenne godhedstal lig med $1{,}8\ \mu m^2$ for fem antenne perioder. Det er 90 gange større end antenne godhedstallet for bølgelederen uden nanocoupler ($0{,}02\ \mu m^2$).

Fabrikationsteknologien for antenne nanocoupler er optimeret. Plasmoniske antenner nanocouplers er fabrikerede. Kobling til plasmonisk slot bølgeleder er eksperimentelt påvist.

List of publications

This thesis is partly based on the work presented in the following publications and talks.

Peer-reviewed journal papers

1. R. Malureanu, A. Alabastri, W. Cheng, R. Kiyan, B.N. Chichkov, **A. Andryieuski**, and A.V. Lavrinenko, "Enhanced broadband optical transmission in metallized woodpiles," *Applied Physics A*, 2011, vol. 103, issue 3, pp.749-753.

2**. A. Andryieuski**, C. Menzel, C. Rockstuhl, R. Malureanu, F. Lederer, and A. Lavrinenko, "Homogenization of resonant chiral metamaterials," *Physical Review B*, vol. 82, 2010, p.235107.

3. R. Malureanu, M. Zalkovskij, **A. Andryieuski**, and A.V. Lavrinenko, "Controlled Ag Electroless Deposition in Bulk Structures with Complex Three-Dimensional Profiles," *Journal of The Electrochemical Society*, vol. 157, 2010, p. K284-K288.

4. **A. Andryieuski**, R. Malureanu, and A.V. Lavrinenko, "Wave propagation retrieval method for chiral metamaterials," *Optics Express*, vol. 18, 2010, pp. 15498-15503.

5. C. Menzel, C. Rockstuhl, R. Iliew, F. Lederer, **A. Andryieuski**, R. Malureanu, and A.V. Lavrinenko, "High symmetry versus optical isotropy of a negative-index metamaterial," *Physical Review B*, vol. 81, p. 195123, 2010.

6. **A. Andryieuski**, R. Malureanu, and A. Lavrinenko, "Wave propagation retrieval method for metamaterials: Unambiguous restoration of effective parameters," *Physical Review B*, vol. 80, 193101, 2009.

7. **A. Andryieuski**, C. Menzel, C. Rockstuhl, R. Malureanu, A. Lavrinenko "The split cube in a cage: bulk negative-index material for infrared applications". *Journal of Optics A: Pure and Applied Optics*, vol: 11, article no. 114010, 2009.

8. **A. Andryieuski**, R. Malureanu, and A. Lavrinenko "Nested structures approach in designing an isotropic negative-index material for infrared", *J. Eur. Opt. Soc.: Rapid Publ.* 4, 2009, pp.09003.

Peer-reviewed proceedings

1. **A. Andryieuski**; S. Ha; A.A. Sukhorukov; Yu.S. Kivshar; A.V. Lavrinenko "Unified approach for retrieval of effective parameters of metamaterials", *Proceedings of the SPIE*, Volume 8070, 2011, pp. 807008 1-7.

2. M. Zalkovskij; R. Malureanu; **A. Andryieuski**; A. V. Lavrinenko "Fabrication and characterization of woodpile structures", *Proceedings of the SPIE*, Volume 8070, 2011, pp. 80700M 1-7.

3. **A. Andryieuski**, C. Menzel, C. Rockstuhl, R. Malureanu, F. Lederer, and A.V. Lavrinenko, "Is It Possible To Homogenize Resonant Chiral Metamaterials?," *AIP Conference Proceedings*, vol. 1291, 2010, pp. 37-39.

4. **A. Andryieuski**, R. Malureanu, and A.V. Lavrinenko, "Wave propagation method as an accurate technique for effective refractive index retrieving," *Theoretical and Computational Nano-Photonics : AIP Conference Proceedings*, vol. 1176, 2009, pp. 37-39.

Conference contributions

1. **A. Andryieuski**, R. Malureanu, A. Lavrinenko "Plasmonic nanoantenna based coupler for telecom range", *International Conference 'Days of Diffraction' (DD)*, Russian Federation, 2011.

2. **A. Andryieuski**, R. Malureanu, S. Ha, A.A. Sukhorukov, Yu.S. Kivshar, A.V. Lavrinenko "Wave propagation phenomena in metamaterials for retrieving of effective parameters", *International Conference 'Days of Diffraction' (DD)*, Russian Federation, 2011.

3. **A. Andryieuski**, R. Malureanu, A. Lavrinenko, V.S. Volkov, I. Radko, S.I. Bozhevolnyi, "Efficient and broadband nanoantenna coupler to plasmonic slot waveguide", *International Conference on Surface Plasmon Photonics – 5 (SPP5)*, South Korea, 2011.

4. M. Zalkovskij; R. Malureanu; **A. Andryieuski**; A. V. Lavrinenko "Fabrication and characterization of woodpile structures", *SPIE conference*, Czech Republic, 2011.

5. **A. Andryieuski**; S. Ha; A.A. Sukhorukov; Yu.S. Kivshar; A.V. Lavrinenko "Unified approach for retrieval of effective parameters of metamaterials", *SPIE conference*, Czech Republic, 2011.

6. **A. Andryieuski**, S. Ha, A.A. Sukhorukov, Yu.S. Kivshar, A. Lavrinenko "Bloch-mode analysis for retrieval of effective metamaterial parameters", *Annual CUDOS Workshop (CUDOS) – 10*, Australia, 2011.

7. **A. Andryieuski**, C. Menzel, C. Rockstuhl, R. Malureanu, F. Lederer, and A.V. Lavrinenko "Is it possible to homogenize resonant chiral metamaterials", *TaCoNa-2010*, Germany, 2010.

8. F. Lederer, C. Rockstuhl, C. Menzel, T. Paul, **A. Andryieuski**, R. Malureanu, A.V. Lavrinenko, "Isotropic optical metamaterials", *Mediterranean Conference on Nanophotonics – 3*, Serbia, 2010.

9. C. Rockstuhl, C. Menzel, T. Paul, **A. Andryieuski**, R. Malureanu, A. Lavrinenko and F. Lederer "Isotropic optical metamaterials" *Metamaterials Congress*, Germany, 2010.

10. **A. Andryieuski**, A.V. Lavrinenko and R. Malureanu "Chiral metamaterials characterisation using the wave propagation retrieval method" *Metamaterials Congress*, 2010.

11. R. Malureanu, **A. Andryieuski** and A.V. Lavrinenko "Optimisation of the electroless metal deposition technique for use in photonics" *ATOM-10*, Romania, 2010.

12. **A. Andryieuski**, R. Malureanu and A.V. Lavrinenko "Homogenization of metamaterials: parameters retrieval methods and intrinsic problems" *ICTON*, Germany, 2010.

13. **A. Andryieuski**, R. Malureanu and A.V. Lavrinenko "Simple effective parameters retrieval employing wave propagation phenomena" *CIMTEC*, Italy, 2010.

14. C. Menzel, T. Paul, C. Rockstuhl, R. Iliew, **A. Andryieuski**, R. Malureanu, A.V. Lavrinenko, and F. Lederer "Optical isotropic negative index metamaterials" *Photonic Metamaterials and Plasmonics (META)*, USA, 2010.

15. **A. Andryieuski**, R. Malureanu, A. Lavrinenko "Wave Propagation Method as a Characterization Tool for Chiral Metamaterials" *PhoNa 2010 International Workshop on Photonic Nanomaterials*, 2010.

16. R. Malureanu, A. Alabastri, W. Cheng, R. Kiyan, B.N. Chichkov, **A. Andryieuski**, and A.V. Lavrinenko, "Enhanced broadband optical transmission in metallized woodpiles," *META10*, Egypt, 2010.

17. **A. Andryieuski**, R. Malureanu, and A.V. Lavrinenko, "Bulk metamaterials: Design, fabrication and characterization," *ICTON-MW'09;3rd,* France: IEEE, 2009, p. 5.

18. **A. Andryieuski**, R. Malureanu, A.V. Lavrinenko "Bulk isotropic negative-index material design for infrared". *Metamaterials Congress 2009*, UK, 2009.

19. **A. Andryieuski**, R. Malureanu, A.V. Lavrinenko "Nested structures approach for bulk 3D negative index materials." *11th international conference on transparent optical networks*, Portugal, 2009.

20. R. Malureanu, **A. Andryieuski**, A.V. Lavrinenko "Isotropic metal deposition technique for metamaterials fabrication". *Danish Physical Society Nordic Meeting*, Denmark, 2009.

21. **A. Andryieuski**, R. Malureanu, A.V. Lavrinenko "Bulk isotropic negative-index metamaterial for infrared". *Danish Physical Society Nordic Meeting*, Denmark, 2009.

22. R. Malureanu, **A.V. Andryieuski**, A.V. Lavrinenko "Design and fabrication activity towards 3D negative refraction index materials in the IR region". *ETOPIM 8*, Greece, 2009.

23. **A. Andryieuski**, R. Malureanu and A. Lavrinenko "Simplified 3D Isotropic Structure for Negative Index Materials in the IR Regime". *PECS VIII*, Australia, 2009.

24. **A. Andryieuski**, R. Malureanu and A. Lavrinenko "Design of a three-dimensional metamaterial exhibiting isotropic properties in the near infrared range". *PIERS*, China, 2009.

25. R. Malureanu; **A. Andryieuski**; A. Lavrinenko "3D geometrically isotropic metamaterial for telecom wavelengths". *NanoMeta-2009*. Austria, 2009.

26. **A. Andryieuski**, R. Malureanu and A. Lavrinenko "3D Isotropic Double Negative Material Design for Infrared". *TaCoNa-Photonics*, Germany, 2008.

Other publications in 2008-2011

1. K. Iwaszczuk, **A. Andryieuski**, A. Lavrinenko, X.-C. Zhang, and P. U. Jepsen, "Non-invasive terahertz field imaging inside parallel plate waveguides", *Applied Physics Letters*, vol.99, 2011, pp. 071113.

2. R. Malureanu, P.U. Jepsen, S. Xiao, L. Zhou, D.G. Cooke, **A. Andryieuski**, and A.V. Lavrinenko, "Fractal THz metamaterials: design, fabrication, and characterisation," *SPIE proceedings*, 2010, pp. 77110M-8.

3. R. Malureanu, P.U. Jepsen, S. Xiao, L. Zhou, D. Cooke, **A. Andryieuski**, and A. Lavrinenko, "Fractal THz metamaterials: design, fabrication and characterisation," *SPIE conference*, Belgium, 2010.

Contents

Acknowledgements

This thesis is the result of my three years of Ph.D. studies at the Metamaterials group at DTU Fotonik, Technical University of Denmark. The results presented in the thesis were mainly obtained by the author that is me. However, I do not feel I can write "I" in the thesis, because I could never make the presented work alone. There were many people who helped me during my studies and along my life. The solutions of the tricky problems were sometimes figured out in hot discussions or by "collective wisdom" in a form of group brain storming. Therefore I will be writing "we" throughout the thesis.

First and foremost I would like to thank my supervisors Andrei Lavrinenko and Radu Malureanu (both from DTU Fotonik, Technical University of Denmark) for their time and efforts, wise guidance and encouragement, practical and social skills teaching, advice on the simulation, fabrication and measurements, discussion of my ideas, support of my initiatives, proof-reading of the presentations, manuscripts and this thesis and for their friendship.

Many thanks to the reviewers Olav Breinbjerg (DTU), Olivier Martin (EPFL, Switzerland) and Morten Willatzen (University of South Denmark) for careful reading of this thesis and for their useful critical comments.

I would like to thank the whole Metamaterials group (A. Boltasseva, R. Nielsen, M. Zalkovskij, A. Novitsky, L. Yang, A. Ivinskaya, A. Panahpour, V. Babicheva, and C. Gritti) for their help, advice, discussion of the ideas at the group meetings and journal clubs. Special thanks to M. Zalkovskij who helped me to get on well with the machines in the cleanroom and to A. Boltasseva and R. Nielsen for their useful advice on fabrication.

I would also like to thank the Danish Council for Technology and Production Sciences for the financial support of the NIMbus project, to which I was hired as a PhD student.

I am thankful to the whole DTU Fotonik for creating such fruitful and friendly working surrounding. More specifically I would like to thank our "lunch club" (N. Gregersen, L. Frandsen, O. Kopylov, M. Schubert,

E. Semenova, I. Kulkova, N. Kuznetsova) for interesting discussions during lunches, my roommates (T. Suhr Skovgård, S. Ek, T. Ansbæk, R. Shirazi) for the cake club that painted dull Mondays in bright colors, group leaders and professors (J. Mørk, P. Lodahl, N.A. Mortensen. K. Yvind, J. Hvam) for the useful criticism on my presentations and DTU Fotonik administration (L.U. Andersen, A. Bjarklev, L. Bjørnstjerne, V. Brackley, A. Sohn Henriksen, A. Lier Møller, B. Lydik Påske) for their help. Many thanks to N. Gregersen and T. Suhr Skovgård for proof-reading of the Danish translation of the thesis abstract. Special thanks to M. Wubs for constructive criticism and for the "Survival guide for scientist" by A. Ladengijk. I am thankful to S. Arslanagic for the discussion on the microwave antennas and O. Sigmund for the discussion on the numerical optimization. I also thank DTU Library for the useful advice on the information search, DTU Teaching Lab and personally B. Lund Hansen for a useful and inspiring seminar on teaching and DTU Mechanical Workshop for fabrication of the fiber holder. I am grateful to the process specialists at Danchip National Center for Micro and Nanofabrication (P. Shi, E. Khomchenko, H. Ouacha, M. Lindhardt, K. Nilson and P.V. Larsen) for teaching me fabrication in the cleanroom.

I would like to express my gratitude to my collaborators from other universities, namely C. Menzel, C. Rockstuhl and F. Lederer from the Friedrich-Schiller University of Jena; S. Ha, A. Sukhorukov and Yu. Kivshar from the Australian National University; G. Biagi and T. Holmgård Stær from Aalborg University; V. Volkov, I. Radko and S.I. Bozhevolnyi from the University of South Denmark, A. Inberg from the Tel-Aviv University. I would like also to acknowledge the people with whom I had useful discussions via emails and in person at the conferences: C.R. Simovski, S.A. Tretyakov, S. Maslovski, P. Belov, I. Shadrivov, D. Chigrin, S. Zhukovski, E. Plum, A. Demetriadou, A. Nabiullin, S. Sun, M. Rill and X. Chen.

I would like to thank with a great gratitude my school physics teacher M.K. Stognij who woke up my interest to physics and provided me a solid background for further growth. A great gratitude to my physics teacher from the Lyceum of BSU A.I. Slabadzianiuk for his extraordinary contagious enthusiasm, his brilliant physics courses, his efforts in my preparation to the International Physics Olympiad and for his friendship. I also thank my professors from the Belarusian State University V.V. Zhilko, M.V. Bortnik,

E.D. Karikh and N.V. Kisel for their fantastic lectures in electrodynamics, thermodynamics, optoelectronics and philosophy, correspondingly, and for that they taught me to think in a structured way. Thanks to my diploma and master thesis supervisors I.S. Manak and A.A. Afonenko as well as to my supervisors and colleagues from the Institute of Physics of the National Academy of Sciences of Belarus G.P. Yablonskii, E.V. Lutsenko, V.N. Pavlovskii, V.Z. Zubelevich, A.V. Danilchyk, A.G. Voinilovich, N.V. Rzheutskii for help in my first scientific steps and valuable practical experience in the optical measurements and simulations.

I would also like to acknowledge my friends A. Mishchuk and M. Sheinin for the mutual help and friendly competition during the preparation for physical olympiads that promoted our scientific growth. Many thanks to the Lyceum of the Belarusian State University, which was my high school in 2000-2002 and my working place in 2004-2008. The lively and inspiring surrounding there promoted creative thinking. I would also like to thank my three-weeks, subject project and internship students, especially Y. Sachkou (Belarusian State University) who calculated nanoantennas impedance.

Many thanks to my father Vatslau, my mother Tatsiana, my sister Maryia and grandmother Tamara for their constant support throughout my life, development of my interest to nature and teaching me to be persistent. Special thanks to my father for his important advice and valuable experience in lasers, photodiodes and optical fibers.

The last, but not the least, I would like to thank my wife Katsiaryna for her support, understanding, inspiration, advice on the work efficiency improvement, time management, literature search and data organization, for manuscripts and presentations proof-reading and discussions on the modern science. I also thank our children Sergei and Kristina for the infinite happiness and joy they give.

List of abbreviations and acronyms

1D, 2D and 3D One, two and three dimensional, respectively

2PP	Two-photon polymerization
3-APTES	3-aminopropyl-triethoxysilane
AFM	Atomic force microscope
AFOM	Antenna figure of merit
CE	Coupling efficiency
CVD	Chemical vapor deposition
EDTA-Na	Ethylenediaminetetraacetic acid disodium salt
EP	Effective parameter
FARBM (method)	Field averaging of the restored Bloch mode
FOM	Figure of merit
IPA	Isopropyl alcohol
LCP	Left circular polarization
MM	Metamaterial
NA	Nanoantenna
NIM	Negative index material
NRW	Nicholson-Ross-Weir (method)
OSA	Optical spectral analyzer
PEC	Perfect electric conductor
PECVD	Plasma enhanced chemical vapor deposition
PEG-1500	Polyethylene Glycol with a relative molecular mass 1500
RCP	Right circular polarization
RMS	Root mean square

SCiC	Split Cube in Cage
SCiCa	Split Cube in Carcass
SCube	Split Cube
SDS	Sodium dodecyl sulfate
SEM	Scanning electron microscope
SNOM	Scanning near-field optical microscope
SPP	Surface plasmon polariton
SR	Split ring
SRR	Split ring resonator
SuperK	Supercontinuum light source
TC	Twisted cross
TSRR	Twisted split ring resonator
WPRM	Wave propagation retrieval method
WPRMC (metamaterials)	Wave propagation retrieval method for chiral

Preface

I should make some comments about my Ph.D. project that experienced several transformations during its implementation. This thesis includes two big chapters devoted to metamaterials and to plasmonic antennas based nanocoupler. That represents the chronological progress of the project.

The project was a part of the "Negative Index Materials based Nano-couplers" (NIMbus) project supported by the Danish Council for Technical and Production Sciences. The NIMbus project started in June 2008. Initially its goal was the development of a negative index metamaterials based coupler only. The metamaterials field was rapidly emerging at that time and plenty of new exciting ideas appeared. I took active part in the design and simulation of the cubic symmetric negative index metamaterials, effective parameters methods development and optimization of the electroless technology for silver metallization. I did also some optical characterization of metalized woodpile photonic crystals with a fiber-based transmission setup.

It is interesting how the research ideas appeared, very often accidentally. For example, I have noticed the homogenization difficulties for some metamaterials by chance when I was testing the wave propagation retrieval method for chiral materials. Or, for example, my initial intention just to check the backward wave behavior in the simulations by looking at the phase distribution in the propagating wave became the ground for the wave propagation retrieval method.

However, by the end of 2009 the project experienced a sort of crisis when it became clear that the initial idea of the negative index metamaterial nanocoupler is hardly doable in a reasonable timeframe. The developed metamaterial design was almost impossible to be fabricated and what was even worse, the cubic symmetric metamaterial did not show optical isotropy. At that critical point I performed a brain storm of the possible nanocouplers realization figuring out the future direction of the project. There were plenty of interesting ideas and it was not easy to choose the best one. Finally, the hot debates at the group meetings revealed that the plasmonic antenna based nanocoupler was the most promising direction to go. So the second part of my project was devoted to the plasmonic nanoantennas. I modelled and

optimized the designs. I also worked a substantial amount of time in the cleanroom fabricating the developed nanoantenna couplers.

As a result, this thesis unites together several fields and directions. It contains the results of numerical modeling and cleanroom fabrication, fundamental investigation of the metamaterials properties and practical application of the plasmonic nanoantennas, methods of metamaterials characterization and methods of chemical metallization of dielectric surfaces. All of them are unified with a single goal of the nanocoupler realization, a single goal that shined as a bright star throughout the whole project.

Chapter 1. Introduction

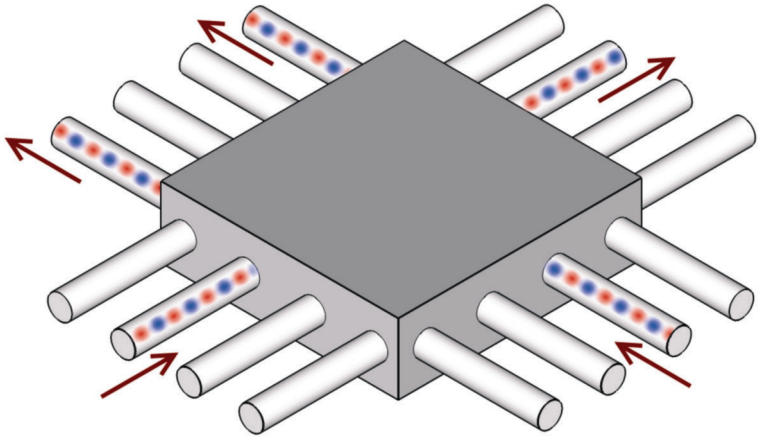

Motivation

Photonic components have advantages comparing to the electronic ones. Infrared and optical frequencies ($10^{14} - 10^{15}\,Hz$) provide much broader operational bandwidth than the fastest electronic circuits. The losses in the optical waveguides are smaller than the losses in the metallic wires. This is why, as David Miller wrote, "the optical interconnects are progressively replacing wires" [1]. To achieve more functionality on an integrated optical chip the optical components have to be miniaturized. However, a natural limitation comes into play – the diffraction limit, which claims that we cannot focus the light better than half of the wavelength. The size of the common dielectric waveguides (for example, silicon waveguides) is also limited to the half of the wavelength.

The problem is not only to create efficient waveguides that provide subwavelength mode confinement, but also to make an efficient interface between free space or an optical fiber and subwavelength waveguide, that is to focus the light and to launch it efficiently to the waveguide. The problem comes from the mode mismatch between the optical fiber (the common single-mode telecommunication fiber has a core of $8\,\mu m$ in diameter) and the nano-sized waveguide. They have an impedance mismatch and small mode overlap that prevents efficient coupling.

Long tapered fibers are usually used for coupling light to the subwavelength waveguide. The tapered region may reach the length of several millimeters that is incompatible with a modern micro- and nano-fabrication.

Goal

The goal of this work was to develop a compact and efficient nanocoupler from an optical fiber to a nanosize waveguide. We understand a nanocoupler as a mode matching device or in other words a mode converter, a sort of optical funnel that collects the light from an optical fiber and launch it into the nano-waveguide.

After an analysis of the possible nanocoupler realizations we focused on two of them: one based on a negative refractive index metamaterials (MMs) and another one based on plasmonic nanoantennas (NAs).

Plasmonics and metamaterials: brief introduction

To obtain a better waveguiding, focusing and coupling the scientific community in general and we in particular turned to plasmonics and metamaterials.

Plasmonics is a branch of physics which describes the interaction of light with freely moving electrons in metals. The combined optical and charge density oscillations (plasmon polaritons) are confined to the surface; this is why they are usually called "surface plasmons". Depending on the geometrical structure, plasmons can be propagating (in this case they are called "surface plasmon polaritons" (SPPs)) or attached to a specific particle (in this case they are called "localized surface plasmons"). Plasmonic metal-dielectric-metal waveguides do not have a cut-off thickness thus providing a subwavelength confinement and focusing.

Metamaterials is another branch of physics, or to say better of the material science, which develops the complex metal-dielectric composites and studies their properties, which can be very unusual comparing to the natural materials. As one application, the metamaterials can provide a negative refractive index which is required for a perfect lens – a device that can achieve unprecedented light focusing. However, such device has not been demonstrated yet.

Thesis structure

The thesis is organized in a following way. Various types of the possible nanocoupler realization are presented and analyzed in the chapter 2.

The chapter 3 describes the development of a three-dimensional (3D) isotropic negative index metamaterial, as well as the methods of metamaterials effective parameters restoration, technology for metallization of complex dielectric surfaces and analysis of the coupling between metamaterial monolayers influence on the metamaterial homogenization.

The chapter 4 provides the results of the nanoantenna based coupler investigation, including methodology of the simulation, fabrication and measurements and the results for the proposed nanoantenna coupler designs.

The chapter 5 concludes the thesis and summarizes the main findings.

Chapter 2. Nanocouplers

Chapter structure

In section 2.1 we introduce the reader into the nanowaveguides and, more specifically, into the plasmonic waveguides. In section 2.2 several physical principles that can be grounds for the nanocoupler realization are listed. The tapered waveguide based nanocouplers are discussed in section 2.3. The directional nanocouplers are regarded in section 2.4. The lenses based nanocouplers are considered in section 2.5. The antenna based couplers are presented in section 2.6. Other ideas are listed in section 2.7. Conclusions summarize the chapter.

2.1. Nanowaveguides

Nanowaveguide definition

We define a nanowaveguide as an electromagnetic waveguide that has lateral sizes in the "nano" range $1-1000\,nm$. Depending on the waveguide material and the wavelength of light a nanowaveguide can be subwavelength or not. We have a specific interest in the telecom range around the wavelength $1.55\,\mu m$. The modal size of the subwavelength waveguide is smaller than the size of a focused light beam can be. Due to the impedances mismatch and small modal size it is difficult to couple the light from the free space to the subwavelength waveguide.

The nanowaveguides can be divided in two groups: dielectric and plasmonic waveguides. Their combinations are also possible (the so-called hybrid waveguides).

Dielectric waveguide

The most popular dielectric waveguide is based on silicon due to its high refractive index and transparency at the telecom wavelengths. The most popular silicon waveguides are rib, ridge and photonic crystal waveguides. A typical size of the silicon waveguide's cross-section is $200 \times 500\,nm^2$ [2]. The dielectric waveguide always has a cut-off wavelength above which the waveguide cannot transport the wave since it leaks out of the waveguide.

Diffraction limit

Miniaturization of optoelectronic components requires decreasing the size of optical waveguides. However, a natural limitation comes into play. The smallest size of an optical beam in a medium is on the order of the wavelength due to diffraction. If we consider a wave of the frequency ω propagating in the medium with the refractive index n, the wavenumber is $k = 2\pi n/\lambda_0$. The wavevector components, for example, k_x can take the values from $-k$ to k, so its maximal uncertainty can be $\Delta k_{x,max} = 2k = 4\pi n/\lambda_0$. Due to the uncertainty principle (or likewise Fourier transformations), the coordinate uncertainty Δx is connected to the wavevector uncertainty Δk_x [3]

$$\Delta x \Delta k_x \geq 2\pi. \tag{2.1}$$

That limits the size of the light beam to

$$\Delta x = \frac{2\pi}{2k} = \frac{\lambda_0}{2n}. \tag{2.2}$$

Considering a telecom wavelength of $\lambda_0 = 1.55\mu m$ and silica $n = 1.5$ we can estimate the smallest size of the light beam as $\Delta x_{min} = 517\ nm$. Light can be confined to smaller spots only using plasmon polaritons at the interface between metal and dielectric.

Plasmonic waveguides

Plasmonic waveguides are metal-dielectric waveguides. They attract a lot of attention since in some configurations they can show the absence of the cut-off at any waveguide size. Therefore the mode size can be reduced to extremely small values, but at the cost of optical losses in metal. Another advantage of the plasmonic waveguide is the presence of metal that can be used not only as a waveguiding structure but also as an electric contact that allows using it for changing the dielectric surrounding (for example, due to electro-optical or thermo-optical effects). Plasmonic waveguides are considered as a replacement of the electronic interconnects in the future generation integrated circuits.

Surface plasmon polaritons are the eigenmodes of metal-dielectric interface. SPPs are combined light – electrons density waves. On a flat metal (permittivity ε_1) – dielectric (permittivity ε_2) interface surface plasmon polaritons are transverse magnetic waves (magnetic field parallel to the interface). The dispersion equation of the SPPs is

$$k = k_0 \sqrt{\frac{\varepsilon_1 \varepsilon_2}{\varepsilon_1 + \varepsilon_2}}. \tag{2.3}$$

In the optical and near-infrared range the permittivity of metal is very dispersive. In a good approximation it can be described with the Drude formula

$$\varepsilon = 1 - \frac{\omega_P^2}{\omega(\omega + i\gamma)}, \tag{2.4}$$

where ω_P is a plasma frequency and γ is a damping rate (sometimes also called collision frequency). The propagating SPP solutions correspond to a

case $Re(\varepsilon_1 + \varepsilon_2) < 0$. For a detailed background on plasmonics theory and applications we refere the reader to [4], [5].

Several types of the plasmonic waveguiding structures have been proposed, e.g. metal-insulator-metal and insulator-metal-insulator structures [6], strip [7], trenches and V-grooves [8], [9], wedge [10], plasmonic slot [11], [12] and metal nanoparticles chain [13] waveguides. A comprehensive overview of the plasmonic waveguides can be found in [4], [5], [14].

Our choice

We decided to develop the nanocoupler for the *plasmonic slot waveguide* since it provides a reasonable trade-off between subwavelength confinement and propagation length. Moreover, two metal parts can be used as electrical contact for the waveguide's properties tuning.

However, the main focus of this work is not the waveguide but the nanocoupler itself. Consequently, the developed nanocoupler design may to a certain extent be modified for dielectric waveguides as well.

2.2. Nanocoupler requirements and possibilities

Nanocoupler definition

A nanocoupler is a device that facilitates coupling of light from the free-space to the nanowaveguide. It can be understood as a focusing device, a sort of an optical funnel that squeezes the light into a small spot. If we talk about matching a thick and a thin waveguides that have different modal distributions, the nanocoupler can be also understood as a mode convertor, a device that transforms a mode of the thick waveguide to a mode of the thin waveguide (see Fig. 2.1).

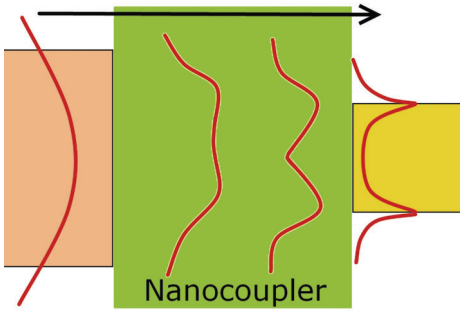

Figure 2.1. Nanocoupler concept: a focusing device or a mode convertor. As an example the mode of the dielectric waveguide is gradually transforming into the mode of the plasmonic waveguide.

Requirements

We understand the nanocoupler as a focusing device or mode convertor satisfying the following requirements:

(1) High coupling efficiency (CE) that is the ratio of the power loaded into the waveguide P_{WG} to the power incident to the nanocoupler from free space or a power incident from a thick waveguide

$$CE = \frac{P_{WG}}{P_{inc}}. \tag{2.5}$$

High coupling efficiency automatically means low losses, including absorption A, reflection R and scattering S.

(2) Small size on the order of several micrometers in contrary to the long tapered fibers that can reach several millimeters.

Additional requirements can be:

(3) Simplicity and small price of fabrication. This requirement is important for the mass production but not so important on the stage of the scientific development.

(4) Spectral selectivity. The importance of this property depends on the application. We are mostly focused on the telecom wavelength. The standard telecom range is from $1.5\ \mu m$ to $1.6\ \mu m$, so such bandwidth is desirable. However some applications are possible where a narrow bandwidth is preferable, for example, if the coupler is used for the wavelength demultiplexing.

(5) Polarization sensitivity. Again the importance of this requirement depends on the application and on the nanowaveguide. Since the plasmonic slot waveguide that we selected as a nanowaveguide works for a specific polarization only, the nanocoupler polarization should be matched with the polarization of the waveguide or it should be polarization insensitive.

Classification

The role of the nanocoupler is to match the impedances and the mode profiles of the incident wave and the accepting nanowaveguide. Depending on the employed physical mechanisms, several types of nanocouplers can be singled out:

1. Tapered waveguides (Fig. 2.2(a)) ("taper coupler"). In this case a gradually changing waveguide compresses the wave.

2. The light can be coupled to a wide silicon waveguide and then with the help of a directional coupler or a resonant stub can be coupled into the plasmonic nanowaveguide (Fig. 2.2(b)) ("directional coupler"). A grating is often used for the light coupling to the wide silicon waveguide [2].

3. The light can be focused with a lens (Fig. 2.2(c)) ("lens coupler"). This is the oldest way of the optical waves focusing.

4. An antenna can be used for the coupling purposes (Fig. 2.2(d)) ("antenna coupler").

5. Some other ideas that do not fall into the abovementioned categories can be employed. Let's call them "exotic" couplers.

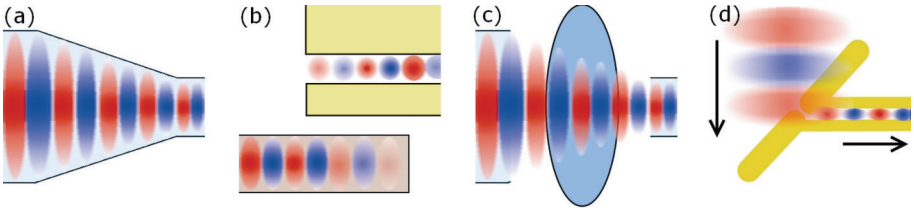

Figure 2.2. Types of the possible nanocouplers realizations: (a) tapered waveguide, (b) directional coupler transferring the power from a wide silicon waveguide to the plasmonic waveguide, (c) lens coupler, (d) antenna coupler.

The combination of these principles is possible. We will consider the mentioned types of the nanocoupler realization possibilities in the next sections.

The nanocoupler can be a separate device (Fig. 2.3(a))or a device integrated with the waveguide on chip (Fig. 2.3(b)). For practical applications the on-chip integrated nanocoupler is preferable, since it simplifies optical alignment.

Two excitation configurations are important for the applications: lateral coupling (Fig. 2.4(a)) when the incident wave direction coincides with the nanowaveguide and vertical coupling (Fig. 2.4(b)) when the light direction is perpendicular to the nanowaveguide. The first can be used in coupling within one layer of an optical integrated circuit whereas the second one can provide the communication of the optical elements between two layers. Other incident angles except 0 and 90 degrees are possible.

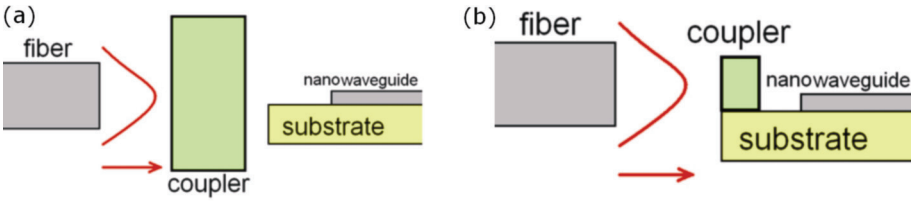

Figure 2.3. Possible geometrical configurations of the coupler: (a) a separate device, (b) integrated with a nanowaveguide on the same chip.

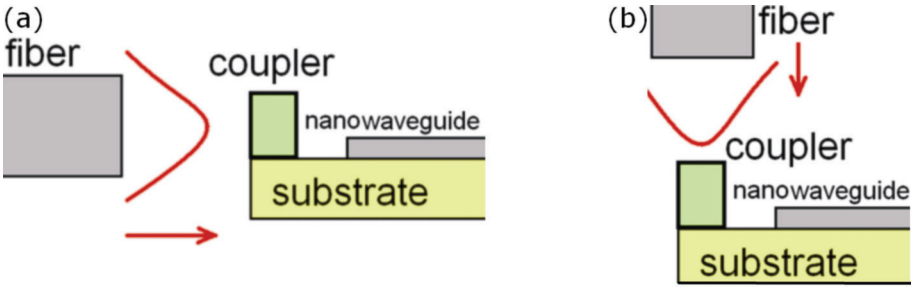

Figure 2.4. Two coupling configuration: (a) lateral, (b) vertical.

Coupler to silicon waveguides

Concluding this section it is worth mentioning which couplers are used in the integrated photonics for silicon waveguides. As L. Zimmermann reported at the Silicon Photonics Workshop in 2011 [2], the commonly used lateral coupler from single mode optical fiber with $8\,\mu m$ core diameter to $200 \times 500\,nm^2$ silicon waveguide is an inverted taper. For this purposes high numerical aperture lensed optical fibers with a spot size of $3\,\mu m$ are used. For the vertical coupling a diffraction grating is typically used. The spot size from the single mode fiber is about $10\,\mu m$. The wave should not be perpendicular to the waveguide, but incident at a small angle to provide the wavevector matching. The maximal coupling efficiency of 69% has been recently shown [15].

2.3. Taper coupler

Classification

Based on the materials used for the tapered waveguide coupler the following classification can be applied:

A. Tapers having dielectric core and dielectric cladding (Fig. 2.5(a)).

B. Tapers having metallic core and dielectric cladding or dielectric core and metallic cladding (Fig. 2.5(b)).

C. Tapers with metamaterial (metal-dielectric composite) core (Fig. 2.5(c)).

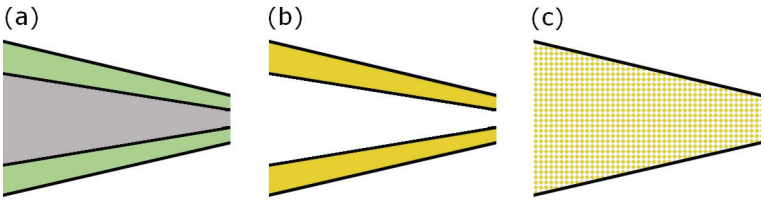

Figure 2.5. The types of taper couplers: (a) dielectric core and cladding taper, (b) metal core or cladding, (c) metamaterial core.

2.3. A. Dielectric core and cladding

If we take an optical fiber, heat it and then pull, the diameter of core and shell decreases. So it is possible to make the core diameter of a nanosize value. Low-loss tapered fibers were fabricated and measured [16]. The optical losses for a fiber of diameter $d = 750\ nm$ at $\lambda_0 = 1.55\ \mu m$ were $-0.017\ dB/mm$.

However, it was also theoretically shown [17] that even an ideal fiber does not allow substantial core thinning, since the propagating mode completely vanishes for the core size of one order of magnitude smaller than the wavelength. In the real fibers with imperfections this limitation is even stricter.

2.3. B. Metallic core or cladding

Tapered fiber tips covered with metal are an essential part of the scanning near-field optical microscope. It allows spatial compression of the light below the diffraction limit [18]. Metal-dielectric-metal tapered plate

waveguides were theoretically and experimentally demonstrated for terahertz [19-21] and the optical ranges [22-24]. In the latter work the maximal transmittivity of 8% was measured for the wavelength $\lambda_0 = 780\,nm$ in adiabatically tapered metalized fiber with a tip opening of about $150\,nm$. The prominent property of such system is that metal-dielectric-metal waveguide does not have a cut-off, only losses limit its performance.

Nanofocusing with a V-shaped metallic groove, which is a similar system, was experimentally demonstrated [25]. A wave with $\lambda_0 = 1.5\,\mu m$ wavelength was focused into a spot of $\lambda_0/40$. The reported energy efficiency was 50%, but there was no information about the incident spot size, it was just "sufficiently large to uniformly illuminate all V-grooves of interest".

In 2004 Mark Stockman predicted that a tapered metallic wire allows giant energy accumulation and intensity enhancement at the tip of the metal taper [26]. The idea is applicable not only in the optical range but also in the terahertz range if the surface of the tapered wire is corrugated [27].

An experimental realization of the tapered wire structure was reported [28]. In this case the light of $\lambda_0 = 1.55\,\mu m$ was compressed from $2000\,nm$ to $90\,nm$ wide wire with a power transmission of 20%. There was also proposed to use long metallic nanocylinders of the radius from 10 to $24\,nm$ separated with $2\,nm$ thick dielectric to focus a Gaussian beam of $200\,nm$ full width into a spot of $20\,nm$ with a power transmission 80% [29]. However, a practical realization of such system is hardly possible at the moment.

2.3. C. Metamaterial core

The idea behind this nanocoupler type is to use a metamaterial as the taper core. The advantage of metamaterials is that their properties can be designed to unusual values, which cannot be provided by natural materials.

An optical funnel containing a metal-dielectric photonic crystal was proposed in [30]. The field compression down to $\lambda_0/30$ with a transmission of 13% was reported. The metamaterial based nanotips for field enhancement were theoretically proposed [31], [32]. The nanotip consists of metallic nanospheres of a gradually changing density. They can be used for field concentration (200 times field enhancement was reported) and the light

compression to a spot of $10\,nm$. In the work [31] it was stated that the power efficiency of such metamaterial tip is larger than of the metalized taper of $10\,nm$ output hole, but the exact values of the transmittivity were not mentioned.

Conclusions

A dielectric adiabatically tapered fiber is a well-known mean of field concentration. However, it can provide either small spot size or high transmission, at the same time preserving long sizes. The metal or metamaterial based tapers can be of significantly smaller length. They can provide field concentration and reasonable transmittivity (e.g. 20%). The difficulties in practical realization are connected with the fabrication technology limitations (for example, fabrication of the metallic cylinders of radius $10\,nm$ separated with $2\,nm$ of dielectric).

2.4. Directional coupler

In this class of our classification we placed the couplers that require silicon waveguide as an intermediate step. So at first the light is coupled to a silicon waveguide (inverted taper or grating) and then from a silicon waveguide to a plasmonic waveguide with the help of a directional coupler. That results in a relatively large size of such systems ($10 - 20\ \mu m$).

Classification

Based on the geometrical position of one waveguide with respect to another, the directional couplers can be divided into the following classes:

A. One waveguide above another (Fig. 2.6(a)).

B. End-fire direct connection of the waveguides (Fig. 2.6(b)).

C. Resonant stub between the waveguides (Fig. 2.6(c)).

D. The waveguides having an overlap region (Fig. 2.6(d)).

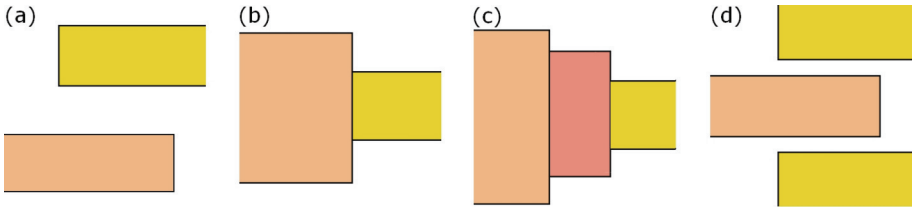

Figure 2.6. Types of the directional couplers: (a) one waveguide above another, (b) direct connection of the waveguides, (c) resonant stub between the waveguides, (d) the waveguides having overlap region.

2.4. A. One waveguide above another

One may obtain light coupling by just placing metal nanowires on top of the dielectric waveguide perpendicular to the latter [33]. However, the reported coupling efficiency of such system is very little, about 1%. Better results can be achieved by placing one waveguide above another such that the waveguides are coupled and the initial waveguides modes become hybridized. In such case the energy from the initial mode is transferred from one waveguide to another and back. Making the overlap region of a specific length one may achieve maximal energy transfer efficiency. Such systems have been proposed, simulated and experimentally realized [34-37]. The theoretical prediction of coupling efficiency of 60% for $\lambda_0 = 1.55\ \mu m$ was

confirmed in measurements [37]. However, we should take into account that the light should be first coupled from a fiber to the silicon waveguide and that the maximal coupling efficiency is on the order of $60-70\%$. That makes the total coupling efficiency of the system about $30-40\%$.

2.4. B. End-fire coupling

End-fire coupling from a dielectric waveguide to a plasmonic slot or nanowires waveguide is not usually very efficient due to the impedances mismatch. However, if an optimization of the geometry is conducted the coupling efficiency more than 70% [38], [39] and even more 90% can be achieved [40], [41]. For example at the wavelength of $\lambda_0 = 1.55\,\mu m$ a coupling efficiency of 80% was measured for long-range surface plasmon polaritons waveguide connected to a silicon waveguide [42]. In another work the coupling from a silicon waveguide to a plasmonic slot waveguide with 30% efficiency at $\lambda_0 = 1.55\,\mu m$ was experimentally demonstrated [43].

2.4. C. Resonant stub between the waveguides

The use of the resonant stubs (for example, $\lambda/4$-transformer) for efficient wave coupling is well-known in the microwave waveguides engineering. It is based on the resonant transmission effect due to constructive interference. The same concept can be used in the optical range, for the plasmonic waveguides of different cross-sections [12], [44-46] and for the silicon and plasmonic waveguides [47] matching.

A $\lambda/4$-transfomer mathing $500\,nm$ and $50\,nm$ wide plasmonic transmission lines with the coupling efficiency of 86% was shown numerically [44]. Matching of a $300\,nm$ wide silicon waveguide with a $40\,nm$ wide plasmonic slot waveguide with the coupling efficiency of 88% was demonstrated [47].

2.4. D. The waveguides having overlap region

In this configuration two waveguides have an overlap region, for example, when one waveguide penetrates another waveguide. For sure this is not possible to all waveguides combination, since one waveguide should contain empty space inside (for example, it is possible to insert a silicon waveguide inside a plasmonic slot waveguide, but not possible to insert one silicon waveguide into another).

Several designs for telecom wavelengths were proposed [48-50] and experimentally realized, giving a theoretical coupling efficiency of 88% and measured coupling efficiency of about 35% [50].

Conclusions

While giving high values of coupling efficiency (directional coupler up to 60% and the overall structure up to 40%) and being feasible for fabrication, the directional couplers require additional structures such as silicon waveguide and coupler to silicon waveguide. First of all, this makes the nanocoupler large (several tens of micrometers). Second, additional structures require additional fabrication steps. It is be desirable to make the nanocoupler in as few steps as possible.

2.5. Lens coupler

Classification

Lens is a well-known focusing device. However, we should emphasize that the requirements for the nanocoupler are stricter than to a focusing device, since nanocoupler should provide, apart from focusing, a high coupling efficiency. To be a nanocoupler the lens should have a high transmission and small focused beam that is matched to the nanowaveguide mode field distribution.

Based on the lens material we have divided lenses into following categories:

A. Dielectric lens (Fig. 2.7(a)).

B. Plasmonic Fresnel lens (Fig. 226(b)).

C. Photonic crystal lens (Fig. 2.7(c)).

D. Negative index lens (Fig. 2.7(d)).

E. Hyperlens (Fig. 2.7(e)).

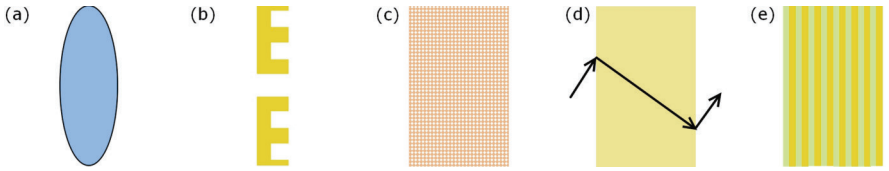

Figure 2.7. Types of lens couplers: (a) dielectric lens, (b) plasmonic Fresnel lens, (c) photonic crystal lens, (d) negative index lens, (e) hyperlens.

2.5. A. Dielectric lens

A dielectric lens is a focusing device known for several centuries. It is well described in the classical optical textbooks [51]. Dielectric lens can provide excellent light transmission, but the resolution of lens is diffraction limited and for coherent light cannot be better than $0.77\lambda_0/NA$, where NA is a numerical aperture. The numerical aperture cannot exceed the refractive index n of a surrounding material. In most of the cases, without using high-index immersion liquids the surrounding material is silica or polymer with refractive index around $n = 1.5$, so the best resolution is about half of the vacuum wavelength, that is $775\,nm$ for the telecom wavelength $\lambda_0 =$

$1.55\,\mu m$. Practical realization of even such resolution requires complex optical setup; therefore a dielectric lens is not a suitable solution for the nanocoupler.

2.5. B. Plasmonic Fresnel lens

The idea of Fresnel lens (or Fresnel zone plate) is also known for a long time. It consists of a set of concentric rings (Fresnel zones), which alternate between transparent and non-transparent. An incident light wave diffracts at the zones' border. An important condition has to be satisfied for that the zone plate works as a lens. The zones should be of such geometrical size that the light wave coming from different zones interferes constructively in the desired focal point.

Using plasmonic effects in the metal-dielectric zone plates is quite new since the fabrication of the fine metallic structures became possible only recently. The plasmons, excited in the concentric grating by the incident light wave, contribute to the energy transfer to the central ring. The constructive interference condition for the light waves should be satisfied not only for the diffracted light waves, but also for the plasmons. A comprehensive review of the plasmonic lenses can be found in [52]. An interesting property of the Fresnel lens is that different wavelengths have different focal points. That gives opportunity to use such lenses for spectroscopy purposes.

Plasmonic lens focusing was experimentally shown in 2002 by Lezec et al. [53]. The theory and performance dependence on the geometry were discussed in the works [54-56]. A lens consisting of concentric rings of holes (so-called nanopinhole lens) was numerically analyzed in the work [57]. Such lens allows for high transmission at $\lambda_0 = 550\,nm$ with focal spot of $250\,nm$, that is just a bit less than half of the wavelength. A subwavelength focusing of the $\lambda_0 = 532\,nm$ monochromatic light into the spot of $\lambda_0/10$ with the transmittivity of 30% has been numerically shown in the work [58]. Such high transmittivity was reached by adding a resonator to the entrance of the lens. Experimental investigation of the subwavelength focusing has also been conducted [59]. Focusing of the visible light with $\lambda_0 = 633\,nm$ to a spot of $468\,nm$ was reported.

As can be seen from the abovementioned results the plasmonic Fresnel lens provides subwavelength focusing but the focal spot is only two times smaller than the wavelength. For the telecom wavelength of $\lambda_0 = 1.55\,\mu m$ that

means focusing to $775\,nm$ that is not much better comparing to the dielectric lens.

2.5. C. Photonic crystal lens.

The negative refraction phenomenon may occur not only in negative index materials but also in photonic crystals at frequencies close to bandgap edge [60]. This effect can be used to make a photonic crystal slab working for light focusing. For example, in the theoretical work [61] a photonic crystal in the so-called canalization regime provided subwavelength focusing down to a spot of $\lambda_0/6$. An antireflection coating, which increases transmission through the photonic crystal lens was investigated numerically in the work [62]. Experimental realization of an $InGaAsP/InP$ photonic crystal lens for $\lambda_0 = 1.5\,\mu m$ was done by Casse et al. in the work [63]. They managed to obtain a focal spot of the area $0.12\lambda_0^2$ that overcomes the diffraction limit. A similar results for $\lambda_0 = 1.55\,\mu m$ and $InP/InGaAsP/InP$ photonic crystal lens was obtained in another work [64], where a focal spot of $0.38\lambda_0$ was obtained.

The photonic crystal lens can indeed provide focusing at specific frequency. However, the resolution of such lens is not much better than a diffraction limit.

2.5. D. Negative index lens

The theoretical idea that a plane slab of a negative index material may focus the light was mentioned by Veselago in 1968 [65]. However, the interest to the negative index material lenses exploded only at the beginning of the 21st century when Pendry showed that a slab of negative index lens not only focus the propagating waves, but also enhance the evanescent waves, which contain the image details [66]. Such perfect lens works in the near-field regime and can provide an ideal image that repeats all the small details of an original source. Moreover, a negative index slab lens may be used not only for focusing and imaging, but also as a coupler between two identical waveguides [67].To work as a super-resolution lens a negative index material should be isotropic. Some special cases of anisotropic materials without spatial dispersion may also be suitable [68].

However, no natural negative index material is known so far and no realistic isotropic optical negative index metamaterials had been proposed by the

time our project began in 2008. We chose the negative index metamaterial lens as the first priority for the nanocoupler realization. Therefore we provide some detailed information on the metamaterials below.

Definition of metamaterials

By definition a metamaterial is an artificial material with unusual electromagnetic properties that are not encountered in nature [69]. Metamaterials can provide very high or very low electric permittivity ε and magnetic permeability μ, very high, close to zero or even negative refractive index n.

The humankind has been using artificial materials for many years in different branches of technique. The ancestors of the metamaterials were frequency-selective surfaces [70]. However, the interest in electromagnetic metamaterials is relatively recent. First, this is due to the fact that resonant structures providing negative electric permittivity [71], negative magnetic permeability [72] and negative refractive index [73] were proposed. Second, development of the cleanroom fabrication technology made possible to structure metals and dielectrics at the nanoscale.

The possibility of materials with high, low and negative refractive index inspired plenty of metamaterials application ideas, such as perfect imaging [66], invisibility cloaking [74], waveguides coupling [67] etc.

Negative electric permittivity

Negative electric permittivity $\varepsilon < 0$ is not exotic in nature. Metals, plasmas, semiconductors, all conductive materials with freely moving electric charges, exhibit negative permittivity in certain frequency ranges. Metals, which are the best for practical applications due to high conductivity and mechanical strength, have "too large" negative permittivity up to a near ultraviolet region. This is why a "diluted metal" – a wire medium has been proposed in 1950-ies [71], [75]. For a comprehensive review of the first "artificial dielectrics" we refer the reader to [76].

The wire medium is a metamaterial that consists of long metallic wires, embedded in dielectric (for examples of 1D and 3D wire medium see Fig. 2.8). The lateral sizes as well as the period of wires should be much less than the wavelength of the incident electromagnetic radiation. The wire medium

possesses strong spatial dispersion [77] that can be reduced by making the wire medium three-dimensional (the wires going along $x-$, $y-$ and $z-$ direction, see Fig. 2.8(b)) and introducing metallic plates attached to the wires [78], [79]. The wire medium shows the Drude-like permittivity spectrum.

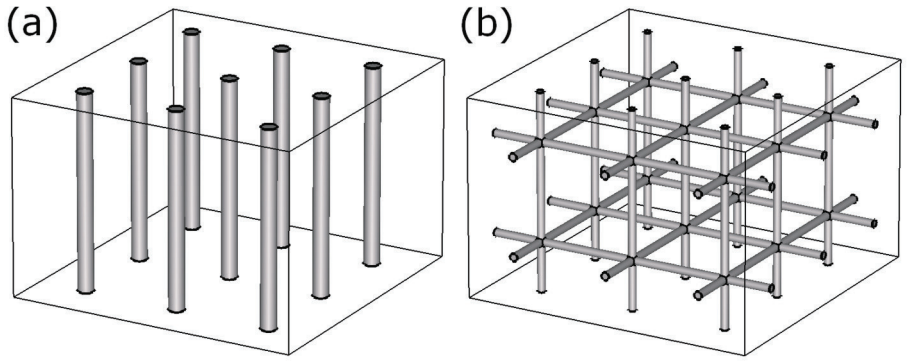

Figure 2.8. Examples of one-dimensional and three-dimensional wire medium metamaterials.

Negative permittivity may also be obtained with resonant electric dipoles. In this case the spectrum is Lorentian, negative ε band is narrow and the losses are higher, since resonant particles are used. So it is advantageous to use the wire medium, which provides non-resonant negative permittivity, rather than resonant dipoles.

Negative magnetic permeability

Even though the split-ring resonator designs providing negative permeability were known since 1950-ies [80-82], the work by Pendry [72] where a negative permeability metamaterial was proposed, caused an explosion of interest to the metamaterials research. This is not strange, since natural material usually have $\mu = 1$ in optical domain. There are negative magnetic materials such as ferrites in the microwave region, but not in the optical range. However, a resonant LC circuit, a split ring resonator [72], allows not only increasing the permeability absolute values but also tuning the frequency response by changing the capacitance and inductance of the circuit. Various designs of the negative permeability materials have been proposed (see Fig. 2.9): split-ring resonators [72], cut-wire pairs [83], [84], magnetodielectric spheres [85] et al.

The smaller the magnetic element (e.g. split-ring resonator), the larger is its resonant frequency. However, it was shown that decreasing the size of the split-ring resonator leads to the saturation in the resonant frequency in the optical region due the kinetic inductance of electrons [86].

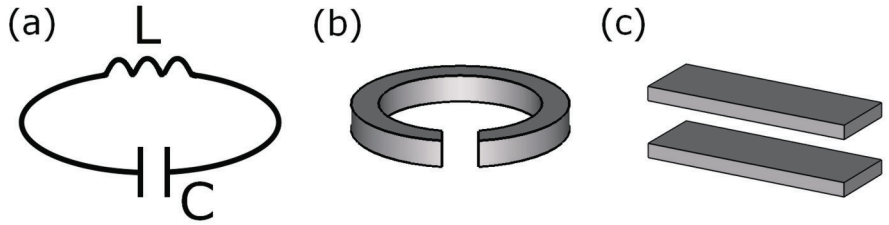

Figure 2.9. Constitutive elements for magnetic resonance and negative permeability: capacitively and inductively loaded loop (a), split ring resonator (b) and cut wire pair (c).

Negative refractive index

The phenomenon of the negative refraction has been considered from the beginning of the 20th century [87-92]. In 1967 V.G. Veselago made an important contribution to the systematic research of negative refraction and negative index metamaterials [65].

The negative refractive index occurs in the materials that simultaneously have negative permittivity and permeability. This is why such materials are also called "double negative". Another denomination for them is "left-handed materials", since the vectors $\vec{k}$, $\vec{E}$ and $\vec{B}$ make a left triad. The waves in the NIMs are backward, that means that the phase of the wave propagates in the opposite direction with the power. For the negative index materials the Snell's law is reverted. However, the negative refraction does not require negative refractive index – it can be observed in the photonic crystals as well.

Even though the concept of negative index materials was proposed several decades ago and the constitutive parts giving negative permittivity and negative permeability were known, only in the beginning of 21st century an idea appeared to combine them to obtain a negative index material [73]. A comprehensive overview of the negative index metamaterials can be found in [93-98].

The materials without active gain medium always have losses. That corresponds to the positive imaginary parts of permittivity $Im(\varepsilon)$, permeability $Im(\mu)$ and refractive index $Im(n)$, if we use the optical convention on the time dependence of the electromagnetic field, namely $\{E, H\}\sim e^{-i\omega t}$. The microwave convention $\{E, H\}\sim e^{j\omega t}$ requires the abovementioned imaginary parts to be negative.

The usual approach to construct a negative index metamaterial, which was first applied in the works [73], [99], suggests combining the negative permittivity constitutive part (wire medium) with the negative permeability elements (SRRs). The idea of double negative metamaterials have been realized with different implementations in microwave and optical regions (see Fig. 2.10): split-ring resonators or cut-wire pairs [100] combined with wire medium [73] and the fishnet structure [101]. Several groups reported fabrication and characterization of negative-index materials (NIMs) [100-103]. Fabrication of such materials is still a challenging task thus triggering the development of new fabrication technologies [104-106].

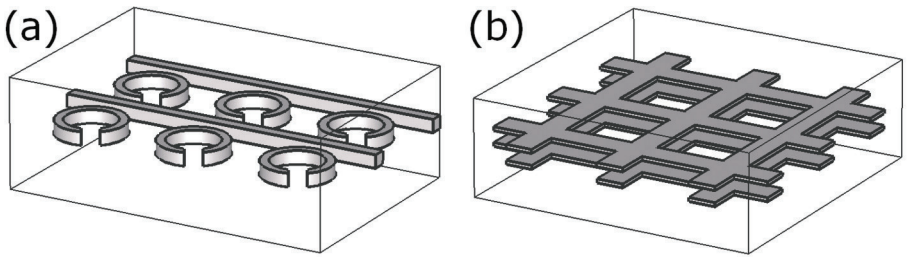

Figure 2.10. Examples of negative index metamaterials: wire medium combined with split-ring resonators (a) and fishnet (b).

Negative refractive index perfect lens

It was shown by V.G. Veselago that a flat slab of negative index material can work as a lens [65]. However, only in 2000 the idea, that a negative index slab does not only provide focusing of the propagating waves but also of the evanescent waves, emerged [66], which have the tangential wave vector component larger than a wavevector in a free space. The fine details, which are transmitted in the evanescent waves, are lost if ordinary dielectric lens is used due to the evanescent waves decay. It was shown that in the negative index material the evanescent waves' amplitude grows due to the

excited surface plasmon polaritons and such lens can focus the light far below the diffraction limit.

Negative index material can find applications in subwavelength imaging, nanolithography and cloaking (see [94] and references number 79-94 therein). We are interested in the application of the negative index perfect lens for nanocoupling [107].

Negative index nanocoupler idea

The idea to use a flat negative index slab for coupling between two identical nano-waveguides was proposed by Degiron et al. [107]. Our idea was to make a concave lens from NIM, thus we can make a coupler between two waveguides with different cross-section (Figure 2.11).

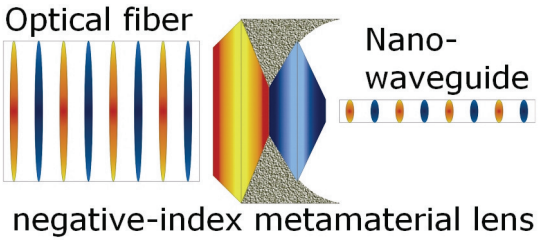

Figure2.11. Idea of negative index nanocoupler, two waveguides and concave lens.

Requirements to negative index material

The material for such coupler should satisfy the following requirement:

1) Negative refractive index,
2) Optical isotropy,
3) Bulkness, that means that the properties of the material should not depend on the slab thickness,
4) Low losses.

Our objective was to develop a material that satisfies these requirements.

Isotropic negative index materials

In the most cases the proposed metamaterials consist of planar layers, since their fabrication is based on the planar technology. That results in the optical anisotropy. Several isotropic NIMs designs have been proposed as well [85], [108-113], but the material parameters needed to obtain the desired resonances in the optical regime can hardly be found, thus limiting the application of such design to the microwave region.

2.5. E. Hyperlens

Another solution for super-resolution imaging implies a material with hyperbolic dispersion, a so-called indefinite medium that simultaneously possesses positive and negative components of the permittivity tensor. This results in not circular or elliptical, as in case of normal positive permittivity dielectric, but hyperbolic isofrequency diagram. An important advantage of the hyperbolic material is that it allows propagating waves with any values of the tangential component of the wavevector.

A medium with hyperbolic dispersion is anisotropic. To reach positive and negative permittivity for different directions one may use either metallic wires or metal-dielectric multilayer stack. In case of wires the effective permittivity can be negative for electric field polarization along the wires, while for the polarization perpendicular to the wires ε is positive. In case of metal-dielectric stack, the polarization parallel to the metallic plates experiences negative ε, while for perpendicular polarization the permittivity is positive.

Hyperlens is a near-field imaging device. The first theoretical work on the wire medium hyperlens [114] showed a subwavelength resolution $\lambda_0/6$ for $\lambda_0 = 1.5\,\mu m$. In another theoretical work [115] $\lambda_0/10$ resolution was achieved in the infrared range. The same device have been successfully simulated and experimentally shown in the microwave range [116-118]. In the work [118] a resolution of $\lambda_0/15$ was demonstrated. Arranging the wires in the taper-like manner, not only image transfer, but also magnification can be achieved. An analysis of the homogeneous medium approximation eligibility for the wire medium superlens was conducted in the work [119]. In the work [120] a lens for color imaging in visible range was proposed. The idea was to engineer the wavelength selective response introducing the gaps in the metallic nanowires. An experimental demonstration of the wire

lens for optical range [121] and for telecom $\lambda_0 = 1.55\ \mu m$ has been recently shown [122]. The resolution measured with a scanning near-field optical microscope was about $\lambda_0/4$. A flat metal-dielectric stack can transfer the subdiffraction image as a near-field lens. Using cylindrical or spherical multilayer system the image may be magnified up to above the diffraction limit. Such magnified image may be registered with an optical microscope afterwards. So the hyperlens can serve as an addition to the standard optical microscope or photolithographic system improving the resolution below the diffraction limit. The first theoretical work [123] showed the resolution of $\lambda_0/4.5$. The hyperlens theory was described in the paper [124]. The experimental realization for the ultraviolet light $\lambda_0 = 365\ nm$, which is a standard wavelength for optical lithography, with resolution less than $\lambda_0/4$ was presented [125]. Theoretical designs for the ultraviolet light giving $\lambda_0/18$ [126] and $\lambda_0/60$ [127] have recently been proposed.

Despite of fantastic resolution, the hyperlens usually has low transmission. This is not so critical for imaging or nanolithography, but of an extreme importance for the nanocoupler.

Conclusions

As we have seen an imaging device such as lens does not necessarily provide high coupling efficiency since the primary goal of imaging is focusing of light, regardless of the transmittivity. Dielectric lens and photonic crystal lens can give high transmittivity (close to 100%) but the focal spot size is limited by the diffraction limit. The plasmonic Fresnel lens can provide a better spatial resolution with the cost of transmittivity. From the resolution point of view, the hyperlens is the best. Theoretically it can provide the resolution as small as $\lambda_0/60$. However, the transmittivity through the hyperlens is not high due to the employment of metal-dielectric multilayer stack or metallic nanowires.

The negative index lens is a promising possibility. Being able to adjust the properties of metamaterial by geometry engineering, it is possible to use it for imaging as well as for the nanocoupling between waveguides. This is why we had chosen it for investigation. The challenges were that there was no isotropic optical negative index metamaterial with small losses proposed and fabricated. It was plenty of work for us.

2.6. Antenna coupler

Definition

According to the definition [128], [129], an antenna is *a device that converts a free propagating radiation into the localized power and vice versa* (Fig. 2.12). For example, television antennas capture the waves propagating in air and transform them into the electrical currents. In other words, an antenna is a coupler that matches together the impedances of the free space and of a waveguide. This application of the antenna accounts for more than one hundred years, since Popov, Markoni and Hertz invented the principles of the radio. Radio and microwave antennas are well-known systems.

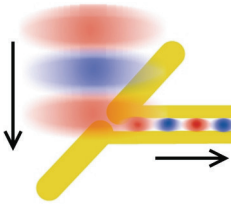

Figure 2.12. An antenna based nanocoupler. The vertically incident light is converted into the localized SPPs propagating to the right in the plasmonic slot waveguide.

Optical nanoantennas have drawn the attention of many research groups [130-139]. NA can be considered as the optical analogue of the microwave and radio antennas [130], [140]. The incident electromagnetic waves excite charges oscillations along the antenna, which are in the optical range nothing else than localized surface plasmons.

Optical vs. radio antennas

Despite a lot of similarities, there are essential differences between radio antennas and plasmonic antennas [141]

1) Metals are not such good conductors in the optical range as in the radio frequencies. Their permittivity is dispersive and it should be described by Drude or Drude-Lorentz formulas [4].
2) The typical penetrations depth is several tens of nanometers [4] and that is very important for metallic nanostructures of comparable size.

3) The usual condition for the resonance of radiofrequency antennas, which is that the length of the antenna must be equal to the integer of the half of wavelength, is not satisfied for the optical antennas and should be corrected [133], [134], [142].

4) The waveguides for plasmons are not much smaller than the antennas. For example, in case of the large television antenna we may neglect the presence of the coaxial cable on the antenna performance. This is not suitable for the plasmonic dipole antenna connected to the plasmonic slot waveguide [143], where metal film is large and influences the antenna performance. However, for the small radio antennas developed in the recent decades the influence of the waveguide is not negligible as well.

Applications

Plasmonic nanoantennas have drawn huge attention in the recent years because of their ability to concentrate the light in the tiny gaps and enhance light intensity [131], [132], [139], [142]. A comprehensive overview of the nanoantennas theory and applications can be found in [128], [141], [144]. Several applications have been proposed for the nanoantennas:

1. Fluorescence enhancement [137], [145-147] and sensing [136], [148], including detection of single nanoparticles [149].
2. Light beam collimation. Nanoantennas were particularly useful for the quantum cascade laser beam collimation [150], [151].
3. Light emitting diodes improvement [152], [153].
4. Solar cells. Nanoantennas may be used to capture the radiation and for non-reflective surfaces as well as for increase in the quantum yield in semiconductor structures [154-157]
5. Directional radiation from quantum emitters [158-164]. In this case a highly directional Yagi-Uda antenna [165] or patch antenna [166] can be used.
6. Photodetectors improvement [167-169].
7. Nanocouplers capturing light from free space to a plasmonic waveguide [143], [170-173] and wireless communication inside a chip [174].

Despite of the fact that from the very beginning antenna served for coupling to the waveguide, the application of an antenna for optical nanocoupling has only recently been proposed [143], [170]. The reason that such natural application of the antenna has not been considered previously is mainly the difficulties of fine metallic structures fabrication.

The advantage of the nanoantenna is that it is very compact. Moreover, the directivity of the antenna coupler can be tuned by design, thus enabling maximal coupling efficiency at any desired angle of incidence. The first nanoantenna couplers theoretical investigations showed the coupling efficiency of 10% [143] for $\lambda_0 = 1.55\,\mu m$ and 28% [170] for $\lambda_0 = 830\,nm$. However, the light in the simulations [143], [170] was focused into a tiny spot of $1\,\mu m$ and $340\,nm$, respectively, that is hardly possible to obtain illuminating the nanocoupler from a single mode optical fiber.

Conclusions

The antenna nanocoupler was a natural but nevertheless underexplored possibility for coupling the light from free space to a waveguide. Moreover, nanoantenna coupler is more compact than other solutions. This is why we chose it is as a second priority for investigation.

2.7. Exotic coupler

In this section we included all other ideas that do not fall into the abovementioned categories. Such coupling ideas are:

A. Random scatterers (Fig. 2.13(a)).

B. Grating coupler (Fig. 2.13(b)).

C. Transformation optics device (Fig. 2.13(c)).

D. Graded index lens (Fig. 2.13(d)).

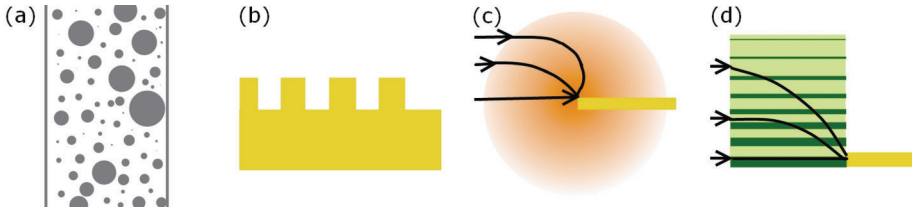

Figure 2.13. Exotic couplers: (a) random scatterers, (b) grating coupler, (c) transformation optics device, (d) graded index lens.

2.7. A. Random scatterers

The nanocoupler can be understood as a mode transforming device. In principle we can designate two extreme cases for mode conversion: a careful adiabatic compression – this is realized by long tapered fibers – and complete mode structure destruction and then construction into another mode in the same way as a new building can be built from the bricks of a ruined house. This analogy would mean introduction of a set of random scatterers. The photons coming from the first waveguide will experience multiple scattering and some of them can couple to the mode of the second waveguide.

It is clear that the coupling efficiency of such random material coupler cannot be high due to the stochastic scattering. However, there has been recently shown that under certain circumstances a disordered medium can work for light focusing [175].

2.7. B. Grating coupler

Grating coupler is one of the most common ways for vertical coupling of the light to a silicon waveguide. It is also used for the excitation of surface plasmon polaritons [28], [176-178]. The grating helps matching the

wavevector with surface plasmon polariton propagation constant. The coupling efficiency up to 68% was theoretically shown [177], [178].

Even though the grating coupler is suitable for the interface surface plasmon polaritons excitation, it cannot be used for the plasmonic slot waveguide due to the specific geometry of the latter.

2.7. C. Transformation optics devices

Inspired by the metamaterials possibilities of obtaining whatever permittivity and permeability values the field of transformation optics has recently emerged [179-181]. The physical problem that the transformation optics solves is the determination of the spatial permittivity and permeability distribution that provides a required wave propagation trajectory. For example, in case of invisibility cloaking engineering it is required that the wave passes around the object not interacting with it [74].

A problem of coupling can be expressed in the transformation optics language. To design the nanocoupler is to determine such permittivity and permeability spatial distribution that provides impedance matching and squeezing of the light from a thick waveguide to a thin one. Some designs for squeezing the light [182] or light concentration [183], [184] have been proposed.

The disadvantage is that very often the transformation optics designs require unusual values of permittivity and permeability that are not realistic even with the help of metamaterials (for example, very large permittivity and permeability without losses or extremely large anisotropy).

2.7. D. Graded index lens

One more interesting way of coupling that is being developed for silicon photonics packaging is a graded index lens. It is called a lens even though its shape is far from lens (etymologically a lens is meant to be of a double convex shape). The idea is to design a multilayer dielectric structure with a gradually changing refractive index in such a way that the wave propagating along the waveguide refracts and concentrates in the thin bottom layer and then is launched into the waveguide. Such device has been proposed for silicon [185] waveguide and it allows for 45% coupling efficiency. The idea of the graded index lens is close to the transformation optics approach. To our knowledge, no graded index lens for plasmonic slot waveguides has

been proposed so far. That can be explained by the subwavelength mode of the latter. Being composed of layered dielectrics, the graded index lens cannot overcome the diffraction limit.

Conclusions

The “exotic” nanocoupling ideas are either non-efficient (random scatterers), non-realistic (transformation optics), or not suitable for the plasmonic slot waveguide (grating and graded index lens).

Chapter conclusions

We figured out 17 possibilities for the nanocoupler realization. Each of them is an interesting direction worth being studied. It is completely impossible to investigate all of them during one PhD project. Therefore we focused on two directions: negative index metamaterial lens and nanoantenna couplers.

The first priority

We chose a negative index metamaterial lens first of all due to promising and underinvestigated properties of optical metamaterials. It was theoretically shown that a flat negative index material slab is able to couple two identical waveguides. We had an idea that structuring the isotropic negative index metamaterial in the form of concave lens we can couple two waveguides of different cross-sections. However, no realistic isotropic optical metamaterial had been proposed before we started the project. The fabrication technology of such materials required improvement. The methods of the metamaterial properties characterization were not ideal. Moreover, the physics of the metamaterials was not completely clear and there were effects to be explored.

We set as an objective to develop a design of the 3D negative index metamaterial for telecom range near $\lambda = 1.55\,\mu m$, that is made from realistic materials and that is optically isotropic, bulk and with low losses. We also needed a reliable method to characterize the metamaterial performance. This is why we spent our time and efforts for the unambiguous and simple method of effective parameters (EPs) retrieval development. Three-dimensional metamaterials with nanosized features are very complex and expensive for the common planar technology fabrication. Therefore we put our efforts into development of an electroless technology of complex dielectric surfaces metallization with silver. During our work on the wave propagation method for chiral metamaterials, we realized the importance of the effects of coupling between metamaterials monolayers and we investigated this question in details on the examples of chiral metamaterials. The results of our work on the negative index metamaterials are described in chapter 3.

The second priority

As a second priority we chose an antenna based coupler. It seemed quite natural to use an antenna for capturing the electromagnetic wave and launching it into the waveguide as it had been done for more than a century in the field of radio- and microwaves. There were very few antenna couplers for the plasmonic slot waveguide proposed and we clearly understood that we can improve the antenna coupler significantly. That was the reason why we chose the antenna coupler as a second priority. The results on the nanoantenna coupler can be found in chapter 4.

Chapter 3. Negative index metamaterial

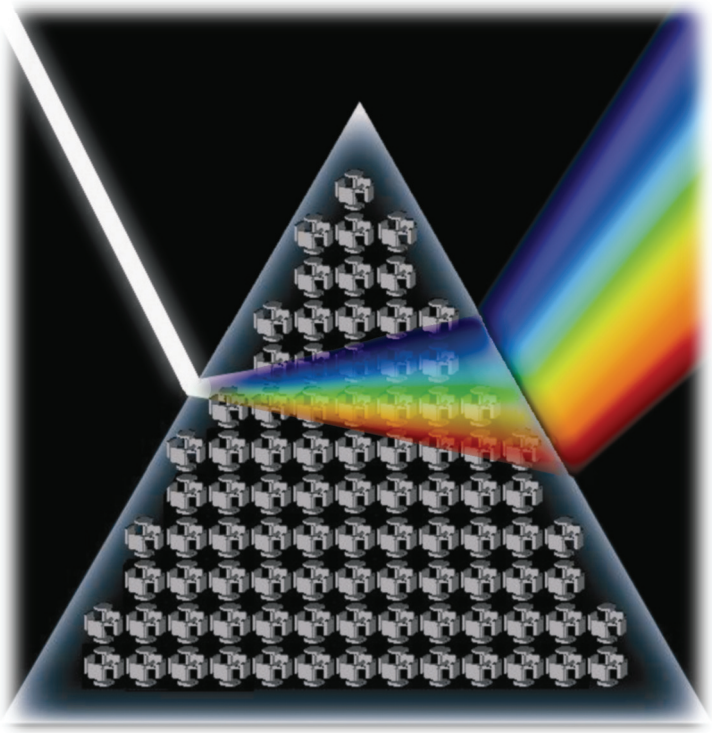

Chapter structure

The chapter is organized in a following way. Section 3.1 reports on the development and simulation of the 3D isotropic negative index metamaterial. Section 3.2 describes the developed effective parameters restoration methods. The details on the electroless metallization technology are provided in section 3.3. The investigation of the coupling effects influence on the homogenization of metamaterials can be found in section 3.4. Conclusions summarize the chapter.

3.1. 3D isotropic negative index material

This chapter describes the development of a three-dimensional isotropic negative index metamaterial design. Section 3.1.1 describes the employed research methodology. The initial "plates and wires" NIM design is presented in the chapter 3.1.2. Section 3.1.3 is devoted to a first cubic symmetric design that gives negative refractive index at the telecom wavelengths, namely "split cube in cage" metamaterial. An improved design, a so-called "split cube in carcass" is described in section 3.1.4. The chapter ends with the conclusions.

3.1.1. Methodology

Effective parameters retrieval

We determined the effective propagation constant in the SCiC by using the S-parameter retrieval method [186-188]. It is based on the inversion of the complex reflection r and transmission t coefficients from the slab of material. The refractive index n and the Bloch (or input) impedance Z_B can be determined via the equations:

$$n = \pm\frac{1}{kd}\arccos\frac{1-r^2+t'^2}{2t'} + \frac{2\pi m}{kd}, \qquad m \in \mathbb{Z} \tag{3.1}$$

$$Z_B = \pm\sqrt{\frac{(1+r^2)-t'^2}{(1-r^2)-t'^2}} \tag{3.2}$$

The modified transmission coefficient is $t' = t\exp(ikd)$ and k is a wavenumber in vacuum.

Effective permittivity ε and permeability μ can be found out as

$$\varepsilon = \frac{n}{Z_B}, \qquad \mu = nZ_B \tag{3.3}$$

The S-parameters based method is widely used, as it is simple. However, it has several limitations, including the ambiguity of the values of the inverse cosine function and applicability of the method to thin slabs only. Applying the inverse cosine function, one obtains several solutions, which differ by $2\pi m/kd$. Only one branch of the refractive index has physical meaning. To select the correct branch we have to start the restoration from low frequencies and then check the continuity of the spectrum (it should be

smooth). We should also mention that the ambiguity in the sign of the refractive index and impedance is removed using the passivity condition for lossy materials, namely $Im(n) > 0$ and $Re(Z_B) > 0$.

Therefore we developed our own wave propagation retrieval method. The overview of the retrieval methods as well as the formulation of the wave propagation method can be found in the chapter 3.2.

For the negative index metamaterial the minus ratio of the real to imaginary parts of the refractive index is usually used as a figure of merit FOM

$$FOM = -\frac{Re(n)}{Im(n)}. \tag{3.4}$$

Isotropy

It is well known that either cubic or random arrangement of the atoms (or meta-atoms) can lead to isotropy in properties [51]. There are three approaches to achieve this goal from the design point of view. The first one proposes to arrange the SRR unit cells into a cubic lattice [110]. A frequency limitation of this design is due to the electromagnetic properties of metals [86], [189], [190]. The second approach suggests exploiting Mie resonances from dielectric spheres [111] arranged in the cubic lattice or distributed randomly [112]. The third approach is the so-called 'nanocircuit paradigm' [113]. The material parameters needed to obtain the desired resonances in the optical regime can hardly be found, thus limiting the application of such design by the microwave region.

We proposed another generic approach for designing an isotropic NIM unit cell in the telecommunication wavelengths as a nested cubic structure [191]. The idea is to combine the cubic symmetric 3D wire medium and 3D split-ring resonators with a cubic unit cell.

However, even if the structure is operated in the subwavelength domain, the required optical isotropy is not straightforward, since the typical resonance wavelengths, evoking magnetic effects, are comparable to the structure size. Here a structure is meant to be subwavelength if the unit cell is smaller than $\lambda/2$ with λ being the wavelength in the outer domains. If this condition is met, only the zero diffraction order is propagating in transmission as well as in reflection for real valued angles of incidence.

There are only a few attempts where the MMs are probed by obliquely incident fields and for different polarizations, mostly restricted to transmission and reflection measurements [110], [192-195]. Since even for an isotropic medium the reflection and transmission coefficients evidently depend on the angle of incidence, it is hardly possible to draw conclusion with respect to the isotropic behavior of the MM.

To ultimately verify whether a highly symmetric split cube in carcass NIM (section 3.1.4) behaves optically isotropic, it is necessary to calculate the dispersion relation $\omega(k_x, k_y, k_z) = const$ where its isofrequency surface $k_z = k_z(k_x, k_y, \omega = const)$ governs the diffraction and refraction properties of the MM [196]. Here, $\omega, k_{x,y}$ and k_z are the frequency, the transverse and the longitudinal wave-vector components, respectively. The latter is frequently termed propagation constant. In the case of the isotropic optical response the surface $\omega(k_x, k_y, k_z) = const$ is spherical. All the other cases correspond to spatial dispersion (dependence of the material properties on the direction of the wave propagation). The details on the calculations can be found in our work Ref. [197].

For computing isofrequency surfaces of a three-dimensional MM we took the complex permittivity of the material into account. This is crucial because most of the band-structure solvers assume lossless media which is certainly incorrect for metamaterials. We use instead a plane wave expansion technique that solves Maxwell's equations in the frequency domain for the periodic structure. The technique solves the respective eigenvalue problem for the generally complex propagation constant of the Bloch modes [198]. Computing the propagation constant as a function of the transverse wave vector for a fixed frequency provides the isofrequency surfaces.

Bulkness

To certify that such assignment of the effective parameters to structures composed of only a small number of functional layers is meaningful and that the homogenization is valid, it is necessary to investigate the convergence of the parameters toward their bulk values [199] when increasing the number of MM monolayers. Additionally, we determined the propagation constant of the Bloch eigenmodes of the infinite structure as well. This is done by

calculating the $\hat{T}$ matrix for a single period and solving the eigenvalue problem

$$\hat{T}\begin{pmatrix} E \\ H \end{pmatrix} = \exp(ik\Lambda)\begin{pmatrix} E \\ H \end{pmatrix} \tag{3.5}$$

to obtain the propagation constant $k = k_{Bloch}$ of the Bloch modes, where Λ is the period in the main propagation direction.

Material properties

The considered metamaterials are assumed to be made from silver (Ag) and embedded in silica (SiO_2). For numerical simulations, silver is regarded as a Drude metal with plasma frequency $\omega_p = 1.37 \times 10^{16}\ s^{-1}$ and collision frequency $\nu_c = 8.50 \times 10^{13}\ s^{-1}$ [200]. Silica's refractive index was assumed to be $n = 1.5$.

Simulation with CST Microwave Studio

The complex reflection and transmission coefficients were numerically calculated with CST Microwave Studio [201], which is based on the final integrals technique. Usually the transient solver (analogue of finite difference time domain method) was used. It allows calculating a broad spectrum in a single simulation cycle. To simulate the infinite array in the lateral direction the prefect electric, perfect magnetic and open boundary conditions were selected for $x-$, $y-$ and $z-$ boundaries respectively. In this case the incident wave (the eigenmodes of the waveguide port) was a plane wave.

We should mention that the perfect electric $x-$boundary and perfect magnetic $y-$boundary are the perfect mirrors in the lateral directions. Two aligned flat perfect mirrors give infinite number of reflections effectively multiplying the array of metaatoms to infinity. This trick may be used only in case of the symmetric unit cell design. In the other cases, for example, when simulating chiral metamaterials, the unit cell (periodic) boundary conditions must be selected and the simulations can be done in CST frequency domain solver. Its disadvantage is that the frequency domain solver cannot handle large structures due to the computer memory limitations. This is not a limitation for the time domain solver; this is why we chose it.

Simulation with Fourier modal method

The split cube in cage and the split cube in carcass (sections 3.1.3-3.1.4) effective properties for an infinite number of layers were calculated with the Fourier modal method [198] by Christoph Menzel at the Friedrich Schiller University of Jena. Up to $31x31$ Fourier orders were retained to achieve convergent results.

3.1.2. Cross and Plates metamaterial

Metamaterial design description

The initial metamaterial unit cell design (see Fig. 3.1) consists of six square plates of size $175\,nm$ and thickness $20\,nm$. The centre of the plate is at $100\,nm$ from the unit cell centre. The plates do not touch each other , so there is a dielectric gap on the edges of the cube created by these plates. Therefore the plates may be regarded as the 3D generalization of the split ring resonator concept. All plates are connected with square $20\,nm$ thick metallic wires, assumed to act as negative permittivity medium.

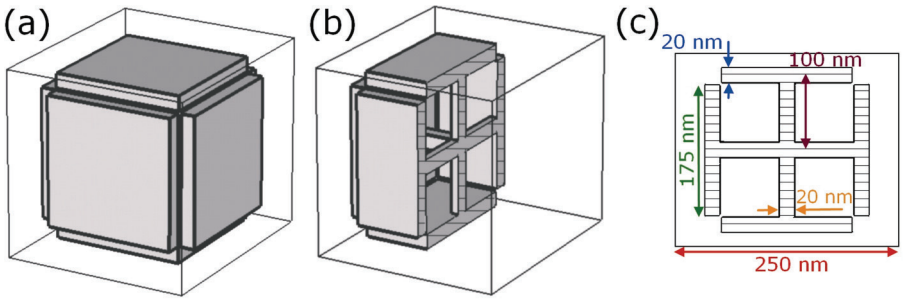

Figure 3.1. Cross and Plates metamaterial design. Prospective view of the unit cell (a) and of the cross-section through the center of the unit cell (b). Side views of the cross-section, geometrical sizes are specified (c).

Effective parameters

We varied several geometrical parameters, but none of them provided negative refractive index in the Cross and Plates metamaterial (see Fig. 3.2). The refractive index is positive and large (up to 4 while the refractive index of silica is 1.5). A similar design with high refractive index was reported in [202].

To understand the behavior of the Cross and Plates metamaterials we simulated the current density and electric field in the structure at the frequency $174\ THz$. The alternating magnetic field induces oscillating loop current (see Fig. 3.3(a)). The electric field induces dipole-like oscillations of the currents in the plates (see Fig. 3.3(b)), but not in the middle cross. Indeed, the plates that form a cube with the narrow slits on the edges screen the cross from the electromagnetic field (see Fig. 3.3(c)). Consequently, the cross inside does not act as a constitutive element providing negative permittivity.

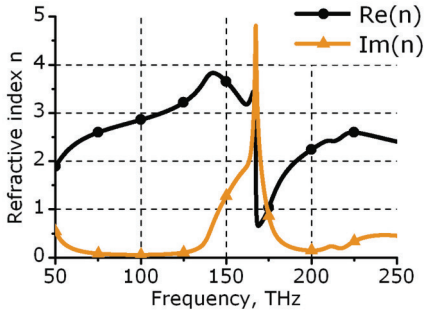

Figure 3.2. Effective refractive index (real part (black circles) and imaginary part (orange triangles)) of the Cross and Plates metamaterial. Refractive index is positive in the full frequency range.

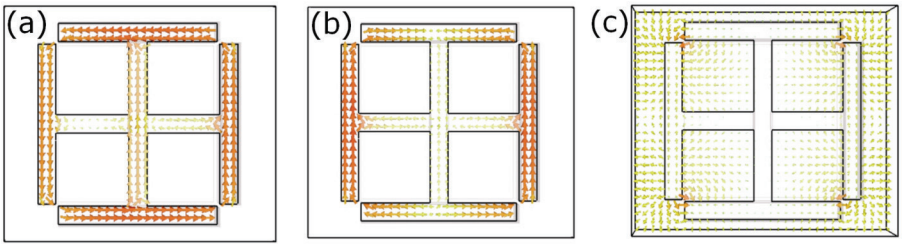

Figure3.3. Cross-section through the middle of the unit cell, side view. Electric field has vertical polarization, magnetic field has polarization perpendicular to the plane of the image. Magnetic field excites an oscillating loop current and a magnetic dipole (a). Electric field excites electric dipole current oscillations (b). Electric field does not penetrate inside the metallic cube and the middle cross does not act as a negative permittivity constitutive element (c).

Conclusion

Cross and Plates metamaterial did not provide a negative refractive index. The crossed wires inside the metallic cube do not act as a wire medium providing the negative permittivity. To be used for negative ε the wires should be place outside the magnetic element and they should be continuous. The plates create a resonant loop that gives a magnetic resonance, but the slits at the edges are very thin and should also be modified. These thoughts lead us to the Split Cube in Cage design.

3.1.3. Split cube in cage

Metamaterial design description

The main modifications of the Cross and Plates design that resulted in the split Cube in Cage design are that we moved the negative permittivity part (wire medium) from the inside to the outside of the cube. The second change is that we made the slits not on the edges of the cubes (that is equivalent to six plates separated with dielectric) but in the middle of the faces.

SCiC unit cell consists of two silver parts embedded in silica (refractive index n = 1.5): the inner split cube (SCube) (Fig. 3.4(a)) and the outer cage (Fig. 3.4(b)). The former acts like an SRR providing negative permeability, whereas the later mimics a 3D wire medium and acts like a diluted metal.

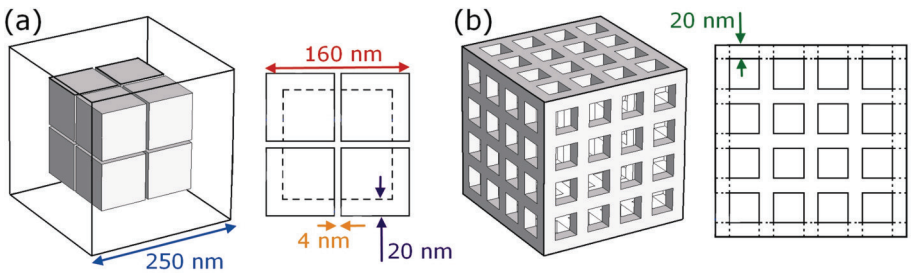

Figure 3.4. Two constitutive parts of the split cube in a cage unit cell design: (a) split cube, (b) cage.

The SCube is a hollow cube with edge length $160\,nm$ and wall thickness $20\,nm$. Symmetrical horizontal and vertical slits of width 4 nm are carved through the centers of the facets (Fig. 3.4(a)).

The cage consists of $a = 250\,nm$ long square wires of width $20\,nm$ equidistantly placed at the periphery of the unit cell, five wires per cube

edge. The cubic structure has lattice constant $a = 250\,nm$, so the cages from the neighboring unit cells are connected. The cage's appearance recalls a design proposed in [202]; however, their physical properties are considerably different. In the structure from [202] the perforated plates of the neighboring unit cells are not connected. As a result such structure does not provide negative $Re(\varepsilon)$but instead exhibits very high positive ε. So it is operating not like a diluted metal, but rather like a dielectric material with high permittivity.

The low wavelength limit below which a MM may be regarded as homogeneous is $\lambda_{lim} = 4an$ [109], with a the lattice constant and n the refractive index of the embedding dielectric. For the defined parameters of the SCiC the homogeneity limit is $1.5\,\mu m$ which corresponds to the frequency $200\,THz$. However, close to the resonances the wavelength can be effectively smaller, so it is always worth checking the correctness of the effective parameter model in the frequency range of interest.

Cage: negative permittivity.

The cage consists of long wires, so it can be regarded as an analogue of a 3D wire medium. The properties of the cage resemble those of plasma [71]. The cage shows high reflectivity (almost 1) and low transmittivity (less than 0.01) even for a single layer. Its effective permittivity has a Drude-like dependence (see Fig. 3.5(a)) similar to that of bulk silver, but approximately one order in magnitude smaller. Increasing the number of wires per edge and simultaneously decreasing the wire width keeping the same amount of metal pushes the permittivity to be 'more negative', i.e. higher in the absolute value. For obtaining large magnitudes of negative dielectric constant ε it is preferable to make a lot of thin wires. At the same time, such an approach poses problems both in simulations, since a large number of fine details require large computational resources, and eventually in fabrication, since multiple processing steps are required. Hence, we consider five wires per edge as a good compromise. Not surprisingly, the effective permittivity and permeability of the cage with wires of width $20\,nm$ show fast convergence with the number of layers. The real part of the effective magnetic permeability is less than 1.0 (see Fig. 3.5(b)), indicating a pronounced diamagnetic response similar to the diamagnetic response of an inductively loaded loop [203].

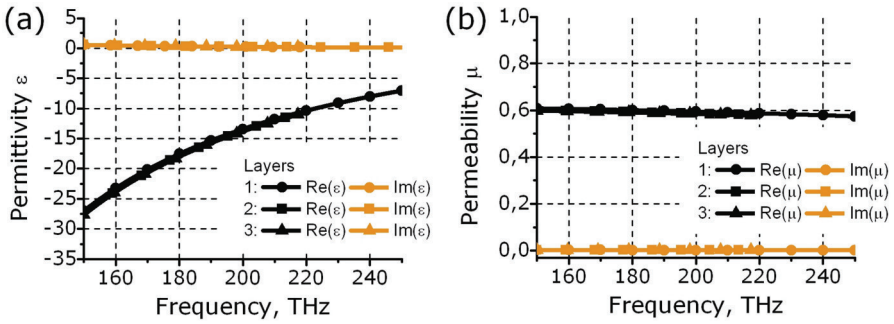

Figure 3.5. Effective parameters of the Cage: permittivity (a) and permeability (b), real part (black) and imaginary part (orange/gray). The cage shows fast convergence of the effective properties with the number of layers: 1 (circles), 2 (squares) and 3 (triangles).

Split cube: negative permeability

The part which brings about a negative magnetic response in our structure is the split cube. The proposed split cube magnetic meta-atom may be regarded as a 3D generalization of a multiple-gap SRR [204]. Magnetic resonance frequency and strength are often explained in terms of an RLC-circuit [205]. In the SCube the slits carved in the centers of the cube's facets play the role of capacitors, while the rest of the SCube plays the role of the inductors and resistors. The size of the slits greatly affects the resonance frequency because of the capacitance associated with it. The variation of the slit from 2 to 7 nm leads to the pronounced resonance frequency shift from 121 to 203 THz (see Fig. 3.6). The minimum of the effective permeability, -0.13, corresponds to the slit size 4 nm, so we chose this value for the negative index metamaterial design.

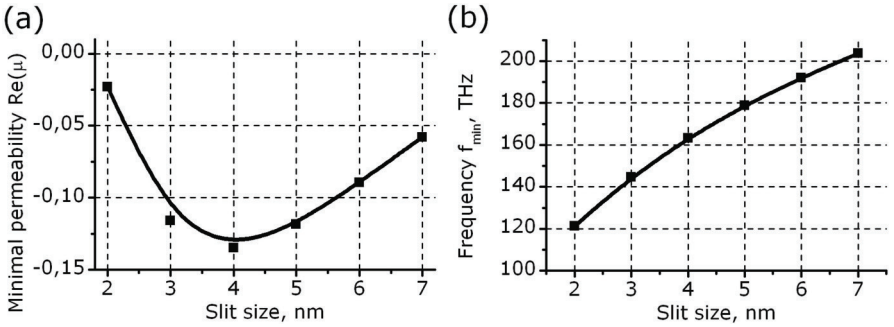

Figure 3.6. Dependence of the minimal value of the SCube permeability (a) and the resonance frequency (b) on the slit size.

The existence of the optimal value for the slit width can be explained by the interplay of the growth of the resonance with the increase of the capacitance and the increasing role of the direct field tunneling through the very thin dielectric gap.

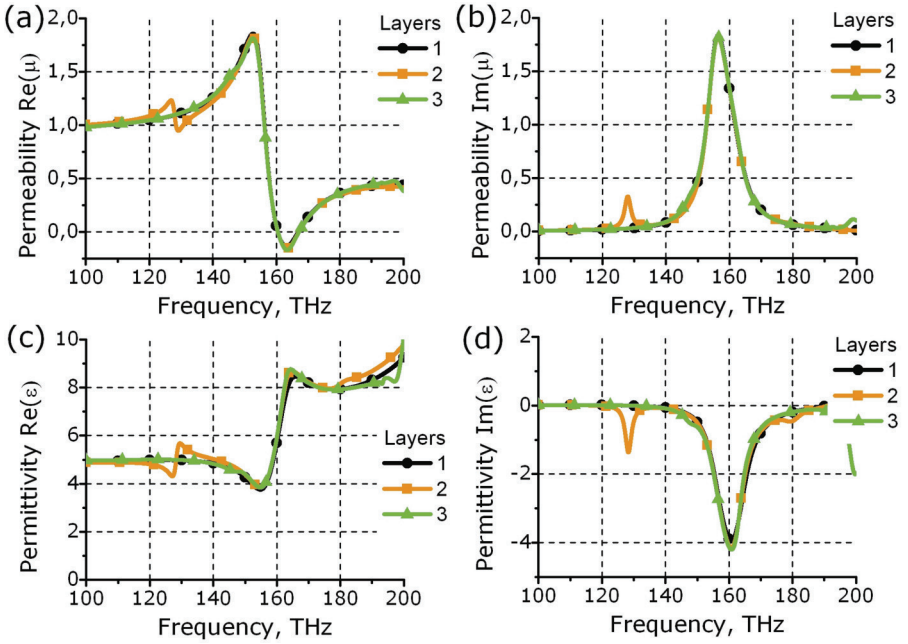

Figure 3.7: Retrieved effective permeability $Re(\mu)$ (a), $Im(\mu)$ (b) and permittivity $Re(\varepsilon)$ (c), $Im(\varepsilon)$ (d) of one (black circles), two (orange/gray squares) and three (green/light gray triangles) layers of the SCube structure. Negative permeability is observed near 165 THz. The permittivity spectrum has anti-resonance around 160 THz.

A decisive effect of such parameters as the SCube's length and wall thickness is that they determine the area of the circuit, and its inductance and resistance. Thickness also influences its capacitance. Higher values for the resonance strength correspond to a larger SCube length and smaller thickness, but as a trade-off the resonance occurs at lower frequency. On one hand the larger length and, consequently, the larger area means easier magnetic dipole excitation. On the other hand the SCube should not be too close to the cage in order to prevent strong interaction between them. The consequence of this interaction is a shift in the effective plasma frequency.

As regards the influence of the thickness we should remember that the SCube is not exactly a SRR, and by increasing the thickness of the side walls

we also change the thickness of the front (and back) walls, which means less penetration of incident waves into the structure. Small thickness allows these waves to penetrate more, but leads in turn to resistance increase, and thus eventually the negative character of $Re(\mu)$ is lost. The optimized value of SCube length is $160\,nm$ and thickness is $20\,nm$. The permeability (Fig. 3.7(a)) and permittivity (Fig. 3.7(b)) restored for a SCube several layers thick show good convergence.

In the imaginary part of the permittivity there is a region of negative values that is occasionally associated with a gain medium. In fact, there is no gain in the SCiC structure and a decision on whether a gain occurs cannot be drawn from the permittivity alone. The quantity that plays a decisive role is the imaginary part of the propagation constant which has to be always positive to ensure an exponentially decaying wave. This holds for all our structures. The encountering of a negative imaginary part of the permittivity is the so called 'anti-resonance' phenomenon, which has been widely discussed in the literature; see for example discussions in [206-209] and is connected to the influence of the excited quadrupole moment which has the same order of magnitude influence on the magnetic field.

Split cube in cage: negative refractive index:

Aiming at a negative refractive index, we insert the split cube into the center of the cage. Transmission through one layer of the SCiC exhibits two peaks, which are better seen as dips in the reflectivity spectra (Fig.3.8(b)).

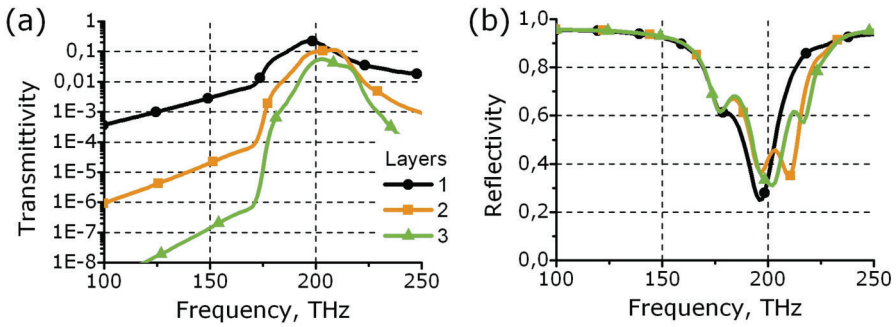

Figure 3.8. Transmittivity (a) and reflectivity (b) spectra of one (black circles), two (orange/gray squares) and three (green/light gray triangles) layers of the SCiC metamaterial.

The first peak around 178 THz shows low transmittivity ($T = 0.05$), but high absorption, $A = 1 - T - R = 0.35$. This peak remains in the spectra with increasing number of layers. This is the frequency region of the magnetic resonance of the SCube and the transmittivity peak corresponds to a region of negative refractive index.

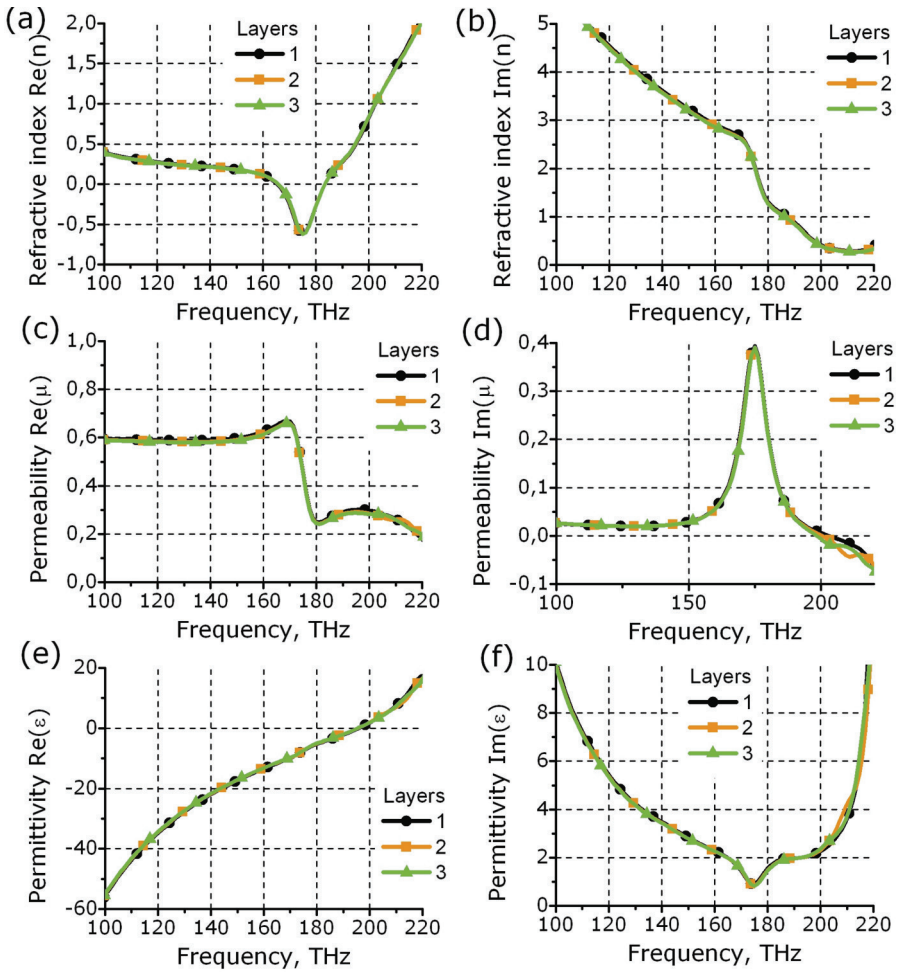

Figure 3.9. Effective refractive index $Re(n)$ (a) and $Im(n)$ (b), permeability $Re(\mu)$ (c) and $Im(\mu)$ (d) and permittivity $Re(\varepsilon)$ (e) and $Im(\varepsilon)$ (f) spectra for one (black circles), two (orange squares) and three (green triangles) SCiC monolayers. Effective parameters show extremely fast convergence with the number of layers.

The remarkable property of our design is that the effective parameters (n, ε, μ, see Fig 3.9) retrieved from the reflection/transmission simulations

converge extremely fast with the number of layers. Within a fairly sufficient approximation we might say that they do not change at all. The effective refractive index $Re(n)$ is negative in the range from $166\,THz$ to $183\,THz$, reaching the minimum value of -0.62 at $175\,THz$ (Fig. 3.9(a)). The maximum figure of merit FOM is 0.33 at $176\,THz$. The SCiC has a large imaginary part of refractive index (Fig. 3.9(b)). And this is not surprising as the SCiC is a singly negative material. There is no negative permeability (Fig. 3.9(c)), in contrast with the case for the SCube itself (Fig. 3.7(a)), and at the same time its permittivity is Drude-like (Fig. 3.9(e)). We conclude that the reduction in the SCiC's magnetic response comes from the interaction between the cage and the SCube structures.

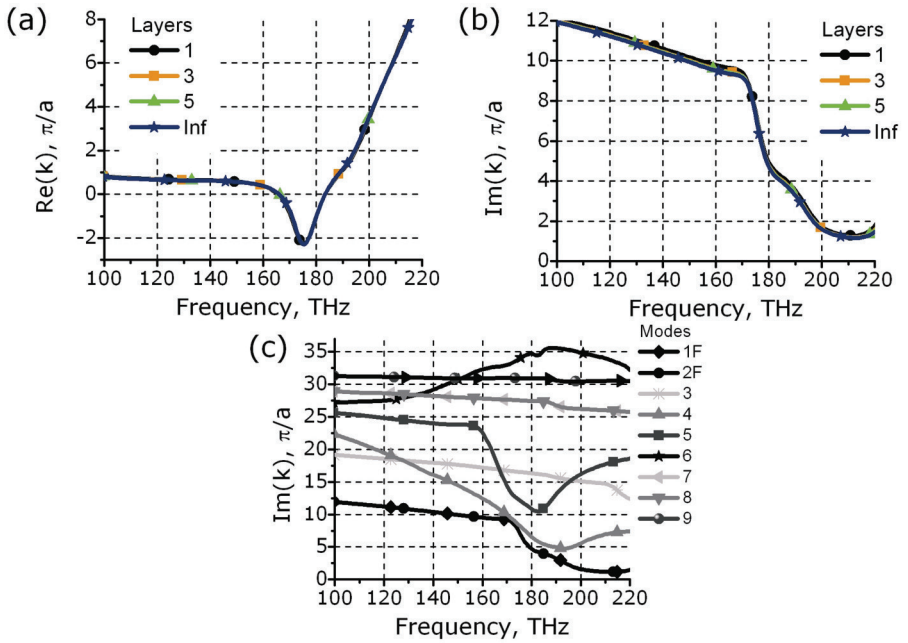

Figure 3.10. Propagation constant for one, three, five and an infinite number of layers of the SCiC $Re(k)$ (a) and $Im(k)$ (b). Damping for different Bloch modes $No\,1-10$ (c). The first two modes are a degenerate fundamental mode.

To confirm that the SCiC metamaterial acts like a bulk material, we calculated its dispersion diagram for waves propagating in the $\Gamma - X$ direction of the simple cubic lattice, imposing periodic boundary conditions and thus mimicking the infinite lattice. The real part of the propagation constant as a function of the frequency for the lowest Bloch mode is

compared with the effective wavenumber $k = k_0$ obtained from the reflection/transmission simulations for the finite number of layers (Fig. 3.10(a)). The graphs completely coincide with each other, thus confirming the thesis that the effective propagation constant is the same for the SCiCs consisting of from one to an infinite number of layers. We would like to note that the lowest mode is doubly degenerate due to polarization independence of the SCiC unit cell.

Discussion

Usually effective wave parameters of MMs are modified depending on the number of layers, but experience convergence with increasing thickness [199]. However, this also pushes the effective parameter concept close to the boundaries of its validity. In our case the effective parameter convergence with the number of layers is impressive. It confirms that we might regard a split cube in a cage as a bulk metamaterial starting from a single(!) layer. Similar fast convergence has been recently reported for meander-like wire metamaterials [210]. Unfortunately, the latter design allows only fixed preferable direction of the electric field.

Poor convergence of the effective parameters can be also explained with the non-negligible impact of higher order Bloch modes. To analyze our structure using such an approach we plot imaginary parts of the wavevector of several Bloch modes extracted with the help of the Fourier modal method (Fig. 3.10(c)). The imaginary part of the k versus ω diagram characterizes losses of the optical modes. The attenuation constants (losses) are comparable for the two modes only. For example, at frequency $173\,THz$ the damping for mode No. 3 is $0.5\pi/a$ higher than the damping of the lowest doubly degenerate mode. However, as this was shown in the work [211] such separation is large enough for the fast effective parameters convergence. Moreover, the higher order mode does not couple at all with the incident plane wave since it has an antisymmetric field distribution, whereas the exciting plane wave only provides a symmetric field distribution [212]. Therefore, it cannot affect the picture of the light propagation in the frequency interval of interest. Otherwise, interaction of two excited modes would lead to slow convergence of the effective parameters that is definitely not observed in our case. The next higher order modes which possess a symmetric field distribution are much more strongly damped as compared to

the lowest order mode and will therefore not contribute to the light transport through the structure. This possibility of exciting only a single mode inside the metamaterial ultimately causes the extraordinary agreement between the effective properties as retrieved for a single layer and those retrieved from the dispersion relation.

The interesting question is that of the nature of the transmission peaks. We identify the first peak at $178\,THz$ as a consequence of NIM behavior occurring in the SCiC unit cell. To prove this we perform time domain simulations (see the map of the electric field in Fig. 3.11(a)). These clearly show the excitation of a loop current (i.e. a magnetic dipole) in the SCube part. As in a $2D$ SRR [72] the electric field in the SCube's slits is much enhanced in comparison with that of the incident wave.

The second peak, which is around $197\,THz$ in the case of one layer, has the highest transmission, around 0.22. The time domain simulation (see the mapping of the electric field in Fig. 3.11(b) reveals the excitation of an electric dipole in the SCube at this frequency. The electric field below and above the SCube is much stronger than the electric field of the incident wave. The field inside the SCube is very weak, as the SCube effectively screens it.

We explain the appearance of this transmission peak as stemming from the introduction of a defect in a conventional Fabry–Perot resonator. Indeed, the cage itself can be regarded as a Fabry–Perot resonator (two reflecting mirrors on either side of a dielectric slab). However, its first transmission maximum according to its spatial parameters is anticipated to be at around $400\,THz$. Therefore, a poor transmission around frequency $200\,THz$ is expected. If we place inside the Fabry– Perot cavity a resonant inclusion with an eigenfrequency somewhere around $200\,THz$, the minimum in transmission will experience significant growth that has a resonant character. This can be easily understood by applying a mechanical model where a massive resonant inclusion rules the properties of the mechanical analogue of the Fabry–Perot resonator—the springs–balls system (Fig. 3.11(c)). For several SCiC layers the Fabry–Perot peak splits corresponding to the number of layers (Fig. 3.8(b)) as a consequence of the coupling between neighboring SCubes.

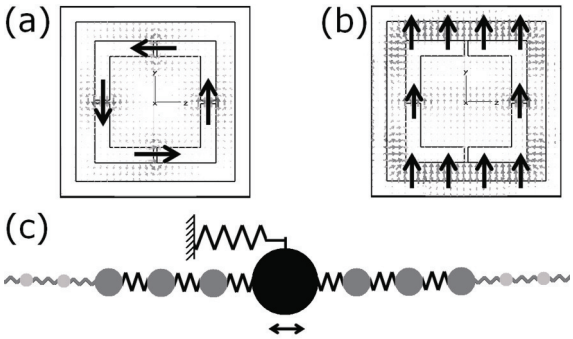

Figure 3.11. Electric field distribution inside the unit cell of the SCiC at magnetic resonance frequency $178\,THz$ (a) and at frequency $197\,THz$ corresponding to the maximum of transmission (b). Mechanical analogy of the Fabry–Perot resonator with resonant inclusion (c).

Conclusion

We analyzed in details the physical behavior and the effective parameters of the split cube in a cage negative-index metamaterial and its constitutive elements. The cage behaves according to the Drude model, giving negative permittivity$Re(\varepsilon)$ over a broad range of frequencies and a diamagnetic response. The split cube is responsible for the negative permeability $Re(\mu)$. Its magnetic resonance strength and frequency strongly depend on the geometrical sizes of SCube.

The transmission spectrum for one layer of the SCiC exposes two pronounced peaks. One is identified as being due to the negative refractive index and another can be explained with the model of a Fabry–Perot resonator with a resonant inclusion. The minimal negative $Re(n)$ for one layer of the SCiC is −0.62. The effective parameters show extremely fast convergence with the number of layers.

Our analysis clearly indicates high sensitivity of the metamaterial design to fabrication tolerances. Even such small changes in slit sizes as $1\,nm$ lead to abrupt transformation of the SCube magnetic and SCiC refractive index behavior. Neither metal–organic vapor phase deposition [105] nor electroless deposition [213] is currently capable of providing metallic nanostructures within the tolerance range below $1\,nm$. To be fabricated, the SCiC design needs considerable simplification. Our attempts to simplify the NIM design resulted in the Split Cube in Carcass metamaterial (section 3.1.4).

3.1.4. Split cube in carcass

Metamaterial design description

The split cube in carcass (SCiCa) structure is a simplified version of the split cube in cage structure [214] containing less number of fine details. Using the nested structures approach the SCiCa is designed such that one element of the unit cell exhibiting magnetic properties is inserted into another element which shows specific dielectric response [191]. The SCiCa unit cell consists of two silver parts embedded in silica.

The outer part, the Carcass, is a three-dimensional wire medium and provides a negative permittivity. The inner part, the split cube, is a hollow cube with slits in the middle of the facets. It is the logical 3D extension of the symmetric split ring resonator concept and provides a magnetic resonance. The details regarding the structure's sizes are indicated in Fig. 3.12.

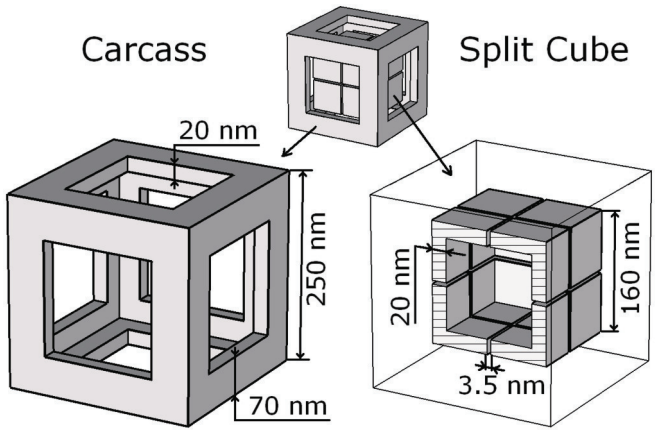

Figure 3.12. Schematic of the split cube in Carcass unit cell. The Carcass (a) serves to provide a plasma-like optical response resulting in a negative effective permittivity. The split-cube (b) provides an artificial magnetic response. Cut of the split cube shows that the split cube is a hollow cube.

Effective parameters and metamaterial homogeneity

To avoid any misinterpretations we will argue at first what we understand as homogeneity. A periodic medium is said to be homogenizable if, at first, it consists of subwavelength unit cells. This first condition simply requires the

period to be smaller than half the wavelength to suppress propagation of higher diffraction orders. At second, light propagation inside the structure is governed by the properties of a single Bloch mode only. And at third, light impinging onto the structure predominantly couples to this particular mode.

Under these assumptions the considered medium is indistinguishable to a homogeneous medium with an arbitrary complex dispersion relation when its properties are probed from an outer medium. Its optical response may be described by nonlocal material parameters which are strongly spatially dispersive in general. The isofrequency surfaces of the dispersion relation, i.e. the normal-mode surfaces, can have an almost arbitrary complex shape. Only if the spatial dispersion is weak the material parameters can become local and the isofrequency surfaces are simply elliptical. Then the so called quasistatic limit is reached for small rations of period over wavelength, i.e. a/λ. The latter assumption is obviously more demanding than homogeneity in general. Hence optical isotropy, i.e., spherical isofrequency surface of the dispersion relation, is attainable only for electrically small objects with cubic symmetry. Therefore a homogeneous medium is not necessarily describable by local material parameters but vice versa.

So to describe a MM as an effectively homogeneous medium, it is necessary to assure at first that light propagation within the MM is exclusively governed by a single Bloch mode. To be sure that this requirement is met, we also have to prove that the incident light field couples only to this particular mode. This is done by comparing the effective plane-wave-propagation constant, as retrieved from reflection and transmission data of a finite structure, with that obtained from the dispersion relation of the lowest-order Bloch mode [212].

The results for the real and imaginary part of both propagation constants (finite homogeneous and infinite periodically structured media) and the formally introduced effective refractive indices $n = ck/\omega$ are shown in Fig. 3.13. For the periodic bulk material we get in general the propagation constants for an infinite number of Bloch modes (which remains nevertheless finite because of the numerical truncation of the number of plane waves retained in the plane-wave expansion) but only the zero-order mode, i.e., the one with the smallest imaginary part is shown. Clearly the values obtained from the finite effectively homogeneous structure are converging astonishingly fast toward the values for the periodic bulk

medium. Thus, two important conclusions can be drawn, first the homogenization of the periodic MM is feasible and second the optical response of a SCiCa-MM consisting of only a few layers equals that of a bulk medium.

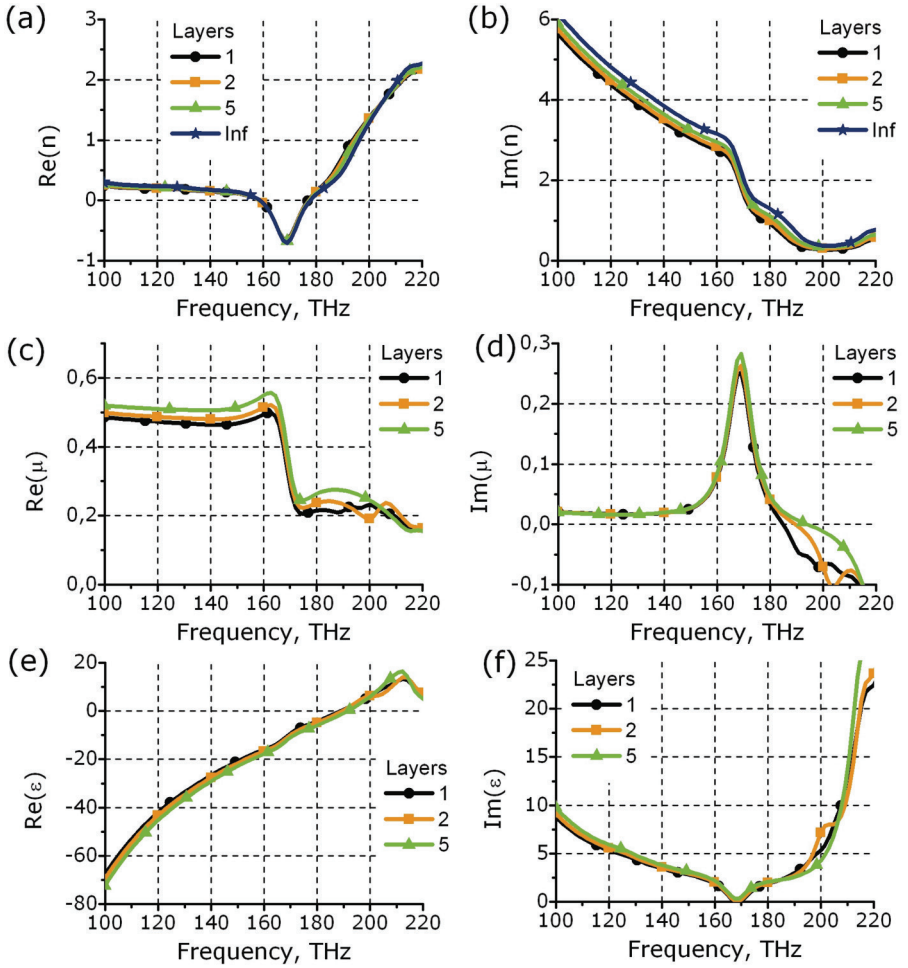

Figure 3.13. Effective parameters of the Split Cube in Carcass metamaterial: refractive index $Re(n)$ (a), $Im(n)$ (b), permeability $Re(\mu)$ (c), $Im(\mu)$ (d) and permittivity $Re(\varepsilon)$ (e), $Im(\varepsilon)$ (f) for the effectively homogeneous finite and the infinite periodic structures at normal incidence. The results for the finite structure are given for an increasing number of layers: one (black circles), two (orange squares), five (green triangles). The blue line with stars corresponds to the values obtained from the Bloch mode with the smallest losses.

The design purpose of the SCiCa is a negative effective propagation constant, and thus a negative effective index of refraction which is clearly achieved for frequencies around $170\,THz$ ($FOM = -Re(n)/Im(n) = 0.35$, ratio of period to vacuum wavelength $a/\lambda = 1/7$). Note that the effective permeability is dispersive but positive in the investigated frequency range. Hence, the SCiCa is a single negative MM resulting in the fairly small figure of merit. For frequencies less than $150\,THz$ the SCiCa is rather a strong absorber due to the large metal fraction.

Since for the scattering problem at the finite system the coupling to different Bloch modes was rigorously considered, we can conclude that the propagation of light through the structure as well as the coupling process is almost entirely dictated by the fundamental Bloch mode only, again underlining the validity of the homogenization procedure. This is clear as the propagation constant values for the finite and the infinite structures coincide. Although not shown here the propagation constants for oblique incidence are also rapidly converging toward the bulk values. Also the effective impedance is converging for normal incidence as well as for oblique incidence.

Hence, we can fully rely on describing light propagation in terms of the dispersion relation assuming that light will couple to this fundamental mode only. Note that from the results above we can also conclude that the SCiCa fulfills all requirements for the homogenization of the MM, namely, the structure is subwavelength (compared to the wavelength of the environment) and light propagation inside the structure is determined by a single Bloch mode to which an external light field predominantly couples.

Isotropy

The SCiCa has the highest possible symmetry for a periodically arranged MM. In particular, it is mirror symmetric with respect to three orthogonal axes. This excludes any effects resulting from first-order spatial dispersion like chirality [110], [215]. Due to the cubic symmetry the three main propagation directions are equivalent. Hence, the optical response of the SCiCa is supposed to be described by scalar effective material parameters in the quasistatic limit, i.e., the optical response should be isotropic. From these symmetry considerations one usually draws the conclusion that the SCiCa might be an ideal candidate for an isotropic negative index metamaterial.

The main property we are interested in is the optical isotropy of the SCiCa, in particular, in the spectral region around $170\,THz$ where the propagation constant is negative. To judge this we proceed in calculating the isofrequency surface.

Due to the symmetry of the structure the complete isofrequency surface can be constructed by only calculating the dispersion relation in the irreducible Brillouin zone. The real and imaginary parts of the propagation constant for a fixed frequency of $170\,THz$ are shown in Figs. 3.14(a) and (b). For comparison we show in Figs. 3.14(c) and (d) the analytically calculated isofrequency surface of an isotropic medium, which has the same refractive index as SCiCa at normal incidence.

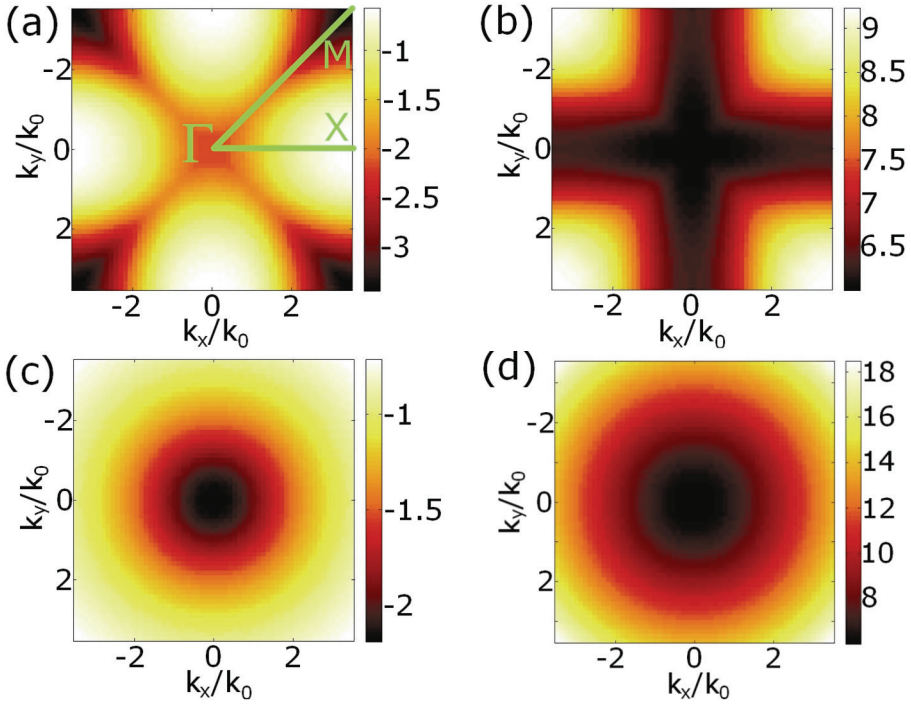

Figure 3.14. (a) Real and (b) imaginary parts of the propagation constant of the lowest-order Bloch mode in the first Brillouin zone. (c) Real and (d) imaginary parts of the propagation constant of an isotropic medium with the same refractive index as the SCiCa at normal incidence.

At first we notice that both the real and the imaginary parts of the propagation constant of the MM are not rotationally symmetric and

monotonically changing with increasing absolute value of the tangential component k_t as for the isotropic medium. In particular, the dependency on the transverse wave vector is tremendously different when compared to the isotropic medium. While the real part is monotonically increasing with k_t in the $\Gamma - X$ direction it is non-monotonously decreasing in the $\Gamma - M$ direction. Also the imaginary part is strongly increasing in the $\Gamma - M$ direction and only slowly varying in the $\Gamma - X$ direction. Hence, any formally introduced effective refractive index would explicitly depend on the transverse wave vector $k_t = (k_x, k_y)$. Therefore, the introduction of a global effective refractive index is pointless since no additional information is obtained. Nevertheless for paraxial wave propagation the introduction of a local effective refractive index is feasible. Near the Γ point the isofrequency surface is approximately spherical where the validity of this approximation strongly depends on the frequency and the wavelength to cell-size ratio as discussed later in detail.

It should be mentioned that the choice of real valued k_x and k_y is arbitrary to a certain extent. In lossy media like metamaterials, in general, the complex nature of the dispersion relation cannot be neglected. Hence the dispersion relation could also be calculated for complex valued k_t. On the other hand it is pointless to provide these values as they are not accessible in any experiment. The tangential wave-vector components are continuous at boundaries and only real valued plane wave solutions can exist in free space, therefore this choice reflects experimental constraint.

To more quantitatively evaluate the optical isotropy of the MM, we monitor in the following the relative deviation between the numerically obtained propagation constant and the ideal spherical isofrequency surface. To quantify this deviation we assume that the effective refractive index at normal incidence is valid also for any other propagation direction. From symmetry considerations and the exemplary results in Fig. 3.14 we conclude that it is sufficient to investigate the dependency in the high-symmetry $\Gamma - X$ and $\Gamma - M$ directions assuming that for a fixed value of $|k_t|$ these points are extremes of the isofrequency surface. In the Fig. 3.15 the real part of the propagation constant is shown as a function of the frequency and of the tangential wavevector component k_t/k_0, where k_0 is the free-space propagation constant. The edge of the first Brillouin zone for the largest possible frequency ($200\ THz$) would be at $k_t/k_0 = 3$ because of

$$\frac{k_t}{k_0} = \frac{\pi}{ak_0} = \frac{\lambda}{2a} = \frac{1.5\ \mu m}{0.5\ \mu m} = 3. \Delta x \Delta k_x \geq 2\pi. \tag{3.6}$$

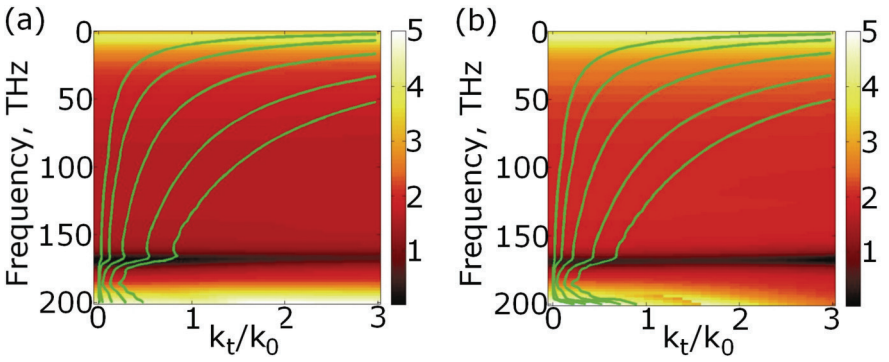

Figure. 3.15. (a) Real part of the propagation constant as a function of the frequency and the angle of incidence where the plane of incidence is parallel to the coordinate axes. (b) The same as (a) with plane of incidence rotated by $\pi/4$ i.e., the $\Gamma - M$ direction. The green is lines correspond to the relative deviations (0.02, 0.1, 0.5, 2, 5) % (from left to right).

The most important frequency region here is the black domain of negative refraction where the split cube provides the artificial magnetic response. Also the isoerror lines for the relative error

$$\Delta = \left| \frac{|k_z| - |k_z|_{ideal}}{|k_z|_{ideal}} \right|, \tag{3.7}$$

with $k_z = \sqrt{k_z^2(k_t = 0) - k_t^2}$ are given for several values as green lines. The quantity Δ is a measure for the relative deviation of the modulus of the propagation constant for oblique incidence from that for normal incidence. We have taken the module because all quantities are complex-valued. The isoerror lines in the non-resonant regime $\omega \leq 150\ THz$ scale approximately as $1/\omega \sim \lambda$. This results from the fact that the homogeneous medium approximation improves with a decreasing unit cell size to wavelength ratio a/λ. For frequencies larger than $160\ THz$ the structure becomes resonant and an abrupt change in the isoerror lines is clearly observable.

Obviously in the resonant regime the MM can be only considered isotropic if the ratio a/λ is much less than in the non-resonant regime. In general the situation is identical for both planes of incidence ($\Gamma - X$ and $\Gamma - M$

directions). However, for larger frequencies the deviation of the calculated isofrequency lines to the ideal ones is slightly smaller in $\Gamma - M$ than in $\Gamma - X$ direction but not significantly.

Note that the introduction of the quantity Δ is just one option to quantify the deviation of the pertinent isofrequency surface from the ideal one. Other measures are also possible, where, for example, the deviation of the length of the actual wave vector compared to the length of the wave vector in an isotropic medium yields qualitatively the same results.

Some remarks concerning the investigated parameter space should be done. Here, the dispersion relation is not calculated up to the edge of the Brillouin zone but for fixed tangential wave vectors which translate for propagating waves into certain angles of incidence. This is more useful since for very low frequencies it is not possible to provide incident plane waves with tangential wavevector components k_t that are in the order of π/a where a is the lattice constant. Furthermore, plane waves with wave vectors in the dimension of the lattice vector will always sense the details of the periodicity. In this case the issue of an optically isotropic structure is pointless. Also for small frequencies the isofrequency surfaces are not rotationally invariant but these domains are not accessible to the experiment. Assuming the outer medium to have a permittivity ε then the line given by $k_t/k_0 = \sqrt{\varepsilon}$ corresponds to a grazing incidence and to the angular domain accessible from free space.

Up to here we have only discussed the properties of the fundamental Bloch mode with the smallest imaginary part since this mode essentially dictates light propagation. While considering the coupling of an external field to this Bloch mode we had to suppose that only this mode is excited thus restricting ourselves to a certain polarization state of the incident light. Nevertheless, in the general case of arbitrarily polarized incident light one has to discuss both eigenstates of the polarization separately, as both may exhibit different propagation constants. Assuming an isotropic homogeneous medium the eigensolutions are always degenerated, i.e., they have the same propagation constant and it is possible to define the eigenmodes as orthogonally and linearly polarized plane waves. This is also the case for normally incident light on a $C4$ symmetric structure as the isotropically designed SCiCa metamaterial. For oblique incidence the situation changes dramatically because both linear-polarized eigenstates may encounter different structures.

Both eigensolutions may have different eigenvalues for the propagation constant. One may compare the situation with a uniaxial crystal, where the optical axis is aligned with the z axis. For normally incident light the structure can be considered as being isotropic whereas at oblique incidence the eigenvalues for the two eigenpolarizations are different. Note that the eigenpolarizations are always orthogonally, linearly polarized for planes of incidence being identical with mirror planes of the metamaterial.

Considering the SCiCa as an effectively isotropic homogeneous medium, we expect that both the two fundamental Bloch modes are degenerated and the effective refractive index is isotropic. So as soon as the eigenvalues for both Bloch modes deviate from each other, the medium cannot be described as being effectively isotropic. This deviation can also serve as a measure for a meaningful MM homogenization.

In Fig. 3.16(a) and (b) we show the real and the imaginary parts of the propagation constant for the two Bloch modes with the smallest losses at a certain angle of incidence and in Fig. 3.16(c) their difference as function of the frequency. Clearly for low frequencies the propagation constants for both modes are identical. As soon as the frequency increases the propagation constants start to deviate from each other hence the SCiCa cannot be considered as optically isotropic anymore. The deviation is of course the stronger the larger the angle of incidence is. At normal incidence they are identical as explained in detail before. The conclusions to be drawn from these figures are of course in line with those from the angular dependency of the first Bloch mode only. The structure can be considered as being isotropic only for small frequencies and a limited range of angles of incidence where this angular range is the larger the smaller the frequency is.

Finally, some further remarks are necessary in order to elucidate the significance of the obtained results for other spectral domains. Although we have investigated a specific high-symmetry metamaterial here designed to operate in the optical domain, we firmly believe that the conclusions to be drawn will not change significantly by modifying the operational wavelength. First of all, the structure sizes when compared to the vacuum wavelength are already quite small. At the frequency of interest the wavelength to cell-size ratio is approximately 7. Even in the gigahertz range this ratio does not exceed 10. From Fig. 3.15 it can be deduced that even in the non-resonant regime for $\lambda/a = 15$ the deviation between the expected

response and the achieved one exceeds 2% already at $k_t/k_0 = 1$. The structure cannot be made significantly electrically smaller if resonant metallic particles are used to achieve the artificial magnetism. But since the unit-cell design itself is already of cubic symmetry the deviations of the expected isotropic optical response to the actually obtained one is hence only due to the insufficiently large wavelength to cell-size ratio.

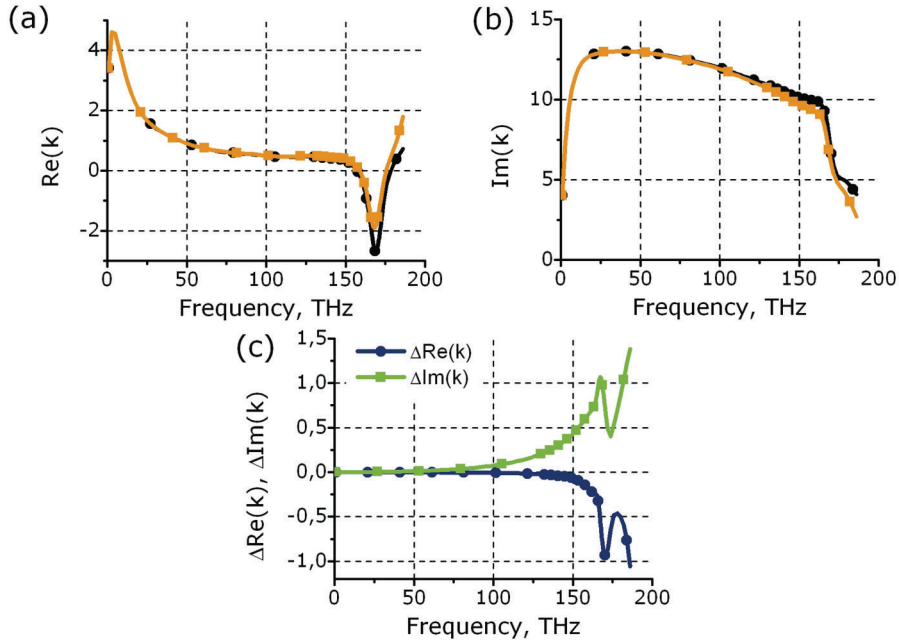

Figure. 3.16. Real part (a) and imaginary part (b) of the propagation constant k, μm^{-1} of the two lowest damped Bloch modes at $k_t = k_0$ that are degenerated at normal incidence. (c) The difference between the real parts (blue, lower line)and the imaginary parts (green, upper line)of these two modes as function of the frequency. In the quasistatic limit, i.e., $\lambda \to 0$ the difference is vanishing and both modes are degenerated.

Conclusion

We investigated the optical response of a highly symmetric SCiCa MM in the negative refraction regime. The SCiCa exhibits cubic symmetry, i.e., the highest possible symmetry for periodic metamaterials and is therefore considered a very promising candidate for an isotropic negative refractive-index material. By investigating at first a finite number of functional layers and the convergence of the corresponding effective parameters to the values

obtained from the dispersion relation of the infinite structure we can conclude that the SCiCa fulfills all requirements of a homogenizable metamaterial. Already a single functional layer can be described by its bulk properties as only a single Bloch mode determines light propagation inside the structure. Nevertheless our investigation of the isofrequency surface of the dispersion relation clearly shows that even this metamaterial with the highest symmetry is far away from having an optically isotropic response in the region of negative refraction. This non-isotropic response is rather due to the large electrical size of the resonant unit cells than due to an insufficient design and will unlikely to be solved by shifting the spectral domain of operation to the microwave regime. An important conclusion is that one must not conclude from high symmetry on an optically isotropic response. Hence, optical isotropy of a MM can be only deduced from a careful inspection of the dispersion relation by taking into account the material dispersion of metal too. This is an important message to the designers of isotropic optical metamaterials.

Conclusions

We proposed a design of a cubic symmetric negative index metamaterial. The initial Split Cube in Cage design was simplified to Split Cube in Carcass. It consists of an analogue of the 3D split ring resonator (Split Cube) embedded into the three-dimensional Carcass, which is a sort of negative permittivity wire medium. The proposed negative index metamaterial is bulk. However, despite of the cubic symmetry, the Split Cube in Carcass material is anisotropic. As the isofrequency diagrams show, the metamaterial exhibits strong spatial dispersion in the resonance region. This makes the Split Cube in Carcass inappropriate for the negative index superlens construction. Moreover, the metamaterial is lossy. However, this is an issue related to all passive optical metamaterials proposed up to date. What concerns spatial dispersion, it is possible to partially overcome it by the design of the metamaterial unit cell. For example, it has been proposed to construct a fishnet super-cell and then to optimize the geometrical parameters of each layer in order to obtain the isofrequency surface as close as possible to the isotropic one. However, the geometric design tuning cannot solve the problem of losses. The losses can be minimized by incorporating active medium in the metamaterial and that is a topic of current research of several scientific groups [216-218].

3.2. Effective parameters restoration

This chapter describes the developed methods for unambiguous and simple effective parameters restoration. Section 3.2.1 makes an overview of the existing restoration methods. The formulation of the wave propagation retrieval method is given in section 3.2.2. Section 3.2.3 is devoted to an extension of the wave propagation retrieval method to the chiral metamaterials. The most advanced method, which is based on the Bloch mode analysis, is presented in section 3.2.4. The chapter ends with the conclusions.

3.2.1. Effective parameters restoration methods overview

Motivation

It is convenient to describe the properties of the MMs with averaged effective parameters (EPs), such as refractive index n, impedance z, permittivity ε and permeability μ, provided that these EPs can be introduced [219]. The EPs simplify significantly the description of the MMs behavior, including the propagation of electromagnetic waves inside a MM slab and their reflection and transmission at the MM slab interfaces.

Classification

The importance of the EPs determination is emphasized by a variety of the existing retrieval methods. They can be divided into several groups according to the simulated or measured parameter that is used for effective properties retrieval.

1. Methods based on reflection/transmission (or S-parameters) [187], [188], [220], which are also known as the Nicholson–Ross–Weir (NRW) methods [219]. These methods are simple to use, and are widespread among the scientific community. Such methods require only the knowledge of reflection and transmission amplitudes and phases. However, these methods have serious limitations. They suffer from the ambiguity of the solutions (so-called "branch problem") as the inverse trigonometric functions are used. That requires simulation or measurement of broad spectra and then making them smooth and continuous starting from low frequencies. The Kramers-Kronig relations may also help to choose the correct solution [221]. Another limitation is that these methods can only be applied to thin MM slabs since

they rely on the transmission simulation/measurements and due to the "branch" problem.

2. Methods based on the wave propagation phenomena [222], [223]. The idea of these methods is to use wave amplitude and phase inside the slab, not the reflection and transmission coefficients. The first method [222] for finding EPs is by fitting the fields inside MM slab by the field inside a Fabry-Perot resonator filled with a homogeneous medium. The second method [223] is much simpler, because it does not involve any fitting procedure and is free from the "branch" problem, since it uses the propagation of a single wave in the quasi-semi-infinite MM.

3. Field averaging methods [224], [225]. These methods use the definition of the material EPs and determine permittivity and permeability as the proportionality coefficients between the field vectors. However, in practical realization these methods are complicated, as they require using various surfaces and contours for averaging different fields. This may be an issue, e.g. when one is optimizing the MM design.

4. Analytical and semi-analytical methods [226-231], which use the solution for the meta-atoms polarizabilities and then analytically find the properties of the whole array of the meta-atoms. These methods are applicable to a limited number of simple systems, for which analytical solution is possible (cylindrical or spherical atoms). We should also mention here the method for retrieving non-local dielectric function with the finite-difference frequency domain simulation [232]. In the latter the dielectric function tensor is defined through the polarization of the meta-atoms and then it may be used to find out the effective permittivity and permeability.

5. Method based on a single-interface scattering problem [233], when the transmission and reflection amplitudes of the plane wave incident on the boundary between uniform half-space and semi-infinite MM are used for the EPs restoration.

6. Quasi-mode method [234] based on the calculation of the optical density of states of the MM unit cell surrounded by the homogeneous medium. The effective parameters are found by changing the surrounding medium permittivity and permeability and maximizing the optical density of states. The method is computation-demanding, since it requires four-parameter optimization for each simulation frequency.

The brief classification above is provided for linear MMs with linear polarization as an eigenmode. Other retrieval methods for bianisotropic [105], [235], [236], chiral [102], [237], nonlinear MMs [238], and MMs with gain [218], [239] are not considered.

The simplest way to restore EPs is to assign reflection and transmission coefficients calculated or measured for a MM slab to a slab of the same thickness made from a uniform material. However, it often leads to violation of passivity condition. This situation has been actively discussed in the literature [206-209], [219], [240], [241]. The discussion reflects the fact that there is no universal procedure of how to determine EPs for three-dimensional metal-dielectric composites with complex topology.

Wave and material effective parameters

The state-of-the-art of homogenization infers that retrieved EPs are of two types [188], [219], [240]:

(1) Material (or local) effective parameters ε_M and μ_M. They give the relation of the field vectors $\vec{D} = \varepsilon_M \varepsilon_0 \vec{E}$ and $\vec{B} = \mu_M \mu_0 \vec{H}$. Their relations to the refractive index n and wave impedance z_W are:

$$n = \sqrt{\varepsilon_M \mu_M}, \tag{3.8}$$

$$z_W = \sqrt{\mu_M / \varepsilon_M}. \tag{3.9}$$

(2) Wave (or non-local) effective parameters ε_W and μ_W. They are usually restored from the reflection and transmission coefficients of a MM slab [220] and they may allow one to calculate the reflection and transmission of a MM slab of another thickness. They often depend on the thickness of the MM slab (see, e.g. Ref. [242]), with only rare exceptions [243].

For a homogeneous medium with the structural element characteristic size a much less than the wavelength λ the material and wave EPs are the same. However, in many practical cases MM's unit cell is only $a \sim \lambda/10 - \lambda/4$ and material and wave parameters are not equivalent to each other [240]. It is obvious that the reflection from a MM slab should depend on whether the MM slab termination coincides with the border or with another cross-section of the unit cell, so the wave EPs depend on the MM opening cross-section. Material EPs depend only on the properties of the material (we do not consider here the problem of the Drude transition layers [219]). Namely

material EPs can describe the wave behavior inside the metamaterial and are important, for example, for the superlens performance of the slab with negative refractive index [66].

Based on these considerations, we can summarize that the existing retrieval methods are either simple but give only wave effective parameters, usually with the branch ambiguity, or they provide the material parameters but at the cost of complexity in realization and/or limited applicability.

Our objective

Our objective was to develop an effective parameters retrieval method that is simple in realization and unambiguous in the metamaterials properties determination.

3.2.2. Wave propagation retrieval method

In this section we propose a direct method of effective parameters restoration that is based on the wave propagation phenomenon [223].

Mathematical formulation

The simulation geometry assumes the MM slab infinite in $x-$ and $y-$ directions and semi-infinite in $z-$ direction of propagation (see Fig. 3.17). The normal incidence of the wave occurs from vacuum. The fields inside each unit cell have complicated spatial distribution, so in order to apply the effective medium description we should abstract from composite intrinsic structure and regard it as a bulk homogeneous material. Thus we average the components of complex field vectors in each of the unit cells. We chose the electric field but the procedure can be easily reformulated for the magnetic field. One more assumption we utilize here for the sake of simplicity is the scalar procedure of restoration, which means linear polarization of the fields with designs exhibiting no chirality or anisotropy in the direction of propagation.

We describe the light wave of frequency ω as a modulated plane wave:

$$E(x,y,z) = E_0 u(x,y,z) \exp(-ik'z - k''z)\,, \qquad (3.10)$$

where $u(x,y,z)$ is a modulation function periodic in the $z-$direction with the same period a as MM, $k' = n'\omega/c$ and $k'' = n''\omega/c$ are the real and imaginary parts of the wavenumber connected with the real n' and imaginary

n" parts of the refractive index. Function $u(x, y, z)$ changes quickly over the unit cell comparing with the exponential ansatz $\exp(-ik'z - k''z)$.

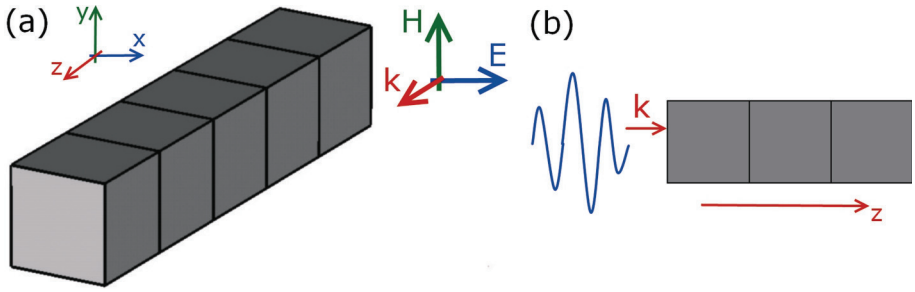

Figure 3.17. Wave propagation simulation configuration, prospective view (a). The wave is assumed to propagate in the positive $z-$direction. Electric and magnetic fields are polarized along $x-$ and $y-$ axes respectively. A short pulse is incident on the effectively semi-infinite waveguide, side view (b).

Assuming the slow variation of the phase, which is valid under the generally accepted homogeneity condition $\lambda_{eff} > 4a$, the averaged over the N^{th} unit cell electric field is equal to

$$\langle E\rangle_N \approx E_0 \exp(-k''z_N)\exp(-ik'z_N) = A\exp(-i\phi), \qquad (3.11)$$

where $z_N = (N - 1/2)a$ is the coordinate of the N^{th} unit cell's center, $A = |\langle E\rangle_N|$ and $\phi = \arg\langle E\rangle_N$ are the amplitude and phase of the field averaged over the N^{th} unit cell volume. Both parts of the refractive index are straightforwardly derived assuming linear changes in phase $\Delta\phi$ and amplitude logarithm $\Delta \ln A$ with a number of unit cells ΔN (see Fig.3.18):

$$n' = -\frac{\Delta\phi}{\Delta N}\frac{c}{a\omega}, \qquad (3.12)$$

$$n'' = -\frac{\Delta \ln A}{\Delta N}\frac{c}{a\omega}. \qquad (3.13)$$

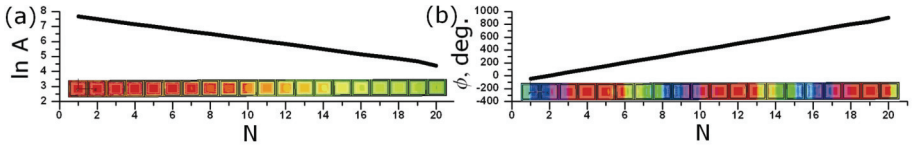

Figure 3.18. An example of (a) amplitude and (b) phase of the averaged field distribution over 20 unit cells of the split-cube in carcass design for the negative refractive index regime.

Imposing semi-infinity in $z-$direction implies only one vacuum-MM interface. In this case Bloch (or input) impedance Z_B can be restored in the unique way from the reflection r at the single interface:

$$Z_B = \frac{1+r}{1-r}. \tag{3.14}$$

Knowing the refractive index and impedance one can easily obtain wave permittivity and permeability $\varepsilon = \frac{n}{Z},\ \mu = nZ$.

Simulation method

We performed the time-domain simulations of the wave propagation inside thick MM slabs (typically $20-50$ periods) using CST Microwave Studio 2009. For broadband excitation a short modulated Gaussian pulse was chosen. As a reference we used the effective parameters retrieved with NRW method. Reflection/transmission through 3 MM layers was simulated with the CST frequency-domain solver. We found out that the results retrieved with the WPRM are equal to that retrieved with the SM in the full pulse bandwidth. An illustration of the WPRM realization for a split-cube in carcass (SCiCa) structure is shown in Fig. 3.18.

WPRM advantages

WPRM has several clear advantages. First, it does not experience the "branch" problem. Second, WPRM does not suffer from such simulation problems as low transmission distorted with noise and long simulation time for sufficient spectra resolution as it uses the amplitude and phase distribution inside the structure. Third, the method works well for thick slabs thus giving bulk effective parameters values. Finally, to avoid the "branch" problem restoring the effective parameters with SM one should always use the continuity of the spectra and therefore broadband simulation. There is no difference for WPRM whether to use broadband or narrowband spectra.

WPRM constraints

WPRM also has some constraints. The normal dependence of the amplitude logarithm on the coordinate is linear (see Fig. 3.19(a)). When the absorption in the metamaterial is very low or the metamaterial slab is thin, the reflection from the back interface leads to standing wave formation (Fig. 3.19(b)). To

retrieve n and Z_B correctly we should make the MM slab thicker and take into account only the first linear part of the graph. Another option is to trace the impulse dynamics and terminate calculations as soon as back-reflected pulse begins to form out. In the other limit of too strong attenuation the signal amplitude is quickly reduced to the noise level (Fig. 3.19(c)). Noise data should be excluded for restoration by taking only first cells where the dependence is linear.

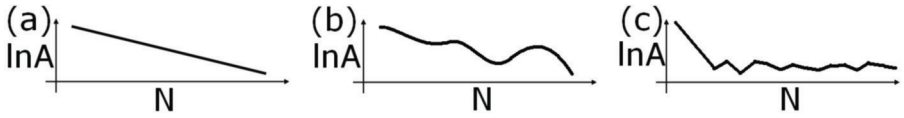

Figure 3.19. Possible problematic cases of simulated average amplitude distribution inside the MM slab: (a) normal case, (b) standing wave formation due to the back interface reflection and slow wave attenuation; (c) large wave attenuation and numerical noise.

To quantify the limitations of WPRM we simulated "the worst case": a homogenous dielectric slab of thickness d with a predefined refractive index n and impedance $Z = 1$ with a perfect mirror (PEC boundary condition) on the other side of the slab. Numerical simulations were performed until the total electromagnetic energy stored in the system dropped down to -80dB with respect to the maximum level. It is obvious that not the value of the refractive index itself but rather terms in exponentials in $\exp(-ik'z - k''z)$ govern phase and amplitude changes. We calculated the relative error of restored n for different $n'k_0d$ and $n"k_0d$, where $k_0 = \omega/c$ is the wavenumber in vacuum. In the case of fast amplitude decay (Fig. 3.19(b)) we should consider d as the distance at which $\ln A$ reaches the noise level. We identified the optimal region where the total relative error is less than 1%. The conclusion is that in the worst case WPRM is applicable with a relative error less than 1% for $-45 \leq n'k_0d \leq 45$ and $5 \leq n"k_0d \leq 56$. In the absence of the perfect reflector at the second interface, like as in conventional MM cases, these limits are extended much further.

The range of applicability of WPRM can be extended to the case of low-loss structures if we excite the MM slab with a short Gaussian pulse and stop the simulation when the center of the pulse reaches the rear interface. So the reflected wave exists only near the rear interface. This part of data must be omitted while retrieving refractive index. As shortcoming we should note

that such simulation is possible only for MMs with low dispersion and requires additional estimation of the time the pulse travels through the slab.

Case Studies

To make a comprehensive validation of the WPRM we chose MM designs operating at different frequencies, i.e. in optical and microwave ranges. We have considered a fishnet, a split cube in carcass and Jerusalem crosses metamaterials. The NRW method [220] results were used for reference.

Fishnet

The fishnet structure [200] is a classical example of the optical negative index MM with high transmittivity. For the WPRM test we took design parameters from [244].

Effective parameters n and Z_B restored with both WPRM and SM are in a perfect agreement (Fig. 3.20). This example also shows that WPRM works well for both single negative and double negative metamaterials as fishnet is single negative below 190 THz.

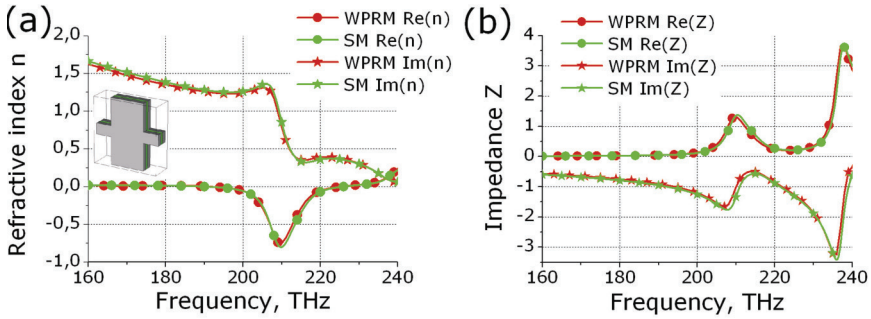

Figure 3.20. Refractive index (a) and impedance (b) of the fishnet structure restored with NRW (red/black) and SM (green/light gray), real (circles) and imaginary (stars) parts.

Split cube in carcass

The Split Cube in Carcass structure [197] has a remarkable property that it shows fast convergence (after one layer only) of the effective parameters to bulk values, the same as a similar design Split Cube in Cage [243]. The structure possesses cubic symmetry that guarantees its polarization insensitivity. As a drawback, SCiCa has high absorption and thus quite low

transmittivity. The SCiCa unit cell consists of two silver parts embedded in silica ($n = 1.5$). Silver is regarded as a Drude metal with plasma and collision frequency as in [200].

Both WPRM and SM provide very similar results (Fig. 3.21). Differences in the retrieved impedance on frequencies above 190 THz (Fig. 3.21(b)) come out from intensive dipole resonances of split cubes and failure of the effective homogeneity approach [243].

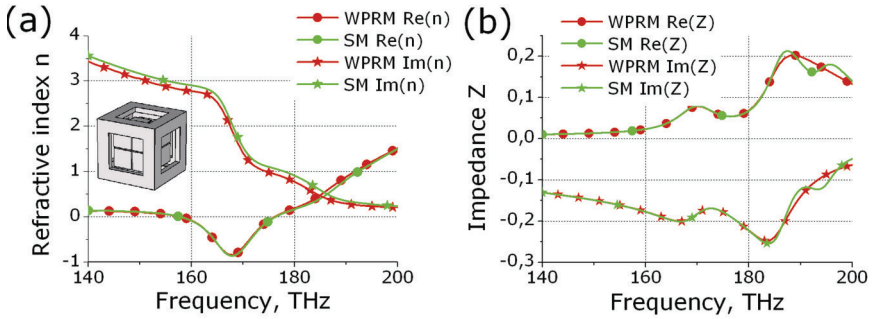

Figure 3.21. Split-cube in carcass effective parameters: (a) refractive index and (b) impedance restored with NRW (red/black) and SM (green/light gray), real (circles) and imaginary (stars) parts.

Jerusalem crosses

Wang et al. [245] has reported a 3D MM design for the microwave region claiming isotropic broadband left-handedness. Design consists of Jerusalem crosses arranged in a cubic lattice (see inset in Fig. 3.22). As the reported losses in this MM are relatively low it was a nice opportunity to check WPRM. All the design parameters were taken the same as in [245]. To our surprise WPRM shows no any negative refractive index in the specified region (around 6 GHz) (Fig. 3.22(a)). WPRM results perfectly coincide with the SM results if one chooses the correct branch. Feasibility of no negative index behavior is easy to explain if we take into account that real and imaginary parts of n must obey the Kramers-Kronig relations [246]. Small and smooth imaginary part corresponds to smooth changes in the real part in contrary to sudden abrupt jumps presented [245]. This is an important message concerning WPRM functionality to avoid errors and misunderstanding in the refractive index restoration and interpretation.

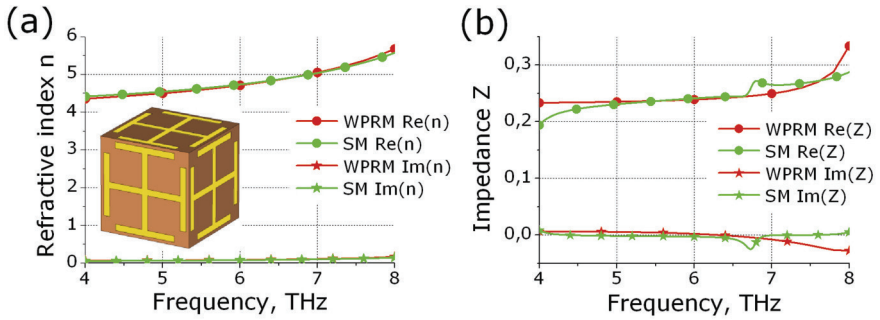

Figure 3.22. Jerusalem crosses MM effective parameters: (a) refractive index and (b) impedance restored with NRW (red/black) and SM (green/light gray), real (circles) and imaginary (stars) parts.

A kink in the impedance spectrum at $6.8\,GHz$ restored with SM (Fig. 3.22(b)) appears due to the finiteness of the system. Additional studies showed that it changes position with the number of layers (thickness) always being exactly at the frequency of the corresponding Fabry-Perot resonance. No such problem is connected with WPRM as multiple reflections from the slab interfaces are successfully avoided.

Low value of $Im(n)$ in Jerusalem crosses MM is restored correctly (Fig. 3.22(a)) that confirms applicability of WPRM not only to lossy structures but also to low-loss ones.

Conclusion

To sum up, we proposed the effective parameters retrieval method based on the wave propagation phenomenon and validate its applicability to lossy and low-loss metamaterials on the case studies in microwaves and optical ranges. The main advantages of WPRM are: unambiguous retrieving of the effective parameters, easy straightforward implementation, applicability to thick (bulky) MM slabs and to broad variety of designs and absence of spurious effects connected with the Fabry-Perot resonances. WPRM can be applied whenever the effective medium approximation is valid. In principle, WPRM can be extended to anisotropic media or media with a non-local response as soon as required observable features of the wave can be detected numerically.

3.2.3. Wave propagation retrieval method for chiral metamaterials

Motivation

It has been suggested that the negative refractive index may be obtained not only in the double negative metamaterial, but also in the chiral metamaterial for one of the eigenwaves [102], [247], [248]. In this case the losses may be smaller than the losses in the resonant metamaterial. Taking into account possibility of the chiral negative index superlens we extended the wave propagation retrieval method to the chiral metamaterials with left and right circular eigenpolarizations [249].

Mathematical formulation

The main idea behind the WPRM is to retrieve the EPs from the cell-averaged electric field E dependence on the coordinate for the wave propagation in a thick (quasi-semi-infinite) metamaterial slab [223]. In this case we can neglect the reflection of the wave from the rear interface and consider only the wave propagating in the forward direction.

Let us consider a linearly x −polarized wave propagating along the z −axis in vacuum that can be decomposed in a sum of RCP and LCP waves:

$$\begin{aligned} \boldsymbol{E}_{LP} &= [1,0,0]\exp ik_0 z \\ &= \tfrac{1}{2}([1,i,0]\exp ik_0 z + [1,-i,0]\exp ik_0 z). \end{aligned} \tag{3.15}$$

It normally impinges onto the flat interface of an isotropic chiral material with the RCP and LCP eigenwaves:

$$\boldsymbol{E}_{RCP} = [1,i,0]\exp ik_0 n_R\, z, \tag{3.16}$$

$$\boldsymbol{E}_{LCP} = [1,-i,0]\exp ik_0 n_L z\,, \Delta x \Delta k_x \geq 2\pi. \tag{3.17}$$

where k_0 is the vacuum wavenumber, n_R and n_L are the RCP and LCP refractive indices correspondingly.

In case of the metamaterial with RCP and LCP eigenwaves, the RCP and LCP Fresnel's transmission coefficients are equal $t_R = t_L = t$, so the electric field of the wave inside the chiral material is:

$$\boldsymbol{E} = \tfrac{1}{2} t(\boldsymbol{E}_{RCP} + \boldsymbol{E}_{LCP}), \tag{3.18}$$

$$E_x = \frac{1}{2}t(\exp ik_0 n_R z + \exp ik_0 n_L z) \tag{3.19}$$

$$E_y = \frac{i}{2}t(\exp ik_0 n_R z - \exp ik_0 n_L z). \tag{3.20}$$

By simple algebraic manipulations we derive

$$n_R = -\frac{i}{k_0}\frac{\Delta \ln(E_x - iE_y)}{\Delta z}, \tag{3.21}$$

$$n_L = -\frac{i}{k_0}\frac{\Delta \ln(E_x + iE_y)}{\Delta z}. \tag{3.22}$$

These formulas are essential for the WPRMC. In practice, the electric field is highly inhomogeneous inside the MM unit cell, so we should use the volume averaged field. Bloch impedance Z_B is retrieved unambiguously from the single reflection r on the vacuum–chiral MM interface

$$Z_B = \frac{1+r}{1-r}. \tag{3.23}$$

Other EPs (refractive index n and chirality κ) can be restored in the following conventional way:

$$n = \frac{n_L + n_R}{2} \tag{3.24}$$

$$\kappa = \frac{n_R - n_L}{2}. \tag{3.25}$$

Strictly speaking, complex logarithm in the equations for the refractive indices n_R and n_L restoration is a multi-valued function, so we can find the values of $i\ln(E_x \pm iE_y)$ with accuracy up to $2\pi m$, where m is an integer. In order to apply a linear fit while using the formulas, the dependence of $Re(i\ln(E_x \pm iE_y))$ on the unit cells coordinates z_{UC} should be made continuous. If the metamaterial is quasi-homogeneous the difference of the wave phase between neighboring unit cells should be less than $\pi/2$, thus aforementioned continuity is easy to persuade.

WPRMC constraints

The constraints of the WPRMC are the same as of the WPRM for linearly polarized waves [223] (section 3.2.2). First, a metamaterial slab should be thick enough to prevent the reflection from the rear interface and standing

wave formation. We found that WPRM gives error less than 1% for $-45 \leq n'k_0d \leq 45$ and $5 \leq n"k_0d \leq 56$, where d is the slab thickness. For the case of low absorption, one can always increase d. The other option is to use time-domain method and to stop the simulation when the excitation pulse reaches the rear interface of the slab. Second, the accuracy of the simulations should be sufficient to observe the linear dependence of $i\ln(E_x \pm iE_y)$ on the coordinate z, for that the electric field has not to drop down to the noise level within less than three unit cells.

Case studies

To check the WPRMC and illustrate its application we consider 3 case studies: homogeneous gyrotropic medium, bi-cross MM and U-shaped MM. CST Microwave Studio [201] was used in simulations. Simulations were performed in the frequency domain with open boundary conditions in the direction of propagation and periodic boundary conditions in the lateral directions.

Homogeneous gyrotropic medium

The main assumption for using WPRMC is that the eigenwaves of the material are RCP and LCP waves, so this means that WPRMC is applicable to any material with circular eigenwaves. Moreover, it is common to check the method on the simplest examples first. As a first example we chose homogeneous plasma magnetized along the direction of the wave propagation z. We should note that such medium is not a chiral medium, but its effective refractive index can be calculated analytically, so it is a reliable reference. It is characterized by the permittivity tensor

$$\varepsilon = \begin{matrix} \varepsilon_1 & i\varepsilon_2 & 0 \\ -i\varepsilon_2 & \varepsilon_1 & 0 \\ 0 & 0 & \varepsilon_3 \end{matrix}, \tag{3.26}$$

$$\varepsilon_1 = \varepsilon_\infty - \frac{\omega_P^2(\omega + i\omega_{col})/\omega}{(\omega + i\omega_{col})^2 - \omega_C^2}, \tag{3.27}$$

$$\varepsilon_2 = -\frac{\omega_P^2\omega_C/\omega}{(\omega + i\omega_{col})^2 - \omega_C^2}, \tag{3.28}$$

$$\varepsilon_3 = \varepsilon_\infty - \frac{\omega_P^2}{\omega(\omega + i\omega_{col})}, \tag{3.29}$$

where ε_∞ is a permittivity at the infinite frequency, ω_P is a plasma frequency, ω_{col} is a collision frequency and ω_C is a cyclotron frequency. The eigenwaves are RCP and LCP with the refractive indices $n_R = (\varepsilon_1 + \varepsilon_2)^{1/2}$ and $n_L = (\varepsilon_1 - \varepsilon_2)^{1/2}$ [250]. For the simulations we chose the plasma frequency $\omega_P = 1.0 \times 10^{15}\ s^{-1}$, the cyclotron frequency $\omega_C = 3.4 \times 10^{14}\ s^{-1}$, $\varepsilon_\infty = 3$ and the collision frequency$\omega_{col} = 3.4 \times 10^{14}\ s^{-1}$. The WPRMC restored effective parameters in perfect agreement with the theoretical ones (Fig. 3.23).

Bi-cross metamaterial

As the second example we investigated a slightly modified bi-cross metamaterial [251], that is a chiral metamaterial for the optical range. The geometrical parameters are indicated in Fig. 3.24. The crosses in the bi-cross are connected in the middle. The bi-cross material is silver, which is approximated as the Drude metal with the plasma frequency $\omega_P = 1.37 \times 10^{16}\ s^{-1}$ and collision frequency $\omega_{col} = 8.5 \times 10^{13}\ s^{-1}$ [200]. The silver structure is embedded into silica (refractive index $n = 1.44$).

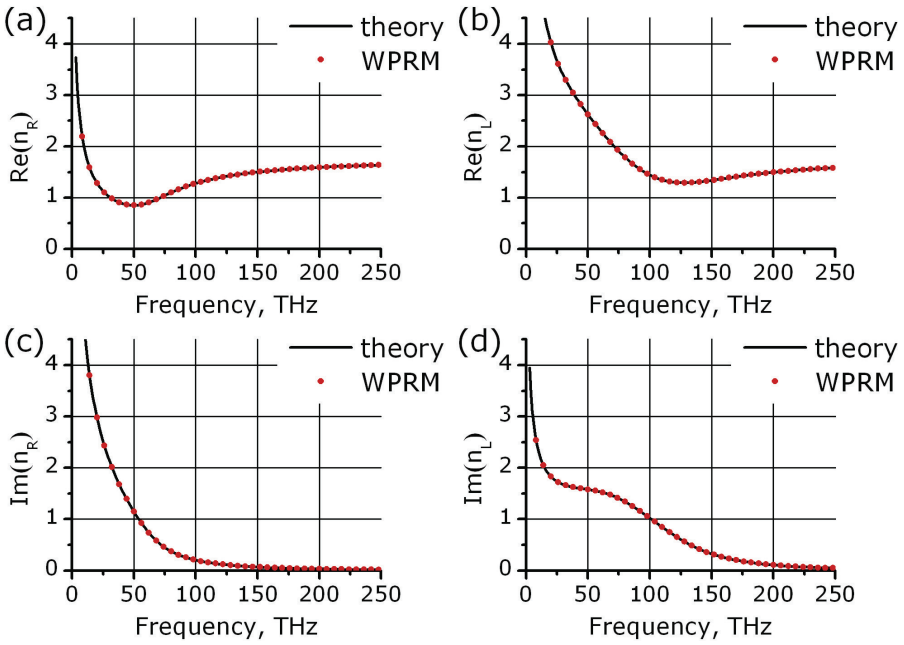

Fig. 3.23. Theoretical (black line) and restored with WPRMC (red circles) refractive indices for RCP and LCP for a homogeneous magnetized plasma: (a) Re(n_R), (b) Re(n_L), (c) Im(n_R), (d) Im(n_L).

In this case we lack the analytical results. Therefore WPRMC results are challenged against the ones, obtained by the standard method [102] as a referenceThe EPs of few MM layers are not the same as the bulk EPs so we do not anticipate the coincidence of the SM and WPRMC results, but the convergence of the SM results to WPRMC with the increasing.

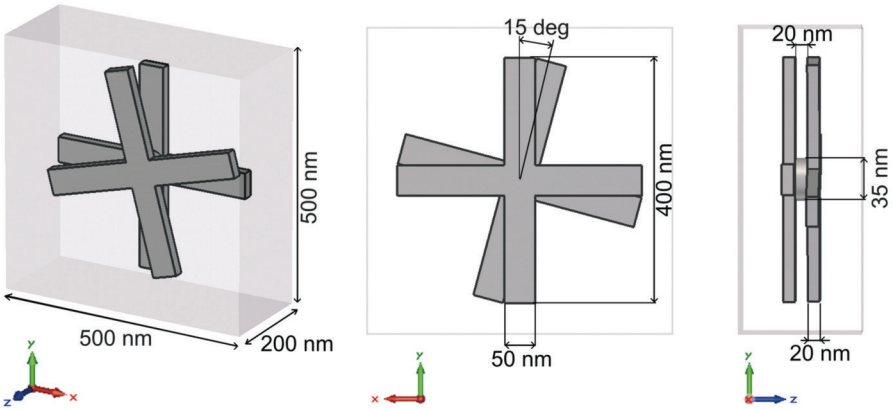

Fig. 3.24. Connected bi-cross unit cell design and its geometry.

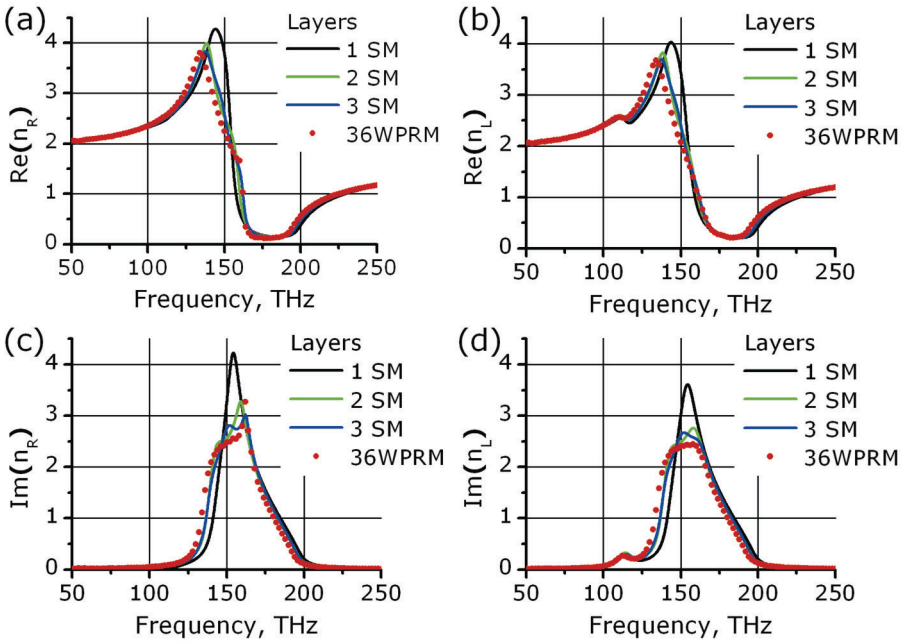

Fig. 3.25. Effective refractive indices of the connected bi-cross MM, retrieved with SM (one layer – black line, two layers – green line, three layers – blue line) and WPRMC (red circles): (a) $Re(n_R)$, (b) $Re(n_L)$, (c) $Im(n_R)$, (d) $Im(n_L)$.

Indeed, the effective refractive indices converge very fast with the increase of the number of MM layers (slab thickness) (Fig. 3.25). The effective properties of 3 layers are similar to the bulk ones restored with WPRMC from simulations of the 36 layers thick slab.

To illustrate the restoration procedure we plotted the logarithm of the electric field amplitude dependence on the distance (layer number) inside the MM slab (Fig. 3.26) for two different cases. At the frequency $110\,THz$ (Fig. 3.26(a)) RCP and LCP have different small absorption but MM shows strong circular dichroism. We see the standing wave above the layer number 20 so we should use data points before that for the retrieval. At the frequency $150\,THz$ (Fig. 3.26(b)) absorption of both modes is similar and large. So we observe linear part of the graph until layer number 19, then wave amplitude is at the noise level, so this noise part should be excluded when restoring refractive index.

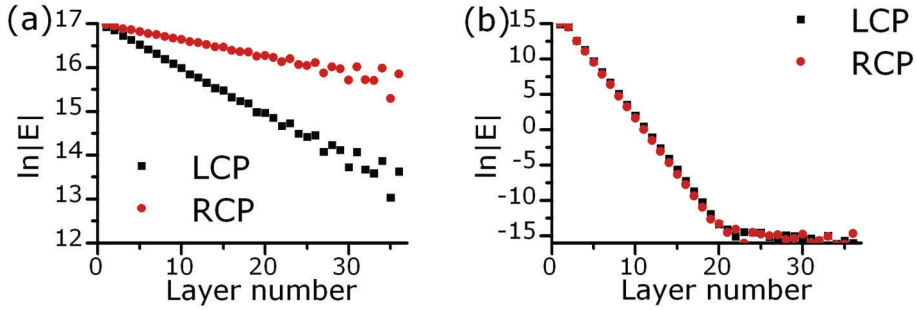

Fig. 3.26. Logarithm of the amplitude of the electric field inside the bi-cross MM slab for the frequency $110\,THz$ (a) and $150\,THz$ (b) for RCP (red circles) and LCP (black squares).

U-shaped metamaterial

To test our method in the microwave range we chose the U-shaped metamaterial design [252]. The original paper presents the structure consisting of only two layers of MM so we stack multiple layers for the WPRMC application (Fig. 3.27 (a)). All the geometrical parameters were taken as in [252].

As we see from Fig. 3.27 (b) and (c), the effective properties change dramatically with the increasing thickness. One bi-layer of the U-shaped MM shows pronounced negative values of the refraction index real part. For

two bi-layers the refractive index is just slightly negative and further it becomes progressively positive for a thick structure (40 bi-layers). We explain this behavior as the result of strong interaction between meta-atoms in the adjacent layers. Such interaction leads to mutual annihilation of total response finishing with a rather mitigated resonance. It is encouraging that correspondingly the absorption is much smaller than that of a single bi-layer (Fig. 3.27 (d) and (e)). The strong coupling between meta-atoms can represent a problem for homogenization of metamaterials on the basis of most of the proposed chiral designs [211]. More details can be found in the section 3.4.

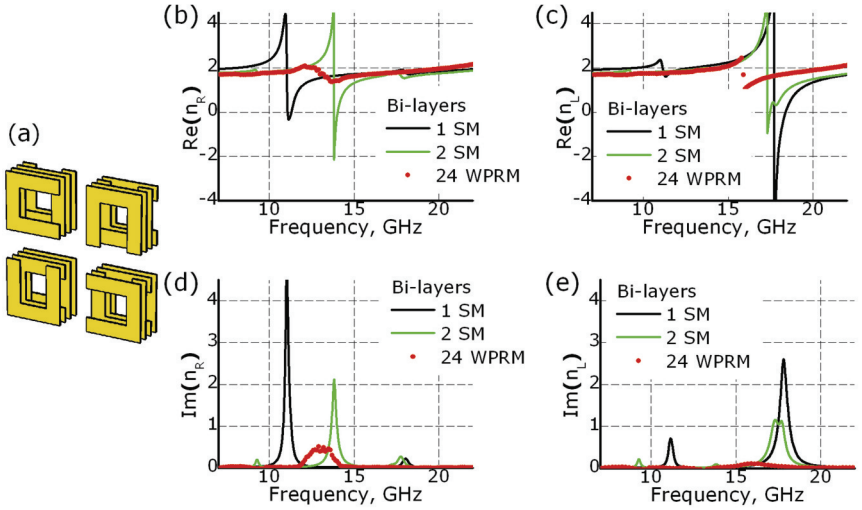

Figure 3.27. U-shaped MM design (a). Effective refractive indices of the U-shaped MM, retrieved with SM (one bi-layer – black line, two bi-layers – green line) and WPRMC (red circles): (b) $Re(n_R)$, (c) $Re(n_L)$, (d) $Im(n_R)$, and (e) $Im(n_L)$.

Conclusion

We presented the wave propagation retrieval method for chiral metamaterials that is suitable to retrieve bulk effective parameters of any kind of materials with RCP and LCP eigenwaves. The method's validity is verified on the case studies of homogeneous magnetized plasma and bi-cross chiral MMs. We also analyzed the case of U-shaped MMs possessing extremely poor convergence of effective parameters with the slab thickness. In such case the WPRMC provides important information on the bulk

effective properties which are difficult or even impossible to obtain by the standard method with the few layers structures. Our method is straightforward in implementation and restores effective properties unambiguously. All this make the WPRMC a useful tool in chiral MMs research.

3.2.4. Field averaging of the restored Bloch mode method

Motivation

Even though the wave propagation retrieval method restores bulk effective refractive index from multi-layer metamaterial slab simulation, the impedance obtained from the reflection coefficient is not a wave impedance, but Bloch (or input) impedance. Therefore the restored effective parameters are wave EPs, not material. The knowledge of material effective parameters is very important since it gives the connection between the electromagnetic field components that is needed for development of the metamaterial based applications. However, the methods that can retrieve material EPs are quite complicated.

Our objective

Our objective was to formulate a simple method that equally well retrieves both material and wave parameters [253]. The method is based on the extraction of the dominating (fundamental) Bloch modes. Then we apply the volume or surface averaging of the electric and magnetic fields of this Bloch mode which lead to the material or wave (respectively) EPs retrieval. We call this approach the *field averaging of the restored Bloch mode* (FARBM) method.

Mathematical formulation

The field averaging of the restored Bloch mode method is based on the Bloch modes expansion of the wave propagating inside the MM slab.

We excite the MM slab, which consists of the periodically arranged unit cells of the period $\boldsymbol{a} = (a_x, a_y, a_z)$, with a plane wave propagating along the $z-$axis and electric field polarized along $x-$axis – in the same way as we do applying WPRM (see Fig. 3.17). In principle, the slab may be arbitrarily

thick. It should only be thicker than 3-4 MM monolayer for that we can neglect the so-called Drude transition layers [219].

We realized the fields excitation and wave propagation in the commercial CST Microwave Studio software [201] based on the finite-integrals simulation method. We used perfect electric, perfect magnetic and open boundary conditions for the $x-$, $y-$ and $z-$ boundaries respectively and time-domain solver for the calculations. Broadband Gaussian pulse was used for the excitation. Only one simulation was needed for the whole spectrum calculation. The fields for different frequencies were calculated through the Fourier transformations from the time-dependent signals collected with 3D field monitors.

Let us consider the plane wave normally incident from vacuum onto the MM slab. Its electric $E_v = E_{v0} \exp ik_0 z$ and magnetic $H_v = H_{v0} \exp ik_0 z$ fields are connected, $k_0 = \omega/c$ is the wavenumber of the free space. The proportionality coefficient between them, $Z_0 = E_{v0}/H_{v0}$, is the impedance of the free space ($Z_0 = \sqrt{\mu_0/\varepsilon_0} \approx 120\,\pi\,Ohm$). We assume the optical convention on the $\exp -i\omega t$ time dependence.

In a general case, several Bloch modes [254-257] may be excited in the slab for each frequency ω, so the overall field may be represented as a sum

$$E(\boldsymbol{r}) = \sum_{m=1}^{M} E_m(\boldsymbol{r}) \tag{3.30}$$

$$H(\boldsymbol{r}) = \sum_{m=1}^{M} H_m(\boldsymbol{r}) \tag{3.31}$$

where m is the Bloch mode number, M is the total number of excited modes, and $\boldsymbol{r} = (x, y, z)$. In the desirable case of local quasi-homogeneous MM there are only two modes in the slab: one forward and one backward propagating. More modes can be excited in the case of MM with strong spatial dispersion [199], [219].

The field profiles of Bloch modes can be represented as [219], [254-256]

$$E_m(\boldsymbol{r}) = \left[E_{m,0}(\boldsymbol{r}_\perp) + \sum_{p \neq 0} E_{m,p}(\boldsymbol{r}_\perp)\, e^{iGpz} \right] e^{iK_m z}, \tag{3.32}$$

$$H_m(\boldsymbol{r}) = \left[H_{m,0}(\boldsymbol{r}_\perp) + \sum_{p \neq 0} H_{m,p}(\boldsymbol{r}_\perp)\, e^{iGpz} \right] e^{iK_m z}, \qquad (3.33)$$

where K_m is the Bloch wavenumber, $G = 2\pi/a_z$, p is an integer number.

We note that such field representation is invariant with respect to a transformation $K_m \to K_m + Gp'$ and $E_{m,p} \to E_{m,p+p'}$ for an arbitrary integer p'. Accordingly, we can always select the value of K_m such that $E_{m,0}$ is the largest harmonic's amplitude, and we use this convention in the following.

We used the high-resolution spectral analysis method [258], [259] to decompose the total field into a sum of Bloch modes. The only information required for the application of this method is the knowledge about the number of the strongest Bloch modes excited in the structure (M). Then, through specialized numerical optimization [258], [259] we extracted the wavenumbers K_m and field profiles $E_m(\boldsymbol{r}), H_m(\boldsymbol{r})$ of all the forward and backward propagating Bloch modes at each frequency ω. By monitoring the accuracy of such decomposition, we also check whether other Bloch modes may have significant excitation amplitudes, and if this is a case we can increase the number M to take those modes into account and repeat the extraction procedure.

It is an important advantage of our approach that the standing wave, which is usually formed inside the slab due to the multiple reflections from the boundaries and brings the restrictions to the conventional wave propagation retrieval method [223], is not an issue in the present case, since we can separate forward and backward propagating Bloch modes. In the following, we denote the field profiles of the dominant forward and backward waves as

$$\{E,H\}_+ \equiv \{E,H\}_{m_+}, \qquad \{E,H\}_- \equiv \{E,H\}_{m_-}, \qquad (3.34)$$

and the corresponding wavenumbers

$$K_+ \equiv K_{m_+}, \qquad K_- \equiv K_{m_-}. \qquad (3.35)$$

where m_+ and m_- are the numbers of the dominant forward and backward Bloch modes, respectively.

In the general case of several Bloch modes excitation the MM cannot be considered as homogeneous and no meaningful EPs can be introduced. The homogeneity of MM and the influence of the higher-order Bloch modes have

been discussed extensively in the Refs. [197], [199], [260]. However, if the fundamental mode has the lowest damping, we might neglect the presence of the higher-order modes. The numerical criterion of homogeneity from the Bloch modes point of view was formulated in [260]. Another possibility to check the single mode domination is to calculate the mismatch δ of the restored sum of forward and backward propagating fundamental mode fields, $E_f = E_+ + E_-$, and the original field E taken directly from numerical simulations:

$$\delta = \frac{\int \left|E - E_f\right|^2 dx\, dy\, dz}{\int |E|^2 dx\, dy\, dz}, \tag{3.36}$$

where integration is performed over the computation domain.

In the case studies that we considered the MMs have a dominant fundamental mode, so we could neglect the higher-order Bloch modes. In all cases presented below the mismatch δ was less than 1.5%.

According to the concept of homogenization, we aim to find effective parameters for an equivalent homogeneous medium, where the wave propagation would be essentially the same as in the periodic structure. After determining the propagation constant K_+ of the fundamental mode we can calculate the effective refractive index $n = K_+/k_0$. Then we use the fields E_+, H_+ for the Bloch z_B and wave z_W impedances restoration. First, we make surface averaging at the (x, y) cross-section of the simulated slab:

$$E_{SA}(z) = \frac{\int_S E_+(x, y, z)\, dx\, dy}{a_x a_y}, \tag{3.37}$$

$$H_{SA}(z) = \frac{\int_S H_+(x, y, z)\, dx\, dy}{a_x a_y}. \tag{3.38}$$

Taking the values of the fields $E_{SA,j}$, $H_{SA,j}$ at the unit cell borders $z_j = ja_z$, where j is an integer number, we determine the Bloch impedance [240]:

$$Z_B = \frac{E_{SA,j}}{Z_0 H_{SA,j}}. \tag{3.39}$$

where Z_0 is the free space impedance. Note that the value of Z_B does not depend on the unit cell number j. In order to restore the wave impedance (Z_W), we need to calculate the volume averaged fields [219] E_{VA} and H_{VA}.

$$Z_W = \frac{E_{VA}}{Z_0 H_{VA}}. \tag{3.40}$$

Since the wavenumbers in the periodic and equivalent homogeneous media are taken to be the same, we need to establish the correspondence of the field amplitudes in front of the common $\exp iK_+ z$ multiplier. Accordingly, we define the volume-averaged fields by performing integration over a single unit cell with the multiplier $\exp -iK_+ z$ to cancel the phase evolution:

$$E_{VA} = \frac{\int_{z_b}^{z_b+a_z} E_{SA}(z) \exp -iK_+ z \; dz}{a_z}, \tag{3.41}$$

$$H_{VA} = \frac{\int_{z_b}^{z_b+a_z} H_{SA}(z) \exp -iK_+ z \; dz}{a_z}. \tag{3.42}$$

where z_b is an arbitrary location inside the structure. We can also express the averaged fields through the harmonic amplitudes

$$E_{VA} = \frac{\int_S E_{m+,0}(x,y) dxdy}{a_x a_y}, \tag{3.43}$$

$$H_{VA} = \frac{\int_S H_{m+,0}(x,y) dxdy}{a_x a_y}, \tag{3.44}$$

The volume-averaged fields do not depend on z_b, since their values are defined through the dominant Bloch-wave harmonic amplitude which is independent on z.

After obtaining the refractive index and impedance we can find the effective permittivity and permeability: material and wave effective parameters

$$\varepsilon_M = \frac{n}{Z_W}, \quad \mu_M = nZ_W, \tag{3.45}$$

$$\varepsilon_W = \frac{n}{Z_B}, \quad \mu_W = nZ_B \, . \tag{3.46}$$

The latter EPs should be equal to these given by the NRW method [220].

The determination of the propagation constant and impedance is straightforward, does not involve inverse functions and therefore provides unambiguous EPs restoration.

We should also mention a practical issue important for the implementation of the proposed FARBM method. Testing the method on the lossless homogeneous slab we found out that there is a phase shift between the electric and magnetic fields. This shift is artificial and is connected to the Yee mesh used in the finite-difference or finite-integral time-domain methods, since the electric and magnetic fields are calculated at different time moments shifted by $\Delta t/2$, where Δt is the simulation time step. For the case of CST Microwave Studio, which we used, the magnetic field phase was always shifted by $\Delta\phi = \omega\Delta t/2$, so we corrected the magnetic field values by multiplying by $\exp i\omega\Delta t/2$.

Case studies

We tested the FARBM method on several examples, starting with the simplest ones. The unit cells sketches of the designs are shown in Fig. 3.28

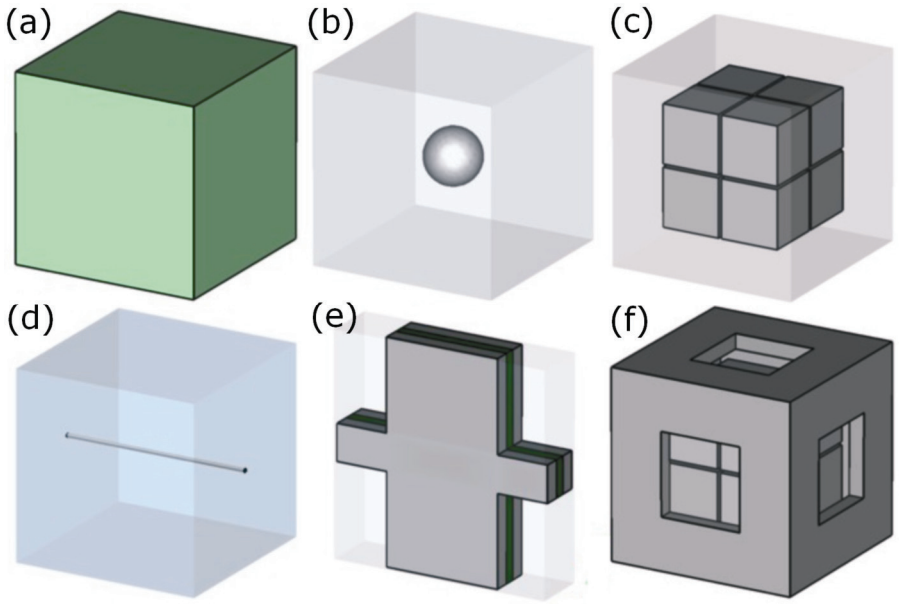

Figure 3.28. Sketches of the metamaterials designs considered: homogeneous material (a), plasmonic nanospheres (b), split cube MM (c), wire medium (d), fishnet MM (e) and split cube in carcass (f).

We considered:

(1) Homogeneous slab (see Fig. 3.28(a) two cases: lossless and Lorentz dispersion in ε and μ with negative index of refraction,

(2) A set of the nanospheres with the plasmonic resonances (see Fig. 3.28(b)),

(3) Split cubes MM that possess magnetic resonance and negative permeability (see Fig. 3.28(c)), (4) Wire medium that gives negative permittivity (see Fig. 3.28(d)),

(5) Negative refractive index fishnet MM (see Fig. 3.28(e)),

(6) Split cube in carcass MM (see Fig. 3.28(f)).

In all cases, the MM slab consisted of 10 monolayers. For comparison, the wave EPs were calculated from three monolayers thick slab with the NRW method [220].

Homogeneous materials

A slab of homogeneous material is the simplest object to test the retrieval method, since the restored EPs can be compared with the theoretical reference values.

A homogeneous slab was artificially divided into 10 meta-atoms of the size $a_x = a_y = a_z = 100\ \mu m$. For the case of the homogeneous medium, the material and wave parameters are identical, so we should only compare the theoretical constitutive parameters with the material ones retrieved with the FARBM method.

For the homogeneous lossless slab with $\varepsilon = 4$ and $\mu = 1$ the EPs were in a perfect agreement with the theoretical permittivity and permeability. The relative retrieval error was less than 0.2 %, which can be attributed to numerical dispersion effect in finite-difference numerical simulations.

In another example, we considered the frequency dispersive permittivity and permeability described with the Lorentz model:

$$\varepsilon(\omega) = \varepsilon_\infty + \varepsilon_{stat} \frac{{\omega_{0e}}^2}{\omega_{0e}^2 - i\gamma_e\omega - \omega^2}, \tag{3.47}$$

$$\mu(\omega) = \mu_\infty + \mu_{stat} \frac{\omega_{0m}^2}{{\omega_{0m}}^2 - i\gamma_m\omega - \omega^2}, \tag{3.48}$$

where $\varepsilon_\infty = 1$, $\varepsilon_{stat} = 1.7$, $\omega_{0e} = 2\pi \times 198 \times 10^9\ s^{-1}$, $\gamma_e = 2\pi \times 10^{10}\ s^{-1}$, $\mu_\infty = 1$, $\mu_{stat} = 1.3$, $\omega_{0m} = 2\pi \times 202 \times 10^9\ s^{-1}$, $\gamma_m = 2\pi \times 10^{10}\ s^{-1}$.

The effective parameters restored with FARBM are in a good correspondence with the theoretical ones (see Fig. 3.29). The small differences are observed only in the resonant region around 200 THz where losses are high. The retrieval results in Fig. 3.29 show that FARBM method is applicable to a wide range of lossless and lossy materials with positive and negative n, ε and μ.

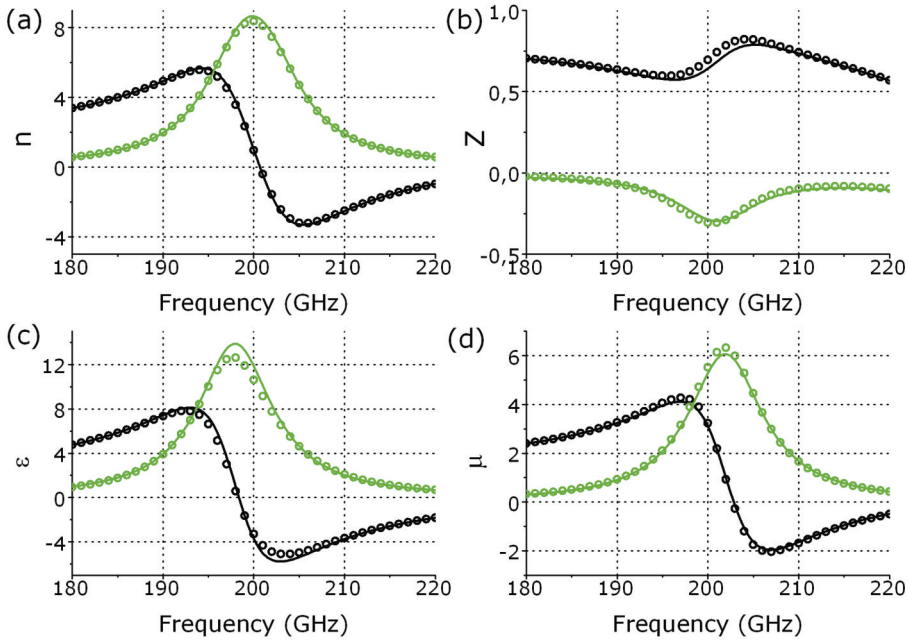

Figure 3.29. Effective parameters of the homogeneous medium with Lorentz dispersion in permittivity and permeability: refractive index (a), impedance (b), permittivity (c) and permeability (d), real (black) and imaginary (green/grey) parts. Results by FARBM method (circles) are compared with theoretical values (solid lines).

Metamaterial composed of plasmonic nanospheres

Metallic nanospheres possess plasmonic resonances at optical frequencies. Being arranged in the regular cubic structure, the nanospheres with a radius $r \ll \lambda$ constitute a MM. It is expected that the nanospheres MM should have

the permittivity which is different from the host permittivity and its permeability should be close to 1, since the nanospheres are non-magnetic.

The silver nanospheres of the radius $r = 30\,nm$ were placed in vacuum in the cubic array with the period $a_x = a_y = a_z = 200\,nm$. Silver was considered as the Drude metal with the plasma frequency $\omega_p = 1.37 \times 10^{16} s^{-1}$ and collision frequency $\gamma_c = 8.5 \times 10^{13} s^{-1}$ [200]. In fact, the permittivity of silver is not described correctly by the Drude formula in the optical range and experimentally measured data [261] should be used instead. However, the exact permittivity model is of a little importance for testing the retrieval method. The sketch of the design is shown in Fig. 3.28(b).

Effective refractive indices restored with the NRW and FARBM methods (see Fig. 3.30(a)) are identical. Bloch impedance z_B, retrieved with the surface averaging is the same as the one restored with the NRW method, as it was expected (see Fig3.30(b)).

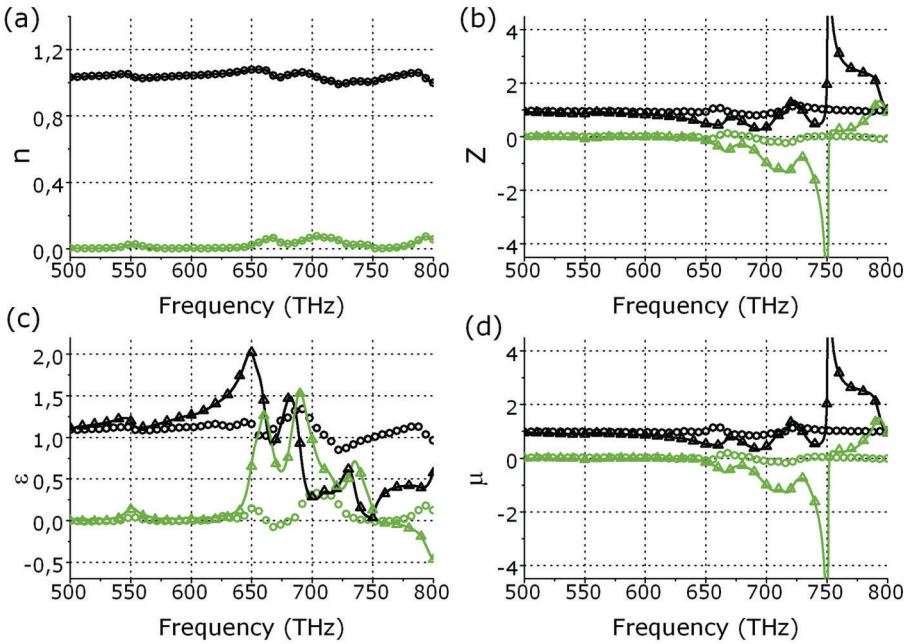

Figure 3.30. Effective parameters of the MM consisting of plasmonic nanospheres: refractive index (a), impedance (b), permittivity (c) and permeability (d), real (black) and imaginary (green/grey) parts. Results by FARBM volume-averaged (circles) and surface averaged (triangles) are compared with the NRW method (solid lines).

The wave impedance z_W (see Fig. 3.30(b), circles) differs from z_B. It experiences only slight oscillations around the value of $z_W \simeq 1 + 0\,i$. At the same time, the Bloch impedance shows several resonances. The usage of Bloch impedance leads to the effective permittivity ε_W showing strong resonances around $660\,THz$, $690\,THz$ and $730\,THz$ (see Fig. 3.30(c)). At the same frequencies, the magnetic permeability shows non-physical negative imaginary part, so-called antiresonance that normally would correspond to the gain in the system. However, material EPs ε_M and μ_M, restored with the FARBM method, do not show anti-resonant behavior. The small negative values of $Im(\varepsilon_M)$ are due to the calculation errors.

The permeability $Re(\mu)$, which is supposed to be around 1 since the nanospheres are non-magnetic, is indeed around 1 for the material $Re(\mu_M)$, but several times larger around $750\,THz$ for $Re(\mu_W)$ (see Fig. 3.30(d)). It looks as we have strong magnetism from the non-magnetic MM consisting of electric dipoles. We found out that at the frequency $750\,THz$ the condition for the first Bragg resonance is satisfied, so the MM cannot be considered as homogeneous and cannot be assigned with meaningful effective parameters [197], [219], [260].

Split-cube metamaterial

We choose a split cube MM as an example of a magnetic material with negative permeability in the infrared range [191], [243]. The sketch of the design, which is a 3D generalization of the symmetric split-ring resonator [204], is shown in Fig. 3.28(c). The cubic unit cell of $a_x = a_y = a_z = 250\,nm$ consists of the silver structures (Drude metal) embedded in silica (permittivity 2.25). The geometrical parameters were taken the same as in the [243].

Similar to the previous examples, the refractive indices retrieved with FABRM and NRW methods are the same, showing a resonance around $160\,THz$ (see Fig. 3.31(a)). A small peak in the impedance restored with the NRW method at the frequency $91\,THz$ appears at the Fabry-Perot resonance of the slab and is an artifact (see Fig. 3.31(b)). The artificial peaks in the EPs due to Fabry-Perot resonances have been also observed in Ref. [223].

While effective material EPs ε_M and μ_M show normal resonance behavior around $160\,THz$ (see Figs. 3.31(c) and (d)), the wave EPs show non-

physical anti-resonance in ε_W. At the same time the amplitude of the resonance in material μ_M is less than the wave μ_W and we do not observe negative magnetism. This means that the NRW retrieval method overestimates the magnetic resonance properties of the split cube MM.

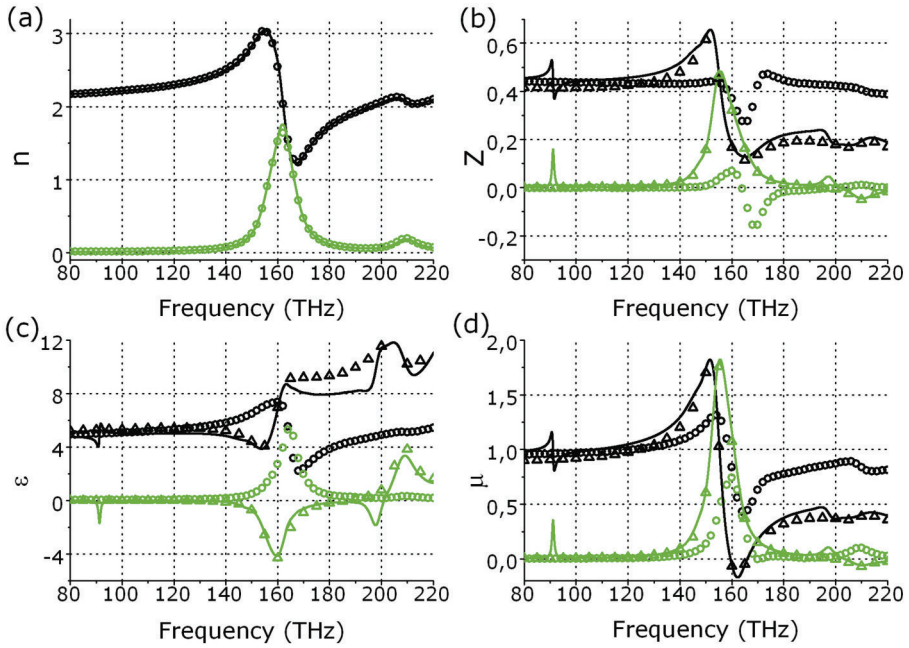

Figure 3.31. Effective parameters of the split cube magnetic MM: refractive index (a), impedance (b), permittivity (c) and permeability (d), real (black) and imaginary (green/grey) parts. Results by FARB volume-averaged (circles) and surface averaged (triangles) are compared with the NRW method (solid lines).

Wire-medium

Wire medium [71] is a well-known example of the negative-permittivity MM. In the case of the square lattice of perfectly conducting wires in vacuum, when radius of the wires r is much less than the unit cell size, $r \ll a \ll \lambda$, the analytical expression for the effective permittivity [77] is:

$$\varepsilon_{eff}(\omega) = 1 - \frac{2\pi c^2}{a^2\omega^2(\log\frac{a}{2\pi r} + 0.5275)}. \qquad (3.49)$$

We simulated the wires of perfect electric conductor of radius $r = 5\ \mu m$ arranged in a square lattice with $a_x = a_y = 500\ \mu m$ in vacuum (see the

sketch in Fig. 3.28(d)). Comparison of the retrieved EPs with the theoretical ones is presented in Fig. 3.32.

Effective permittivity, retrieved with the NRW method differs from that obtained with the FARBM method, and it is closer to the theoretical prediction (see Fig.3.32(c)). We attribute the difference to the rectangular spatial discretization of the round wires in the simulations. What concerns permeability, the NRW method retrieves $\mu_W \approx 1.2$ (see Fig. 3.32(d)), while wire medium is non-magnetic MM. With the FARBM method the retrieved μ_M perfectly coincides with the theoretical prediction.

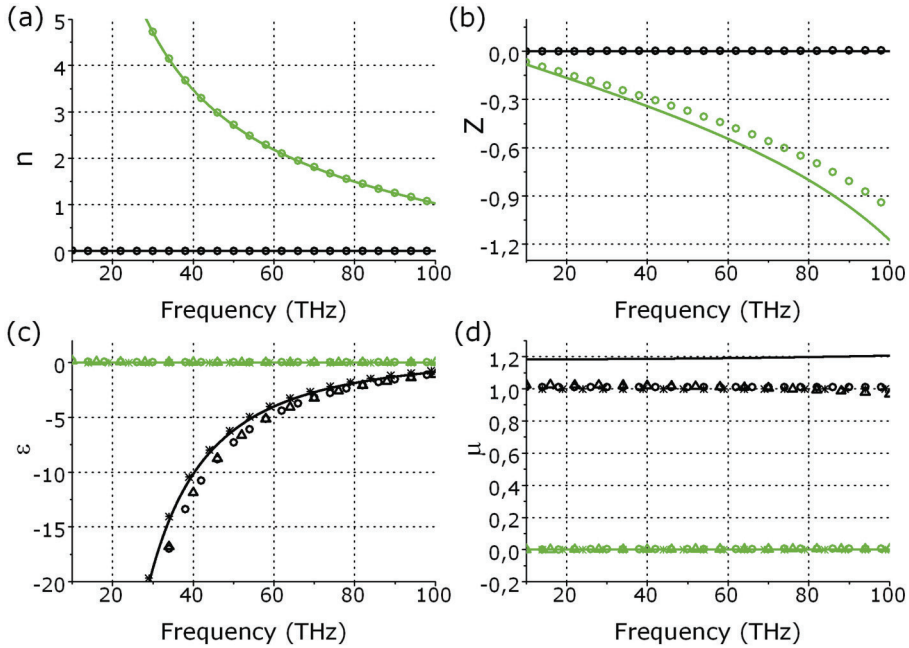

Figure 3.32. Effective parameters of the wire medium: refractive index (a), impedance (b), permittivity (c) and permeability (d), real (black) and imaginary (green/grey) parts. Results by FARBM volume-averaged (circles) and surface averaged (triangles) and NRW method (solid line) are compared with the theoretical predictions (stars).

Fishnet metamaterial

The fishnet MM [200] is one of the most promising negative-index metamaterials for the optical and infrared regions. It consists of the metallic double wires extending in the $x-$ and $y-$ directions (see the sketch in Fig. 3.28(e)).

We used the geometrical and material parameters of the fishnet MM from the Ref. [199] except adjusting the period in $z-$direction to $a_z = 150\,nm$. The unit cell's transverse sizes are $a_x = a_y = 600\,nm$. Silver layers (Drude metal) of the thickness $45\,nm$ are separated with the MgF_2 dielectric of refractive index $n = 1.38$ and thickness $30\,nm$. This metal-dielectric sandwich is placed in vacuum.

The refractive indices retrieved with NRW and FARBM methods are different in the resonance region (see Fig. 3.33(a)). This is not so surprising since the wave EPs were retrieved with the NRW method from only three monolayers thick slab. It is well known that the thin-slab effective refractive index of the fishnet converges slowly to the bulk values with the increase of the slab thickness [242], [262]. The FARBM method gives bulk refractive index, which differs from the thin-slab one. Bloch and wave impedances are different as well (see Fig. 3.33(b)).

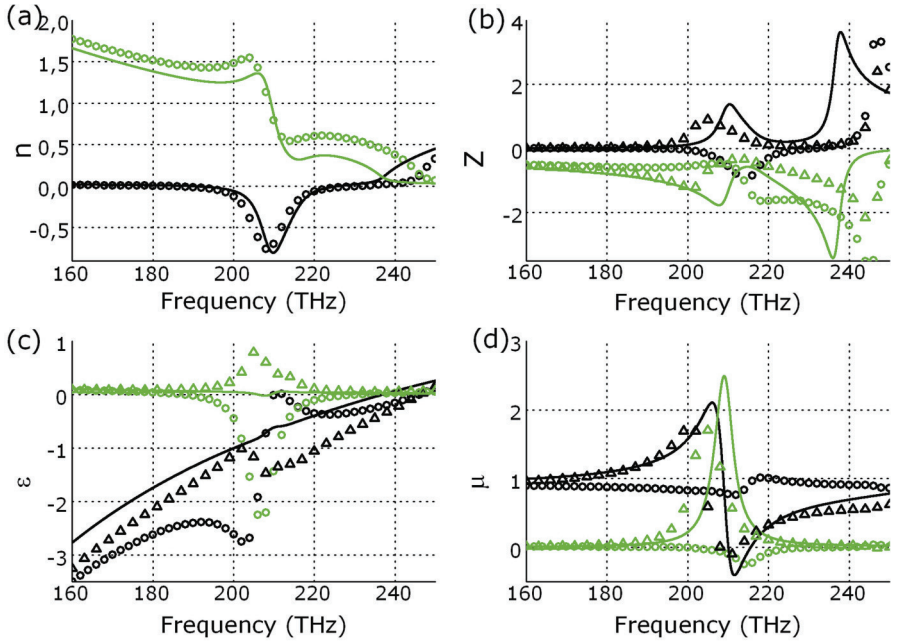

Figure 3.33. Effective parameters of the fishnet negative-index MM: refractive index (a), impedance (b), permittivity (c) and permeability (d), real (black) and imaginary (green/grey) parts. Results by FARBM volume-averaged (circles) and surface averaged (triangles) are compared with the NRW method (solid lines).

As we analyze the calculated permittivity and permeability dependencies (see Fig. 3.33(c) and (d)), it appears surprising that the material permeability $Re(\mu_M)$ does not differ much from 1 and that material, not wave, EPs ε_M and μ_M show antiresonance behavior around $210\,THz$. We have a hypothesis that this anti-resonance behavior of the material EPs comes from non-locality of the fishnet MM. As this was shown in Ref. [263], fishnet possesses strong spatial dispersion in the resonant region and local EPs cannot be introduced. However, FARBM method with volume-averaging procedure is formulated for the material EPs of the local MM. Therefore, being applied to non-local MM, FARBM method gives spurious results.

Split cube in carcass metamaterial

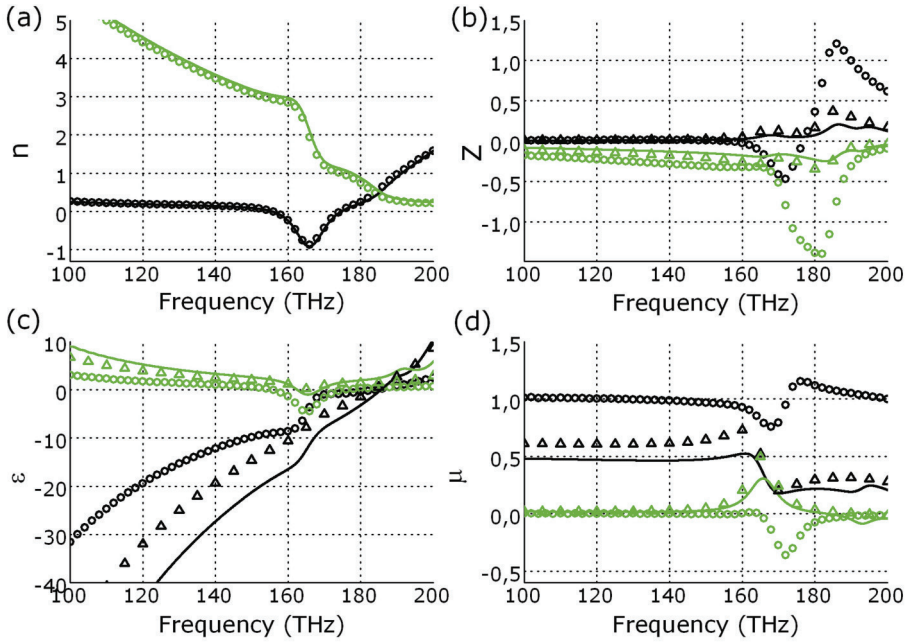

Figure 3.34. Effective parameters of the split cube in carcass negative index MM: refractive index (a), impedance (b), permittivity (c) and permeability (d), real (black) and imaginary (green/grey) parts. Results by FARBM volume-averaged (circles) and surface averaged (triangles) are compared with the NRW method (solid lines).

To check that the non-physical values of the material EPs are not the property of the fishnet MM only, we consider another negative-index metamaterial with strong spatial dispersion, namely split cube in carcass

[197], [223] (see the sketch in Fig. 3.28(f)). Its remarkable property is that its effective refractive index is the same for the thin slab and for the bulk MM. However, as this was shown in Ref. [264], even being 3D cubic symmetric, split cube in carcass is anisotropic due to a spatial dispersion.

The cubic unit cell of $a_x = a_y = a_z = 250\ nm$ (Fig. 3.28(f)) consists of the silver split cube nested in the silver carcass, which is a kind of 3D wire medium. The metallic structures are embedded in silica.

Since the effective refractive index of the split cube in carcass does not depend on the slab thickness, it is not surprising that the NRW method and the FARBM method give the same results (see Fig. 3.34).

However, impedances, permittivity and permeability are different (see Figs. 3.34 (c) and (d)). Again, as in case of the fishnet, we observe non-physical $Im(\varepsilon_M)$ and $Im(\mu_M)$. We should also note that diamagnetism observed in the wave $Re(\mu_W)$ does not remain in the material $Re(\mu_M)$, which is close to 1 everywhere except the resonant region. We make a conclusion that non-physical negative material EPs $Im(\varepsilon_M)$ and $Im(\mu_M)$ are not the specific feature of the fishnet, but possibly of any non-local MM with strong spatial dispersion.

FARBM advantages and constraints

Our retrieval method is able to retrieve both material and wave EPs for a wide range of materials, which can be lossy or lossless, dispersive, possess negative permittivity, permeability and refractive index values. The FARBM method uses the field of the fundamental Bloch mode, not the total field in the structure. It is simple and unambiguous, free of the "branch" problem which is an issue for the reflection/transmission based NRW method. The FARBM method does not require averaging different fields' components at various surfaces or contours. All that is needed for material EPs retrieval is the volume averaging of the electric and magnetic fields. Both retrievals (wave and material EPs) are performed within a single computational cycle, because fields on the unit cells entrance facets or in their volumes are available and can be exported from Maxwell's solver data arrays. The FARBM method has no limitations on a MM slab thickness. Homogeneity of a MM may be also checked during the retrieval process from the fields mismatch. Moreover, material EPs of local MMs restored with FARBM

method have no non-physical "anti-resonances" (negative $Im(\varepsilon_M)$ and $Im(\mu_M)$) for local MMs. The FARBM method may be extended to chiral and anisotropic local MMs as well as MMs with multiple dominating Bloch modes.

Concerning the method's constraints, we must admit that the material EPs that are restored with FARBM method for the non-local metamaterials (e.g. fishnet or split cube in carcass) possess anti-resonances. This is the evidence that the method, which is developed for material (local) effective parameters, cannot be applied to the non-local MMs with strong spatial dispersion. In such a case another method, for example, non-local dielectric function restoration [232] should be used. From the other side, the FARB method may be used to check locality of the MM. We may say that if the MM is non-local, the FARBM method gives non-physical results. We have not proved the opposite statement, that if the FARBM method gives non-physical EPs, then the MM is non-local. However, the presence of the negative $Im(\varepsilon_M)$ and $Im(\mu_M)$ in the spectra allows one to suspect non-locality of the MM.

Conclusion

We formulated the FARBM effective parameters restoration method that is unambiguous, simple and may be applied to lossy and lossless local metamaterials.

The effective refractive indices restored with the NRW method and volume or surface averaged FARBM method are identical except for the case of the thin slab EPs of the fishnet MM, where the MM experiences poor convergence to the bulk properties. However, impedances are not identical, so it is very important which method to choose for the EPs restoration.

We should admit that the direct extension of the FARBM method for the experimental characterization of MMs in the optical range is hardly possible, since there are no such small electric and magnetic field detectors that could be placed inside the MM unit cell without noticeable influence on its functionality. What concerns radio and microwave frequency range, it is possible to record the fields at the spatial points inside the metamaterial [259]. Therefore, we anticipate that the proposed FARBM method will become a useful tool for the characterization of both wave and material effective properties of MMs.

Conclusions

In this chapter we proposed the wave propagation retrieval method for metamaterials with linear and circular eigenpolarizations and the field averaging of the restored Bloch mode method. Both of them are based on averaging of the fields within unit cell. In the case of WPRM averaging of the raw field is made, while in case of FARBM the Bloch modes are first restored from the raw electromagnetic field.

Both of the proposed methods are simple and provide unambiguous restoration of the effective parameters: wave EPs in case of WPRM and both wave and material EPs in case of FARBM. An important advantage is that WPRM and FARBM can restore the bulk effective parameters from the thick metamaterial slab, which is a limitation of the commonly used Nicholson-Ross-Weir method.

Both of the proposed methods can be applied to lossy and lossless, positive and negative refractive index, permittivity and permeability metamaterials. We confirmed that on multiple metamaterials examples.

We believe that our wave propagation retrieval method and field averaging of the restored Bloch mode method will become a useful mean of the metamaterials characterization and new designs development.

3.3. Metallization of 3D surfaces

This chapter describes the developed fabrication method for electroless metallization of complex three-dimensional surfaces. Section 3.3.1 makes an overview of common metallization methods. Section 3.3.2 describes a method which is based on the silver reduction with a hydrazine hydrate, while section 3.3.3 describes a formaldehyde based electroless metallization. Conclusions end the chapter.

3.3.1. Metallization methods overview

Motivation

Deposition of thin and smooth metal layers on complex three-dimensional (3D) structures is one of the challenges within the thin film fabrication. Such structures have been proved to be extremely useful in a number of research fields and technical applications, such as in medicine [265], spectroscopy [266], electronics [267] and photonics [94]. We are interested in the fabrication methods for 3D optical metamaterials, so we focused on the isotropic metal deposition (metallization) on 3D samples with complex topology, which are aimed for metamaterials research. However, the applicability of such technique has emerging potential for much broader area than the presented example.

3D metamaterials fabrication options

Several fabrication techniques can be used for 3D metamaterials fabrication:

1) Layer-by-layer planar technology. A layer by layer approach for fabrication of 3D metamaterials in the infrared region has been demonstrated [104]. The fabrication process may involve metal and dielectric deposition, electron beam or nanoimprint [268] lithography or focused ion beam milling, lift-off, planarization, lateral alignment, and stacking. So it is complicated and it can provide only limited thickness of the resulting 3D metamaterial due to accumulation of unavoidable misalignments. Moreover, the designs that can be fabricated are limited within planar multilayer geometries.

2) Metallization of the complex dielectric surface. An alternative approach to planar technology is the fabrication of a 3D polymer skeleton structure with further partial or complete metallization of its surface. The two-photon polymerization technique (2PP) [269] is proven to be very flexible and

efficient technology for fabrication of 3D polymer layouts, including structures for photonic applications. Its potential in photonics has been confirmed by successful fabrication of woodpile constructions considered as efficient 3D photonic crystals with pronounced photonic band gaps [270-272]. However, even though various designs of 3D cubic symmetric metamaterials have been proposed [85], [243], [273], their manufacturability is hampered by the difficulty of the controlled metal deposition on 3D structures with complex topology.

Metallization of the complex surfaces

Quite often the electrochemical growth technique is used for metallic nanostructures fabrication in the polymer templates [274]. However, the electrochemical growth requires a conductive substrate that is unacceptable in many cases, for example, for microelectronics or metamaterials fabrication, where different metallic constitutive parts should be electrically disconnected.

To the best of our knowledge, there are two main non-galvanic methods for depositing metals on a 3D dielectric structure. The first one is based on the chemical vapor deposition (CVD), and the second is the electroless deposition technique. The CVD method shows great promise for depositing metals on the desired three-dimensional structure [105]. However, the parameter space for such technique is large and therefore optimization of the technology is very difficult. The electroless deposition technique provides much more reduced parameter space, thus easier optimization, and lack of volatile poisonous products in the deposition process. This is why we chose it.

We focused on the electroless silver deposition [275] since silver is a good metal for optical applications due to high conductivity and high plasma frequency. Moreover, the electroless silver metallization (silverization) is based on the well-known silver mirror reaction.

Electroless technique

Electroless plating has been used for silverization of dielectric nanospheres [276-279], fabrication of metallic nanowires and nanotubes [280-283], complex-shaped structures [284], fabrication of metallic nanoplates [285]. The electroless technique is based on the existence of a metallic complex

dissolved in a solution and then its reduction to the constituent metal at structure's surface [286]. Some features are generated by the liquid environment that this technique needs, thus making it both cheaper for utilization and less sensitive to dust particles. The equipment used can be found in virtually any chemical laboratory, making its implementation extremely easy and cheap. Another important advantage of the electroless deposition is that the method is intrinsically isotropic; therefore, it offers the possibility of metal deposition on 3D structures irrespective of its shape and topology. Also, using such technique one can, by selectively treating the sample, control where the deposition takes place. Hence, in principle, silver can be deposited only at prescribed locations [284]. Unlike the conventional metal deposition techniques that are limited to low aspect-ratio structures (evaporation, sputtering) or need a conductive substrate (electrochemical growth), the electroless method can be used for depositing metal on almost arbitrary aspect-ratio patterns and substrates. This characteristic allows using such method to cover and fill in topologically complex 3D patterns and profiles and to create high-aspect-ratio metalized structures on dielectric substrates.

There are various recipes for making the electroless deposition of silver, each having its own pros and cons. To our knowledge, the best result in silver depositing for metallization of photonic structures has been shown so far by Chen et al. [287]. For this purpose, they used the three-step recipe. The initial step consists in binding of alkyl-amine groups to the surface of interest, followed by binding of gold nanoparticles to aminated sites. The final step is the silver deposition. The presented recipe shows selectivity between the substrate and the polymer structures, but, in the same time, the grain sizes were big, leading to increased roughness and layer thickness. As a result the reported layers were about 200–300 nm thick [287].

The recipe is a nice example of possibilities the electroless deposition technique presents, but it needs more refinement in order to reach the smoothness and thickness control required for the optical metamaterial structures. One of the best silver electroless plating results was published by Koo et al. [288]. The Ag layers are both thin and very smooth, but unfortunately the TiN substrate cannot be used for photonic applications due to very high losses in the optical domain.

Our objective

Our objective was to develop a recipe for the electroless silverization of the silica or silica-like polymer surface such as the quality of the fabricated surface is suitable for the optical metamaterials fabrication.

Out of many electroless recipes we chose two. Both of them are based on the silver mirror reaction. For the first one (section 3.3.2) the hydrazine hydrate (N_2H_4) is used for silver reduction. The second recipe (section 3.3.3) uses formaldehyde for this purpose.

3.3.2. Hydrazine hydrate based electroless metallization

Process flow

The process flow of the developed deposition method is shown in the Table 3.1. A detailed description of each step is given below. The recipe was developed on the basis of Refs. [289-292] and personal communication with A. Inberg (Tel Aviv University).

1) Preparation of silica surface. The silica surface used for the first proof-of-principle and following optimization of the deposition characteristics was obtained by plasma enhanced chemical vapor deposition (PECVD) in a surface technology systems (STS) equipment. Deposition was performed in $SiH_4/N_2O/N_2$ atmosphere. The power and pressure used were $60\,W$ and $550\,mTorr$, respectively. Using the 12, 1420, and $392\,sccm$ flows for SiH_4, N_2O, and N_2, we obtained a deposition rate of $81\,nm/min$ with better than 1% uniformity. The total deposition time was $15\,min$, thus depositing the total silica thickness of $1.2\,\mu m$.

2) Cleaning. It is very important to clean the surface thoroughly before further steps, especially if there have been several preceding fabrication steps. To clean from metal contamination we kept the sample for $10\,min$ at temperature 80℃ in the solution of hydrogen peroxide H_2O_2 (30%), ammonia hydroxide NH_4OH (25%) and deionized water H_2O in the $1:1:6$ volumetric proportions. Then the sample was rinsed with water.

To clean the sample from organic contamination we used a solution of hydrochloric acid HCl (37%), hydrogen peroxide H_2O_2 and deionized water H_2O in $1:1:5$ volumetric proportions. The sample was kept in the solution heated to 80℃ for $10\,min$. Then the sample was rinsed with water.

Table 3.1. Process flow of the hydrazine hydrate based electroless metallization method

Step	Sketch	Comments
1) Preparation of silica surface		PECVD, 1.2 μm of silica on Si substrate
2) Cleaning		Metal contamination: NH_4OH + H_2O_2, T=80 C Organic contamination: HCl + H_2O_2, T=80 C
3) Adhesion improvement		3-APTES, T=70 C
4) Seed layer formation	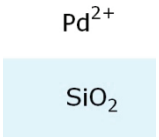	$PdCl_2$ in HCl + NaOH + citric acetic acid, T=room temperature
5) Silver layer deposition	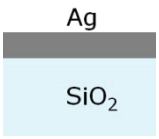	Silver ammonia-acetic complex and hydrazine hydrate + additives, T=5 C.

3) Adhesion improvement. To enhance the adhesion of silver to the sample, the sample was treated with 3-aminopropyltriethoxysilane ($3-APTES$). For this purpose 2.14 ml of $3-APTES$ (99%) was mixed with 98 ml of water H_2O, heated to 70℃ and the sample was kept in the solution for 20 min. Then the sample was rinsed with water.

4) Seed layer formation. For a smooth silver layer growth a seed layer is needed. We used palladium chloride for seed layer creation. Palladium ions Pd^{2+} attach to silica surface and then serve as the starting point for silver reduction.

A palladium chloride stock solution (A) was prepared by dissolving 1.00 g of $PdCl_2$ in 10 ml of hydrochloric acid HCl (35%). The hydrochloric acid is needed since palladium chloride does not dissolve well in the pure water. After $PdCl_2$ dissolves completely, deionized water was added until the total volume reached 100 ml.

For the surface treatment 1 ml of the stock solution (A) was mixed with 0.735 g of citric acid, 0.875 ml of sodium hydroxide $NaOH$ (8.0 M), 0.542 ml of hydrochloric acid HCl (37%) and water until the total volume of the solution reaches 100 ml. $NaOH$ and HCl were used to tune the pH to be equal to 3. The sample was kept in the solution at room temperature for 10 min and then rinsed with water.

5) Silver layer deposition. Before the solution mixing all the components were cooled down to 5°C in the refrigerator. The beaker where the mixing and further silver deposition took place was put on the Peltier cooler to keep the constant temperature 5°C. The chemicals were added in the following sequence:

1) 5.00 ml of silver nitrate $AgNO_3$ (0.60 M).

2) 1.00 ml of sodium dodecyl sulfate (SDS) (0.10 M). It works as a surfactant.

3) 7.47 ml of ammonia hydroxide NH_4OH (25%).

4) 2.86 ml of acetic acid CH_3COOH (99%), being added by small portions upon constant stirring with magnetic mixer.

5) 64 ml of MilliQ water H_2O.

After mixing all the above mentioned chemicals the solution was filtered through the filtration paper. Ammonia-acetic silver complex was formed.

6) 17 ml of ethylenediaminetetraacetic acid disodium salt ($EDTA - Na$) (0.10 M). It works as a complexing agent and also plays a role in pH regulation.

7) 1.00 ml of sodium saccharin (0.40 M). It plays a role of brightener [293].

8) 1.00 ml of polyethileneglycol with the molecular mass 1500 ($PEG-1500$) ($6.0 \times 10^{-6}\ M$). It was empirically found out that $PEG-1500$ improves the metallization of the trenches in silica.

9) Finally 0.595 ml of hydrazine hydrate N_2H_4 (25%) was added and the reaction started. The solution became dark grey. Hydrazine hydrate works as a reducing agent.

All the chemicals mentioned above were obtained from Sigma-Aldrich [294].

The main chemical reaction is a reduction of Ag from Ag^{2+}-ammonia-acetate complex [293]:

$$4Ag^{2+} + N_2H_4 + 4OH^- \rightarrow 4Ag + 4H_2O + N_2 \qquad (3.50)$$

Immediately after adding hydrazine hydrate and mixing the solution the sample was put into it. The growth rate usually decreases with an increasing pH value [293]. We have made the thickness measurements for various deposition times and found out that the deposition starts only after 60 min from hydrazine hydrate addition. Then the growth was proportional to immersion time and equal to 4.5 nm/min for $pH = 10$ (see Fig. 3.35).

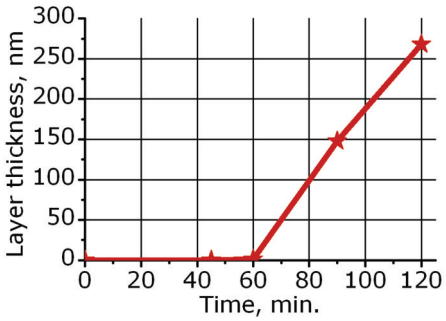

Figure 3.35. Silver layer growth dynamics. The starting point corresponds to the time point, when the reducing agent (hydrazine hydrate) was added. The deposition starts only after 60 min.

Results

We have tried the hydrazine hydrate based recipe several times, varying the pH of the solution between 9 and 10 by adding $NaOH$. In the most cases the silver film was polycrystalline with the grain size more than 100 nm (see Fig. 3.36). Larger clusters were also observed on the metal surface

(Fig. 3.36(a)). These clusters are most probably created in the solution volume and then drop onto the sample surface. After 90 min of deposition the thickness of the continuous metal film was 148 nm.

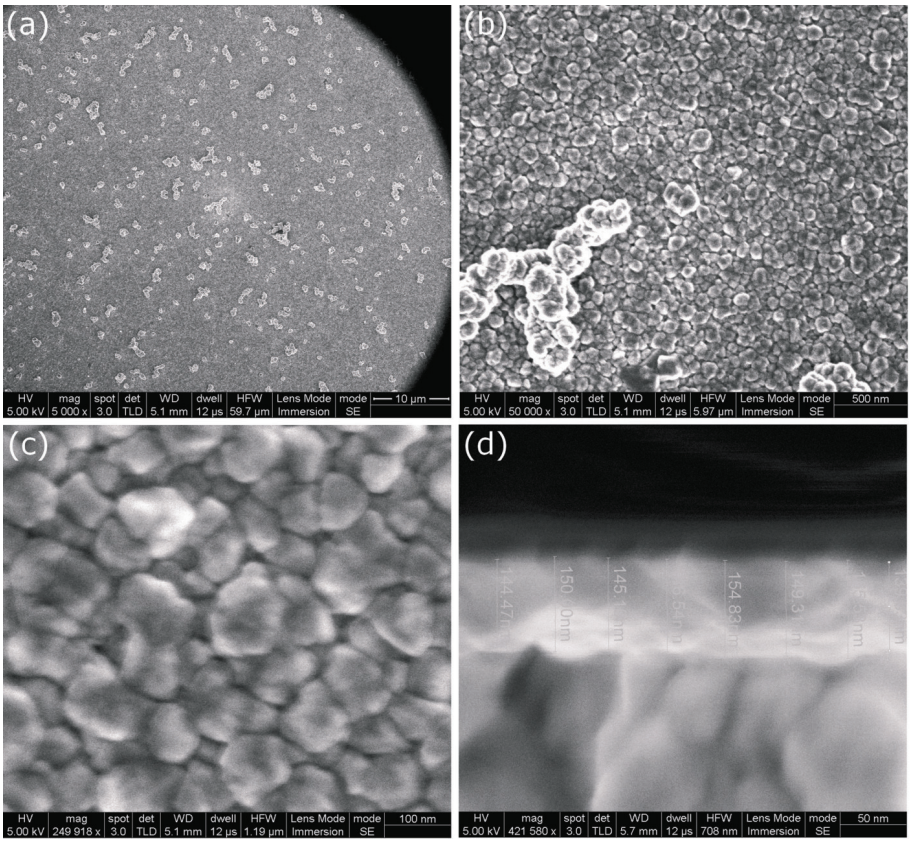

Figure 3.36. A silver layer deposited with a hydrazine-based electroless method, top view shown with $5k$ (a), $50k$ (b) and $250k$ (c) magnification. Except the continuous metal film, big clusters are observed on the surface. The deposition time of 90 min resulted in 148 nm thick silver film, side view (d).

In the solutions with lower $pH = 9$ the surface was even rougher with the large clusters all over the place (Fig. 3.37(a)). At the same time, some regions of flat and smooth surfaces were also observed (see Fig. 3.37(b)). The grain size in them was less than 30 nm.

A larger size of the clusters on the surface was due to a faster growth of the silver. We explain the presence of the smooth regions by the appropriate chemical conditions for such surfaces creation. It is likely that the surfaces

were crystallized in the solution volume as flakes and then fell down on the sample surface. A similar effect but with much smoother surface (down to the atomically flat level) has been recently demonstrated as a technology for the plasmonic circuitry fabrication [295].

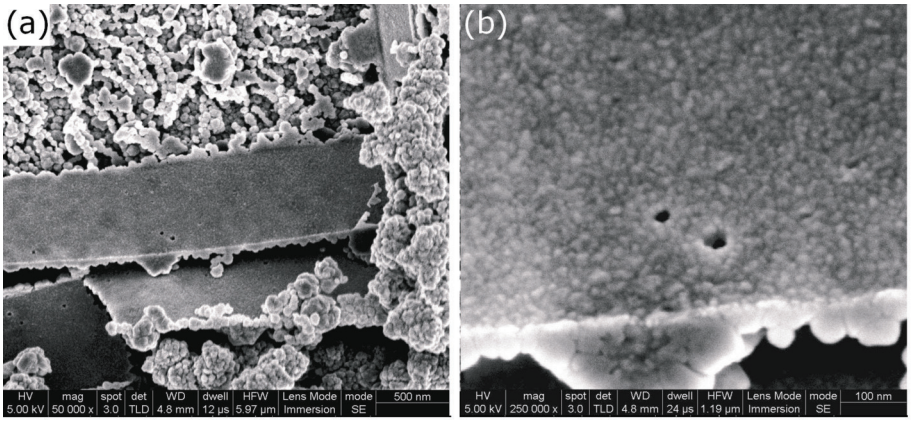

Figure 3.37. The results of the hydrazine hydrate based metallization in the solution with $pH = 9$. The silver surface is covered with large chaotically placed cluster, but some regions of very smooth surface can be found (a). A zoom-in of the smooth surface (b). The grain size is less than 30 nm.

Conclusion

We tried the hydrazine hydrate reduction of silver from the silver-ammonia-acetate complex. In some cases a regions of smooth and flat surface were observed. However, these structures were not regular and large metallic clusters dominated on the surface. The size of the clusters was more than 100 nm.

Except the rough deposited metal layer the hydrazine-based process takes a lot of time for sample preparation (cleaning, adhesion improvement and seed layer formation) and requires many chemicals to be used. All that makes difficult the optimization of the process. It can hardly be used for optical metamaterials fabrication.

3.3.3. Formaldehyde based electroless metallization

Process flow

The process flow of the developed electroless method [21,22] is presented in the Table 3.2. A detailed description of each step is given below. The steps 1a) and 1b) correspond to the test flat surface samples and woodpile photonic crystals cases, respectively.

Table 3.2. Process flow of the formaldehyde based metallization method

Step	Sketch	Comments
1a) Preparation of silica surface		PECVD, 1.2 μm of silica on Si substrate
1b) Preparation of 3D samples	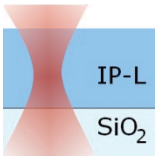	Nanoscribe 2PP on the IP-L resist
2) Surface treatment for adhesion improvement	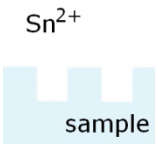	$SnCl_2$ in HCl and acetic acid, then deionized water rinsing
3) Silver layer deposition		Silver complex $Ag(NH_3)_2OH$ and formaldehyde solutions, then deionized water rinsing.

1a) Preparation of silica surface. The silica surface used for the first proof-of-principle and following optimization of the deposition characteristics was obtained by plasma enhanced chemical vapor deposition (PECVD) in a surface technology systems (STS) equipment. Deposition was performed in $SiH_4/N_2O/N_2$ atmosphere. The power and pressure used were $60\,W$ and $550\,mTorr$, respectively. Using the 12, 1420, and 392 $sccm$ flows for SiH_4, N_2O, and N_2, we obtained a deposition rate of 81 nm/min with better

than 1% uniformity. The total deposition time was 15 min, thus depositing the total silica thickness of 1.2 μm.

1b) Preparation of 3D samples. The samples were fabricated by two-photon polymerization (2PP) on the IPL resist using the Nanoscribe system [298], [299]. The photoresist layer was deposited on a one-inch, 150 μm thick glass slide. The laser beam was focused into the volume of the photoresist through the glass slide by the oil immersion 100 × microscope objective with numerical aperture 1.4.

2) Surface treatment for adhesion improvement. In order to improve the adhesion of an Ag layer on silica and IP-L surfaces, the sample was immersed in acidic solution of $SnCl_2$ [300]. The pretreatment solution was prepared by dissolving 2 g of tin chloride $SnCl_2$ into 3 ml glacial acetic acid and 1 ml of hydrochloric acid HCl and then diluting the obtained solution in a 1: 100 volumetric proportion in MilliQ water. All the substances were obtained from Sigma-Aldrich. The total immersion time was 10 min and then the samples were thoroughly rinsed in distilled running water for 15 min. Careful rinsing is required since otherwise the silver deposition solution is readily contaminated, and thus the reducing process is not optimal [300]. Immediately after the samples are surface treated, the silver deposition takes place.

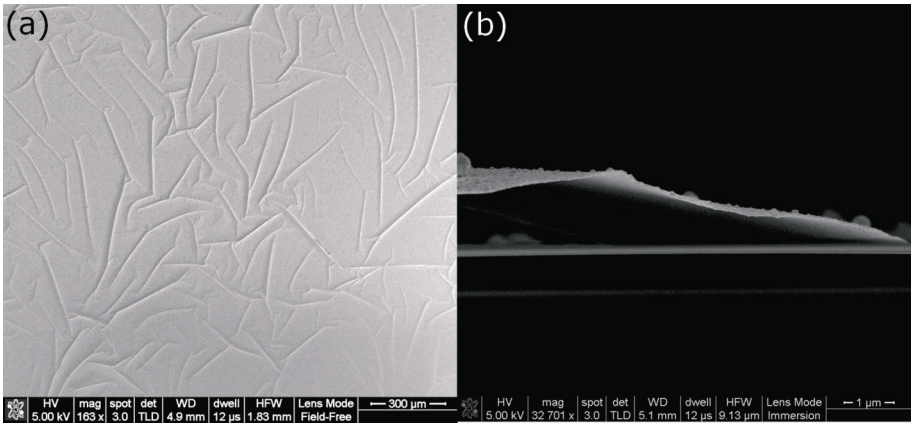

Figure 3.38. Example of weak adhesion of the silver layer to the untreated silica surface. It illustrates the importance of pretreatment for good adhesion. (a) Top view of a layer with poor adhesion. (b) Cross-section showing the detachment of the Ag layer from the untreated silica surface.

The surface pretreatment is an important part of the process. To prove its significance we tried to deposit silver without pretreatment. As it can be seen from Fig. 3.38, in its absence, the silver layer is not adhering to the silica substrate. In the same time this non-adhesion shows that, if needed, silver can be selectively deposited on a structure by deliberate pretreatment of the surface.

3) Silver layer deposition. To obtain thin and smooth metallic layers we optimized the recipe known as Tollen's test or the silver mirror reaction [300]. Within such recipe the three main reaction steps are as follows:

1. In the diluted solution of silver nitrate the ammonia hydroxide is added in order to form brown precipitate (silver oxide)

$$2AgNO_3 + 2NH_4OH \rightarrow Ag_2O \downarrow + 2NH_4NO_3 + H_2O \qquad (3.51)$$

2. Continuously adding ammonia hydroxide leads to the formation of ammoniac silver nitrate. The solution becomes transparent again

$$\begin{aligned} Ag_2O + 2NH_3 + 2NH_4NO_3 + H_2O \\ \rightarrow 2Ag(NH_3)_2NO_3 + 2NH_4OH \end{aligned} \qquad (3.52)$$

that readily splits into its polar constituents

$$\begin{aligned} Ag(NH_3)_2NO_3 + NH_4OH \\ \rightarrow Ag(NH_3)_2^+ + NO_3^- + NH_4^+ + OH^- \end{aligned} \qquad (3.53)$$

At this point the silver compound is fully formed and can be reduced to silver and ammonia.

3. The reducing reaction takes place in the presence of a reducing agent, for example, aldehyde (formaldehyde in our case) and is generally used for determining the presence of such aldehydic groups

$$\begin{aligned} HCOH + 2OH^- + 2Ag(NH_3)_2^+ \\ \rightarrow HCOOH + H_2O + 2Ag \downarrow + 4NH_3 \end{aligned} \qquad (3.54)$$

Even if the reaction process is well understood, the practical implementation is not a direct one, so we spent much time optimizing the recipe. The first challenge was the time instability of the ammoniac silver nitrate solution; thus, it was prepared every time from stock solutions.

The first solution (A) was obtained by mixing $2.5\,ml$ $0.2\,M$ silver nitrate $AgNO_3$ solution with 0.114 ml 25% ammonia NH_3 solution. At the beginning, silver oxide AgO_2 is formed in the phase of brown precipitate. Ammonia hydroxide was added continuously to carry on the reaction until the silver ammonia complex was obtained. The solution was then diluted in MilliQ water in order to obtain the total $5\,ml$ of reagent. The second solution (B) was the 8% formaldehyde $HCOH$ solution. The concentrations of reagents were thoroughly optimized.

The deposition procedure involves immersing the surface treated sample in $30\,ml$ of MilliQ water and then adding $500\,\mu l$ of formaldehyde solution (B) and then $5\,ml$ of silver ammonia complex solution (A). The solution becomes dark and the reaction takes place. At room temperature, due to the fast reaction time, the reaction is difficult to control; therefore, the solutions were cooled down to 5°C. The deposited silver film thickness varies with the immersion time, having the approximate growth rate of $30\,nm/min$ at this temperature. After the layer was formed, the samples were thoroughly rinsed in running water for $5\,min$. The non-reacted solution must be carefully disposed of and the containers used must be thoroughly rinsed in order to prevent the formation of explosive silver nitride.

Results

Optimization steps in the abovementioned technique were made within the first rounds of tests on simple planar samples. The thinnest uniform silver layer obtained was of about $30\,nm$ (Fig. 3.39(a)). The layer thickness is directly proportional to the immersion time. Using the presented recipe, thicknesses of up to $200\,nm$ have been achieved (not shown) simply by increasing the immersion time. Silver layers thinner than $30\,nm$ were not completely formed but exhibited randomly placed clusters. We think that this effect is due to the mechanism of the silver seeds growth in the solution.

In the Fig. 3.39(b) we present a top view showing high uniformity in the layer formation. The substrate is uniformly covered, but few silver nanoparticles can be observed on the top of its surface. These Ag nanocrystals are formed in the solution and then deposited in the ready form on sample's surface. Still, such nanocrystals' formation is minimal and does not restrain the overall deposition process.

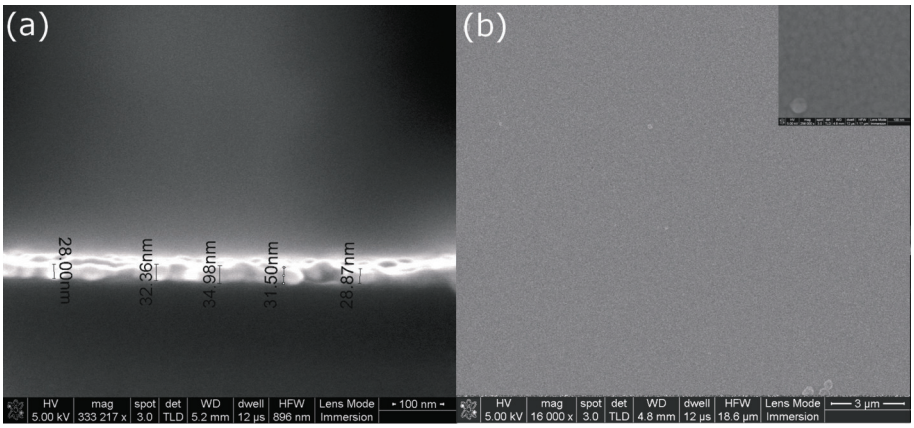

Figure 3.39. (a) Ultra-thin uniform silver layer deposited by the electroless technique on the silica substrate. Numbers show the thickness of the silver coating. (b) Top view of $30 \times 30\mu m^2$ sample's area showing high deposition uniformity over a large area. Some single Ag nano-crystals deposited on top of the layer are visible. In the inset, the zoomed in surface is shown

In the inset of Fig. 3.39(b), one can see a top-view of the layer at a higher magnification. Thus, the polycrystalline growth of silver is noticeable. The samples were up to $1 \times 1\ cm^2$ in size, and no pronounced difference in layer properties was noticeable over such extended surface. So it validates that such technique has no limitations by the depositing area and can be applied to samples of, in principle, whatever dimensions.

For optimizing the deposition technique, we employed the quantitative criteria of the average roughness calculated on a sample portion, where there were no Ag nanocrystals. The roughness was calculated from atomic force microscope (AFM) measurements obtained in the tapping mode. While single nanocrystals can reach dimensions of up to $100\ nm$, the average roughness in the "clean" areas was of the order of $4\ nm$ and the roughness mean square value (RMS) was about $6\ nm$, which is comparable with the RMS for evaporated films (see Fig. 3.40). Taking into account that the substrate average roughness measured in the same conditions was $2\ nm$, we conclude that the metallic layer is adding approximately $2\ nm$ of roughness.

What is very interesting, the silver layers deposited with electroless technology did not oxidized exposed to the air for a long time (more than a month), while evaporated silver is covered very quickly with silver oxide

that worsens metal's properties. We attribute this fact to some kind of silver passivation that happens during electroless deposition.

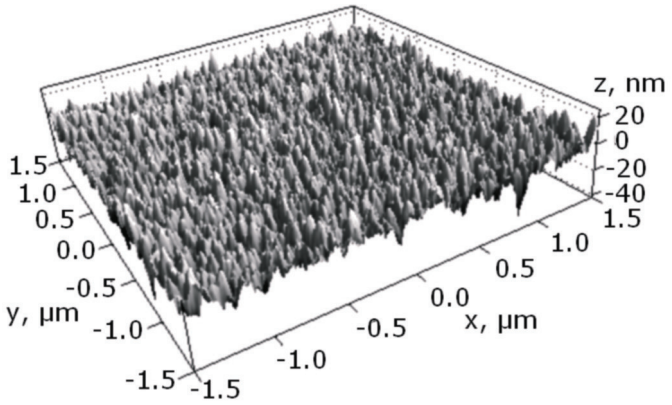

Figure 3.40. 3D AFM image used for roughness analysis. The average roughness of 4 nm with an RMS of 6 nm was calculated excluding the areas with silver clusters on.

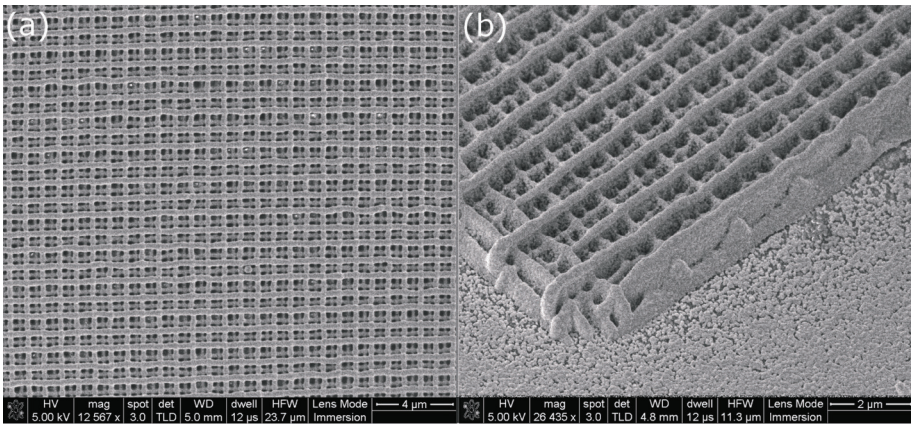

Figure 3.41. A 3D woodpile structure covered by silver after electroless deposition. (a) Top view of the sample showing uniform deposition over a big surface area. (b) Tilted imaging showing deposition on the structure's sidewalls.

Following the process optimized for flat surface we deposited a silver layer on a structure with 3D topology. As a sample for thorough checking of deposition on volumetric structures with complex profiles, we chose a 2PP polymer woodpile [301]. This way we were able to check the Ag deposition both on structure's sidewalls as well as in the bulk volume deep inside it.

The woodpiles are $100 \times 100\ \mu m^2$ and have a height of $2\ \mu m$ corresponding to two periods (eight single layers) of the lattice. Sizes of the bar cross-section are $150 \times 150\ nm^2$.

We immersed the woodpiles into the deposition bath for $2\ min$. This produces approximately $50\ nm$ thick regular silver layer of the woodpile surfaces. Results of silver deposition are presented in Fig. 3.41. The Ag layer was deposited not only on the top of the structure but also on its sidewalls. There is still particle formation in the solution followed by their adhesion to the deposited layer, but it can be further minimized.

Upon inspecting the metalized structure at higher magnification (Fig. 3.42) we can observe the presence of the silver layer inside the bulk structure as well. The layer quality when depositing on a $3D$ structure is different from the one on a plane silica surface. We believe that this dissimilarity is mainly due to the modified surface chemistry of IP-L polymer used in the 2PP fabrication of the $3D$ samples. The reaction is diffusion driven. Due to this aspect, the silver layer quality is monotonously degrading from the top to the bottom of the structure (Fig. 3.43). Nevertheless, deposition took place everywhere, covering the whole woodpile with a $50\ nm$ thick silver layer in one $2\ min$ approach only. With further optimization and decreasing of the reaction speed, this effect can be minimized.

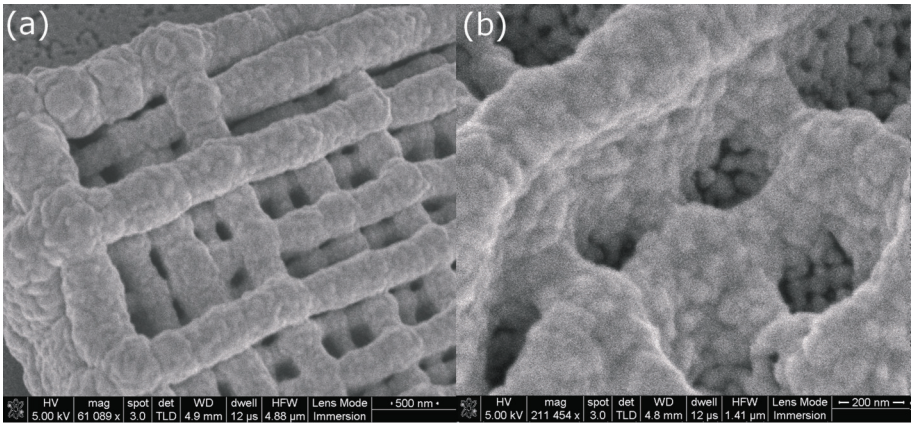

Figure 3.42. High magnification SEM image of the $3D$ structure showing the deposition took place also inside the woodpile. (a) $60k$ magnification showing deposition of Ag several layers inside the woodpile. (b) $200k$ magnification allowing the inspection of the Ag deposition inside small dimension holes.

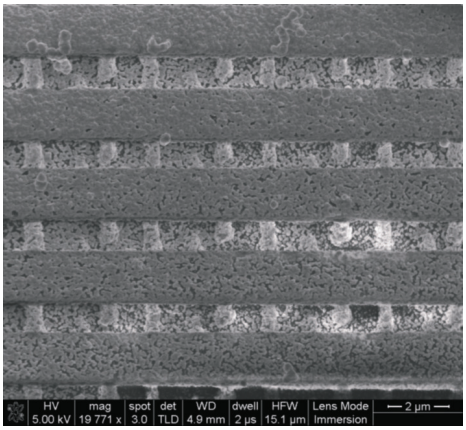

Figure 3.43. Side wall SEM image of a $3D$ periodic structure made by two photon polymerization. As can be seen, the deposited layer's quality decreases from the top to the bottom of the structure. Here five periods in the vertical direction are presented.

Conclusion

The developed electroless metallization method allows depositing continuous silver layers of the thickness starting from $30\ nm$ on the silica or silica-like polymer. The obtained roughness mean square value was $6\ nm$. To reach such smooth deposition the concentrations of reagents were carefully optimized. The advantages of the developed electroless method are the simplicity of the implementation. It is much simpler to use and takes less time than hydrazine hydrate based metallization process (section 3.3.2). The method does not require any special chemical equipment. It is also easily scalable to mass production.

Conclusions

One of the main bottlenecks in advancing the fabrication of metamaterials is due to the difficulty of realizing low-cost isotropic $3D$ deposition of metals on desired structures. We believe that by using a combination of the electroless deposition and 2PP techniques a viable solution for fabricating $3D$ bulk metamaterials can be found.

We tried two recipes of electroless surface silverization. The results of the hydrazine hydrate based method were unsatisfactory. An optimized formaldehyde-based method resulted in the smooth silver layer deposition on

silica and IP-L polymer surface. The obtained results are easily reproduced on various samples of different dimensions as long as the deposition conditions are the same. Varying the deposition time one may obtain a continuous silver layer of thickness starting from 30 nm.

The presented technology is not sufficient for fabrication of the proposed Split Cube in Carcass negative index metamaterial (section 3.1), since it requires hollow cubes and long wires of 20 nm in thickness. However, it proved to be useful for larger structures fabrication, such as woodpile photonic crystals and it can be easily used for the metamaterials fabrication for longer-wavelength range, for example, far infrared and terahertz. The proposed technique is not limited to the metamaterials field, but it can be used in other research areas where depositing of metals is required. Electroless metal plating bears great potential in many aspects of metal deposition in nanophysics and nanotechnology.

3.4. Homogenization of resonant metamaterials

This chapter describes the investigation of the homogeneity of the resonant metamaterials. Homogenization of metamaterials is a crucial issue since it allows description of their optical response in terms of effective wave parameters as, e.g., propagation constants.

Our objectives

The objective of this investigation was to provide a systematic and comprehensive analysis of the influence of the coupling effects on the EPs of chiral MMs and on the chiral MMs homogenization. Another objective was to formulate the quantitative measure for homogeneity evaluation.

Why chiral metamaterials?

We chose a chiral metamaterials for the investigation since the coupling effects usually play a big role in them. Another reason was that the effects described below were spotted while we were working on the wave propagation method for chiral metamaterials. However, the presented methodology and the conclusions are general and not attached to a specific metamaterial.

Chiral metamaterials and their effective properties

By definition, the unit cell of a chiral material is not superimposable with its mirror image and any chiral material exhibits gyrotropy, in general. There are many manifestations of this potential of chiral MMs as giant optical activity [302-304], circular dichroism [236], [305], [306] and negative index of refraction [247], [248], [307-310], which are either considerably enhanced in comparison with the naturally occurring phenomena or cannot be observed in nature at all.

However, a giant gyrotropy requires strong intrinsic resonances of the elementary constitutive components, i.e., the chiral "meta-atoms," For nonresonant structures the optical rotary power per meta-atom layer is usually vanishingly small. Even for resonant structures the achievable polarization rotation is often below the requirements of applications. This limitation can be overcome by stacking of several functional layers. Conventionally, light propagation in multilayered MMs is described by

assigning effective wave parameters (EPs) to this MM [102], [220], [237], [252], [307], [309], [311], such as, e.g., the propagation constant k or the effective refractive index introduced as $n = kc/\omega$. Such EPs simplify the design and the description of functional MM devices. However, before assigning EPs it is of utmost importance to assure that the respective MM may be actually homogenized [219].

Coupling effects in metamaterials

When the mutual coupling between adjacent functional layers in a stack is strong, the convergence of, e.g., the effective refractive index with the stack thickness toward its bulk value is poor [242].Then, and this is a common situation, the EPs depend on the MM slab thickness. Such effective properties have very limited sense [240] since they cannot predict the response (for example, reflectance and transmittance) of a MM slab with an arbitrary thickness. The EPs are very rarely identical for a single and an infinite number of monolayers, though designs exist exhibiting this property [243]. Near field coupling has been investigated for the constitutive elements of metaatoms [312-314], magnetic plasmon structures [315], [316] and chiral MM bilayers [317]. The latter work [317] showed that the functional properties of the bilayered MM with coupling between layers are different from the properties of a monolayer. However, up to our knowledge, the general analysis of the coupling effects on the EPs of chiral metamaterials has not been conducted yet.

Metamaterial designs

We investigated two specific MM designs: the twisted-cross (TC) MM (Ref. [302]) and the twisted split-ring resonator (TSRR) MM [252], [318]. The choice of the specific metamaterials was arbitrary to a certain extent. We conjectured on the base of the geometrical design that the twisted-cross MM was feasible for homogenization whereas the split-ring resonator MM was not. These metamaterials were chosen only as specific examples at which the important physical effect can be revealed. However, a large number of similar structures could have been used as well.

Wave effective parameters considered

We considered only effective wave parameters rather than any material EPs [188], [240]. Hence, effects caused by the mesoscopic structure of MMs (nonlocality, spatial dispersion, see, e.g., Refs. [240] and [197] are not in our focus. The aim is rather to show under which conditions a multilayered periodic chiral MM may be described as an effectively homogeneous medium, similar to the investigations performed for the fishnet MM (Refs. [199] and [233]) and multilayered dielectric stack in Ref. [257]. To avoid any complications with the tensorial properties of homogenized materials, the direction of propagation is fixed along the axis pointing normal to the MM surface and the responses of the media are probed upon illumination with left-and right-circular-polarized waves only. Because of normal incidence the eigenvalue problem reduces to a scalar problem.

Homogeneity conditions

An adequate description of a MM as homogeneous requires the following:

(i) The operating frequency must be below the first Bragg resonance $Re(ka) < \pi$, where a is the meta-atom size in the direction of wave propagation. Otherwise, the MM constitutes a photonic crystal and its homogenization is meaningless[219].

(ii) The lateral MM periodic must be such that the propagation of nonzero diffraction orders is suppressed [197], i.e., the transverse size of a unit cell is required to be smaller than half the wavelength.

(iii) For each polarization state the light propagation must be governed by a single (fundamental) Bloch mode only [197] having the smallest losses.

(iv) The incident light should predominantly couple to this Bloch mode [197], [199]. In general, the situations may occur where light couples to a higher-order Bloch mode more efficiently than to the fundamental one. If this higher-order Bloch mode is more damped than the fundamental one, its impact becomes negligible above a certain thickness of the MM slab and EPs converge to those of the bulk. However, if the attenuation coefficients for all Bloch modes to which light can couple are comparable, then this leads to thickness-dependent EPs and results in the lack of homogeneity. The rigorous mathematical approach in the theory of homogenization of the periodic chiral metamaterials can be found in Ref. [319].

Dispersion relations as a research tool

As the tool to analyze the above mentioned questions we rely on the dispersion relation of Bloch modes (see an example in Fig. 3.44). The respective dispersion diagrams provide comprehensive information about the eigenmodes that are sustained by the MM.

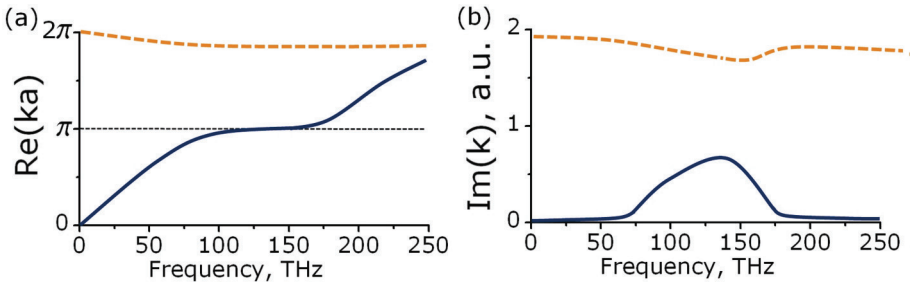

Figure 3.44. An example of a dispersion diagram for the Bloch modes. Real (a) and imaginary (b) parts.

The occurrence of a Bragg resonance can be extracted from the dispersion relation and occurs whenever $Re(ka) = \pi$ (Fig. 3.44(a)). From the analysis of the dispersion of the imaginary part of the wave number $Im(k)$ (Fig. 3.44(b)) we can evaluate the propagation losses. So it is easy to infer about requirements (iii) and (iv) – the number of dominating modes and their losses – by considering in detail the dispersion relations. Thus, the Bloch modes dispersion diagram is an efficient mean of MM homogeneity characterization. We would like to remark that in the case of chiral media with $C4$ symmetry there are two fundamental modes: right and left circular polarized (RCP and LCP).

The first homogeneity requirement implies that a smaller lattice period a in the propagation direction is beneficial. To check this statement we calculated the Bloch modes dispersion diagrams for both the twisted-cross metamaterials [302] (Fig. 3.45(a)) and twisted split-ring resonator metamaterials [318] (Fig. 3.45(b)). The lateral sizes of their unit cells are such that the homogeneity requirement (ii) is satisfied in the whole frequency range of interest.

Chirality parameter

The chiral properties of a MM are determined through their effective refractive indices for the LCP and RCP waves the n_L and n_R, respectively.

The chirality parameter is given by $\kappa = (n_R - n_L)/2$. Its real part $Re(\kappa)$ describes the rotation of the polarization ellipse (or optical activity)whereas the imaginary part $Im(\kappa)$ governs the circular dichroism [311].

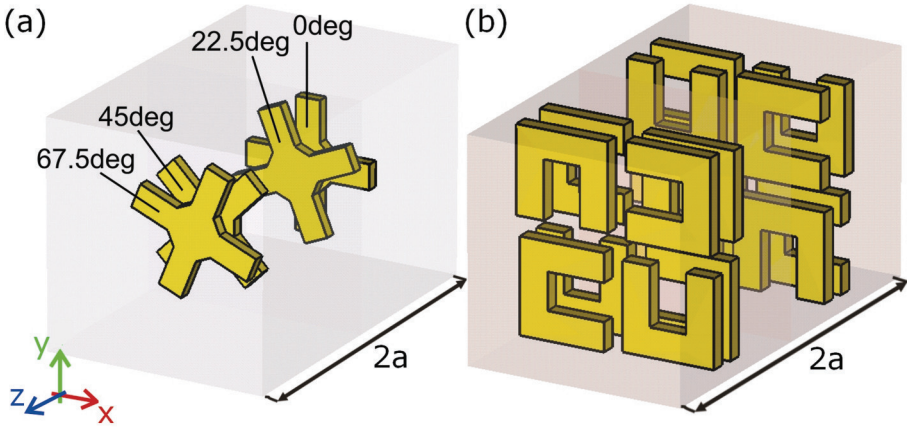

Figure.3.45. Metamaterial designs under consideration: (a) twisted cross (TC) and (b) twisted split ring resonator (TSRR) metamaterials. Wave propagation and metamaterial stacking direction is along $z-$ axis.

Simulation methods

To simulate the optical response of MM slabs with various thicknesses we rely on the commercially available CST Microwave Studio software [201] that implements the finite-integral method in the frequency domain. The thin-slab EPs are retrieved from the complex reflection/transmission coefficients [102], which we refer to as the standard method. The thick slab EPs, which are close to bulk parameters, are restored from the spatial dependence of the wave field with the wave-propagation retrieval method (WPRM) [223], [249]. The Bloch dispersion diagram calculations are performed for infinite periodic media using a plane-wave expansion method [198] and taking into account the dispersion of the metal permittivity. Details of the calculation method can be found elsewhere [197], [199], [264]. Comparing the spectral simulations of finite structures, performed with the CST Microwave Studio, with those done with the plane-wave expansion method we observed a steady blueshift in spectra of about 20 THz for the latter method. This shift that happens due to different numerical approaches is of minor importance for our conclusions.

Twisted cross metamaterial design

The TC MM [302] (see Fig. 3.45(a)) is an example of a chiral MM that provides strong optical activity. Its meta-atoms consist of two golden crosses embedded into a dielectric. One cross is 22.5° twisted with respect to the other. Lateral unit-cell sizes are $a_x = a_y = 500\,nm$. The metallic crosses of thickness $25\,nm$ are separated with a dielectric spacer of $37.5\,nm$. The eigenfunctions of the TC are RCP and LCP because of the $C4$ symmetry of the MM. For our investigation we use the parameters of Ref. [302]. However, in Ref. [302] only a monolayer is characterized. To access the bulk properties of such a MM we stack multiple monolayers as presented in Fig. 3.45(a). The meta-atom size in the propagation direction a is subject to variations. The crosses in each meta-atom are twisted by 45° with respect to each other. Details can be seen in Fig. 3.45(a) where the angles of consecutive layers are indicated.

Note that, although the real unit-cell size in propagation direction is $2a$, the size a is actually the length scale of importance because it denotes the periodic distance of consecutive functional layers. Since the optical responses of the two parts of the unit cell are close to identical, we wish to regard this distance a as the period. In fact, calculating the dispersion diagrams for the structure with the second double cross being identical to the first one, i.e. leading to a true period a, results qualitatively in the identical characteristics. This holds except for the case of dense stacking, where the material becomes achiral. The Bragg resonances for the present structure are caused by the reflection of light at the consecutive layers of the unit cell rather than by the boundary between two unit cells. Bragg gaps due to the period $2a$ are not observed. Therefore, we will call the parameter a in the following the period of the structure.

Standard retrieval for TC

To challenge the third requirement of the homogeneity we applied the standard retrieving (based on reflection/ transmission) to thin MM slabs and the wave-propagation method to thick MM slabs. The aim of such retrieval with different methods was to check the convergence of the effective parameters. We studied MMs with two different center-to-center separations, the dense ($a = 125\,nm$) and the sparse stacking ($a = 250\,nm$). The thin-slab case consisted of $1-3$ meta-atom layers for both MMs. For the thick

slab EPs retrieval, 48 monolayers were stacked, thus mimicking the bulk material.

The structures exhibit completely different types of convergence with the slab thickness. For the dense stacking the convergence in the resonant region is very slow (Fig. 3.46(a) and (b)). So we suspect that the TC is not homogeneous there due to strong coupling between consecutive unit cells. The coupling can be reduced by separating the unit cells more. Indeed, for the sparse stacking, the effective refractive index of the thin slab quickly converges to the bulk values that are retrieved with the wave-propagation retrieval method (Fig. 3.46(c) and (d)). This is a clear indication that such MMs might satisfy the homogeneity conditions.

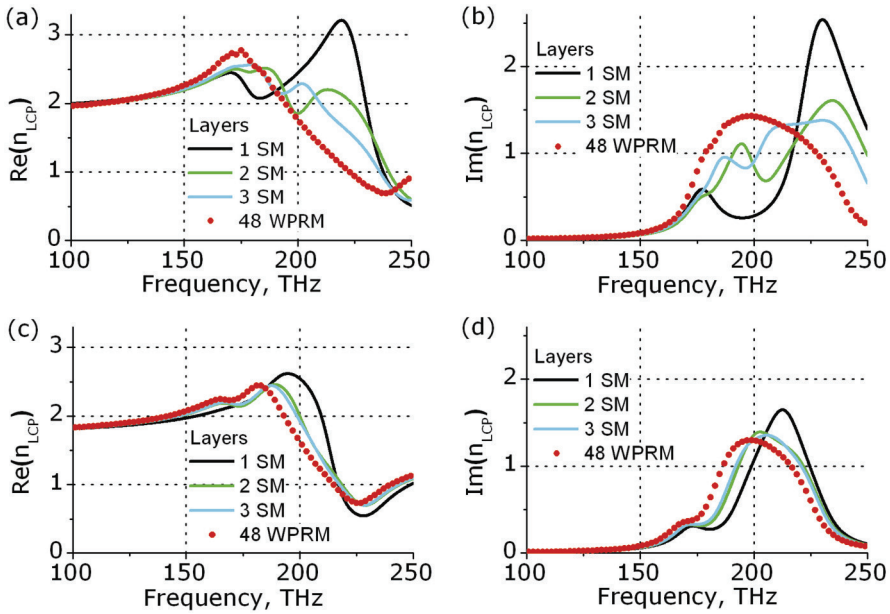

Figure. 3.46. Effective refractive index of left circular polarized light of a twisted-cross metamaterial as a function of frequency and for different numbers of layers that form the MM. Dense stacking (period $a = 125\ nm$): (a) $Re(n_{LCP})$, (b) $Im(n_{LCP})$ and sparse stacking (period $a = 500\ nm$) (c) $Re(n_{LCP})$, (d) $Im(n_{LCP})$. Effective parameters are retrieved with the standard NRW method (Ref. [102]) (SM) for one (black line), two (green/gray line), and three (cyan/ light gray line) monolayers and with the WPRM (Ref. [249]) for 48 layers (red/dark gray dots).

Bloch modes dispersion diagram for TC

To check the limits where TC homogenization fails we calculated the Bloch modes dispersion diagram for increasing separation, as shown in Fig. 3.47. It is clearly seen that for the dense stacking ($a = 125\ nm$) higher-order Bloch modes have a damping comparable with the fundamental modes in the resonant region (Fig. 3.47(a)). Slow convergence of the EPs as seen in Fig. 3.46(a) and (b), confirms that light couples to the higher-order Bloch modes, thus homogeneity requirement (iv) is violated.

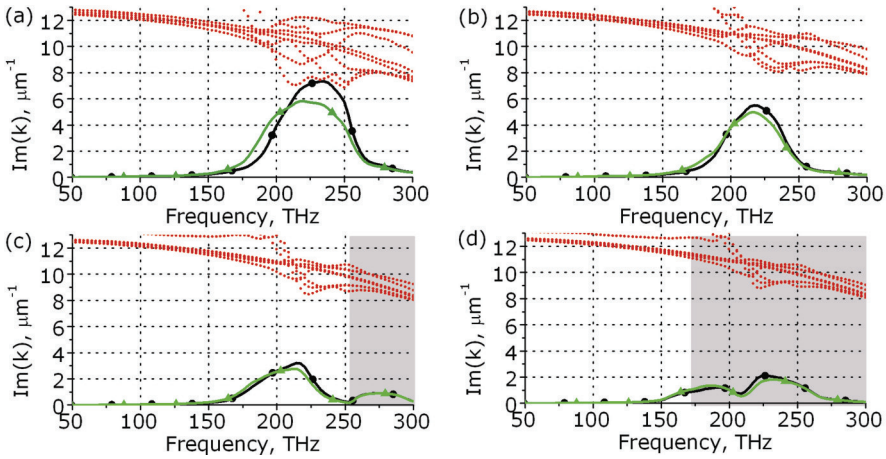

Figure. 3.47. Bloch modes damping I(k) dispersion spectra for twisted-cross MM for different separations a: (a) $125\ nm$, (b) $250\ nm$, (c) $400\ nm$, and (d) $500\ nm$. Fundamental modes are shown as black line with circles and green/gray line with triangles; all the higher-order Bloch modes are shown in red/dark gray dots. The frequency region above the first Bragg resonance is shadowed.

For the sparse stacking case of $a = 250\ nm$ (Fig. 3.47(b)) the continuum of the higher-order Bloch modes is separated from the fundamental ones in terms of losses. The higher-order modes are much stronger damped than the fundamental ones. Thus one may expect that only the fundamental modes govern the light propagation. Moreover, the MM unit cells are still subwavelength (the resonant response occurs at frequencies far below the lowest order Bragg resonance), so all four requirements are satisfied, and the TC MM can be considered as homogeneous.

Increasing the period to $a = 400\ nm$ we observe a new peak in $Im(k)$ emerging at around $275\ THz$ and which is separated from the lowest

resonance by a local minimum in losses at $250\,THz$ (Fig. 3.47(c)). The Bragg condition $Re(ka) = \pi$ is satisfied between 250 and $300\,THz$, therefore, this peak can be clearly identifed as the first Bragg resonance. In the frequency region above the first Bragg resonance $Re(ka) > \pi$ the properties of periodic arrangement of unit cells dominate and according to requirement (i) the homogenization fails. The frequency ranges where photonic crystal properties prevail are shadowed in Fig. 3.47.

Increasing a even further to $500\,nm$ we face the situation where the first Bragg resonance overlaps with the intrinsic resonance of the meta-atoms at $220\,THz$ (Fig. 3.47(d)). Interestingly, the dip in the absorption spectrum at $210\,THz$ appears instead of the peaks for all other separations (Fig. 3.47(a)–(c)). This resembles the phenomenon of electromagnetically induced transparency [148], [320] when two coupled oscillators with small detuning show absorption dip at the frequency, where the individual oscillators resonance is observed. If we compare the magnitudes of mode losses extracted from Fig. 3.47, we conclude that losses of the higher-order Bloch modes remain almost constant while decreasing the unit cell size. On the contrary, the losses of the fundamental modes increase considerably for smaller separation due to the increase in the metal filling fraction.

Homogeneity numerical evaluation

The brief summary of the presented results is that there exists a range of optimal longitudinal periods to achieve the best homogeneity for the twisted cross MM, which is limited by the influence of the higher-order Bloch modes from one side and the Bragg resonance from the other side. To determine this range we plotted the difference $\Delta = \min_{i\geq 3} Im(k_i a) - \max_{i=1,2} Im(k_i a)$ between the attenuation constants of the least damped higher-order Bloch mode and the most damped fundamental mode (Fig. 3.48(a)).

We suggest neglecting higher-order Bloch modes in the consideration if the difference in damping per unit cell is $\Delta \geq 0.5$. In this case the intensity of the higher-order modes will be attenuated e times more over the period a, comparing to the fundamental modes. In the resonant region between 200 and $250\,THz$ the homogeneity condition $\Delta \geq 0.5$ is satisfied for $a >$

$200\,nm$ (Fig. 3.48(a)). Outside the resonant region this condition is much more moderate and the TC can be homogenized for smaller a.

The dependence of the minimum of the damping difference $\delta = \min\Delta$ as a function of the period a is shown in Fig. 3.48(b). Surprisingly, this dependence is not only monotonously rising but also close to linear. This fact points out the predictive potential of the used methodology. Thus, it suffices to calculate the Bloch modes for only two periods in order to approximately predict the homogenization limit for the designed metamaterial.

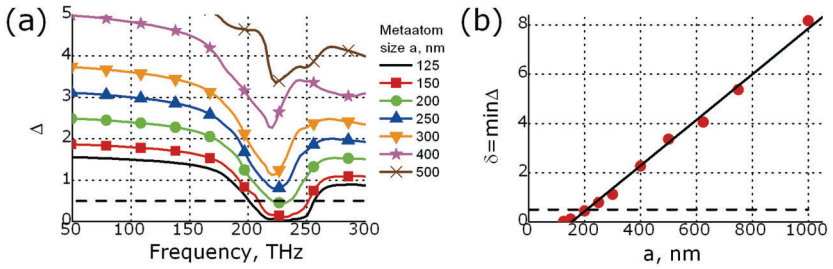

Figure 3.48. (a) The difference of the propagation constants $\Delta = \min_{i\geq 3} Im(k_i a) - \max_{i=1,2} Im(k_i a)$ of the least damped higher-order Bloch mode and the most damped fundamental mode for various unit cell sizes a: $125\,nm$ (black line), $150\,nm$ (red squares), $200\,nm$ (green circles), $250\,nm$ (blue triangles up), $300\,nm$ (orange triangles down), $400\,nm$ (magenta stars), and $500\,nm$ (brown crosses). (b) The minimum $\delta = \min\Delta$ as a function of the period a (red circles). The straight line represents a linear fit of δ on a. The dashed line corresponds to the homogenization limit $\Delta = 0.5$.

We also checked the homogenization criterion $\Delta \geq 0.5$ for the split cube in cage negative index MM (see section 3.1.3). This MM shows very fast convergence of the EPs with the number of monolayers as the refractive index is the same from one monolayer to infinite number of monolayers. In the whole frequency range of interest higher-order Bloch modes are well separated from the fundamental ones ($\Delta > 1.5$). That explains why the EPs of the split cube in cage do not depend on the slab thickness.

Twisted split ring resonator metamaterial design

It is natural to make a hypothesis that for some metamaterial designs with strong coupling between consecutive layers, the MM cannot be

homogenized in the resonance region at all. In other words, $\Delta < 0.5$ even for the large separation of meta-atoms where homogenization is prevented by the appearance of Bragg resonances. To check this hypothesis we investigated the TSRR MM, which was first proposed by Xiong et al.[252] for the microwave frequency region (see Fig. 3.45(b)) and which was understood as an extension to a previous metamaterial design [321]. We used the design for the infrared range and adopted the geometrical parameters from the Ref. [318]. It consists of the golden U-shaped split-ring resonators embedded in a dielectric. The in-plane lattice constants are $a_x = a_y = 885\,nm$. The split rings of thickness $60\,nm$ are separated by a dielectric spacer of $85\,nm$. All geometrical and material parameters are taken as in Ref. [318] except the period a. The stacked split-ring resonators are turned 90° in each subsequent layer (see Fig. 3.45(b))around the axis, which passes through the center of the quadrant, where the split ring is placed, in the direction of stacking. The TSRR also possess $C4$ symmetry, as the TC does.

Bloch modes dispersion diagram for TSRR

We calculated the Bloch modes dispersion diagram for three center-to-center separations of the monolayers: $a = 290\,nm$, $a = 450\,nm$ and $a = 600\,nm$. One of the fundamental modes designated by the black solid line in Fig. 3.49 fails to satisfy the homogeneity requirements even for the sparsest stacking at $a = 600\,nm$. Its losses are higher than those for a few of the higher-order modes. The other fundamental mode (Fig. 3.49 green/gray line) exhibits a comparable $Im(k)$ with one of the higher-order Bloch mode for $a = 290\,nm$ and $a = 450\,nm$.

For the sparsest stacking $a = 600\,nm$, this fundamental mode experiences a slightly lower but still insufficient for homogenization, damping, since $\Delta = 0.09 < 0.5$. A further increase in the lattice period to $a = 600\,nm$ shifts the real part of the wave vector into the first band gap $Re(ka) = \pi$ for frequencies above $80\,THz$, so the requirement (i) is not met. We would hardly term a metamaterial homogeneous if only one eigenwave (for example, RCP) fulfills the homogenization requirements. We may conclude that the TSRR does not satisfy requirement (iii) around the resonance frequency for any period. This is caused by the strong coupling between its

meta-atoms. Thus, we prove our hypothesis that there exist MMs that cannot be considered homogeneous at the resonance frequency region.

It is important to mention that such MM keeps its optical functionality, i.e. affecting the state of polarization. However, one must not extrapolate the properties of a single or a few functional layers toward a stack of more functional layers.

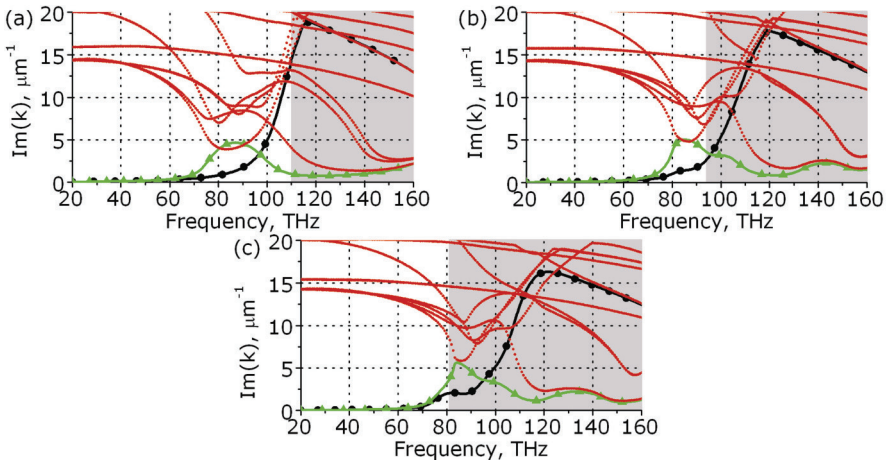

Figure. 3.49. The loss spectrum for TSRR MM for different periods a: (a) 290 nm, (b) 450 nm, (c) 600 nm. Fundamental modes are shown as black lines with dots and green/gray lines with triangles, all higher-order Bloch modes are shown as red/dark gray dots. The frequency region above the first Bragg resonance is shadowed.

Discussion

The homogeneity criterion (i) requires a unit cell/ wavelength ratio to be as small as possible. However, in this case, as shown above, in the resonance region requirements (iii) (single Bloch mode) and (iv) (efficient coupling of light to this specific mode) are frequently not met. When decreasing the unit-cell size a, the fundamental modes' damping increases (see Fig. 3.47), so sooner or later it becomes comparable with the higher-order Bloch modes' damping. The higher-order Bloch modes then have a comparable impact on the wave propagation in a MM slab as a direct consequence of the strong interaction of the meta-atom monolayers.

This conclusion, which is basically applicable to any MM, is extremely important for chiral MMs where the coupling of monolayers is usually

strong. For example, for a negative-permeability configuration of the split-ring (SR) resonator metamaterial in the side-coupled arrangement, where the wave vector lies in the SR plane, SRs are weakly coupled due to the mutual inductance (magnetic field penetration) (see the sketch in Fig. 3.50(a)). The induced current in SR A creates a magnetic field that penetrates SR B. However, the number of the field lines penetrating SR B is not very large. On the contrary, for a chiral configuration, when the stacking direction is perpendicular to the SR plane (see Fig. 3.50(b)), the magnetic field of SR A strongly penetrates SR B.

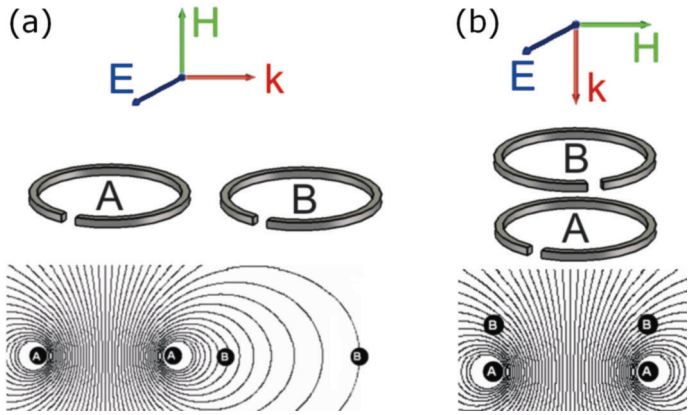

Figure. 3.50. The sketch of the split-ring resonators stacking (a) in the negative-permeability configuration and (b) in the chiral configuration. Arrows represent the direction of the wave propagation, electric and magnetic field vectors. Black lines in the lower pictures represent the cross-sectional view of the lines of the magnetic field created by SR A and penetrating SR B.

Most chiral metamaterials consist of split-ring resonators or gammadions, where the meta-atoms are stacked similarly as in Fig. 3.50(b). The other configuration, where the magnetic field of one meta-atom penetrates weakly into the other one, corresponds to the twisted-cross MM. It is basically an extension of the cut-wire pairs toward $C4$ symmetry. The currents excited in the double crosses create the magnetic field perpendicular to the stacking direction and are thus weakly penetrating into the adjacent monolayer (similar as in Fig. 3.50(a)).

Mechanical analogy

Historically, e.g., by Newton, Lagrange and others, wave phenomena were frequently illustrated by taking advantage of mechanical analogies. The historical overview of a periodic medium description with a spring-ball system can be found in Brillouin's book [322].We likewise employ a mechanical spring-ball system to illustrate the coupling effect in our MM system, see Fig. 3.51. The host dielectric medium is represented by chains of small balls and springs. Meta-atoms are represented in Fig. 3.51 as massive oscillators having their own resonance frequency.

When the distance between the meta-atoms is large such that $Re(ka) > \pi$, the periodic medium is in the photonic crystal regime (Fig. 3.51(a)). The massive oscillators periodically arranged in the system scatter the wave individually. Then constructive or destructive interference leads to the formation of stop bands and pass bands.

When the distance between meta-atoms decreases, but coupling between monolayers is still weak, we get a kind of coupled resonator waveguide, where only nearest-neighbor coupling matters (Fig. 3.51(b)). Such a waveguide has one fundamental mode (two in case of chiral metamaterials), which is dominating the light propagation. Thus the periodic medium may be homogenized, and the extraordinary properties of MMs originate from the meta-atom resonances.

When the distance between the meta-atoms is further reduced, the coupling gets stronger and the nearest-neighbor scenario ceases to hold. Now higher-order modes come into play (Fig. 3.51(c)) and participate in the energy transfer together with the fundamental mode. So, this is the regime, when higher-order Bloch modes can propagate in the structure, and homogenization is not feasible.

As can be inferred from the spring-ball model the effect of higher-order modes is negligible if there is no strong interaction between the meta-atoms. In this case the effective properties are solely determined by the resonances of the individual meta-atoms. However, to ensure a decoupling while the period has to remain small in comparison to the wavelength, the constitutive elements of the meta-atoms have to be very small. Obviously, in this case the resonance features of the meta-atoms disappear for a given frequency. Such MM would hardly exhibit any extraordinary properties.

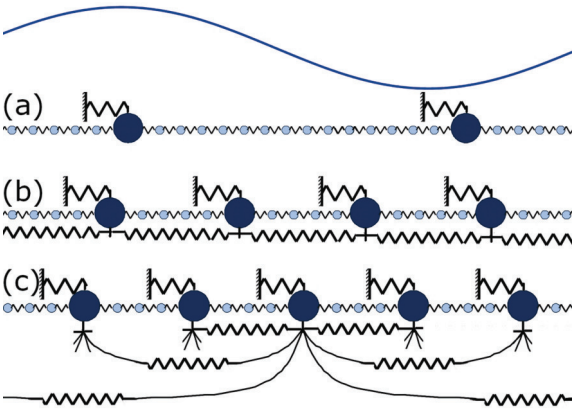

Figure 3.51. (a) Mechanical analogy of the metamaterial in the photonic crystal regime, (b) homogeneous and (c) inhomogeneous medium. Small balls and springs represent host medium. Large balls represent resonant inclusions.

Conclusions

It turns out that the possibility of homogenization of chiral MM depends crucially on the coupling strength between meta-atoms. For weak coupling between monolayers the MM can be homogenized. Then the optimal meta-atom separation can be identified by looking at the Bloch mode dispersion relation in the frequency domain below the Bragg resonance. In this contribution we propose the quantitative homogenization criterion $\Delta \geq 0.5$. The proposed evaluation criterion has a prognostic potential since the calculation of the dispersion relation for two unit-cell sizes a is sufficient to estimate the lower homogeneity limit of a metamaterial.

For strong coupling between meta-atoms, the homogenization of MMs might be impossible at all. In this case the functionality of a MM, e.g., a stack of several monolayers, must be characterized rather than retrieving EPs of one monolayer and extrapolating them to the properties of a multilayered stack.

However, the absence of strong coupling does not guarantee the possibility of MM homogenization even in long-wavelength limit. The counterexample was reported by Poulton et al. [323]

We want to emphasize that the applied methodology is general, since it is not attached to any specific type of metamaterials, so it can be applied to a broad range of chiral and achiral periodic MMs.

Chapter conclusions

We proposed the Split cube in Cage and its simplified version the split cube in Carcass design of the cubic symmetric negative index metamaterial for the telecom frequencies. It is bulk since it showed an extremely fast convergence of the effective properties with the number of layers. However, despite of the cubic symmetry and cubic crystal lattice the Split Cube in Carcass exhibits spatial dispersion in the frequency range of interest. That prevents treating it as an isotropic negative index material and using as a negative index nanocoupler building block. This is an issue for most of the existing metamaterials that have the unit cell comparable to the wavelength in the resonant frequency region of the extraordinary electromagnetic properties. Moreover, the losses in the Split Cube in Carcass are large that is also inappropriate for the nanocoupling application.

We proposed the wave propagation retrieval method for the effective properties characterization for metamaterials with linear and circular eigenpolarizations and the field averaging of the restored Bloch mode method. The methods are based on observation of the wave propagation in the metamaterial slab. The methods are simple, can be applied to lossy and lossless negative and positive refractive index, permittivity and permeability metamaterials. They provide unambiguous restoration of the effective properties.

We developed a technology of silver metallization of complex 3D dielectric structures. The metallization is based on silver reduction from the silver-ammonia complex. The reducing agent is formaldehyde. Continuous and smooth silver layers can be deposited starting from 30 nm. The technology can be used for the complex photonic structures fabrication for the infrared frequencies.

We investigated the coupling between metamaterials monolayers effects on the example of chiral metamaterials. We showed that some metamaterials can be treated as homogeneous in the resonant frequency region, but some cannot at any value of the metamaterials period. We formulated a quantitative homogenization condition.

As this has been shown in recent work [324], although subwavelength resolution is possible in metamaterial based lenses, practical imaging beyond the diffraction limit is challenging and when designing such device one

should consider “granularity, degree of isotropy and transverse size of the metamaterial lens”. We should emphasize that the requirements for the nanocouplers are stricter than for subwavelength imaging devices, since the high coupling efficiency is desirable, but not mandatory for the latter.

Spatial dispersion, high losses and the skepticism on the negative index metamaterial superlens made us considering another possibility of the nanocoupler realization, namely nanoantenna based coupler that is described in the chapter 4.

Chapter 4. Plasmonic nanoantenna coupler

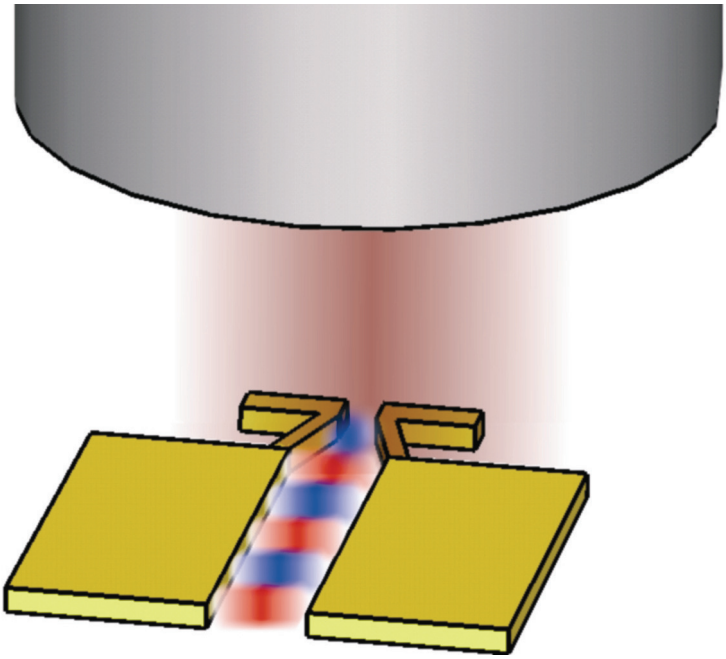

Chapter structure

This chapter consists of two big parts. Section 4.1 presents the methodology used, including the idea behind the antenna nanocoupler, necessary antenna theory, description of the simulation environment and optimization method, fabrication technology and measurement setup. Section 4.2 describes the developed designs of the nanoantenna couplers and the simulation, fabrication and characterization results. Chapter ends with the conclusions.

4.1. Methodology

This chapter describes the methods that we used for theoretical analysis, simulation, fabrication and characterization of the nanocoupler. Section 4.1.1 introduces our ideas on the nanoantenna coupler design. The necessary antenna theory basics are provided in section 4.1.2. Section 4.1.3 is devoted to the description of the simulation methodology. Fabrication technology details are provided in section 4.1.4. Section 4.1.5 contains the description of the optical characterization setup.

4.1.1. Antenna nanocoupler ideas

Sea waves analogy

To illustrate the problem of coupling the light from the free space to the plasmonic slot waveguide, let us use the analogy with the sea waves.

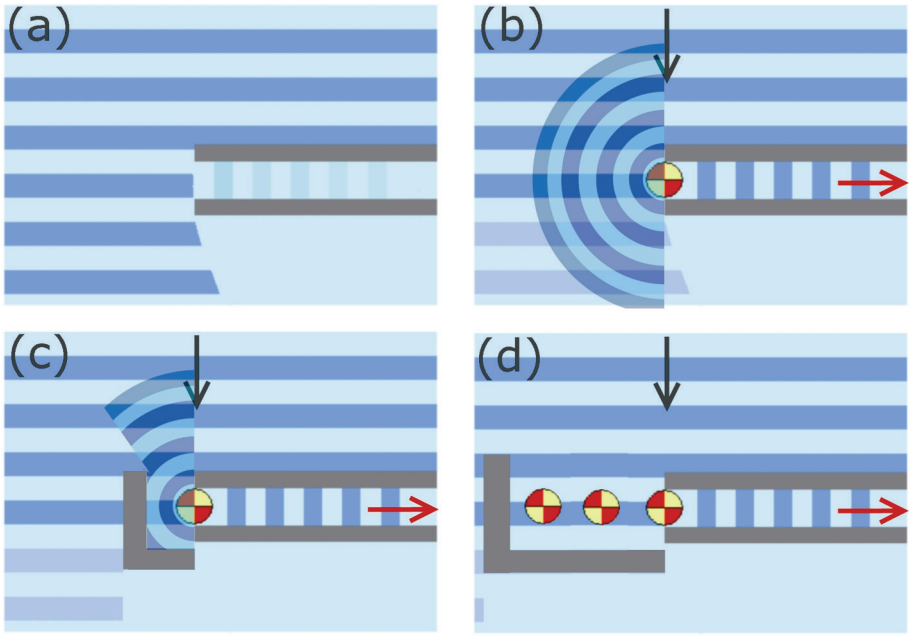

Figure 4.1. Sea wave analogy of the nanocoupler. Coupling a sea wave to a narrow channel perpendicular to the wave direction is not very efficient (a). The coupling efficiency increases if one adds a resonant float near the channel entrance (b). It increases even more if one adds reflectors (c) and if one uses several floats (d).

Imagine that we wish to couple the sea wave to a narrow channel perpendicular to the wave direction (Fig. 4.1). If we use the channel only the coupling is not very efficient (Fig. 4.1(a)). But if we put a resonant float close to the channel entrance, the wave makes it oscillating. The float itself creates secondary waves that will be partially launched into the channel (Fig. 4.1(b)). In other words, the float captures the power from the wave and launches it into the channel.

Some power is radiated back to the free space. However, if we place reflectors at the sides of the float (Fig. 4.1(c)) this power will be returned back and partially launched into the waveguide. It is very important that the reflected wave returns to the float in phase. Moreover, we can increase the capture area if we use not a single float but several floats (Fig. 4.1(d)). In this case the distance between floats should be approximately equal to the wavelength of the wave for that the waves from each float come in phase.

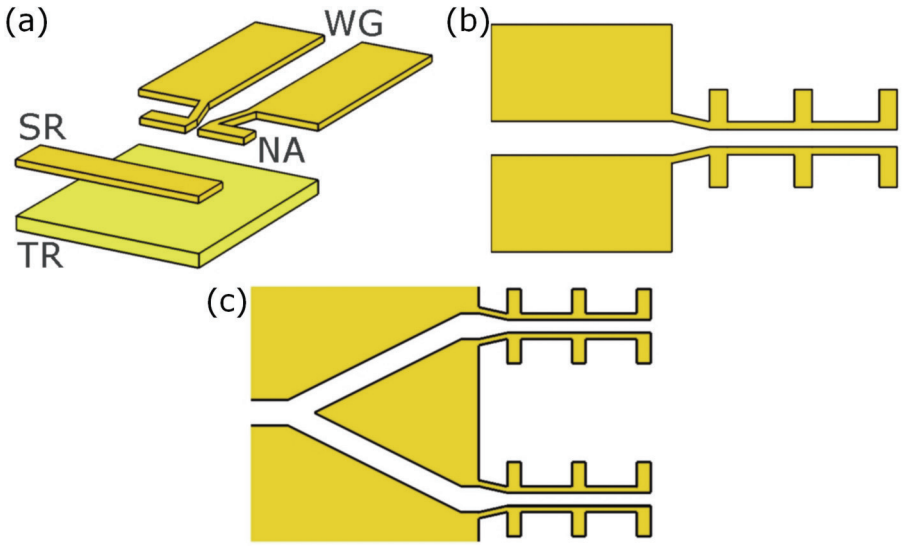

Figure 4.2. Plasmonic antenna coupler design ideas. (a) Single nanoantenna (NA) coupler to a plasmonic waveguide (WG). Side (SR) and top (TR) reflectors returns part of the reradiated power back. (b) A branch of several connected antennas. (c) Parallel branches combined with Y-coupler.

Plasmonic nanoantenna coupler

In our case the narrow channel is a plasmonic slot waveguide, the resonant float is a nanoantenna and the reflectors are metallic mirrors on side and on

top (see Fig. 4.2(a)). We may achieve an additional increase in the captured power if we use several connected antennas (Fig. 4.2(b)) and several parallel branches of the connected antennas (Fig. 4.2(c)). These are the possibilities that we explored. However, before looking at the results we should mention some antenna theory.

4.1.2. Antenna theory basics

The history of the radio antennas accounts for more than a hundred years. During this time the theory of the antennas was well developed. However, the interest to the optical nanoantennas is not very old, since only recently it became possible to fabricate them reproducibly. Since metal's properties are different in the optical domain, some adjustments to the antenna's theory have been done [130], [133], [134], [140], [142], [165].

Antenna principles

An antenna is a device that converts free-space propagating radiation into the localized form and vice versa [128], [325]. IEEE Standard Definition of Terms for Antennas defines antenna as a "mean for radiating and receiving radio waves" [325]. The physics behind the antenna functionality is the following. Accelerating or decelerating charges (for example, oscillating) always create radiation. In principle, every object that can create electromagnetic waves through the oscillation of charges or currents may be called an antenna. An antenna is a reciprocal device, so an incident electromagnetic wave creates charges and currents oscillations in it. Attaching a detector to an antenna we may receive electromagnetic waves and thus use an antenna for practical purposes.

Equivalent circuit

An antenna and its interaction with the incident wave (Fig. 4.3(a)) in the receiving mode can be schematically represented as an equivalent circuit (Fig. 4.3(b)). An important characteristic of the antenna is its impedance $Z_A = R_A + jX_A$, which consists of the capacitance C_A, the inductance L_A of the antenna, the loss resistance R_L and the radiation resistance R_R

$$Z_A = R_A + jX_A = (R_L + R_R) + j\left(\omega L_A + \frac{1}{\omega C_A}\right), \qquad (4.1)$$

Ph.D. thesis by Andrei Andryieuski, DTU Fotonik, 2011

Antenna impedance is defined as the "ratio of the voltage to current at the pair of terminals or the ratio of the appropriate components of the electric and magnetic fields at a point" [325].

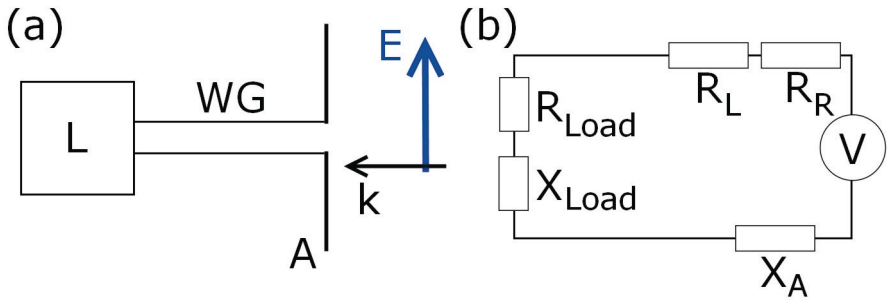

Figure 4.3. (a) Schematic representation of an antenna (A) in the receiving mode. The antenna is connected via a waveguide (WG) to the load (L). (b) Equivalent circuit for the antenna and the load.

In a general case the waveguide and the load (Fig. 4.3) are represented as single equivalent impedance Z_{Load}. However, in the case of the effectively semi-infinite waveguide that is a case of our interest (long and lossy plasmonic waveguide may be considered as semi-infinite) we can consider only the waveguide as a load with the impedance Z_{WG}, which is also defined a ratio of the voltage to current or electric field to magnetic field.

Impedances conjugate matching

An antenna in the receiving mode delivers maximal power to the load (in our case to the connected transmission line), if their impedances are matched. That happens when the impedance of the antenna is equal to the complex conjugate of the impedance of the waveguide:

$$Z_A = Z_{WG}^*, \quad R_A = R_{WG}, \quad X_A = -X_{WG}. \tag{4.2}$$

We should also mention that the performance of the antenna in the receiving regime depends not only on its geometry but also on the polarization and direction of the incident wave, so the antennas characteristics listed below are considered for a specific incidence direction and wave polarization.

In the case of the perfect matching the electromagnetic power P_{inc} incident to the antenna is partially launched into the waveguide (power P_{WG}), partially absorbed due to Ohmic losses (P_{Ohm}) and partially reradiated back in the free space (P_{FS}). Analysis of the antenna in the receiving mode shows

that in the best case of the conjugate matching and absence of Ohmic losses the maximum that we can launch in the waveguide is half of the power, captured by the antenna – another half is reradiated in the free space [325].

Coupling efficiency

Coupling efficiency CE of the antenna is an important characteristic and it is defined as the ratio of the power launched into the waveguide P_{WG} to the power incident to the antenna P_{inc}:

$$CE = \frac{P_{WG}}{P_{inc}}. \tag{4.3}$$

The coupling efficiency is a good figure-of-merit for the coupler between different waveguides. However, it is not the best for quantitative evaluation of the efficiency of the nanoantenna coupler, since it depends not only on the antenna properties but also on the properties of the incident beam. Imagine that we have two identical antennas and two differently focused Gaussian beams incident on the antennas (Fig. 4.4). The coupling efficiency will be different for these two cases. And if we consider the true plane wave infinite in the lateral directions, the coupling efficiency will be zero.

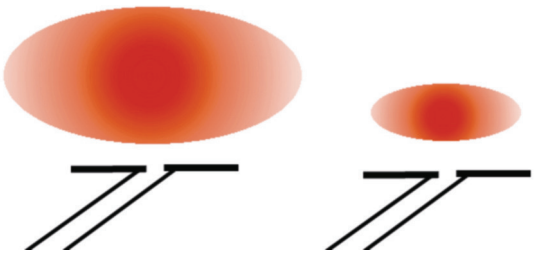

Figure 4.4. Two differently focused waves incident to the identical antennas. The coupling efficiency for these two cases is different.

Effective area

A better characteristic for the antenna coupler is its effective area, which is defined as the power available at the terminals of the antenna P_A to the incident power flux S_{inc} for the plane wave incidence

$$A_{eff} = \frac{P_A}{S_{inc}}. \tag{4.4}$$

The effective area is the characteristic of the antenna only. It is connected to the gain G of the antenna:

$$A_{eff} = G\frac{\lambda^2}{4\pi}. \tag{4.5}$$

Antenna gain is the product of antenna directivity and power efficiency $G = D \times E_{antenna}$. The directivity D is defined as the ratio of the radiation intensity in a given direction from the antenna to the radiation intensity averaged over all directions. Directivity is a useful numerical and graphical representation of the antenna radiation pattern.

Antenna array

The simplest dipole antenna has low directivity and therefore low effective area: it is cylindrically symmetric and such is its radiation. One can increase the antenna's directivity by using, for example, reflectors and directors. That is done in the directive Yagi-Uda antenna [326]. Another solution is to use an array of the identical antennas with a specific phase difference and distance between them. In optics that in some sense corresponds to the diffraction grating.

Optical vs. radio antenna array

However, we should mention an important difference between the array of radio and optical antennas. While in the former each antenna can be connected by a cable to a common point that means that the power accepted by each antenna can be delivered to the main line with the same amplitude and phase, such connection cannot be realized for the optical antennas array. That limitation comes from the fabrication technology. This is highly desirable to fabricate the whole array and the connecting wires in plane during the same fabrication cycle. This technological requirement makes that more difficult to analyze the optical antenna arrays since we have to take into account the amplitude and phase difference of the plasmon wave excited by different antennas and decayed during propagation.

4.1.3. Simulation method

Material properties

We made the simulations with the commercially available software CST Microwave Studio [201]. The metallic parts of the antennas and waveguides were assumed to be made from gold (Au) and embedded into silicon dioxide (silica or SiO_2). The permittivity of gold was modeled using the Drude formula:

$$\varepsilon = 1 - \frac{\omega_P^2}{\omega(\omega + i\gamma)}, \tag{4.6}$$

where the plasma frequency $\omega_P = 1.37 \times 10^{16}\ s^{-1}$ and collision frequency $\gamma = 8.0 \cdot \times 10^{13}\ s^{-1}$ [327]. The refractive index of silica was taken $n_{SiO2} = 1.47$. All golden structures (waveguides, antennas and side reflectors) were considered to be $50\ nm$ thick (Fig. 4.5). In the case of symmetric waveguide the superstrate material was also silica, while for the asymmetric waveguide it was air.

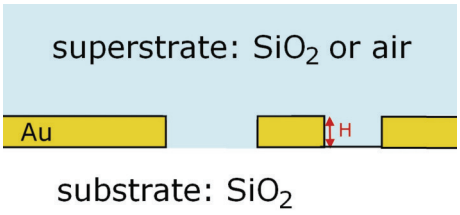

Figure 4.5. The typical cross-section of the simulated nanocoupler structure. The substrate is silica. Metallic structures are made from gold. The superstrate material is silica in case of symmetric waveguide and air in case of asymmetric waveguide.

Excitation

The excitation of the nanocoupler was performed with a large waveguide port 1 (Fig. 4.6(a)) that gives the field distribution close to Gaussian (see Fig. 4.6(b)). Since the antenna was much smaller than the incident beam, the incident field distribution near the antenna was close to the plane wave. The power launched into the waveguide was accepted by the port 2 (see Fig. 4.6(a)), which captured the desired eigenmode of the plasmonic slot waveguide (Fig 4.6(b)).

The simulation mesh was refined in the waveguide slot area to take into account the fast spatial plasmon field variations. The numerical mesh consisted of $100.000 - 750.000$ mesh cells (depending on the simulated structure). The simulation termination criterion was set as $-40\ dB$ energy decay. This means that when the total energy in the simulated system decreased to $-40\ dB$ from the maximal value, the simulation stopped.

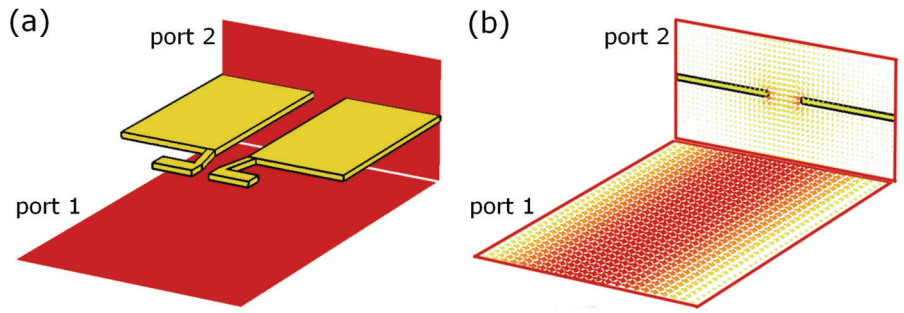

Figure 4.6 Excitation and detection geometry (a). The port number 1 excites the nanocoupler. The port 2 measures the power delivered to the plasmonic slot waveguide. (b) Electric field distribution of the ports eigenmodes. In the region of the antenna the excitation field is close to a homogeneous.

Antenna figure-of-merit

Effective area is a good characteristic of the antenna coupling performance. It is formulated for the incident plane wave. However, in the numerical calculations we are limited in space by the computational power of the computer. For example, in our case the lateral size of the simulation domain was $2000\ nm$ for the antennas outside and inside waveguide (sections 4.2.1-4.2.2 and 4.2.4), $3000\ nm$ for the battle-axe coupler (section 4.2.5).

Two types of boundary conditions can be used: perfect electric conductor (PEC) and open. Each of the boundary conditions leads to specific field distribution of the excitation port– this is the way how CST Microwave Studio works. The PEC gives a plane wave incident on the structure. However, the structure itself is effectively multiplied from a single nanoantenna to an array with the periodicity of $2000\ nm$, since every PEC plane is a mirror and two parallel perfect conducting planes result in the infinite number of mirror reflections. The antenna itself is of around

$1000\ nm$, so if the PEC boundary conditions are selected, the antenna has effective neighbors at a distance of $1000\ nm$. This is why we decided to use open boundary conditions that allow simulating a single structure only.

The open boundary conditions give a field distribution close to Gaussian: maximum in the center and decaying field to the sides. In the region of the antenna the field does not change very much so the antenna is almost in the field of the plane wave. We fixed the width of the simulation domain to $2000\ nm$ or $3000\ nm$, but varied the length of the port.

Since the incident wave is not exactly the plane wave, we cannot use the definition of the effective area for its calculation. However, we do not want to use the coupling efficiency either, since different length of the simulation domain and excitation source does not characterize well the performance of the nanoantenna coupler. Instead, we introduced the antenna figure-of-merit ($AFOM$), which we define as the product of the coupling efficiency CE and the area of the port A_{port}:

$$AFOM = CE \cdot A_{port} = S_{21}^2 \cdot A_{port}, \tag{4.7}$$

where S_{21} is amplitude transmission from port 1 to port 2. The $AFOM$ has the dimensionality of the area and correlates with the effective area, but is not equal to it in a general case. When the incident wave is a plane wave the $AFOM$ coincides with the effective area.

Symmetric and asymmetric waveguides

Two cases of the plasmonic slot waveguide were considered: a symmetric golden waveguide embedded in silica (Fig. 4.7(a)) and asymmetric silica-gold-air waveguide (Fig. 4.7(b)). The width of the waveguides was in the most cases equal to $300\ nm$.

The asymmetric waveguide has larger propagation length than a symmetric waveguide (Fig. 4.7(c)). However, even though the symmetric waveguide has lower propagation length, it is better from the waveguiding point of view, since the waveguide mode has always larger effective index, than the surface plasmon polaritons propagating at the gold-silica interface (see Fig. 4.7(d)) [11], [12]. That means that there is no efficient coupling from the slot mode to the surface plasmon modes. The same time the mode of the asymmetric waveguide has the effective index between the silica-gold and

air-gold surface plasmons (Fig. 4.7(d)). In this case the power is lost to the surface modes during the wave propagation in the slot. This is undesirable for the real applications. However, an open asymmetric waveguide is better for the measurements with the scanning near-field optical microscope (SNOM), since it allows close access for the SNOM tip. This is why we switched from the initial symmetric waveguide coupler (section 4.2.1) to the designs with air superstrate (sections 4.2.2-4.2.5).

We have considered five nanocoupler designs: dipole antennas outside the symmetric waveguide, dipole antennas outside the asymmetric waveguide, grating of the antennas, antennas inside the waveguide, and bow-tie antennas in the slots ("battle-axe" nanocoupler). The specific geometrical parameters of the optimized structures are reported in the chapter 4.2.

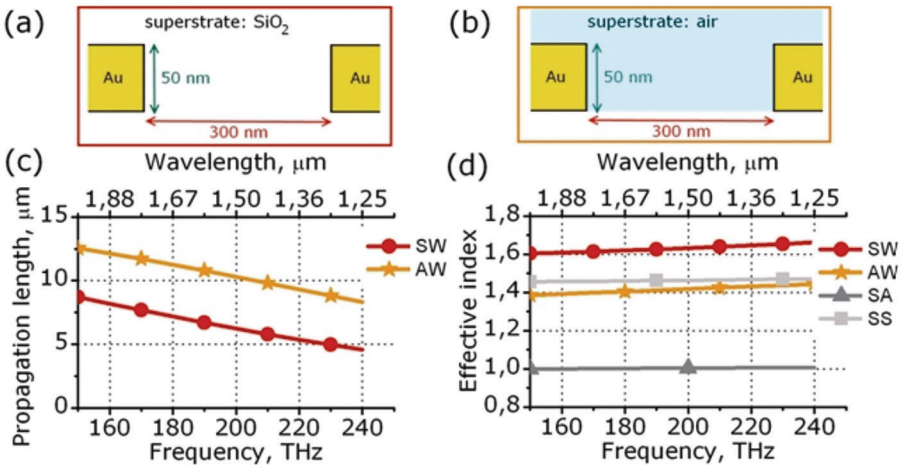

Figure 4.7. Two types of plasmonic slots waveguides considered for nanocoupler: symmetric waveguide with silica substrate and superstrate (a) and asymmetric waveguide with silica substrate and air superstrate. (c) Propagation length of the fundamental mode of the symmetric (SW, red circles) and asymmetric (AW, orange stars) slot waveguide. (d) Effective index of the fundamental mode of the symmetric (SW, red circles) and asymmetric (AW, orange stars) waveguide, surface plasmon polaritons at the gold-silica (SS, light gray squares) and gold-air (SA, dark gray triangles) interface. The effective index of the asymmetric waveguide lies below gold-silica SPP. Therefore the power from the asymmetric slot waveguide couples to the silica-gold SPPs and that introduces additional energy losses.

Impedance matching

The usual approach in the microwave antenna design is to calculate the impedance of the waveguide first, then to design the antenna for that its impedance is matched to the waveguide impedance. This approach can also be used in the optical regime [130], [143], [170]. Initially we used that approach and we calculated the impedance of an isolated nanoantenna and its dependence on geometrical parameters.

However, the knowledge the isolated nanoantenna impedance is not very helpful for maximization of the effective area and $AFOM$. First, the waveguide which is situated close to the nanoantenna influences its properties. Second, an antenna and a waveguide can be perfectly matched, but this does not ensure the maximal effective area. Therefore we found more efficient to make a direct numerical optimization in CST Microwave Studio.

Optimization

Usually the optimization was done as follows. On the first stage we varied the geometrical parameters one by one and looked at the effective area changes. This gives a good estimation of the initial point for the automatic optimization. On the second stage we set the CST built-in numerical optimization around this initial point within the range of ±50% of parameter's initial value.

We tested several optimization strategies proposed by CST on a simple model problem (maximization of the transmission through a Fabry-Perot dielectric slab): genetic optimization, swarm optimization, quasi-Newton and Nelder-Mead simplex methods. The Nelder-Mead simplex method was the most efficient, and therefore we chose it.

4.1.4. Fabrication technology

The developed antenna nanocoupler designs contain fine features; the smallest ones are $50\,nm$ wide. Therefore advanced nanofabrication technology was required. Ultraviolet lithography does not allow so high resolution; this is why we used electron beam lithography.

The fabrication was done in the cleanroom of DTU Danchip – National Center for Micro and Nanofabrication. In the most cases the recipes were developed by Danchip process specialists, so the recipes and the regimes not specified in details below are the standard Danchip recipes and regimes.

Process flow

The process flow is presented in the Table 4.1. The detailed description of each step is provided below.

Table 4.1. Nanocoupler fabrication process flow.

Step	Sketch	Machine and chemicals
1. Substrate choice	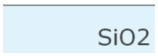	JB357 (JINSOL) borofloat glass
2. ZEP resist spinning		III-V dielectric spinner, ZEP520A 5.5%
3. Thermal Al evaporation	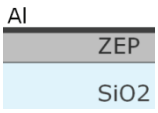	Wordentec, Al
4. Electron beam exposure	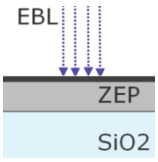	JEOL

5. Al removal and resist development		Fumehood, MF322, ZED N50
6. Metal deposition	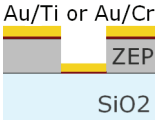	Wordentec, Au with Ti or Cr adhesion layer
7. Lift-off	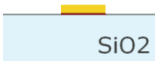	Fumehood, acetone, MR1165
8. SEM characterization	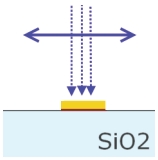	SEM FEI
The next steps were done for the structures with top reflector only		
9. Silica evaporation	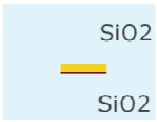	III-V dielectric evaporator, SiO_2
10. ZEP resist spinning		III-V dielectric spinner, ZEP520A 11%
11. Thermal Al evaporation	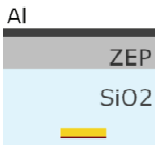	Wordentec, Al
12. Electron beam exposure	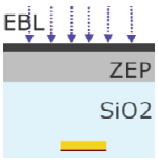	JEOL

13. Al removal and resist development	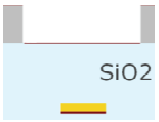	Fumehood, MF322, ZED N50
14. Metal deposition	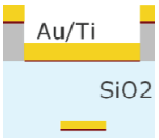	Wordentec, Au with Ti adhesion layer
15. Lift-off		Fumehood, acetone, MR1165

1. Substrate choice. Initially we considered two types of substrates for fabrication: glass and silicon. Both of these materials are transparent in telecom range around $\lambda = 1.55\ \mu m$. Later on we decided to use glass substrate only, because it is easier to make optical alignment when doing near-field measurements. Therefore we used borofloat glass $4-$inch wafers JB357 (JINSOL) with the refractive index $n = 1.47$. The wafers were $500\ \mu m$ thick.

2. ZEP resist spinning. We used ZEP 520A electron-beam lithography resist, which is commercially available. The thickness of the spun resist depends on the rotation speed and acceleration as well as on the viscosity, that can be tune by dilution of ZEP 520A in anisole.

For ZEP 520A 5.5% spinning we used the $III - V$ spinner (SÜSS RC8 Spin Coater). The spinning was made in two steps:

1) Pre-spinning with angular speed $500\ rpm$, acceleration $100\ rpm/s$ during $5\ s$,

2) Spinning with angular speed $2500\ rpm$, acceleration 1000 rpm/s during $60\ s$.

Such process should result in resist thickness of around $150\ nm$ that is enough for the $50\ nm$ thick metallic structures fabrication. A larger thickness would result in a lower resolution, while smaller thickness is not

sufficient for the lift-off process. After spinning, the wafers were baked at 180℃ for 5 min.

3. Thermal Al evaporation. Aluminum is required to be evaporated on top of ZEP resist for electron beam exposure. ZEP is a good dielectric, so without metal on top or conductive substrate on the bottom the charge accumulates on the surface and that decreases the resolution.

To prevent the charges accumulation, an aluminum layer of 20 nm was thermally evaporated. This process was done in the Wordentec (Wordentec QCL 800) machine. The thermal deposition is based on evaporation of Al when it is heated by the electric current in high vacuum. It is very important to use thermal, not electron-beam Al heating, since otherwise the scattered electrons reach the resist and make unwanted exposure.

4. Electron beam exposure. The nanocoupler structures were defined using the 100 kV JEOL JBX-9300FS electron beam lithography system. The structures were drawn in the L-Edit commercial software and then converted to the format necessary for JEOL. Proximity effects corrections were done with the Beamer software.

We spent some time optimizing the electron charge dose. We found out that a high base dose of 200 $\mu C/cm^2$ is required for fabrication of the small nanocoupler features (wires connecting nanoantennas). Lower doses resulted in the absence of the connecting wires.

5. Resist development. Before ZEP resist development, the aluminum film had to be removed. We did that in the commercial MF-322 solution. The sample was kept in MF-322 until no visible signs of aluminum were present, that was around 1 min and then rinsed with water and isopropanol (IPA).

The development itself was done in the ZED N50 developer. The sample was kept for 120 s in ZED N50. Then it was rinsed with IPA for 60 s and then dried with nitrogen flow.

We also tried to improve the development and to remove of the resist residuals using Plasma Asher (300 Plasma Processor from TePla) with the O_2 flow= 70 ml/min, N_2 flow = 70 ml/min and power = 150 W for 3 min. However, the resist was completely removed from the substrate, so we decided not to use the Plasma Asher.

6. Metal deposition. For metal deposition we tested two machines: Alcatel (Alcatel SCM600 e-beam and sputter tool) and Wordentec (Wordentec QCL 800). The structures deposited with Wordentec showed better quality this is why we used it for the nanocoupler fabrication.

Since gold has low adhesion to glass, we used adhesion promoters to improve it. Most frequently titanium and chromium are used. In the case of nanoantennas and symmetric waveguides fabrication (section 4.2.1) we used $2\ nm$ of Ti and then deposited $48\ nm$ of Au to make the total thickness of the structure equal to $50\ nm$. For the other designs (sections 4.2.4-4.2.5) we used $1\ nm$ of Cr, which was followed by $49\ nm$ of Au.

7. Lift-off. The lift-off is the crucial step of the nanocoupler fabrication. Initially the fabricated antennas were not connected to each other (see Fig. 4.8) and we spent a considerable amount of time optimizing the fabrication technology. As mentioned above, we varied the development time and the exposure dose. However, the most important step for fine structure fabrication was the lift-off.

Initially we used Microposit Remover 1165 and light ultrasound for $5\ min$. That gave no fine connecting wires between nanoantennas (Fig. 4.8) so we tried different procedures.

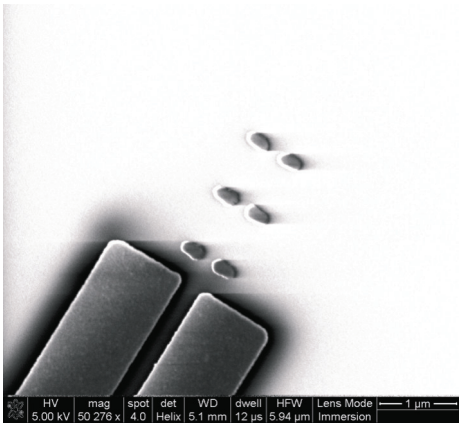

Figure 4.8. Initially fabricated nanoantenna coupler. There are no connecting wires between nanoantennas.

We tried to improve lift-off rinsing the sample with a syringe under the MR1165 surface. The tiny wires of the width of $50\ nm$ were not fabricated (Fig. 4.9(a)). We made the lift-off in the MR1165 heated to 50℃ and

keeping the sample for $60\ min$ – that did not give a good result either (see Fig. 4.9(b)).

Finally we managed to fabricate the structure using the following lift-off method (Fig. 4.9(c)). First, the structure was rinsed for $10\ min$ in acetone. We used a squeezed bottle to get rid of the excess foil. After that the sample was turned upside down and left overnight in Microposit Remover 1165. After that the sample was rinsed for $1\ min$ in acetone, then for $1\ min$ in IPA and finally dried with N_2 flow. The fabricated nanoantenna couplers are shown in the chapter 4.2.

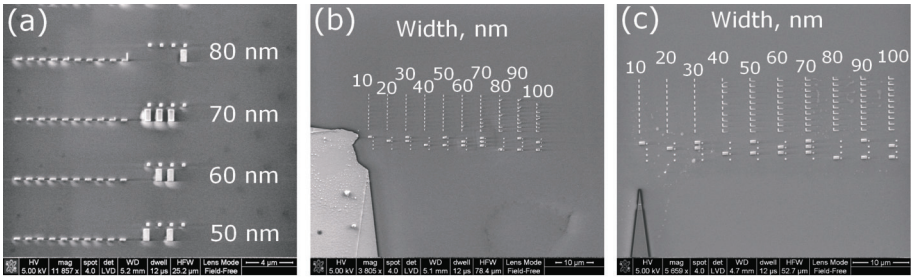

Figure 4.9. SEM photos of the test fabrication of angles. A wider shoulder of an angle is of constant width $100\ nm$. Another shoulder is of a variable width from $10\ nm$ to $100\ nm$ with a step $10\ nm$. Pictures show different lift-off methods: (a) lift-off with a syringe, (b) the sample is left for $60\ min$ in the Microposit Remover 1165 heated to $50℃$, (c) The sample is left in the Microposit Remover overnight. Only the last sample contain the metallic parts of $50\ nm$ wide

8. SEM characterization. Scanning electron microscope (SEM) characterization was done with FEI Nova 600 NanoSEM system.

9. Silica evaporation. Silica glass of $270\ nm$ was deposited with III-V dielectric evaporator machine. The deposition is based on silica evaporation in high vacuum when heated with electron beam.

10. ZEP resist spinning. The difference from the step 2 is that we would like to make the top reflector $100\ nm$ thick, not $50\ nm$. Therefore we need a thicker resist. We used ZEP 520A 11%. The spinning was done in two steps:

1) Pre-spinning with angular speed $500\ rpm$, acceleration $100\ rpm/s$ during $5\ s$,

2) Spinning with angular speed 3000 rpm, acceleration 1000 rpm/s during 60 s.

The resist was around 380 nm thick. The wafer was baked at 180℃ for 5 min after spinning.

The steps 11-15 were exactly the same as the steps 3-7, respectively.

4.1.5. Optical characterization setup

Transmission setup

Initially we wanted to use a fiber-based transmission setup that was available at DTU Fotonik. Its schematic picture and photos is shown in Fig. 4.10. It was developed for the measurements when both excitation and collection fibers are horizontal. We modified it for vertical excitation with the help of the metallic curved fiber holder. The setup contains a supercontinuum broadband ($\lambda = 0.5 - 2.4\ \mu m$) coherent light source (SuperK from NKT Photonics), a polarizer, moving stages and a microscope allowing fine optical alignment of the excitation and detection fibers and an optical spectrum analyzer (ANDO OSA, working range $0.35 - 1.7\ \mu m$). Due to the mismatch between the light source bandwidth and the OSA one, the useful range is 0.5 – 1.7 μm.

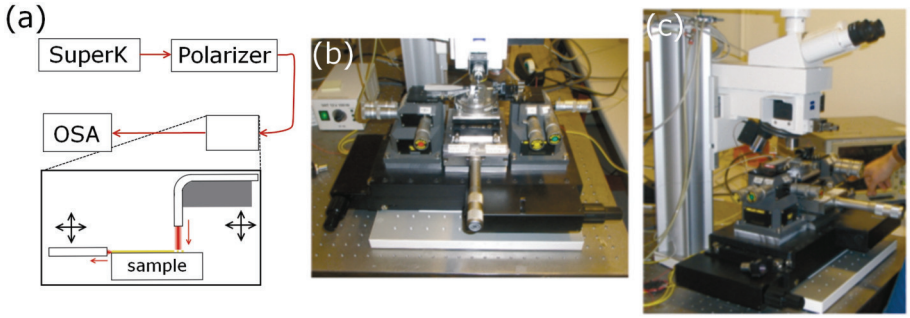

Figure 4.10. (a) Schematic picture of the fiber-based transmission setup. The broadband light beam from the supercontinuum source (SuperK) passes through polarizer and then is incident normally to the nanocoupler sample from the single-mode optical fiber. The light coming out from the waveguide is collected with another fiber and then launched into the optical spectrum analyzer (OSA). Front (b) and perspective view of the fiber-based transmission setup.

However, the first measurements and estimations showed that this setup is hardly possible to be used for the plasmonic slot waveguide measurements. The noise threshold of the OSA is $-80\,dBm$, while a straight connection of the SuperK source to the OSA gave the signal $-28\,dBm$. Taking into account high losses in the slot waveguide (propagation length around $10\,\mu m$), low collection efficiency of the collecting fiber and that the estimated ratio of the power coupled to the waveguide is 2% we understood that it is not possible to measure the nanocoupler with this transmission setup so we decided to use the scanning near-field optical microscope (SNOM) technique.

Scanning near-field optical microscope

Scanning near-field optical measurements were done by Giulio Biagi and Tobias Holmgaard Stær at Aalborg University. The schematic picture and the photo of the setup are shown in the Fig. 4.11.

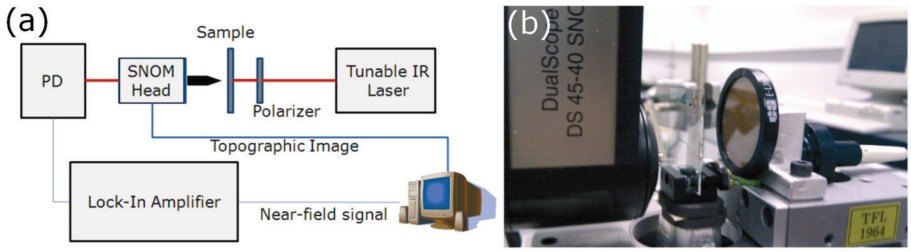

Figure 4.11. Schematic picture of a scanning near-field optical microscope (a). The light from a tunable infrared laser ($\lambda = 1.500 - 1.650\,\mu m$) passes through polarizer and then is focused in a $10\,\mu m$ large spot on the surface of the sample. The excitation is made through the substrate. A scanning SNOM head with a tapered fiber collects the light or measures the structure topography. Then the light is detected with photodiode. To increase the signal-to-noise ratio a lock-in amplifier is used. (b) Photo of the SNOM setup.

An infrared tunable laser ($\lambda = 1.500 - 1.650\,\mu m$) is used for excitation. Before incidence on the sample the light is polarized and focused in the spot of $10\,\mu m$ in diameter. Thin tapered fiber collects optical near field. The fiber tip is glued on a tuning piezoelectric fork which goes to resonant mechanical oscillations. When the fiber tip is close to the sample surface (almost in contact) its mechanical oscillations are damped due to the interaction with

the surface. Scanning the surface and measuring the damping of the tip mechanical oscillations, it is possible to measure the topography of the sample. Scanning is performed with a moving stage (SNOM head). The collected optical radiation is then detected with a photodiode. A lock-in amplified is used to increase the signal-to-noise ratio.

4.2. Nanoantenna coupler designs

In this chapter the designs of the developed nanocouplers are presented, as well as simulation, fabrication and characterization results. We have considered five different nanocouplers designs: dipole antennas outside the symmetric waveguide (section 4.2.1), dipole antennas outside the asymmetric waveguide (section 4.2.2), grating of the antennas (section 4.2.3), antennas inside the waveguide (section 4.2.4) and bow-tie antennas in the slots ("battle-axe" nanocoupler) (section 4.2.5).

4.2.1. Dipole antennas outside symmetric waveguide

An initial design was a dipole nanoantenna outside the symmetric plasmonic slot waveguide (Fig. 4.12(a)). The working principle of the antenna nanocoupler is the following. The incident wave makes the free charges in the antenna oscillate. Since the antenna is connected to the waveguide with narrow metallic wires, this leads to charges oscillations at the edges of the waveguide, and such oscillations are exactly the slot plasmons.

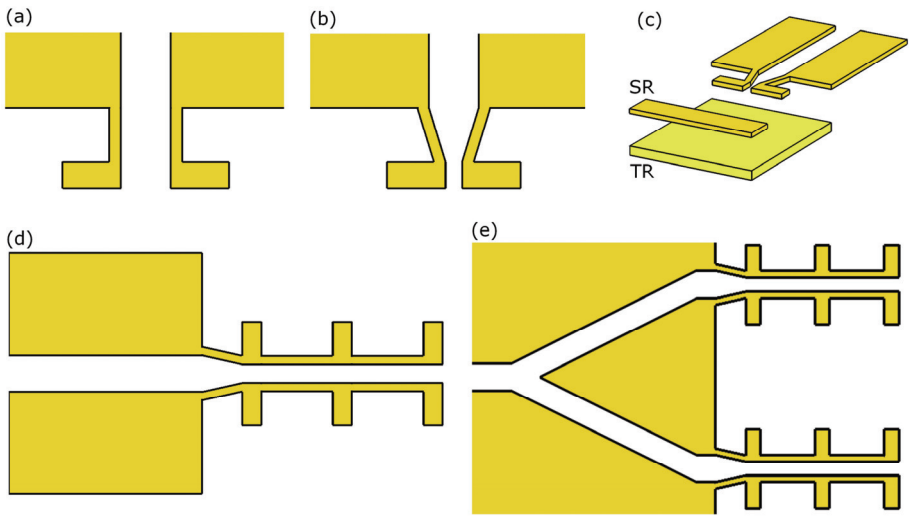

Figure 4.12. Nanoantenna coupler designs. Initial design of the dipole antenna nanocoupler, view from top (a). Nanoantenna coupler with tapered connectors: antenna gap is not equal to the waveguide width, view from top (b). Nanoantenna coupler with top (TR) and side (SR) reflectors, prospective view (c). Several connected nanoantennas, view from top (d). Parallel branches of nanoantennas and waveguides combined with Y-coupler, view from top (e).

It is very important, that the connecting wires are not very wide; otherwise the slot plasmons, which are confined to the edges of the slot waveguide, are not excited efficiently. In principle, the excitation of the slot plasmons may be made when the antenna is not connected to the waveguide with the wires – via near-field interaction between the waveguide and antenna [328]. However, such way is not very efficient, so the use of connecting wires is preferable.

Improvement ideas

We investigated the following possibilities for the nanocoupler improvement: use of tapered connectors, side and top reflectors, several connected antennas and parallel branches of nanoantennas.

Tapered connectors. Usually the nanoantenna gap is assumed to be the same as the waveguide width [143], [170], [174]. This is not mandatory, and making the gap different from the waveguide width gives us an additional degree of freedom for tuning the nanoantenna properties. So, first thing that we changed was using the tapered connectors instead of straight ones (see Fig. 4.12(b)).

Side and top reflectors. The side reflector is just a stripe of metal on the side; the top reflector is a metallic plate above the antenna (Fig.4.12(c)). The antenna and top reflector are separated by a layer of silica. The distance from them to the antenna should be such that the wave radiated by the antenna and reflected by the reflector returned back to the antenna in phase. Since we are looking for the most compact design, the phase change should be equal to 2π. Moreover in the configuration when the wave's incidence is perpendicular to the waveguide, the top mirror is also a mirror for the incident wave. Thus the nanoantenna is situated in the maximum of the standing wave formed by the incident and reflected waves. If the metal was a perfect conductor this would mean that the distance from the antenna to the reflectors should be equal to $\lambda/4n$, where λ is the wavelength in vacuum and n is the effective index of dielectric. We consider here that the light wave experience π change when travelling along the forward and backward path $\lambda/4n$ and additional π change while it is reflected from the metallic flat mirror. However, due to plasmonic properties of metal in the optical range the reflected wave does not experience exactly π change in phase. Moreover, antenna is not very small comparing to the wavelength. Therefore we

decided to use $\lambda/4n$ as an initial approximation and then to optimize numerically the distances to the side and top reflectors.

Several connected antennas. To increase the effective area of the nanocoupler, we may use several connected antennas (Fig. 4.12(d)). The distance between nanoantennas should be equal to the wavelength of the surface plasmon polariton in the waveguide formed by connecting wires. In this case the plasmon waves created by all the antennas are in phase when they reach the waveguide. So one can, for example, calculate the effective wavelength for the required mode of the connecting wires solving a $2D$ eigenvalue problem and then place the antennas at such a distance.

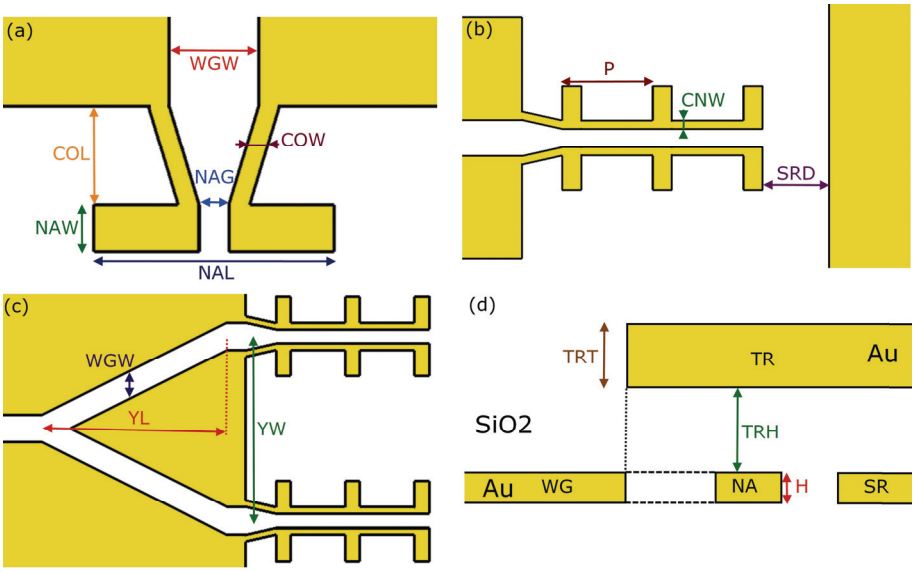

Figure 4.13. Optimized nanoantenna coupler geometry. Waveguide and nanoantenna, top view (a). Several connected antennas and side reflector, top view (b). Parallel branches of nanoantennas combined with Y-coupler, top view (c). The first layer (waveguide (WG), nanoantenna (NA) and side reflector (SR)) and the second layer (top reflector (TR)) of the metallic structures, side view (d). Dashed lines remind that antenna is connected to the waveguide. Dotted line shows that the top mirror begins exactly at the position where waveguide ends. All the structures are made from gold and embedded in silicon dioxide.

However, such approach does not take into account that the antenna width (about $150\,nm$) is not very small comparing to the plasmon wavelength

(about 800 nm), so the periodically placed antennas change the properties of the connecting wires. Therefore we decided to use the effective wavelength of the waveguide formed by connecting wires as an initial approximation and then make numerical optimizations.

Parallel branches of antennas. To increase the effective area even more we may use two parallel branches of the nanoantennas (Fig. 4.12(e)). The plasmonic waves excited in the parallel branches should then be combined with Y-coupler. The antennas should be far enough from each other not to influence each other greatly. We decided to put the antennas at the distance of 2000 nm between them. In such case the capacitive and inductive coupling between the antennas might only slightly change their resonant frequency.

Optimized design

The specific details of the optimized nanocoupler geometry are specified in the Fig. 4.13. The optimized values of the geometrical parameters are provided in the Table 4.2.

Simulation results

Coupling efficiency to the slot waveguide only is very low. It is not equal to zero, since incident wave excites some plasmons. However, when propagating in the waveguide these excited plasmon waves have different phases, continuously changing from 0 to 2π. As a result of plasmon waves interference, the amplitude of the wave launched in the plasmonic waveguide is small. In our case $AFOM = 0.025\ \mu m^2$ at 193.5 THz ($\lambda_0 = 1.55\ \mu m$) (see Fig. 4.14(a)).

When we add a nanoantenna, $AFOM$ increases to 0.4 μm^2 (see Fig. 4.14(a)). It increases even more when we add a side ($AFOM = 0.5\ \mu m^2$) and top reflectors ($AFOM = 0.8\ \mu m^2$). The bandwidth measured at $AFOM$ half-maximum is very broad: from 143 THz to 217 THz for a single antenna and from 164 THz to 213 THz for antenna with side and top reflectors. This range covers all the standard telecom range around $\lambda_0 = 1.55\ \mu m$.

Table 4.2. Optimized values of geometrical parameters for dipole antenna nanocoupler for symmetric waveguide

Parameter	Value	Physical meaning
H, nm	50	Thickness of the waveguide and nanoantenna
WGW, nm	300	Width of the waveguide
NAL, nm	859	Nanoantenna length
NAW, nm	158	Nanoantenna width
NAG, nm	153	Nanoantenna gap width
COL, nm	330	Distance between the waveguide and the nanoantenna
COW, nm	53	Width of the connecting wire
P, nm	825	Period of the antenna array
CNW, nm	50	Width of the wires connecting antennas in the array
SRD, nm	411	Distance from the rear antenna to the side reflector
YL, nm	2000	Y-coupler length
YW, nm	2000	Distance between parallel branches
TRT, nm	100	Thickness of the top reflector
TRH, nm	150	Distance from the antenna to the top reflector

We should admit that additional reflectors increase the $AFOM$, but at the same time decrease the bandwidth comparing to a single antenna structure. That happens since reflectors are places at specific distance from the antenna (the distances should satisfy constructive interference condition), and this distance is optimized for a selected frequency range.

When we increase the number of the connected antennas in the array, $AFOM$ also increases for antenna and antenna with side reflector nanocoupler (see Fig. 4.14(b) and 4.14(c)). At the same time the spectrum becomes narrower. This happens again due to the constructive interference condition: the plasmons excited by different antennas should arrive to the waveguide in phase. The influence of the side reflector is the most pronounced for one antenna (see Fig. 4.14(a)). However, for two and three antennas the influence of the side reflector is almost negligible. This occurs due to the losses in the wires connecting nanoantennas. Consequently, $AFOM$

experiences a saturation behavior: $AFOM$ increases less when we change the coupler design from two to three antennas, then from one to two antennas.

However, another situation occurs when we add top reflector and vary the number of antennas (see Fig. 4.14(d)). Adding top reflector to the nanocoupler with two antennas and side reflector brings $AFOM$ to 1.0 μm^2. That corresponds to 40 times increase in comparison with just a waveguide. We may expect even larger $AFOM$ for three nanoantennas with side and top reflectors, but in fact we observe a decrease of the $AFOM$ (see Fig. 4.14(d)).

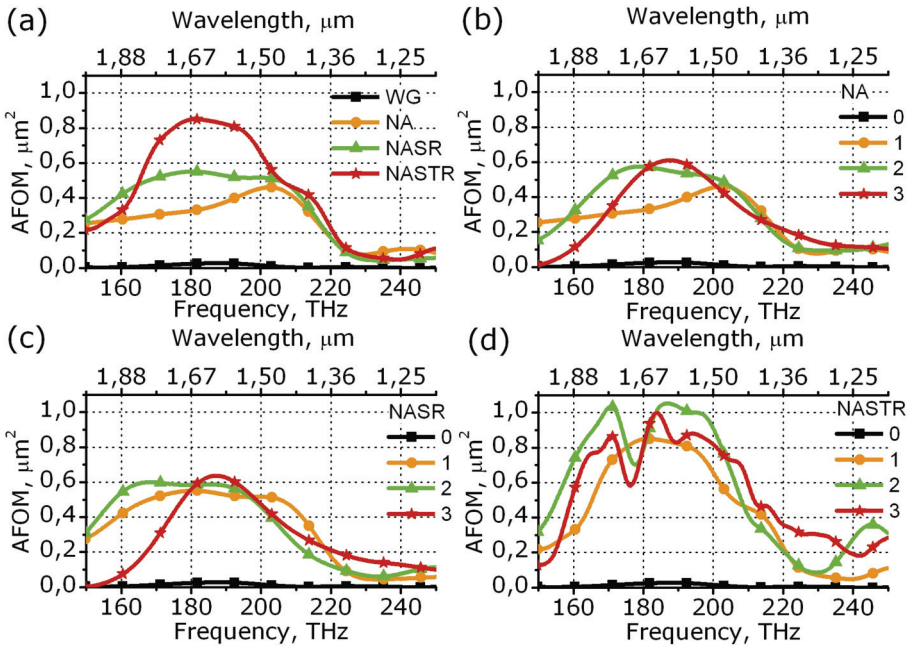

Figure 4.14. Antenna figure of merit for different nanocoupler designs. (a) Comparison of $AFOM$ for a waveguide only (WG, black squares), single nanoantenna (NA, orange circles), nanoantenna with side reflector (NASR, green triangles) and nanoantenna with side and top reflectors (NASTR, red stars). Comparison of $AFOM$ for several nanoantennas without reflectors (b), with side reflector (c) and with side and top reflectors (d): no antennas (black squares), 1 (orange circles), 2 (green triangles) and 3 (red stars) nanoantennas.

As an explanation of this phenomenon we consider the interplay between optical waves that are reflected from the top mirror and then launched into the waveguide. First of all, the top mirror works as a mirror for an incident wave, so the incident and reflected waves for a standing wave and we place

the nanoantennas in the maximum of the standing wave to increase the coupling efficiency. All the antennas are in the same conditions from the excitation point of view. The distance between the antennas is such that the plasmon waves are all in phase. However, there are additional waves that are reradiated by the antennas. The top reflector works as a mirror for these waves also (see Fig. 4.15).

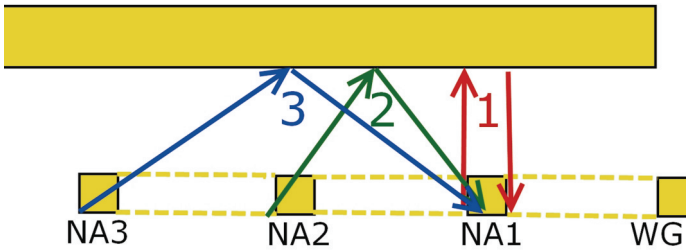

Figure 4.15. Schematic representation from side of the optical paths of the waves reradiated by the antennas and returned back to the first antenna, and then launched into the waveguide (WG). The numbers 1, 2, 3 mark the optical paths of the waves reradiated by the first (NA1), second (NA2) and third (NA3) antennas. Dashed lines remind that the antennas are connected with the wires.

In the case of a single antenna the radiation that returns back to the antenna is travelling perpendicular to the top reflector, so the constructive interference condition is satisfied. The phase change for the wave consists of the phase change due to propagation φ_P and due to reflection φ_R. The case of constructive interference for path 1 (see Fig. 4.15) $\varphi_1 = \varphi_{P1} + \varphi_{R1} = 2\pi$.

The radiated waves from the neighbor antennas are not negligible. Since these waves propagate in silica, which is lossless, they are not absorbed in comparison with the plasmon waves in the waveguide formed by connecting wires, which has a propagation length of 2.5 μm. So the waves coming from the NA2 and NA3 (see Fig. 4.15) may contribute out of phase thus reducing the total coupling efficiency.

Concerning the use of parallel branches combined with Y-coupler, the results obtained are poorer than expected and will not be taken into consideration for further analysis. The best optimized Y-coupler gives coupling efficiency less than 0.5 for the whole frequency range of interest (see Fig. 4.16). This means that even accepting two times more power with two branches of antennas we can deliver less power to the waveguide due to

the losses in the Y-coupler. So the two antennas with side and top reflectors nanocoupler showed the largest antenna figure of merit and the best performance for radiation coupling.

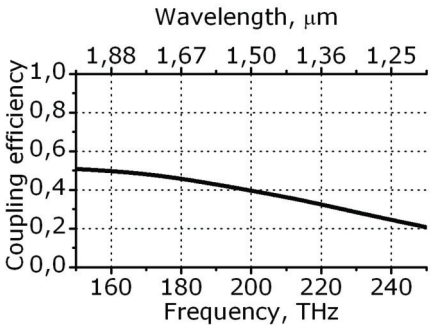

Figure 4.16. Coupling efficiency of the optimized Y-coupler.

Nanocoupler in action

Let's look at the nanocoupler in action. The incident wave and the excited slot plasmon wave are shown in the Fig. 4.17. The Figure 4.18 shows the power flow (Pointing vector) from the excitation port to the waveguide. In case of the waveguide only the power mostly comes through (Fig. 4.18(a)). In case of one nanoantenna with side and top reflectors the incident wave is captured by the antenna and launched into the waveguide (Fig. 4.18(b)).

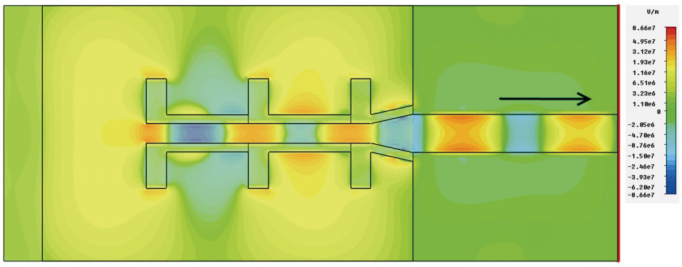

Figure 4.17. Nanocoupler in action, view from top: electric field (vertical polarization) of the incident wave and excited slot plasmon wave for three nanoantennas with side reflector. A black arrow shows the direction of plasmon propagation.

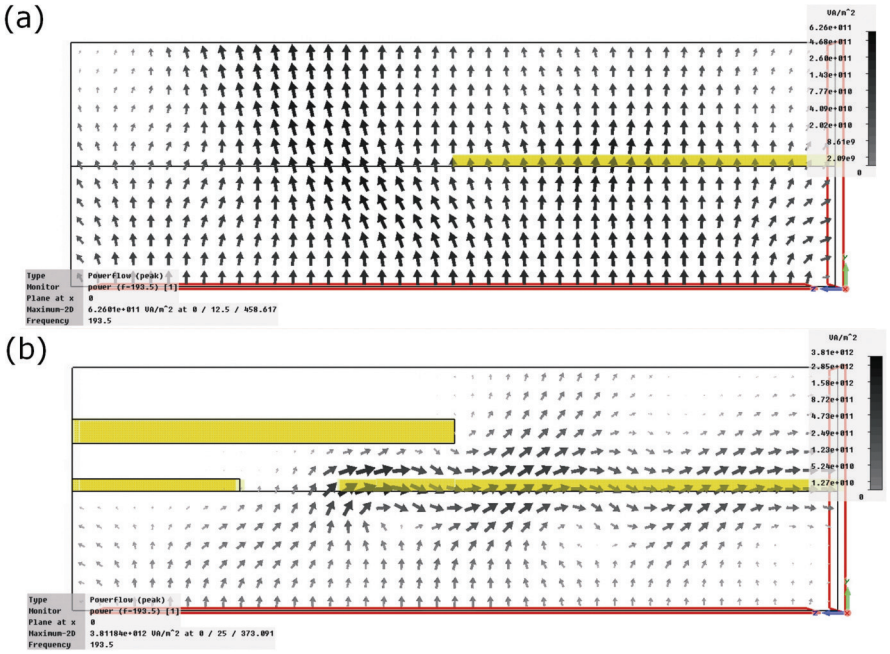

Figure 4.18. Nanocoupler in action, side view: power flow (Pointing vector) from the excitation port to the slot waveguide in case of the waveguide only (a) and one antenna with side and top reflectors nanocoupler (b).

Fabrication results

The first electron-beam lithography fabrication of the nanoantenna coupler showed the absence of the connecting wires, which are only $50\,nm$ wide. We spent a lot of time optimizing the fabrication technology. The details are described in the section 4.1.4. Finally the desired structures were fabricated (Fig. 4.19 and 4.20).

The size of the nanoantennas is of the order of the visible light wavelength, so they can be even seen in the optical microscope. In the Fig. 4.19 optical microscope (Nikon Eclipse) photos are presented for the waveguide only (Fig. 4.19(a)), one nanoantenna (Fig. 4.19(b)) and one antenna with side and top reflectors nanocouplers (Fig. 4.19(c)).

For the structural characterization we used the scanning electron microscope. The photos are presented in the Fig. 4.20. What is interesting, in the structures with no side reflector only up to three connected nanoantennas

were fabricated, the next antennas were disconnected. However, in the structures with side reflector up to six connected antennas could be made. We attribute this fact to the differences in lift-off process and poor adhesion of gold to silica wafer. In case of the side reflector the lift-off went more gently, since only a narrow strip between the waveguide and side reflector was removed in contrast to the no side reflector case, when a large sheet of gold was removed.

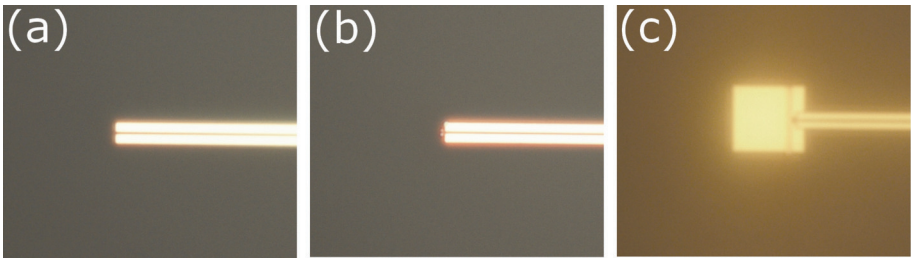

Figure 4.19. Optical microscope photos of the fabricated nanocoupler: waveguide only, view from top (a), waveguide and nanoantenna, view from top (b), nanoantenna with side and top reflectors, view from bottom through 500 μm silica substrate.

Table 4.3. Structural characterization of the fabricated nanocoupler

Parameter	Designed value	Measured value
WGW, nm	300	276±10
NAL, nm	859	850±17
NAW, nm	158	171±13
NAG, nm	153	149±4
COL, nm	330	250
COW, nm	53	57±5
P, nm	825	788±20
SRD, nm	411	337

The results of the structural characterization are summed up in the Table 4.3. As a rule the size of the metallic parts is larger than expected, while the size of the gaps is less. This can be attributed to the proximity effects, since the focused electron beam has Gaussian distribution. Consequently, the resist in the neighborhood of the exposed structure is also exposed. We made the

proximity effects correction with the BEAMER software. However, as the results show, this did not lead to the ideal fabrication.

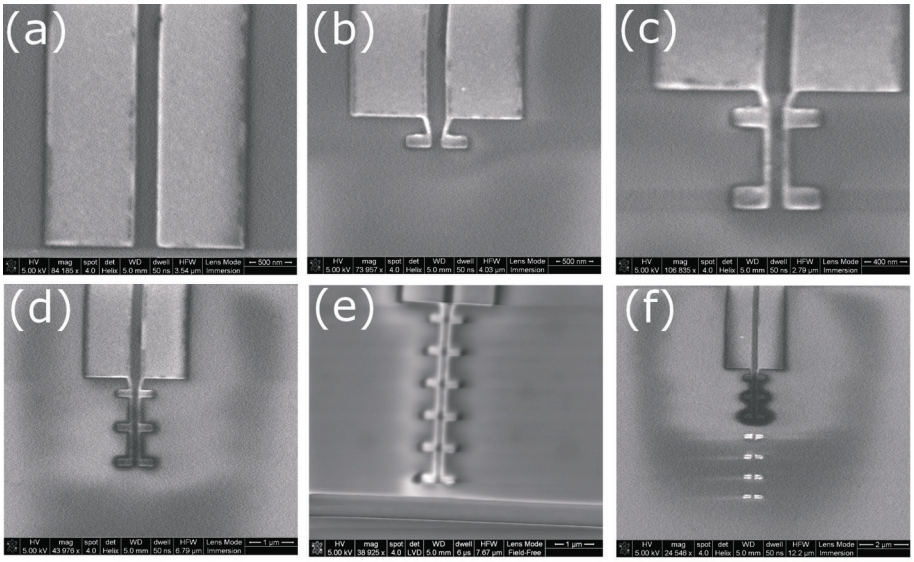

Figure 4.20. SEM photo of the nanocouplers before silica evaporation and top mirror fabrication: waveguide (a), one (b), two (c) and three (d) antennas, six antennas with (e) and without (f) side reflectors. With side reflector up to six connected nanoantennas were fabricated.

Near-field optical characterization

The results of the measurements are presented in the Fig. 4.21. Unfortunately, no visible signal in the plasmonic waveguide was observed. We figured out several reasons for that. First of all, the sizes of the fabricated device were different from the designed ones (see Table 4.3) and that decreases the coupling efficiency. Second, let's make estimations of the power which is captured by the detector. The laser power $0.1\,mW$ was focused in the Gaussian spot of the size $10\,\mu m$. The nanocoupler with the effective area around $0.8\,\mu m^2$ would capture only 1% of the incident power. Taking in account the propagation losses, and that the intensity outside the waveguide is 10 times smaller than inside the waveguide, and additionally that only about 10% of the intensity is captured by the SNOM fiber, will result in that less than 0.01% of the incident power is captured by the fiber. This was not enough to observe any signal on the strong background of the laser spot.

The way to increase the signal-to-noise ratio is to remove the thick silica layer. This does not allow fabrication of the top reflector. It also worsens the waveguiding properties, since the slot waveguide becomes asymmetric. However, the absence of silica layer allows us reach the waveguide with the SNOM fiber tip. This is why we turned to the nanocoupler to the asymmetric waveguide designs (sections 4.2.2-4.2.5), that means the metallic structures on the silica substrate with air superstrate.

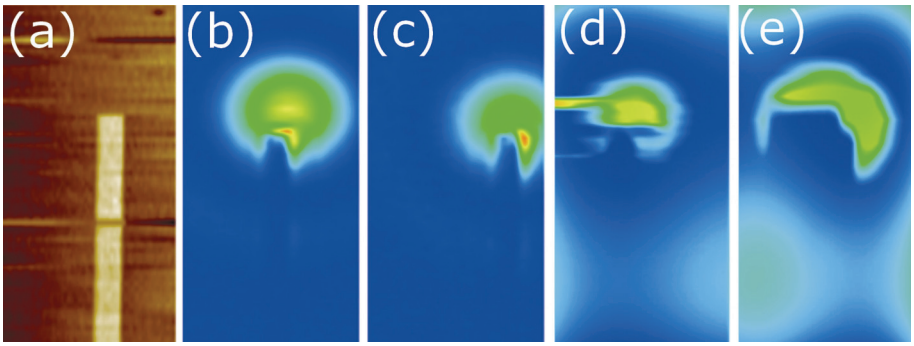

Figure 4.21. The results of the near-field optical characterization of the nanocoupler samples. Topology of the waveguide measurements (a). Near-field measurements of the waveguide only (b), nanoantenna (c), nanoantennas with side reflector (d), nanoantennas with side and top reflector (e). The excitation was performed with $0.1\,mW$ laser power at $\lambda_0 = 1.55\ \mu m$. The Gaussian laser beam was focused in a $10\ \mu m$ diameter spot.

Conclusion

The best performance was shown by the two antennas with side and top reflectors nanocoupler. The structure was fabricated, but the thick silica layer did not allow SNOM characterization and we decided to investigate nanocouplers for the asymmetric waveguide.

4.2.2. Dipole antennas outside asymmetric waveguide

Design geometry

The second design that we considered was a dipole antenna nanocoupler for an asymmetric waveguide (see Fig. 4.22). The geometrical shapes are the same as for the dipole antenna coupler for the symmetric waveguide (section 4.2.1). However, the presence of the air superstrate (see Fig. 4.22(d)) changes substantially the properties of the nanoantennas. Therefore a new optimization of all the geometrical parameters was required. All the following designs (sections 4.2.3-4.2.5) have the same waveguide and antenna thickness ($H = 50\ nm$). The optimized parameters are listed in the Table 4.4. We should admit that the optimized design of the nanocoupler for asymmetric waveguide contains larger elements, so it is simpler for fabrication.

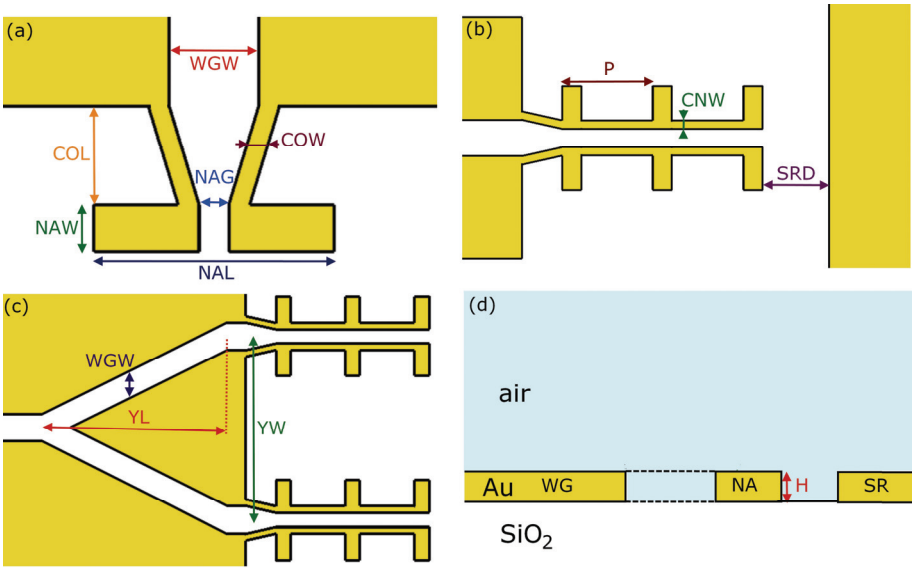

Figure 4.22. Dipole nanoantenna coupler to the asymmetric waveguide geometry. Waveguide and nanoantenna, top view (a). Several connected antennas and side reflector, top view (b). Parallel branches of nanoantennas combined with Y-coupler, top view (c). Nanocoupler side view (waveguide (WG), nanoantenna (NA) and side reflector (SR)) (d). Dashed lines remind that antenna is connected to the waveguide. The structures are made from gold. The substrate is silica, the superstrate is air.

Table 4.4. Optimized geometrical parameters for dipole antenna nanocoupler for asymmetric waveguide

Parameter	Value	Physical meaning
H, nm	50	Thickness of the waveguide and nanoantenna
WGW, nm	300	Width of the waveguide
NAL1, nm	949	Length of the first nanoantenna
NAL2, nm	1100	Length of the second and third nanoantennas
NAW, nm	157	Nanoantenna width
NAG, nm	257	Nanoantenna gap width
COL, nm	381	Distance between the waveguide and the nanoantenna
COW, nm	83	Width of the connecting wire
P, nm	1100	Period of the antenna array
CNW, nm	80	Width of the wires connecting antennas in the array
SRD, nm	400	Distance from the rear antenna to the side reflector
YL, nm	2000	Y-coupler length
YW, nm	2000	Distance between parallel branches

Simulation results

The physics of the nanocoupler for the asymmetric waveguide is the same as of the nanocoupler for the symmetric waveguide. So the results are similar as well (see Fig. 4.23). The waveguide only has low $AFOM$ of 0.1 μm^2. With a nanoantenna $AFOM$ increases to 0.5 μm^2, and to 0.7 μm^2 when the side reflector is added (Fig. 4.23(a)).

It should be mentioned that for the last case the maximum of $AFOM$ is 0.9 μm^2 at $\lambda_0 = 1.65\ \mu m$. So the $AFOM$ for the antenna coupler with air superstrate is larger than for a similar structure embedded in silica. $AFOM$ shows a similar dependence on the number of antennas (Fig. 4.23(b)), it increases with the number of antennas experiencing a saturation behavior. It is not worth using the Y-coupler for combining parallel branches for this case as well. The coupling efficiency of the optimized Y-coupler is low, only 0.22 at $\lambda_0 = 1.55\ \mu m$ (see Fig. 4.24).

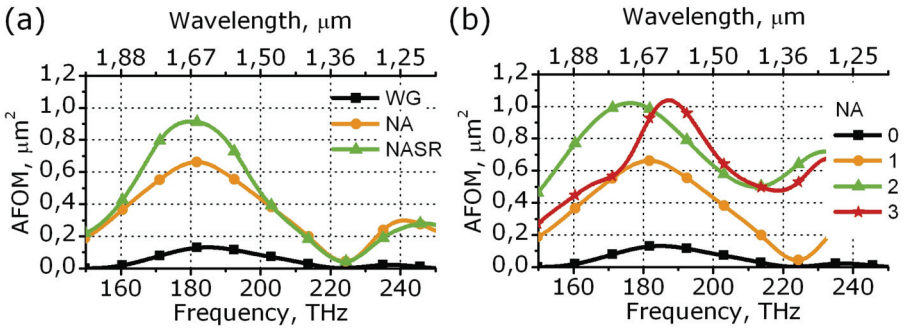

Figure 4.23. *AFOM* for various nanocouplers designs. (a) Comparison of *AFOM* for a waveguide only (WG, black squares), single nanoantenna (NA, orange circles) and nanoantenna with side reflector (NASR, green triangles). (b) Comparison of *AFOM* for no antennas (black squares), 1 (orange circles), 2 (green triangles) and 3 (red stars) nanoantennas without side reflector.

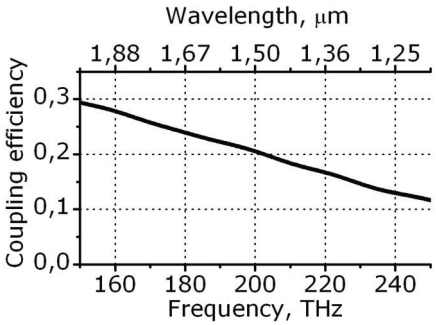

Figure 4.24. Coupling efficiency of the optimized Y-coupler.

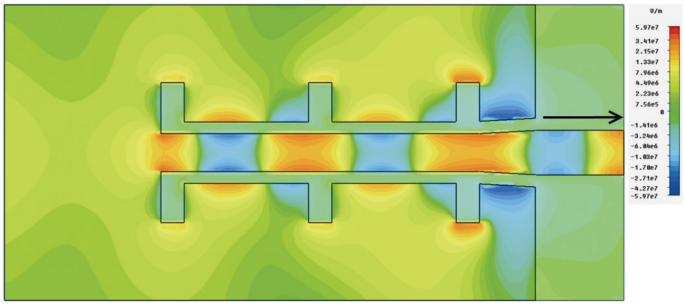

Figure 4.25. Nanocoupler in action, view from top: electric field (vertical polarization) of the incident wave and excited slot plasmon wave for three nanoantennas with side reflector. A black arrow shows the direction of plasmon propagation.

This can be seen that the optimal period of the antennas corresponds to the wavelength of the plasmon in the wires connecting the antennas.

Fabrication results

The SEM photos of the fabricated structures are shown in the Fig. 4.26. The structural characterization is summarized in the Table 4.5. The fabricated structures are of a good quality. The same as for the symmetric coupler, the size of metallic parts is larger than expected, while the size of the gaps is less.

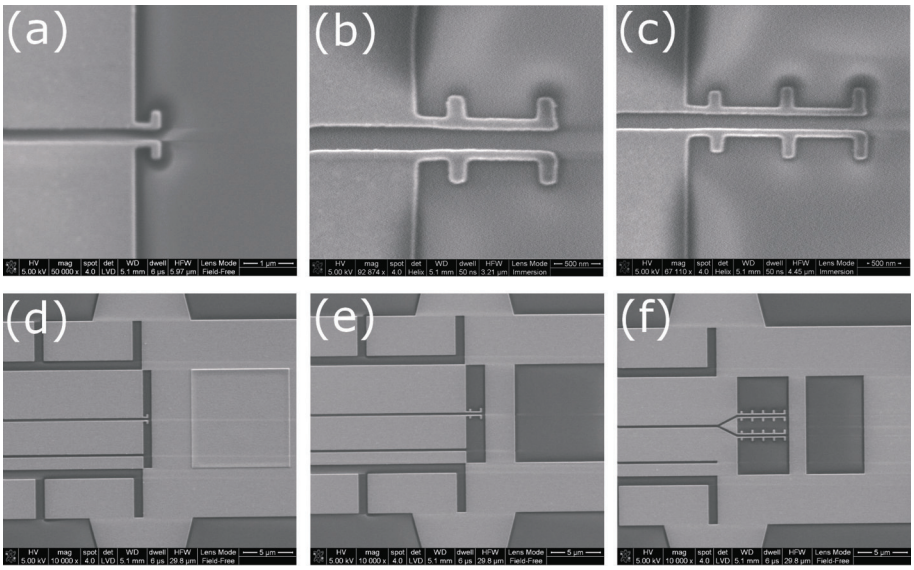

Figure 4.26. SEM photos of the fabricated nanocouplers for the asymmetric waveguide: one (a), two (b), three (c) dipole antennas, one (d), two (e) antennas and two branches of five antennas (f) with side reflector.

Near-field optical characterization

The results of the near-field measurements for one antenna and three antennas nanocouplers are presented in the Fig. 4.27. The field intensity of the plasmon wave excited with one antenna was insufficient to be detected (Fig. 4.27(a)). Two nanoantennas with side reflector coupler have larger coupling efficiency and the excited slot plasmon can be seen in the Fig. 4.27(b). The coupling efficiency is even larger in the coupler design with three nanoantennas. The intensity of the slot plasmon is larger in this

case (Fig. 4.27(c)). This result clearly demonstrates the experimental confirmation of the plasmonic antenna nanocoupling.

Table 4.5. Structural SEM characterization of the dipole antenna nanocoupler for the asymmetric waveguide.

Parameter	Designed value	Measured value
WGW, nm	300	254±9
NAL1, nm	949	939±13
NAL2, nm	1100	1050±9
NAW, nm	157	163±6
NAG, nm	257	231±13
COL, nm	381	345±10
COW, nm	83	101±8
P, nm	1100	1095±14
CNW, nm	80	114±8
SRD, nm	400	374±8

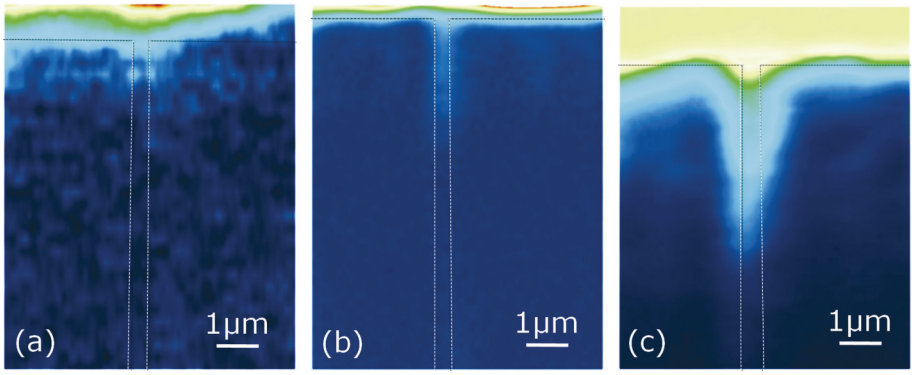

Figure 4.27. The results of the near-field characterization of the nanocoupler samples. Near-field measurements of the waveguide with one nanoantenna (a), two antennas with side reflector (b) and three nanoantennas (c). The dash lines mark the slot waveguide. The excitation was performed with 0.1 mW laser power at $\lambda_0 = 1.55$ μm. The Gaussian laser beam was focused in the 10 μm diameter spot.

Conclusion

Y-coupler's low coupling efficiency prevents several parallel branches of nanoantennas exploiting. The reason for that is that the losses in the Y-coupler are large. The best optimized Y-coupler has the length of $2000\ nm$ which is a trade-off between propagation losses and reflection. In order to reduce the losses in the Y- coupler, it should be made shorter and this is only possible if we put the branches of the nanoantennas closer to each other. In this case they interact strongly with their neighbors. The extreme case is to put the branches so close that they touch each other. We decided to investigate this case in order to reduce the coupling losses of the Y-coupler and consequently, to increase the coupler's $AFOM$.

The best performance was shown by three antennas nanocoupler with $AFOM$ exceeding $1\ \mu m^2$. The structure was successfully fabricated. The near-field optical characterization experimentally confirmed the excitation of the slot plasmons with the help of the dipole antenna nanocoupler.

4.2.3. Nanoantennas gratings

Design geometry

We made the branches of the nanoantennas so close that now they touch each other (see Fig. 4.28). In this case each antenna works for plasmon excitation in both waveguides connected to it. So we expected that such antenna coupler could work more efficiently, since every antenna's both ends are used for SPPs excitation in difference with the dipole antenna outside the waveguide, where the plasmons are excited in the antenna gap. We considered many connected antennas from the beginning and this design remind the grating, this is why we called it antenna grating coupler.

We considered two types of nanoantennas in grating: dipole and bow-tie. The geometry of the regarded design is shown in the Fig. 4.28. The optimized values of the geometric parameters are provided in the Table 4.6.

Table 4.6. Optimized values of geometrical parameter of the dipole and bow-tie antenna gratings.

Parameter	Value	Physical meaning
H, nm	50	Thickness of the waveguide and nanoantenna
WGW1, nm	274	Width of the waveguide
NAL1, nm	550	Dipole nanoantenna length
NAW1, nm	176	Dipole nanoantenna width
P1, nm	1008	Period of the dipole nanoantennas
NAL2, nm	500	Bow-tie nanoantenna length
NAW2, nm	176	Bow-tie nanoantenna width near waveguide
NAC2, nm	600	Bow-tie nanoantenna centre width
P2, nm	1008	Period of the bow-tie nanoantennas
CW, nm	80	Connecting wire width
TL, nm	289	Width of the connecting wire
YL, nm	400	Period of the antenna array

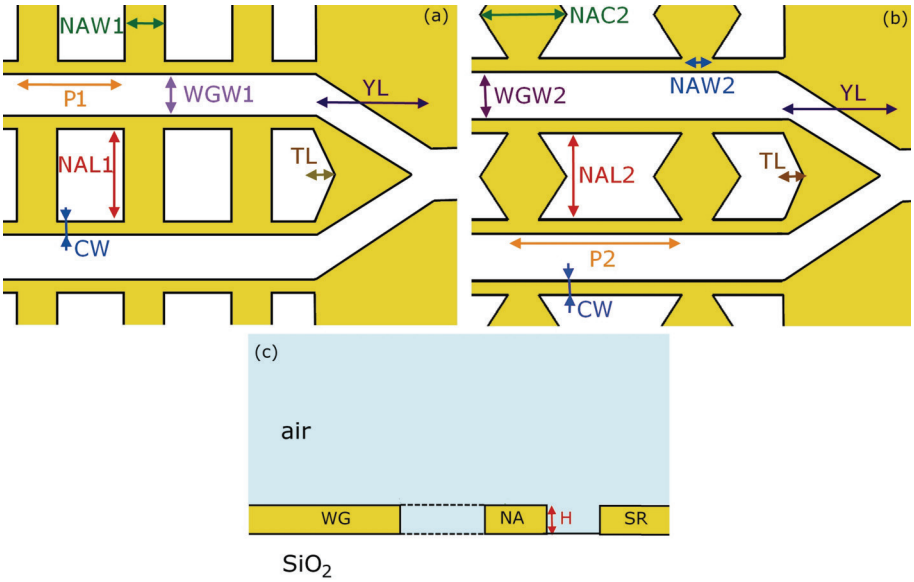

Figure 4.28. Optimized geometry of the dipole antenna grating (a) and bow-tie antenna grating (b), view from top.

Simulation results

For the case of the nanoantenna grating we simulated the single branch with periodic boundary conditions and plane wave excitation. The calculated $AFOM$ for single waveguide channel for 5 periods of nanoantennas is shown in the Figure 4.29(a). $AFOM$ is larger for the dipole antenna grating (DAG) than for the bow-tie antenna grating (BAG). However, none of them exceeds 0.7 μm^2 that is less than $AFOM$ for 3 dipole antennas outside waveguide (Fig. 4.23(b)). The coupling efficiency of the Y-coupler (Fig. 4.29(b)) is 0.4 at $\lambda = 1.55\,\mu m$ that is more than for the Y-coupler combining two branches of dipole antennas (Fig. 4.24), but less than needed. Combined with such coupler, two branches of grating have lower $AFOM$ than one. Y-coupler is not worth being used in this case as well.

The Fig. 4.30 shows how the incident wave excites the surface plasmons in the wires connecting the antennas. Since this waveguide consists of thin wires, there is some plasmon field outside the slot.

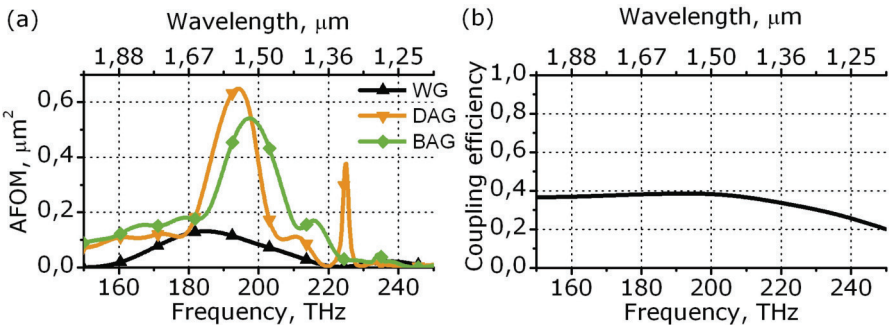

Figure 4.29. (a) *AFOM* for the waveguide only (WG, black triangles up), grating of dipole antennas (DAG, orange triangles down) and grating of bow-tie antennas (BAG, green diamonds) calculated for 5 periods of the grating. (b) Coupling efficiency of the Y-coupler combining two channels of the grating.

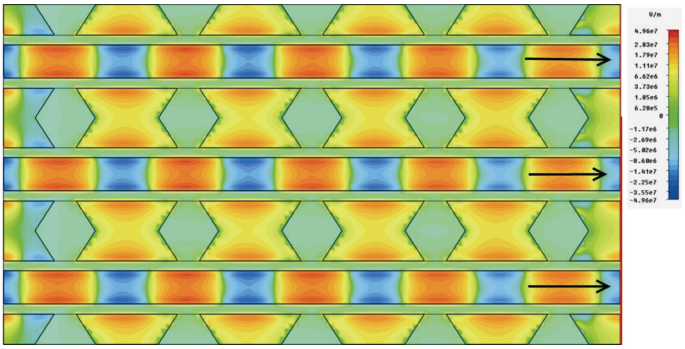

Figure 4.30. Nanocoupler in action, view from top: electric field (vertical polarization) of the incident wave and excited slot plasmon wave for three nanoantennas with side reflector. A black arrow shows the direction of plasmon propagation.

Fabrication results

The SEM photos of the fabricated antenna gratings are shown in the Fig. 4.31. The fabrication technology optimized for the nanoantennas outside the waveguide (sections 4.2.1-4.2.2) did not work well for the grating fabrication and the metal was not well removed with the lift-off. The reason for that is that some metal was deposited on the sides of the resist. Even being thin, this metallic layer prevents the solvent reaching the resist. This is not a problem for long metallic parts, but is a problem for small isolated islands. Since the structure was not well fabricated we did not make structural and optical characterization.

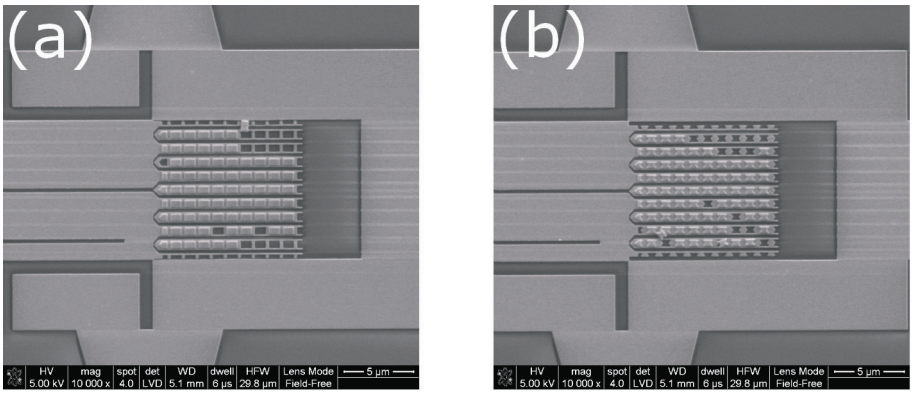

Figure 4.31. The SEM photos of the fabricated dipole (a) and bow-tie (b) antenna gratings. Some metal was deposited on side walls of the resist islands thus preventing the resist reaching the resist.

Conclusion

We expected that grating of the nanoantennas can have larger $AFOM$, since each antenna excites simultaneously two plasmonic waveguides and antennas and closely packed. However, the gratings of the dipole and bow-tie nanoantennas do not show better performance than dipole antennas outside the waveguide. The fabrication of them was not successful. So we decided to investigate some other designs.

There is one common issue for all the previous designs considered (sections 4.2.2-4.2.3). The large excitation beam mostly comes through the coupler, since the antennas capture only a part of the incident power. First of all, that makes problematic the SNOM measurements due to a strong background laser signal. Second, for some applications it would be desirable to have a reflecting surface where nanocoupler is. For example, attaching the nanocoupler to the vertical cavity surface emitting laser we can obtain electrically pumped source of surface plasmon polaritons in the slots.

Moreover, the fabrication of the thin connecting wires was challenging so the design without fine details would be desirable. Additional issue is that several nanoantennas are connected in a branch by connecting wires which form a waveguide with high losses and low propagation length 3 μm. So the radiation captured by the last nanoantennas is not efficiently delivered to the waveguide. All that made us looking for other designs than dipole antenna outside the waveguide.

4.2.4. Antennas inside waveguide

Nanocoupler design

The forth design was the antennas inside the waveguide (see Fig 4.32). Such design is the closest to the inspiring analogy with the sea waves and floats in the channel. In this configuration the incident wave creates the charges oscillations in the nanoantennas. The charges are therefore periodically accumulated at the ends of the antenna. A strong electric field is created, and plasmons are excited in the waveguide through the near-field interaction with the antenna.

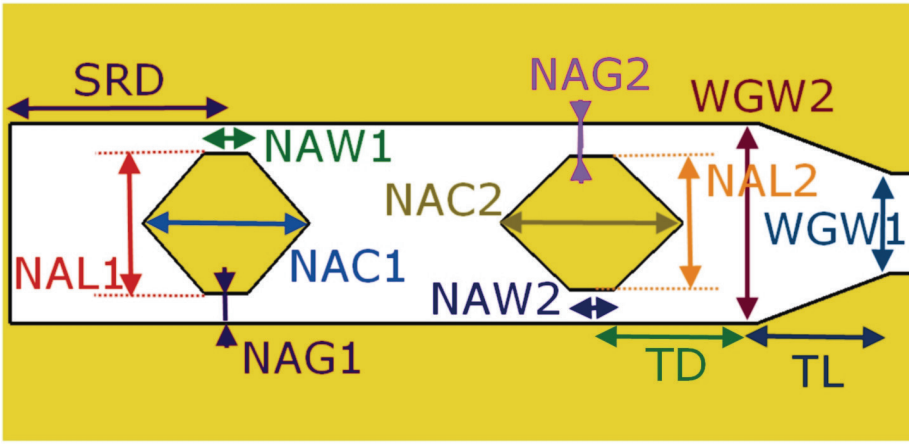

Figure 4.32. Optimized geometry of the antennas inside the waveguide nanocoupler. The incident field is supposed to be polarized perpendicular to the waveguide. The charges accumulated at the narrow ends of the hexagons excited the slot plasmons via near-field interaction.

The optimized antennas have hexagonal shape; they are broad in the middle and narrow at the ends (see Fig. 4.32). Narrow ends are required for efficient plasmons excitation, while broad centre decreases the Ohmic resistance of the antenna. To satisfy the resonant condition for the nanoantenna we made the waveguide wider than the slot waveguide, namely 600 nm wide. The termination of the waveguide on the left plays the role of the side reflector. The first antenna and the subsequent ones have different sizes (see Table 4.7). That can be explained by the fact that the second antenna does not only excite the plasmons but the plasmon excited by the first one should pass through the part of the waveguide where nanoantenna is, so the gaps

between the antenna and the waveguide. So the second, third, etc. antennas are broader than for the first antenna. The values of the geometrical parameters are specified in the Table 4.7.

The space around the antenna is covered by metal (see Fig. 4.32). In such configuration the surface can be used as a mirror. This design is also simpler for fabrication than the previous ones, since there are no fine connecting wires.

Table 4.7. Optimized values of geometrical parameter of the antennas inside waveguide.

Parameter	Value	Physical meaning
H, nm	50	Thickness of the waveguide and nanoantenna
WGW1, nm	300	Width of the slot waveguide
WGW2, nm	600	Width of the waveguide where nanoantennas are
NAL1, nm	420	Length of the first nanoantenna
NAW1, nm	132	Width of the first nanoantenna end
NAC1, nm	500	Width of the first nanoantenna centre
NAG1, nm	90	Width of the gap between the first nanoantenna and a waveguide
NAL2, nm	400	Length of the 2^{nd} and 3^{rd} nanoantenna
NAW2, nm	132	Width of the 2^{nd} and 3^{rd} nanoantenna end
NAC2, nm	550	Width of the 2^{nd} and 3^{rd} nanoantenna centre
NAG2, nm	100	Width of the gap for the 2^{nd} and 3^{rd} nanoantenna
TL, nm	400	Length of the tapered waveguide
P, nm	1100	Period of the structure
SRD, nm	650	Distance from the first antenna to the side reflector
TD, nm	500	Distance from the rear nanoantenna to the tapered part

Simulation results

The bottle-shaped waveguide without antennas has low $AFOM = 0.09\ \mu m^2$ at $\lambda_0 = 1.55\ \mu m$ (see Fig. 4.33), which is, however, larger than $AFOM$ for the waveguides in the sections 4.2.1-4.2.3. One, two and three nanoantennas have $AFOM$ equal to $0.4\ \mu m^2$, $0.5\ \mu m^2$ and $0.6\ \mu m^2$ respectively. That is less than $AFOM$ for the same number of the dipole antennas outside the waveguide.

The Fig. 4.34 shows the excitation of the slot plasmons with the incident wave. Field concentration is clearly seen at the narrow ends of the hexagonal antennas. The waveguide termination on the left works as a side reflector.

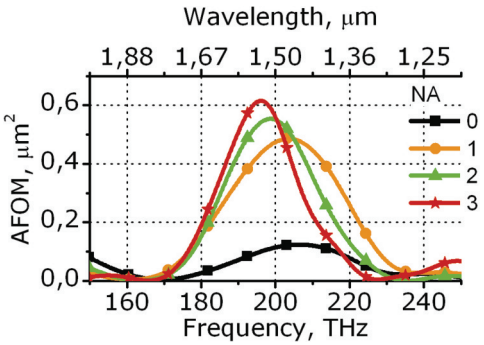

Figure 4.33. Comparison of $AFOM$ for no antennas (black squares), 1 (orange circles), 2 (green triangles) and 3 (red stars) nanoantennas

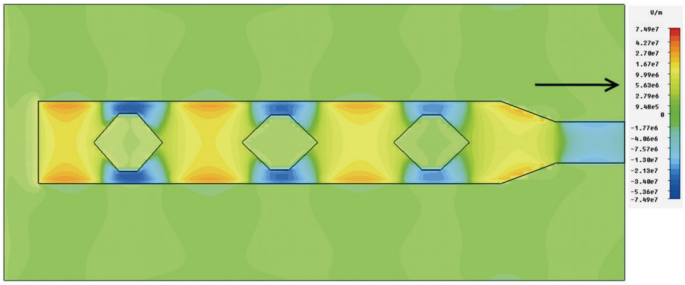

Figure 4.34. Nanocoupler in action, view from top: electric field (vertical polarization) of the incident wave and excited slot plasmon wave for three nanoantennas with side reflector. A black arrow shows the direction of plasmon propagation.

Fabrication results

One, two and three antennas inside waveguide nanocoupler are shown in the SEM photos in the Figure 4.35. The structures are well fabricated. The Table 4.8 provides the results of structural characterization with SEM. Metallic parts are also larger than designed and the gaps are narrower.

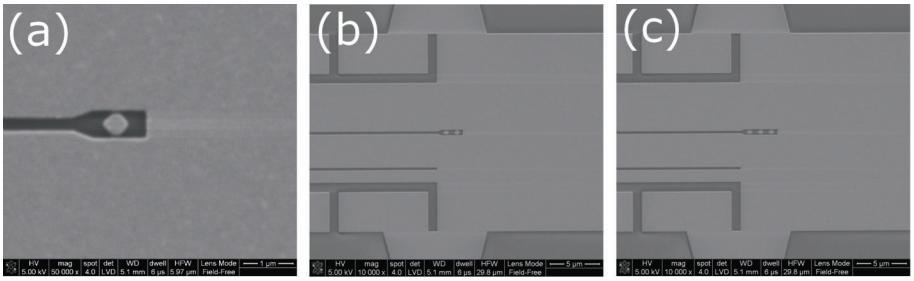

Figure 4.35. The SEM photos of one (a), two (b) and three (c) nanoantennas inside waveguide coupler.

Table 4.8. Structural SEM characterization of the dipole antenna nanocoupler for the asymmetric waveguide.

Parameter	Designed value	Measured value
WGW1, nm	300	276±10
WGW2, nm	600	543±22
NAL1, nm	420	404±24
NAW1, nm	132	181±14
NAC1, nm	500	491±8
NAG1, nm	90	63±8
NAL2, nm	400	383±15
NAW2, nm	132	181±14
NAC2, nm	550	532±13
NAG2, nm	100	72±11
P, nm	1100	1111±27
TL, nm	400	395±16
SRD, nm	650	624±21
TD, nm	500	497±17

Conclusion

The antennas inside the waveguide can work as a nanocoupler to the plasmonic slot waveguide. They do not contain fine details that make them more reliable for fabrication. The surrounding metal screens the background incident wave and may serve as a mirror. However, the $AFOM$ of the antennas inside the waveguide is not as high as the $AFOM$ of the dipole antennas outside the waveguide. Therefore we decided to combine the advantages of the dipole antennas and metal surrounding in the nanocoupler based on the bow-tie antennas in the slots ("battle axe" coupler).

4.2.5. Battle-axe nanocoupler

Nanocoupler design

The idea of combining the advantage of high $AFOM$ of the dipole antennas with the metallic surrounding resulted in the design of antennas in the slots that resembles a battle axe (see Fig. 4.36). The battle axe nanocoupler is surrounded by metal all over around, so it can also be used as a mirror and it eliminates the background laser signal when making the SNOM measurements. We used here not the dipole antennas but bow-tie antennas assuming that they result in a more compact device. The slots are enough large for that bow-tie antenna does not interact with the surrounding and does not excite the plasmons on the interface but in the slot waveguide only.

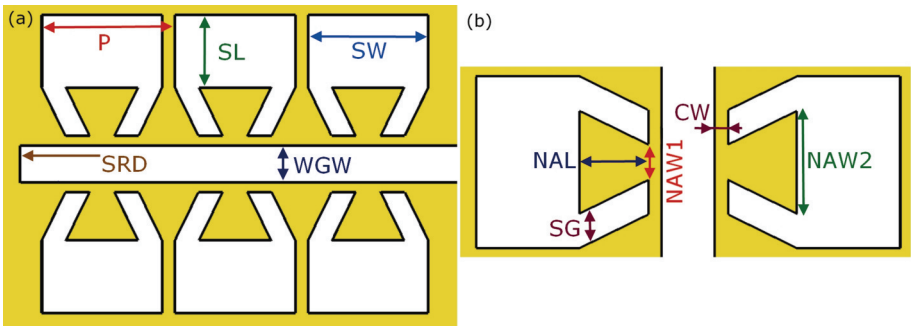

Figure 4.36. Optimized geometry of the bow-tie antennas in slots ("battle axe") nanocoupler. (a) Three periods and side reflector. (b) One period of the structure.

The nanocoupler resembles the dipole nanoantennas outside the waveguide (section 4.2.2). But in contrary to the designs 4.2.1-4.2.3 the nanoantennas are connected not with the narrow wires all the way through, but there are regions of the thick connectors (see Fig. 4.36(a)). The purpose of the thick metallic part is to increase the propagation length of the connecting wires (propagation length of the wire connectors like in the section 4.2.2 is only 3 μm, while the slot waveguide itself has the propagation length of 10 μm). The design is shown in the Fig. 4.36. The termination of the waveguide on the left works as a side reflector. The geometrical parameters values are specified in the Table 4.9.

Table 4.9. Optimized values of geometrical parameter of the "battle axe" nanocoupler.

Parameter	Value	Physical meaning
H, nm	50	Thickness of the waveguide and nanoantenna
WGW, nm	300	Width of the waveguide
NAL, nm	388	Length of the nanoantenna
NAW1, nm	199	Width of the nanoantenna, where it contact waveguide
NAW2, nm	578	Nanoantenna width at the end
CW, nm	75	Width of the connecting wire
SG, nm	195	Gap between nanoantenna and surrounding metal
SW, nm	968	Slot width
SL, nm	584	Slot length
P, nm	1070	Period of the antenna array
SRD, nm	578	Distance from the rear antenna to the side reflector

Simulation results

The simulation results are shown in the Fig. 4.37. In the agreement with all the previous nanocouplers the $AFOM$ experiences a saturation behavior and narrowing of the bandwidth with the increasing number of nanoantennas. However, the value of $AFOM$ is significantly larger than for the previous designs. The waveguide only has very low $AFOM = 0.02\ \mu m^2$ at $\lambda_0 = 1.55\ \mu m$. One antenna gives $AFOM = 0.2\ \mu m^2$, two antennas $AFOM = 0.7\ \mu m^2$, three antennas $AFOM = 1.4\ \mu m^2$ and five antennas $AFOM = 1.8\ \mu m^2$ (Fig. 4.37), that is 90 times larger than for the waveguide only. Such high $AFOM$ and employment of many periods (for instance, the other couplers designs showed saturation of the $AFOM$ with the number of layers already at 3 periods) becomes possible due to better waveguiding properties of the connecting waveguides in contrary to the thin wires transmission line which has high losses. The electric field of the incident wave and excited slot plasmons are shown in the Fig. 4.38.

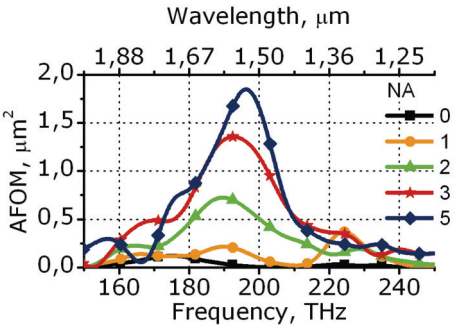

Figure 4.37. $AFOM$ for the battle-axe nanocoupler for different number of periods: 0 -waveguide only (black squares), 1 (orange circles), 2 (green triangles), 3 (red stars), 5 (dark blue diamonds).

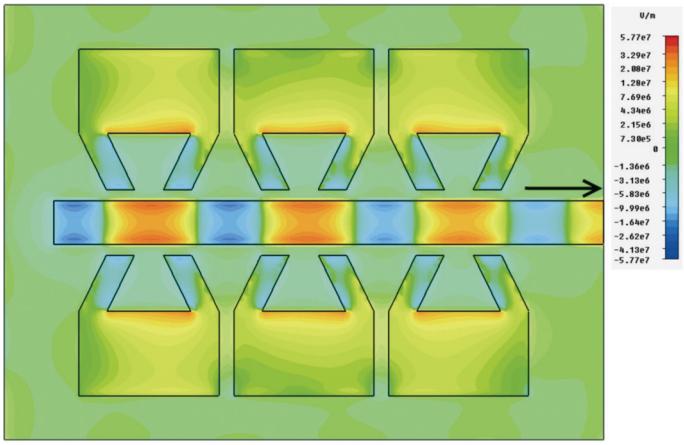

Figure 4.38. Nanocoupler in action, view from top: electric field (vertical polarization) of the incident wave and excited slot plasmon wave for three nanoantennas with side reflector. A black arrow shows the direction of plasmon propagation.

Fabrication results

The SEM photos of the fabrication results are shown in the Figure 4.39. The fabrication of the battle axe coupler experienced the same difficulty as the fabrication of the antenna gratings (section 4.2.3). Small isolated islands of resist were not lifted off well (see Fig. 4.39). As a solution for the next fabrication a thicker resist layer should be deposited. Since the structure was not well fabricated we did not make structural and optical characterization.

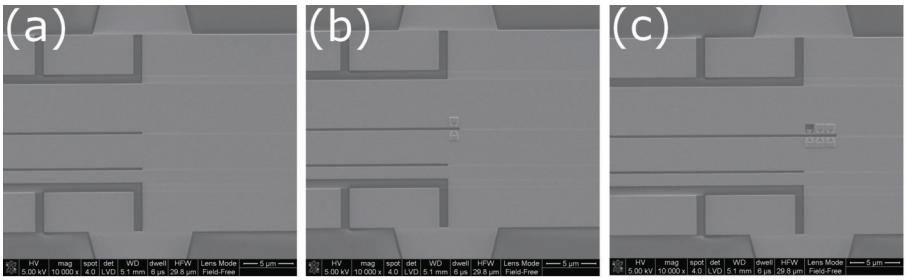

Figure 4.39. The SEM photos of waveguide (a), one (b) and three (c) nanoantennas battle axe coupler.

Conclusion

The battle axe design shows the largest $AFOM = 1.8\ \mu m^2$ for five periods. The saturation of $AFOM$ with the number of periods is not as fast as for the previous cases (sections 4.2.1-4.2.4) that becomes possible due to improved waveguiding properties of the wires connecting the nanoantennas.

The fabrication technology, optimized for the dipole antenna fabrication, did not result in the well-fabricated structures. Some technology modification (increase of the resist thickness) is required for the successful battle axe nanocoupler fabrication.

The surrounding space is covered with metal, so the battle axe can be used as a mirror. However, this is not mandatory, so the surrounding metal may be removed without significant influence on the nanocoupler performance. All that makes the battle axe nanocoupler the best of the considered designs.

Chapter conclusions

We developed five types of the nanoantenna based couplers: dipole antennas outside symmetric and asymmetric waveguide, antennas gratings, antennas inside waveguide and battle axe nanocoupler.

The nanocouplers showed the same tendency of the $AFOM$ saturation with the increasing number of periods. The use of the side and top reflectors generally increases the $AFOM$. However, using the top reflector one has to be careful and take into account the reflection of the reradiated waves from the top reflector. Such waves may return to the nanocoupler in or out of phase.

The best performance was shown by the battle axe nanocoupler. It has antenna figure of merit equal to $1.8\ \mu m^2$ for five periods. That is 90 times larger than $AFOM$ of the waveguide without nanocoupler ($0.02\ \mu m^2$).

Dipole antennas outside waveguide and antennas inside waveguide were successfully fabricated. The fabrication of the antenna gratings and battle axe coupler experienced some difficulties that can be removed by further fabrication technology optimization. Initial design of the nanocoupler embedded in silica was difficult to measure with the near-field optical microscope and therefore we removed the silica layer.

The near-field optical characterization experimentally confirmed the excitation of the slot plasmons with the help of the dipole antenna nanocoupler for the asymmetric waveguides (silica substrate and air superstrate).

Chapter 5. Summary and conclusions

Main findings

This thesis summarizes the work on negative index metamaterials and plasmonic antenna based nanocouplers. The main focus of the project was on the development, simulation and fabrication of the nanoantenna based coupler, on the design of negative index metamaterials, on development of the effective parameters retrieval methods and on improvement of silver nanometallization technology. Multiple possibilities of the nanocoupler realization are figured out and critically analyzed. The choice of the negative index metamaterial superresolution lens and plasmonic nanoantenna nanocoupler is justified.

The cubic symmetric negative index metamaterial Split cube in Cage and Split cube in Carcass designs for the telecom frequencies are proposed. It is shown that despite the exceptional bulkness (effective properties do not depend on the number of layers) and cubic symmetry the abovementioned designs exhibit strong spatial dispersion in the frequency range of interest. That prevents treating them as an isotropic negative index material and using as a negative index nanocoupler building block.

The wave propagation retrieval method for the effective properties characterization for metamaterials with linear and circular eigenpolarizations and the field averaging of the restored Bloch mode method are proposed. The methods are based on observation of the wave propagation in the metamaterial slab, they are simple, can be applied to lossy and lossless negative and positive refractive index, permittivity and permeability metamaterials. They provide unambiguous restoration of the effective properties.

The technology of silver nanometallization of complex $3D$ dielectric structures is developed. The metallization is based on silver reduction from the silver-ammonia complex with formaldehyde as a reducing agent. The continuous and smooth silver layer can be deposited starting from $30\,nm$. The technology can be used for fabrication of the integrated circuits and complex photonic structures fabrication for the infrared frequencies.

The coupling between metamaterials monolayers effects are investigated on the example of chiral metamaterials. It is shown that some metamaterials can be treated as homogeneous in the resonant frequency region, but some

cannot at any value of the metamaterials period. The quantitative homogenization condition is formulated.

Five types of the nanoantenna based couplers are developed: dipole antennas outside symmetric and asymmetric waveguide, antennas gratings, antennas inside waveguide and battle axe nanocoupler.
It is shown that the usage of the side and top reflectors generally increases the power captured by the nanocoupler from the incident wave. The optimized geometrical parameters of the nanoantenna couplers are found out. The best performance is shown by the battle axe nanocoupler. It has antenna figure of merit equal to $1.8\ \mu m^2$ for five periods that is 90 times larger than antenna figure of merit for the waveguide without nanocoupler ($0.02\ \mu m^2$).

Dipole antennas outside waveguide and antennas inside waveguide are successfully fabricated. The near-field optical characterization with the SNOM experimentally confirms the excitation of the slot plasmons with the help of the antenna based nanocoupler.

Possible applications

The investigation of the metamaterials properties, more specifically of the optical anisotropy of the cubic symmetric metamaterial and of the coupling effects between metamaterials monolayers, provide an important information for the metamaterial based devices development. It should be taken into account that if meta-atoms are not much smaller than the wavelength, the metamaterial cannot be treated as optical isotropic in the resonant region even if the metaatoms are cubic symmetric and arranged in the cubic structure. The interaction between the metamaterials monolayers may also prevent homogenization.

The proposed effective parameters retrieval methods, which are simple and give unambiguous restoration, can be useful for researchers and engineers for metamaterials development and characterization.

The developed electroless technology can be used for complex dielectric surfaces metallization. The proposed technique is not limited to the metamaterials field, but it can be used in other research areas where depositing of metals is required. Electroless metal plating bears great

potential in many aspects of metal deposition in nanophysics and nanotechnology.

The designed nanoantenna based coupler can be used for coupling the radiation to the optical integrated circuit from the optical fiber or free space. Moreover, the developed nanoantennas can be used for the short range wireless communication inside the chip and as the emitting and receiving devices in the lab-on-chip systems.

Bibliography

[1] D. A. B. Miller, "Optical interconnects to electronic chips.," *Applied Optics*, vol. 49, no. 25, p. F59-F70, Sep. 2010.

[2] L. Zimmermann, "State of the art and trends in silicon photonics packaging. http://www.siliconphotonics.eu/workshop230511_slides.html." 2011.

[3] S. Kawata, M. Ohtsu, and M. Irie, *Nano-optics*, vol. 84. Springer Verlag, 2002.

[4] S. A. Maier, *Plasmonics: fundamentals and applications*. Springer Verlag, 2007.

[5] S. I. Bozhevolnyi, *Plasmonic nanoguides and circuits*. Pan Stanford, 2008.

[6] R. Zia, M. D. Selker, P. B. Catrysse, and M. L. Brongersma, "Geometries and materials for subwavelength surface plasmon modes.," *Journal of the Optical Society of America. A*, vol. 21, no. 12, pp. 2442-2446, Dec. 2004.

[7] A. Boltasseva, T. Nikolajsen, K. Leosson, K. Kjaer, M. S. Larsen, and S. I. Bozhevolnyi, "Integrated optical components utilizing long-range surface plasmon polaritons," *Journal of Lightwave Technology*, vol. 23, no. 1, pp. 413-422, Jan. 2005.

[8] S. I. Bozhevolnyi, "Effective-index modeling of channel plasmon polaritons.," *Optics Express*, vol. 14, no. 20, pp. 9467-9476, Oct. 2006.

[9] S. Bozhevolnyi, V. Volkov, E. Devaux, and T. Ebbesen, "Channel Plasmon-Polariton Guiding by Subwavelength Metal Grooves," *Physical Review Letters*, vol. 95, no. 4, p. 046802, Jul. 2005.

[10] E. Moreno, S. Rodrigo, S. Bozhevolnyi, L. Martín-Moreno, and F. García-Vidal, "Guiding and Focusing of Electromagnetic Fields with Wedge Plasmon Polaritons," *Physical Review Letters*, vol. 100, no. 2, p. 023901, Jan. 2008.

[11] L. Liu, Z. Han, and S. He, "Novel surface plasmon waveguide for high integration.," *Optics Express*, vol. 13, no. 17, pp. 6645-6650, Aug. 2005.

[12] G. Veronis and S. Fan, "Modes of Subwavelength Plasmonic Slot Waveguides," *Journal of Lightwave Technology*, vol. 25, no. 9, pp. 2511-2521, Sep. 2007.

[13] S. Maier, P. G. Kik, and H. Atwater, "Observation of coupled plasmon-polariton modes in Au nanoparticle chain waveguides of different lengths: Estimation of waveguide loss," *Applied Physics Letters*, vol. 81, no. 9, pp. 1714-1716, 2002.

[14] M. L. Brongersma and P. G. Kik, *Surface plasmon nanophotonics*, vol. 131. Springer Verlag, 2007.

[15] D. Vermeulen et al., "High-efficiency fiber-to-chip grating couplers realized using an advanced CMOS-compatible silicon-on-insulator platform.," *Optics Express*, vol. 18, no. 17, pp. 18278-18283, Aug. 2010.

[16] G. Brambilla, V. Finazzi, and D. J. Richardson, "Ultra-low-loss optical fiber nanotapers," *Optics Express*, vol. 12, no. 10, pp. 4421-4425, 2004.

[17] M. Sumetsky, "How thin can a microfiber be and still guide light?," *Optics Letters*, vol. 31, no. 7, pp. 870-872, 2006.

[18] N. M. Arslanov and S. A. Moiseev, "Ultrahigh interference spatial compression of light inside the subwavelength aperture of a near-field optical probe," *Journal of the Optical Society of America. A*, vol. 24, no. 3, pp. 831-838, Mar. 2007.

[19] A. Rusina, M. Durach, K. A. Nelson, and M. I. Stockman, "Nanoconcentration of terahertz radiation in plasmonic waveguides," *Optics Express*, vol. 16, no. 23, pp. 18576-18589, Oct. 2008.

[20] J. Liu, R. Mendis, and D. M. Mittleman, "The transition from a TEM-like mode to a plasmonic mode in parallel-plate waveguides," *Applied Physics Letters*, vol. 98, no. 23, p. 231113, 2011.

[21] K. Iwaszczuk, A. Andryieuski, A. Lavrinenko, X. Zhang, and P. U. Jepsen, "None-invasive terahertz field imaging inside parallel plate waveguides," *accepted to Applied Physics Letters*, pp. 1-4, 2011.

[22] D. F. P. Pile and D. K. Gramotnev, "Adiabatic and nonadiabatic nanofocusing of plasmons by tapered gap plasmon waveguides," *Applied Physics Letters*, vol. 89, no. 4, p. 041111, 2006.

[23] S. Vedantam, H. Lee, J. Tang, J. Conway, M. Staffaroni, and E. Yablonovitch, "A plasmonic dimple lens for nanoscale focusing of light.," *Nano Letters*, vol. 9, no. 10, pp. 3447-52, Oct. 2009.

[24] F. Renna, D. Cox, and G. Brambilla, "Efficient sub-wavelength light confinement using surface plasmon polaritons in tapered fibers.," *Optics Express*, vol. 17, no. 9, pp. 7658-63, Apr. 2009.

[25] H. Choi, D. F. Pile, S. Nam, G. Bartal, and X. Zhang, "Compressing surface plasmons for nano-scale optical focusing.," *Optics Express*, vol. 17, no. 9, pp. 7519-24, Apr. 2009.

[26] M. Stockman, "Nanofocusing of Optical Energy in Tapered Plasmonic Waveguides," *Physical Review Letters*, vol. 93, no. 13, p. 137404, Sep. 2004.

[27] S. Maier, S. Andrews, L. Martín-Moreno, and F. García-Vidal, "Terahertz Surface Plasmon-Polariton Propagation and Focusing on Periodically Corrugated Metal Wires," *Physical Review Letters*, vol. 97, no. 17, p. 176805, Oct. 2006.

[28] E. Verhagen, M. Spasenović, A. Polman, and L. Kuipers, "Nanowire Plasmon Excitation by Adiabatic Mode Transformation," *Physical Review Letters*, vol. 102, no. 20, p. 203904, May. 2009.

[29] Z. Xiu-Li, F. Yong-Qi, W. Shi-Yong, P. An-Jin, and C. Zhong-Heng, "Funnel-Shaped Arrays of Metal Nano-Cylinders for Nano-Focusing," *Chinese Physics Letters*, vol. 25, no. 9, pp. 3296-3299, Sep. 2008.

[30] A. Govyadinov and V. Podolskiy, "Metamaterial photonic funnels for subdiffraction light compression and propagation," *Physical Review B*, vol. 73, no. 15, p. 155108, Apr. 2006.

[31] S. Mühlig, C. Rockstuhl, J. Pniewski, C. R. Simovski, S. A. Tretyakov, and F. Lederer, "Three-dimensional metamaterial nanotips," *Physical Review B*, vol. 81, no. 7, p. 075317, Feb. 2010.

[32] C. Rockstuhl, C. R. Simovski, S. A. Tretyakov, and F. Lederer, "Metamaterial nanotips," *Applied Physics Letters*, vol. 94, no. 11, p. 113110, 2009.

[33] A. L. Pyayt, B. Wiley, Y. Xia, A. Chen, and L. Dalton, "Integration of photonic and silver nanowire plasmonic waveguides.," *Nature Nanotechnology*, vol. 3, no. 11, pp. 660-5, Nov. 2008.

[34] R. Yan, P. Pausauskie, J. Huang, and P. Yang, "Direct photonic-plasmonic coupling and routing in single nanowires.," *Proceedings of the National Academy of Sciences of the United States of America*, vol. 106, no. 50, pp. 21045-50, Dec. 2009.

[35] Q. Li and M. Qiu, "Structurally-tolerant vertical directional coupling between metal-insulator-metal plasmonic waveguide and silicon dielectric waveguide.," *Optics Express*, vol. 18, no. 15, pp. 15531-43, Jul. 2010.

[36] Q. Li, Y. Song, G. Zhou, Y. Su, and M. Qiu, "Asymmetric plasmonic-dielectric coupler with short coupling length, high

extinction ratio, and low insertion loss.," *Optics Letters*, vol. 35, no. 19, pp. 3153-5, Oct. 2010.

[37] C. Delacour et al., "Efficient Directional Coupling between Silicon and Copper Plasmonic Nanoslot Waveguides: toward Metal−Oxide−Silicon Nanophotonics," *Nano Letters*, vol. 10, pp. 2922-2926, Jul. 2010.

[38] S.-yeol Lee, J. Park, M. Kang, and B. Lee, "Highly efficient plasmonic interconnector based on the asymmetric junction between metal- dielectric-metal and dielectric slab waveguides," *Optics Express*, vol. 19, no. 10, pp. 4403-4411, 2011.

[39] Y. Song, J. Wang, Q. Li, M. Yan, and M. Qiu, "Broadband coupler between silicon waveguide and hybrid plasmonic waveguide," *Optics Express*, vol. 18, no. 12, p. 13173, Jun. 2010.

[40] X.-W. Chen, V. Sandoghdar, and M. Agio, "Nanofocusing radially-polarized beams for high-throughput funneling of optical energy to the near field.," *Optics Express*, vol. 18, no. 10, pp. 10878-10887, May. 2010.

[41] X.-W. Chen, V. Sandoghdar, and M. Agio, "Highly efficient interfacing of guided plasmons and photons in nanowires.," *Nano Letters*, vol. 9, no. 11, pp. 3756-61, Nov. 2009.

[42] R. M. Briggs, J. Grandidier, S. P. Burgos, E. Feigenbaum, and H. a Atwater, "Efficient Coupling between Dielectric-Loaded Plasmonic and Silicon Photonic Waveguides.," *Nano Letters*, pp. 4851-4857, Oct. 2010.

[43] Z. Han, a Y. Elezzabi, and V. Van, "Experimental realization of subwavelength plasmonic slot waveguides on a silicon platform.," *Optics Letters*, vol. 35, no. 4, pp. 502-4, Feb. 2010.

[44] P. Ginzburg and M. Orenstein, "Plasmonic transmission lines: from micro to nano scale with lambda/4 impedance matching.," *Optics Express*, vol. 15, no. 11, pp. 6762-7, May. 2007.

[45] J. Liu, H. Zhao, Y. Zhang, and S. Liu, "Resonant cavity based antireflection structures for surface plasmon waveguides," *Applied Physics B*, vol. 98, no. 4, pp. 797-802, Oct. 2009.

[46] Ş. Kocabaş, G. Veronis, D. Miller, and S. Fan, "Modal analysis and coupling in metal-insulator-metal waveguides," *Physical Review B*, vol. 79, no. 3, p. 035120, Jan. 2009.

[47] A. Pannipitiya, I. D. Rukhlenko, M. Premaratne, H. T. Hattori, and G. P. Agrawal, "Improved transmission model for metal-dielectric-metal

plasmonic waveguides with stub structure," *Optics Express*, vol. 18, no. 6, pp. 229-232, 2010.

[48] Z. Wang, N. Zhu, Y. Tang, L. Wosinski, D. Dai, and S. He, "Ultracompact low-loss coupler between strip and slot waveguides.," *Optics Letters*, vol. 34, no. 10, pp. 1498-500, May. 2009.

[49] J. Gosciniak, V. S. Volkov, S. I. Bozhevolnyi, L. Markey, S. Massenot, and A. Dereux, "waveguides," *Optics Express*, vol. 18, no. 5, pp. 5314-5319, 2010.

[50] J. Tian, S. Yu, W. Yan, and M. Qiu, "Broadband high-efficiency surface-plasmon-polariton coupler with silicon-metal interface," *Applied Physics Letters*, vol. 95, no. 1, p. 013504, 2009.

[51] M. Born, E. Wolf, and A. B. Bhatia, *Principles of optics*, vol. 10. Pergamon Pr., 1975.

[52] Y. Fu and X. Zhou, "Plasmonic Lenses: A Review," *Plasmonics*, vol. 5, no. 3, pp. 287-310, Jun. 2010.

[53] H. J. Lezec et al., "Beaming light from a subwavelength aperture.," *Science (New York, N.Y.)*, vol. 297, no. 5582, pp. 820-2, Aug. 2002.

[54] A. G. Curto, A. Manjavacas, and F. J. García de Abajo, "Near-field focusing with optical phase antennas.," *Optics Express*, vol. 17, no. 20, pp. 17801-11, Sep. 2009.

[55] D. R. Jackson, J. Chen, R. Qiang, F. Capolino, and a a Oliner, "The role of leaky plasmon waves in the directive beaming of light through a subwavelength aperture.," *Optics Express*, vol. 16, no. 26, pp. 21271-81, Dec. 2008.

[56] L. Martín-Moreno, F. García-Vidal, H. Lezec, A. Degiron, and T. Ebbesen, "Theory of Highly Directional Emission from a Single Subwavelength Aperture Surrounded by Surface Corrugations," *Physical Review Letters*, vol. 90, no. 16, p. 167401, Apr. 2003.

[57] Y. Fu, C. Du, W. Zhou, and L. E. N. Lim, "Nanopinholes-Based Optical Superlens," *Research Letters in Physics*, vol. 2008, p. 148505, 2008.

[58] M. Consonni, J. Hazart, G. Lérondel, and a Vial, "Nanometer scale light focusing with high cavity-enhanced output," *Journal of Applied Physics*, vol. 105, no. 8, p. 084308, 2009.

[59] J. Wang and W. Zhou, "Experimental Investigation of Focusing of Gold Planar Plasmonic Lenses," *Plasmonics*, vol. 5, no. 4, pp. 325-329, Jun. 2010.

[60] M. Notomi, "Theory of light propagation in strongly modulated photonic crystals: Refractionlike behavior in the vicinity of the photonic band gap," *Physical Review B*, vol. 62, no. 16, pp. 10696-10705, Oct. 2000.

[61] P. Belov, C. Simovski, and P. Ikonen, "Canalization of subwavelength images by electromagnetic crystals," *Physical Review B*, vol. 71, no. 19, p. 193105, May. 2005.

[62] W. Smigaj, B. Gralak, R. Pierre, and G. Tayeb, "Antireflection gratings for a photonic-crystal flat lens.," *Optics Letters*, vol. 34, no. 22, pp. 3532-4, Nov. 2009.

[63] B. D. F. Casse et al., "Imaging with subwavelength resolution by a generalized superlens at infrared wavelengths.," *Optics Letters*, vol. 34, no. 13, pp. 1994-6, Jul. 2009.

[64] M. Hofman, N. Fabre, X. Mélique, D. Lippens, and O. Vanbésien, "Defect assisted subwavelength resolution in III–V semiconductor photonic crystal flat lenses with n=−1," *Optics Communications*, vol. 283, no. 6, pp. 1169-1173, Mar. 2010.

[65] V. G. Veselago, "The electrodynamics of substances with simultaneously negative values of \epsilon and \mu," *Soviet Physics Uspekhi*, vol. 10, no. 4, pp. 509-514, 1968.

[66] J. Pendry, "Negative refraction makes a perfect lens," *Physical Review Letters*, vol. 85, no. 18, pp. 3966-9, Oct. 2000.

[67] A. Degiron, D. R. Smith, J. J. Mock, B. J. Justice, and J. Gollub, "Negative index and indefinite media waveguide couplers," *Applied Physics A*, vol. 87, no. 2, pp. 321-328, Feb. 2007.

[68] N.-H. Shen et al., "Compact planar far-field superlens based on anisotropic left-handed metamaterials," *Physical Review B*, vol. 80, no. 11, p. 115123, Sep. 2009.

[69] N. Engheta and R. W. Ziolkowski, *Metamaterials: physics and engineering explorations*. Wiley-IEEE Press, 2006.

[70] B. A. Munk, *Frequency selective surfaces: theory and design*. Wiley-Interscience, 2000.

[71] W. Rotman, "Plasma Simulation by Artificial Dielectrics and Parallel-Plate Media," *IRE Transactions on Antennas and Propagation*, pp. 17-19, 1962.

[72] J. B. Pendry, a J. Holden, D. J. Robbins, and W. J. Stewart, "Magnetism from conductors and enhanced nonlinear phenomena," *IEEE Transactions on Microwave Theory and Techniques*, vol. 47, no. 11, pp. 2075-2084, 1999.

[73] R. A. Shelby, D. R. Smith, and S. Schultz, “Experimental verification of a negative index of refraction.,” *Science*, vol. 292, no. 5514, pp. 77-9, Apr. 2001.

[74] J. B. Pendry, D. Schurig, and D. R. Smith, “Controlling electromagnetic fields.,” *Science*, vol. 312, no. 5781, pp. 1780-2, Jun. 2006.

[75] J. Brown, “Artificial dielectrics having refractive indices less than unity,” *Proceedings of the IEE-Part IV: Institution Monographs*, vol. 100, no. 5, pp. 51-62, 1953.

[76] R. Rotman, “Early Work on Artificial Dielectrics, Periodic Structures and Their Relationship to Modern Metamaterials,” in *Electromagnetics in Advanced Applications, 2007. ICEAA 2007. International Conference on*, 2007, pp. 313-316.

[77] P. A. Belov, S. A. Tretyakov, and A. J. Viitanen, “Dispersion and reflection properties of artificial media formed by regular lattices of ideally conducting wires,” *Journal of Electromagnetic Waves and Applications*, vol. 16, no. 8, pp. 1153-1170, 2002.

[78] A. Demetriadou and J. B. Pendry, “Taming spatial dispersion in wire metamaterial,” *Journal of Physics: Condensed Matter*, vol. 20, no. 29, p. 295222, Jul. 2008.

[79] M. G. Silveirinha and C. A. Fernandes, “Homogenization of 3-D-connected and nonconnected wire metamaterials,” *IEEE Transactions on Microwave Theory and Techniques*, vol. 53, no. 4, pp. 1418-1430, Apr. 2005.

[80] S. A. Schelkunoff and H. T. Friis, *Antennas: Theory and practice*. Wiley, 1952.

[81] H. J. Schneider and P. Dullenkopf, “Slotted tube resonator: A new NMR probe head at high observing frequencies,” *Rev. Sci. Instrum.*, vol. 48, no. 1, pp. 68-73, 1977.

[82] W. N. Hardy and L. A. Whitehead, “Split-ring resonator for use in magnetic resonance from 200--2000 MHz,” *Review of Scientific Instruments*, vol. 52, no. 2, pp. 213-216, 1981.

[83] V. Podolskiy, A. Sarychev, and V. Shalaev, “Plasmon modes and negative refraction in metal nanowire composites.,” *Optics express*, vol. 11, no. 7, pp. 735-45, Apr. 2003.

[84] T. A. Klar, A. V. Kildishev, S. Member, V. P. Drachev, and V. M. Shalaev, “Negative-Index Metamaterials: Going Optical,” *IEEE Journal of Selected Topics in Quantum Electronics*, vol. 12, no. 6, pp. 1106-1115, 2006.

[85] I. Vendik, O. Vendik, and M. Odit, “Isotropic artificial media with simulateneously negative permittivity and permeability,” *Microwave and Optical Technology Letters*, vol. 48, no. 12, pp. 2553-2556, 2006.

[86] S. Tretyakov, “On geometrical scaling of split-ring and double-bar resonators at optical frequencies,” *Metamaterials*, vol. 1, no. 1, pp. 40-43, Mar. 2007.

[87] H. Lamb, “On group-velocity,” *Proceedings of the London Mathematical Society*, vol. 2, no. 1, p. 473, 1904.

[88] S. A. Schuster, *An introduction to the theory of optics*. E. Arnold, 1904.

[89] H. C. Pocklington, “Growth of a Wave-group when the Group-velocity is Negative,” *Nature*, vol. 71, no. 1852, pp. 607-608, Apr. 1905.

[90] L. I. Mandelshtam, “Group velocity in a crystal lattice,” *Zhurnal Eksperimentalnoi i Teoreticheskoi Fiziki*, vol. 15, no. 9, pp. 476-478, 1945.

[91] D. V. Sivukhin, “The energy of electromagnetic waves in dispersive media,” *Opt. Spektrosk*, vol. 3, pp. 308-312, 1957.

[92] R. A. Silin, “Waveguiding properties of two-dimensional periodical slow-wave systems,” *Voprosy Radioelektroniki, Elektronika*, vol. 4, pp. 11-33, 1959.

[93] N. M. Litchinitser and V. M. Shalaev, “Metamaterials□: transforming theory into reality,” *Journal of Optical Society of America B*, vol. 26, no. 12, pp. 161-169, 2009.

[94] V. M. Shalaev, “Optical negative-index metamaterials,” *Nature*, vol. 6, pp. 41-48, 2007.

[95] B. C. M. Soukoulis and M. Kafesaki, “Negative-Index Materials□: New Frontiers in Optics,” *Advanced Materials*, pp. 1941-1952, 2006.

[96] K. Busch, G. Von Freymann, S. Linden, S. Mingaleev, L. Tkeshelashvili, and M. Wegener, “Periodic nanostructures for photonics,” *Physics reports*, vol. 444, no. 3-6, pp. 101–202, 2007.

[97] W. J. Padilla, D. N. Basov, and D. R. Smith, “Negative refractive index metamaterials,” *Materials Today*, vol. 9, no. 7, pp. 28-35, 2006.

[98] F. Capolino, “Metamaterials Handbook.” CRC Press, 2009.

[99] D. R. Smith, D. C. Vier, N. Kroll, and S. Schultz, "Direct calculation of permeability and permittivity for a left-handed metamaterial," *Applied Physics Letters*, vol. 77, no. 14, pp. 2246-2248, 2000.

[100] V. M. Shalaev et al., "Negative index of refraction in optical metamaterials.," *Optics Letters*, vol. 30, no. 24, pp. 3356-8, Dec. 2005.

[101] S. Zhang, W. Fan, N. Panoiu, K. Malloy, R. Osgood, and S. Brueck, "Experimental Demonstration of Near-Infrared Negative-Index Metamaterials," *Physical Review Letters*, vol. 95, no. 13, p. 137404, Sep. 2005.

[102] E. Plum et al., "Metamaterial with negative index due to chirality," *Physical Review B*, vol. 79, no. 3, p. 035407, Jan. 2009.

[103] H. J. Lezec, J. A. Dionne, and H. A. Atwater, "Negative refraction at visible frequencies.," *Science*, vol. 316, no. 5823, pp. 430-2, Apr. 2007.

[104] J. Valentine et al., "Three-dimensional optical metamaterial with a negative refractive index.," *Nature*, vol. 455, no. 7211, pp. 376-9, Sep. 2008.

[105] M. S. Rill et al., "Photonic metamaterials by direct laser writing and silver chemical vapour deposition.," *Nature materials*, vol. 7, no. 7, pp. 543-6, Jul. 2008.

[106] A. Boltasseva and V. Shalaev, "Fabrication of optical negative-index metamaterials: Recent advances and outlook," *Metamaterials*, vol. 2, no. 1, pp. 1-17, May. 2008.

[107] A. Degiron, D. R. Smith, J. J. Mock, B. J. Justice, and J. Gollub, "Negative index and indefinite media waveguide couplers," *Applied Physics A*, vol. 87, no. 2, pp. 321-328, Feb. 2007.

[108] A. K. Iyer and G. V. Eleftheriades, "A three-dimensional isotropic transmission-line metamaterial topology for free-space excitation," *Applied Physics Letters*, vol. 92, no. 26, p. 261106, 2008.

[109] C. Caloz and T. Itoh, *Electromagnetic metamaterials: transmission line theory and microwave applications: the engineering approach*. Wiley-IEEE Press, 2006.

[110] T. Koschny, L. Zhang, and C. Soukoulis, "Isotropic three-dimensional left-handed metamaterials," *Physical Review B*, vol. 71, no. 12, p. 121103, Mar. 2005.

[111] V. Yannopapas and A. Moroz, "Negative refractive index metamaterials from inherently non-magnetic materials for deep

infrared to terahertz frequency ranges.," *Journal of physics: Condensed matter*, vol. 17, no. 25, pp. 3717-34, Jun. 2005.

[112] A.-G. Kussow, A. Akyurtlu, and N. Angkawisittpan, "Optically isotropic negative index of refraction metamaterial," *Physica Status Solidi (B)*, vol. 245, no. 5, pp. 992-997, May. 2008.

[113] A. Alù and N. Engheta, "Three-dimensional nanotransmission lines at optical frequencies: A recipe for broadband negative-refraction optical metamaterials," *Physical Review B*, vol. 75, no. 2, p. 024304, Jan. 2007.

[114] J. Elser, R. Wangberg, V. a Podolskiy, and E. E. Narimanov, "Nanowire metamaterials with extreme optical anisotropy," *Applied Physics Letters*, vol. 89, no. 26, p. 261102, 2006.

[115] M. Silveirinha, P. Belov, and C. Simovski, "Subwavelength imaging at infrared frequencies using an array of metallic nanorods," *Physical Review B*, vol. 75, no. 3, p. 035108, Jan. 2007.

[116] P. A. Belov, P. Ikonen, C. R. Simovski, Y. Hao, and S. A. Tretyakov, "Magnification of subwavelength field distributions using a tapered array of wires operating in the canalization regime," *Antennas and Propagation Society International Symposium*, pp. 8-11, 2008.

[117] Y. Zhao, P. Belov, and Y. Hao, "Subwavelength internal imaging by means of a wire medium," *Journal of Optics A: Pure and Applied Optics*, vol. 11, no. 7, p. 075101, Jul. 2009.

[118] P. Belov, Y. Hao, and S. Sudhakaran, "Subwavelength microwave imaging using an array of parallel conducting wires as a lens," *Physical Review B*, vol. 73, no. 3, p. 033108, Jan. 2006.

[119] A. Fang, T. Koschny, and C. Soukoulis, "Optical anisotropic metamaterials: Negative refraction and focusing," *Physical Review B*, vol. 79, no. 24, p. 245127, Jun. 2009.

[120] S. Kawata, A. Ono, and P. Verma, "Subwavelength colour imaging with a metallic nanolens," *Nature Photonics*, vol. 2, no. 7, pp. 438-442, Jun. 2008.

[121] J. Yao et al., "Imaging visible light using anisotropic metamaterial slab lens.," *Optics Express*, vol. 17, no. 25, pp. 22380-5, Dec. 2009.

[122] B. D. F. Casse, W. T. Lu, Y. J. Huang, E. Gultepe, L. Menon, and S. Sridhar, "Super-resolution imaging using a three-dimensional metamaterials nanolens," *Applied Physics Letters*, vol. 96, no. 2, p. 023114, 2010.

[123] Z. Jacob, L. V. Alekseyev, and E. Narimanov, "Optical Hyperlens: Far-field imaging beyond the diffraction limit.," *Optics Express*, vol. 14, no. 18, pp. 8247-56, Sep. 2006.

[124] Z. Jacob, L. V. Alekseyev, and E. Narimanov, "Semiclassical theory of the hyperlens.," *Journal of the Optical Society of America. A*, vol. 24, no. 10, pp. A52-9, Oct. 2007.

[125] C. Jeppesen, R. B. Nielsen, A. Boltasseva, S. Xiao, N. a Mortensen, and A. Kristensen, "Thin film Ag superlens towards lab-on-a-chip integration.," *Optics Express*, vol. 17, no. 25, pp. 22543-52, Dec. 2009.

[126] Y. Xiong, Z. Liu, and X. Zhang, "A simple design of flat hyperlens for lithography and imaging with half-pitch resolution down to 20 nm," *Applied Physics Letters*, vol. 94, no. 20, p. 203108, 2009.

[127] Q. Meng et al., "Deep subwavelength focusing of light by a trumpet hyperlens," *Journal of Optics*, vol. 13, no. 7, p. 075102, Jul. 2011.

[128] P. Bharadwaj, B. Deutsch, and L. Novotny, "Optical Antennas," *Advances*, pp. 438-483, 2009.

[129] C. A. Balanis, *Antenna theory*. Wiley New York, 1997.

[130] A. Alù and N. Engheta, "Input impedance, nanocircuit loading, and radiation tuning of optical nanoantennas," *Physical review letters*, vol. 101, no. 4, p. 043901, 2008.

[131] K. B. Crozier, a Sundaramurthy, G. S. Kino, and C. F. Quate, "Optical antennas: Resonators for local field enhancement," *Journal of Applied Physics*, vol. 94, no. 7, p. 4632, 2003.

[132] R. M. Bakker et al., "Near-field excitation of nanoantenna resonance," *Optics Express*, vol. 15, no. 21, pp. 13682-13688, 2007.

[133] L. Novotny, "Effective Wavelength Scaling for Optical Antennas," *Physical Review Letters*, vol. 98, no. June, p. 226802, 2007.

[134] E. Cubukcu and F. Capasso, "Optical nanorod antennas as dispersive one-dimensional Fabry – Pérot resonators for surface plasmons," *Applied Physics Letters*, vol. 95, p. 201101, 2009.

[135] Z. Fang, L. Fan, C. Lin, D. Zhang, A. J. Meixner, and X. Zhu, "Plasmonic coupling of bow tie antennas with Ag nanowire," *Nano letters*, 2011.

[136] C. E. Talley et al., "Surface-Enhanced Raman Scattering from Individual Au Nanoparticles and Nanoparticle Dimer Substrates," *Nano Letters*, vol. 5, no. 8, pp. 1569-1574, 2005.

[137] J. J. Greffet, "Nanoantennas for Light Emission," *Science*, vol. 308, no. June, 2005.

[138] M. Schnell, A. Garcia-Etxarri, A. J. Huber, K. Crozier, J. Aizpurua, and R. Hillenbrand, "Controlling the near-field oscillations of loaded plasmonic nanoantennas," *Nature Photonics*, vol. 3, no. April, pp. 287-291, 2009.

[139] J. A. Schuller, E. S. Barnard, W. Cai, Y. C. Jun, J. S. White, and M. L. Brongersma, "Plasmonics for extreme light concentration and manipulation.," *Nature materials*, vol. 9, no. 3, pp. 193-204, Mar. 2010.

[140] A. Alù and N. Engheta, "Tuning the scattering response of optical nanoantennas with nanocircuit loads," *Nature photonics*, vol. 2, no. 5, pp. 307–310, 2008.

[141] Q.-han Park, "Optical antennas and plasmonics Optical antennas and plasmonics," *Contemporary Physics*, vol. 50, no. 2, pp. 407-423, 2009.

[142] P. Mühlschlegel, H. Eisler, O. J. F. Martin, B. Hecht, and D. W. Pohl, "Resonant Optical Antennas," *Science*, vol. 1607, no. 2005, pp. 1607-9, 2007.

[143] J. Wen, S. Romanov, and U. Peschel, "Excitation of plasmonic gap waveguides by nanoantennas," *Optics Express*, vol. 17, no. 8, pp. 5925-5932, 2009.

[144] P. Biagioni and B. Hecht, "Nanoantennas for visible and infrared radiation," *Arxiv preprint arXiv:1103.1568*, 2011.

[145] A. Kinkhabwala, Z. Yu, S. Fan, Y. Avlasevich, K. Müllen, and W. E. Moerner, "Large single-molecule fluorescence enhancements produced by a bowtie nanoantenna," *Nature Photonics*, vol. 3, no. 11, pp. 654-657, Oct. 2009.

[146] A. Mohammadi, F. Kaminski, V. Sandoghdar, and M. Agio, "Fluorescence Enhancement with the Optical (Bi-) Conical Antenna," *Journal of Physical Chemistry C*, vol. 114, pp. 7372-7377, 2010.

[147] R. M. Bakker et al., "Nanoantenna array-induced fluorescence enhancement and reduced lifetimes," *New Journal of Physics*, vol. 10, p. 125022, 2008.

[148] N. Liu et al., "Planar metamaterial analogue of electromagnetically induced transparency for plasmonic sensing.," *Nano Letters*, vol. 10, no. 4, pp. 1103-7, Apr. 2010.

[149] W. Zhang, L. Huang, C. Santschi, and O. J. F. Martin, "Trapping and sensing 10 nm metal nanoparticles using plasmonic dipole antennas.," *Nano Letters*, vol. 10, no. 3, pp. 1006-11, Mar. 2010.

[150] D. Dey, J. Kohoutek, R. M. Gelfand, A. Bonakdar, and H. Mohseni, "Quantum-cascade laser integrated with a metal – dielectric – metal-based plasmonic antenna," *Optics Letters*, vol. 35, no. 16, pp. 2783-2785, 2010.

[151] N. Yu et al., "Quantum cascade lasers with integrated plasmonic antenna-array collimators," *Optics Express*, vol. 16, no. 24, pp. 19447-19461, 2008.

[152] C.-Y. Cho et al., "Surface plasmon-enhanced light-emitting diodes using silver nanoparticles embedded in p-GaN.," *Nanotechnology*, vol. 21, no. 20, p. 205201, May. 2010.

[153] D.-M. Yeh, C.-F. Huang, C.-Y. Chen, Y.-C. Lu, and C. C. Yang, "Localized surface plasmon-induced emission enhancement of a green light-emitting diode," *Nanotechnology*, vol. 19, no. 34, p. 345201, Aug. 2008.

[154] H. A. Atwater and A. Polman, "Plasmonics for improved photovoltaic devices.," *Nature materials*, vol. 9, no. 3, pp. 205-13, Mar. 2010.

[155] J. R. Cole and N. J. Halas, "Optimized plasmonic nanoparticle distributions for solar spectrum harvesting," *Applied Physics Letters*, vol. 89, no. 15, p. 153120, 2006.

[156] S. Pillai, K. R. Catchpole, T. Trupke, and M. a Green, "Surface plasmon enhanced silicon solar cells," *Journal of Applied Physics*, vol. 101, no. 9, p. 093105, 2007.

[157] D. Derkacs, W. V. Chen, P. M. Matheu, S. H. Lim, P. K. L. Yu, and E. T. Yu, "Nanoparticle-induced light scattering for improved performance of quantum-well solar cells," *Applied Physics Letters*, vol. 93, no. 9, p. 091107, 2008.

[158] T. Kosako, Y. Kadoya, and H. F. Hofmann, "Directional control of light by a nano-optical Yagi – Uda antenna," *Nature Photonics*, no. March, pp. 1-4, 2010.

[159] Y. Chen, P. Lodahl, and A. Koenderink, "Dynamically reconfigurable directionality of plasmon-based single photon sources," *Physical Review B*, vol. 82, no. 8, p. 081402(R), Aug. 2010.

[160] T. Pakizeh and M. Ka, "Unidirectional Ultracompact Optical Nanoantennas 2009," *Nano Letters*, 2009.

[161] S. Zhang, Y.-S. Park, J. Li, X. Lu, W. Zhang, and X. Zhang, "Negative Refractive Index in Chiral Metamaterials," *Physical Review Letters*, vol. 102, no. 2, p. 23901, Jan. 2009.

[162] J. Li, A. Salandrino, and N. Engheta, "Shaping light beams in the nanometer scale: A Yagi-Uda nanoantenna in the optical domain," *Physical Review B*, vol. 76, no. 24, p. 245403, Dec. 2007.

[163] K. G. Lee et al., "A planar dielectric antenna for directional single-photon emission and near-unity collection efficiency," *Nature Photonics*, vol. 5, no. March, Jan. 2011.

[164] J. Li, A. Salandrino, and N. Engheta, "Optical spectrometer at the nanoscale using optical Yagi-Uda nanoantennas," *Physical Review B*, vol. 79, no. 19, p. 195104, May. 2009.

[165] T. H. Taminiau, F. D. Stefani, and N. F. V. Hulst, "Enhanced directional excitation and emission of single emitters by a nano-optical Yagi-Uda antenna," *Optics Express*, vol. 16, no. 14, pp. 10858-10866, 2008.

[166] R. Esteban, T. V. Teperik, and J. J. Greffet, "Optical Patch Antennas for Single Photon Emission Using Surface Plasmon Resonances," *Physical Review Letters*, vol. 104, no. January, p. 026802, 2010.

[167] L. Cao, J.-shik Park, P. Fan, B. Clemens, and M. L. Brongersma, "Resonant Germanium Nanoantenna Photodetectors," *Nano*, pp. 1229-1233, 2010.

[168] L. Tang, S. E. Kocabas, S. Latif, A. L. I. K. Okyay, K. C. Saraswat, and D. A. B. Miller, "Nanometre-scale germanium photodetector enhanced by a near-infrared dipole antenna," *Group*, vol. 2, no. April, pp. 1-4, 2008.

[169] M. W. Knight, H. Sobhani, P. Nordlander, and N. J. Halas, "Photodetection with Active Optical Antennas," *Science*, vol. 332, no. 6030, pp. 702-704, May. 2011.

[170] J. Huang, T. Feichtner, P. Biagioni, and B. Hecht, "Impedance matching and emission properties of nanoantennas in an optical nanocircuit," *Nano Letters*, vol. 9, no. 5, pp. 1897-1902, 2009.

[171] Z. Fang, Y. Lu, L. Fan, and C. Lin, "Surface Plasmon Polariton Enhancement in Silver Nanowire – Nanoantenna Structure," *Plasmonics*, vol. 5, pp. 57-62, 2010.

[172] Z. Fang, L. Fan, C. Lin, D. Zhang, A. J. Meixner, and X. Zhu, "Plasmonic Coupling of Bow Tie Antennas with Ag Nanowire," *Nano*, vol. 11, pp. 1676-1680, 2011.

[173] J. Wen, P. Banzer, A. Kriesch, D. Ploss, B. Schmauss, and U. Peschel, "Experimental cross-polarization detection of coupling far-field light to highly confined plasmonic gap modes via nanoantennas," *Nano Letters*, pp. 3-5, 2011.

[174] A. Alu and N. Engheta, "Wireless at the Nanoscale□: Optical Interconnects using Matched Nanoantennas," *Physical Review Letters*, vol. 104, no. May, p. 213902, 2010.

[175] I. M. Vellekoop, A. Lagendijk, and A. P. Mosk, "Exploiting disorder for perfect focusing," *Nature Photonics*, vol. 4, no. February, pp. 320-322, 2010.

[176] J. Wang, X. Chen, and W. Lu, "High-efficiency surface plasmon polariton source," *Journal of the Optical Society of America B*, vol. 26, no. 12, p. B139, Nov. 2009.

[177] J. Andkjær, S. Nishiwaki, T. Nomura, and O. Sigmund, "Topology optimization of grating couplers for the efficient excitation of surface plasmons," *JOSA B*, vol. 27, no. 9, pp. 1828–1832, 2010.

[178] M. W. Maqsood, R. Mehfuz, and K. J. Chau, "surface-plasmon-polariton coupling by a super-wavelength slit," *Optics Express*, vol. 18, no. 21, pp. 967-971, 2010.

[179] A. J. Ward and J. B. Pendry, "Refraction and geometry in Maxwell's equations," *Journal of Modern Optics*, vol. 43, pp. 773-792, 1996.

[180] D. Shyroki, "Note on transformation to general curvilinear space," *Arxiv preprint arXiv: 0307029*, 2003.

[181] U. Leonhardt and T. G. Philbin, "Transformation Optics and the Geometryy of Light," *Progress in Optics*, vol. 53, no. 8, pp. 69-152, 2009.

[182] J. Zhang, Y. Luo, and N. A. Mortensen, "Transmission of electromagnetic waves through sub-wavelength channels.," *Optics Express*, vol. 18, no. 4, pp. 3864-70, Feb. 2010.

[183] A. V. Kildishev and V. M. Shalaev, "Engineering space for light via transformation optics," *Optics Letters*, vol. 33, no. 1, pp. 43-45, 2008.

[184] E. E. Narimanov and A. V. Kildishev, "Optical black hole: Broadband omnidirectional light absorber," *Applied Physics Letters*, vol. 95, no. 4, p. 041106, 2009.

[185] T.-H. Loh et al., "Ultra-compact multilayer Si/SiO(2) GRIN lens mode-size converter for coupling single-mode fiber to Si-wire waveguide.," *Optics Express*, vol. 18, no. 21, pp. 21519-33, Oct. 2010.

[186] D. R. Smith and S. Schultz, "Determination of effective permittivity and permeability of metamaterials from reflection and transmission coefficients," *Physical Review B*, vol. 65, no. 19, p. 195104, Apr. 2002.

[187] X. Chen, T. M. Grzegorczyk, B.-ian Wu, J. Pacheco, and J. A. Kong, "Robust method to retrieve the constitutive effective parameters of metamaterials," *Physical Review E*, vol. 70, no. February, p. 016608, 2004.

[188] C. Menzel, C. Rockstuhl, T. Paul, F. Lederer, and T. Pertsch, "Retrieving effective parameters for metamaterials at oblique incidence," *Physical Review B*, p. 195328, 2008.

[189] J. Zhou, T. Koschny, M. Kafesaki, E. Economou, J. Pendry, and C. Soukoulis, "Saturation of the Magnetic Response of Split-Ring Resonators at Optical Frequencies," *Physical Review Letters*, vol. 95, no. 22, p. 223902, Nov. 2005.

[190] M. W. Klein, C. Enkrich, M. Wegener, C. M. Soukoulis, and S. Linden, "Single-slit split-ring resonators at optical frequencies: limits of size scaling.," *Optics Letters*, vol. 31, no. 9, pp. 1259-61, May. 2006.

[191] A. Andryieuski, R. Malureanu, and A. Lavrinenko, "Nested structures approach in designing an isotropic negative-index material for infrared," *Journal of the European Optical Society: Rapid Publications*, vol. 4, Jan. 2009.

[192] C. Enkrich et al., "Magnetic Metamaterials at Telecommunication and Visible Frequencies," *Physical Review Letters*, vol. 95, no. 20, p. 203901, Nov. 2005.

[193] T. F. Gundogdu et al., "Experimental demonstration of negative magnetic permeability in the far-infrared frequency regime," *Applied Physics Letters*, vol. 89, no. 8, p. 084103, 2006.

[194] C. Menzel et al., "Angular resolved effective optical properties of a Swiss cross metamaterial," *Applied Physics Letters*, vol. 95, no. 13, p. 131104, 2009.

[195] C. Menzel, R. Singh, C. Rockstuhl, W. Zhang, and F. Lederer, "Effective properties of terahertz double split-ring resonators at oblique incidence," *Journal of the Optical Society of America B*, vol. 26, no. 12, p. B143, Nov. 2009.

[196] T. Paul, C. Rockstuhl, C. Menzel, and F. Lederer, "Anomalous refraction, diffraction, and imaging in metamaterials," *Physical Review B*, vol. 79, no. 11, p. 115430, Mar. 2009.

[197] C. Menzel et al., "High symmetry versus optical isotropy of a negative-index metamaterial," *Physical Review B*, vol. 81, no. 19, p. 195123, May. 2010.

[198] Z.-Y. Li and L.-L. Lin, "Photonic band structures solved by a plane-wave-based transfer-matrix method," *Physical Review E*, vol. 67, no. 4, p. 046607, Apr. 2003.

[199] C. Rockstuhl et al., "Transition from thin-film to bulk properties of metamaterials," *Physical Review B*, p. 035126, 2008.

[200] G. Dolling, C. Enkrich, M. Wegener, and S. Linden, "Low-loss negative-index metamaterial at telecommunication wavelengths," *Optics Letters*, vol. 31, no. 12, pp. 1800-1802, 2006.

[201] CST, "Computer Simulation Technology, AS," *http://cst.com*. [Online]. Available: http://cst.com.

[202] J. Shin, J.-T. Shen, and S. Fan, "Three-Dimensional Metamaterials with an Ultrahigh Effective Refractive Index over a Broad Bandwidth," *Physical Review Letters*, vol. 102, no. 9, p. 093903, Mar. 2009.

[203] E. Economou, T. Koschny, and C. Soukoulis, "Strong diamagnetic response in split-ring-resonator metamaterials: Numerical study and two-loop model," *Physical Review B*, vol. 77, no. 9, p. 092401, Mar. 2008.

[204] R. S. Penciu et al., "Multi-gap individual and coupled split-ring resonator structures.," *Optics Express*, vol. 16, no. 22, pp. 18131-44, Oct. 2008.

[205] S. Tretyakov, *Analytical modeling in applied electromagnetics*. Artech House Publishers, 2003.

[206] T. Koschny, P. Markoš, D. Smith, and C. Soukoulis, "Resonant and antiresonant frequency dependence of the effective parameters of metamaterials," *Physical Review E*, vol. 68, no. 6, p. 065602, Dec. 2003.

[207] R. Depine and A. Lakhtakia, "Comment I on 'Resonant and antiresonant frequency dependence of the effective parameters of metamaterials'," *Physical Review E*, vol. 70, no. 4, p. 048601, Oct. 2004.

[208] A. Efros, "Comment II on 'Resonant and antiresonant frequency dependence of the effective parameters of metamaterials'," *Physical Review E*, vol. 70, no. 4, p. 048602, Oct. 2004.

[209] T. Koschny, P. Markoš, D. Smith, and C. Soukoulis, "Reply to Comments on 'Resonant and antiresonant frequency dependence of

the effective parameters of metamaterials','' *Physical Review E*, vol. 70, no. 4, p. 048603, Oct. 2004.

[210] D. O. Güney, T. Koschny, M. Kafesaki, and C. M. Soukoulis, "Connected bulk negative index photonic metamaterials.," *Optics Letters*, vol. 34, no. 4, pp. 506-8, Mar. 2009.

[211] A. Andryieuski, C. Menzel, C. Rockstuhl, R. Malureanu, F. Lederer, and A. Lavrinenko, "Homogenization of resonant chiral metamaterials," *Physical Review B*, vol. 82, no. 23, p. 235107, Dec. 2010.

[212] C. Rockstuhl, C. Menzel, T. Paul, T. Pertsch, and F. Lederer, "Light propagation in a fishnet metamaterial," *Physical Review B*, vol. 78, no. 15, p. 115102, Oct. 2008.

[213] S. M. Kuebler, A. Tal, and Y.-S. Chen, "Preparation of metallo-dielectric photonic crystals by multi-photon direct laser writing," *Proceedings of SPIE*, vol. 6901, p. 69010Z-69010Z-8, 2008.

[214] A. Andryieuski, C. Menzel, C. Rockstuhl, R. Malureanu, and A. V. Lavrinenko, "The split cube in a cage: bulk negative-index material for infrared applications," *Journal of Optics A: Pure and Applied Optics*, vol. 11, no. 11, p. 114010, Nov. 2009.

[215] J. Baena, L. Jelinek, and R. Marqués, "Towards a systematic design of isotropic bulk magnetic metamaterials using the cubic point groups of symmetry," *Physical Review B*, vol. 76, no. 24, p. 245115, Dec. 2007.

[216] A. Fang, Z. Huang, T. Koschny, and C. M. Soukoulis, "Overcoming the losses of a split ring resonator array with gain," *Optics Express*, vol. 19, no. 13, pp. 12688-12699, 2011.

[217] A. N. Lagarkov and A. K. Sarychev, "Loss and gain in metamaterials," *Journal of the Optical Society of America B*, vol. 27, no. 4, p. 648, Mar. 2010.

[218] Y. Sivan, S. Xiao, U. K. Chettiar, A. V. Kildishev, and V. M. Shalaev, "Frequency-domain simulations of a negative- index material with embedded gain," *Optics Express*, vol. 17, no. 26, pp. 24060-24074, 2009.

[219] C. R. Simovski, "Material Parameters of Metamaterials (a Review)," *Optics and Spectroscopy*, vol. 107, no. 5, pp. 766-793, 2009.

[220] D. R. Smith, S. Schultz, P. Markos, and C. M. Soukoulis, "Determination of effective permittivity and permeability of metamaterials from reflection and transmission coefficient," *Physical Review B*, vol. 65, p. 195104, 2002.

[221] J. J. H. Cook, K. L. Tsakmakidis, and O. Hess, "Ultralow-loss optical diamagnetism in silver nanoforests," *Journal of Optics A: Pure and Applied Optics*, vol. 11, no. 11, p. 114026, Nov. 2009.

[222] B. I. Popa and S. A. Cummer, "Determining the effective electromagnetic properties of negative-refractive-index metamaterials from internal fields," *Physical Review B*, p. 165102, 2005.

[223] A. Andryieuski, R. Malureanu, and A. Lavrinenko, "Wave propagation retrieval method for metamaterials: Unambiguous restoration of effective parameters," *Physical Review B*, vol. 80, no. 19, p. 193101, Nov. 2009.

[224] J. Lerat, N. Malléjac, and O. Acher, "Determination of the effective parameters of a metamaterial by field," *Journal of Applied Physics*, pp. 1-9, 2006.

[225] D. R. Smith and J. B. Pendry, "Homogenization of metamaterials by field averaging," *Journal of the Optical Society of America B*, vol. 23, no. 3, pp. 391-403, 2006.

[226] C. R. Simovski and S. A. Tretyakov, "Local constitutive parameters of metamaterials from an effective-medium perspective," *Physical Review B*, p. 195111, 2007.

[227] R.-L. Chern and Y.-T. Chen, "Effective parameters for photonic crystals with large dielectric contrast," *Physical Review B*, p. 075118, 2009.

[228] D. K. Morits and C. R. Simovski, "Negative effective permeability at optical frequencies produced by rings of plasmonic dimers," *Physical Review B*, vol. 81, no. 20, p. 205112, May. 2010.

[229] J. Petschulat et al., "Analytical modelling of linear and nonlinear properties of metamaterials based on multipole expansion," *Proceedings of SPIE*, vol. 7353, p. 73530D-73530D-13, 2009.

[230] J. Petschulat et al., "On the dispersion relation in metamaterials: an analytic approach," *Proceedings of SPIE*, vol. 6987, no. 2008, p. 69871T-69871T-9, 2008.

[231] J. Petschulat et al., "Simple and versatile analytical approach for planar metamaterials," *Physical Review B*, p. 075102, 2010.

[232] J. T. Costa, M. G. Silveirinha, and S. I. Maslovski, "Finite-difference frequency-domain method for the extraction of effective parameters of metamaterials," *Physical Review B*, vol. 80, no. 23, p. 235124, Dec. 2009.

[233] J. Yang, C. Sauvan, T. Paul, C. Rockstuhl, F. Lederer, and P. Lalanne, "Retrieving the effective parameters of metamaterials from

the single interface scattering problem," *Applied Physics Letters*, pp. 3-5, 2010.

[234] S. Sun, S. T. Chui, and L. Zhou, "Effective-medium properties of metamaterials : A quasimode theory," *Physical Review E*, p. 066604, 2009.

[235] X. Chen, B.-I. Wu, J. A. Kong, and T. M. Grzegorczyk, "Retrieval of the effective constitutive parameters of bianisotropic metamaterials," *Physical Review E*, no. April, p. 046610, 2005.

[236] D.-H. Kwon, D. H. Werner, A. V. Kildishev, and V. M. Shalaev, "Material parameter retrieval procedure for general bi-isotropic metamaterials and its application to optical chiral negative-index metamaterial design," *Optics Express*, vol. 16, no. 16, pp. 11822-11829, 2008.

[237] B. Wang, J. Zhou, T. Koschny, M. Kafesaki, and C. M. Soukoulis, "Chiral metamaterials: simulations and experiments," *Journal of Optics A: Pure and Applied Optics*, vol. 11, no. 11, p. 114003, Nov. 2009.

[238] S. Larouche and D. R. Smith, "Invited paper A retrieval method for nonlinear metamaterials," *Optics Communications*, vol. 283, no. 8, pp. 1621-1627, 2010.

[239] A. Fang, T. Koschny, M. Wegener, and C. Soukoulis, "Self-consistent calculation of metamaterials with gain," *Physical Review B*, vol. 79, no. 24, p. 241104, Jun. 2009.

[240] C. R. Simovski, "Bloch material parameters of magneto-dielectric metamaterials and the concept of Bloch lattices," *Metamaterials*, vol. 1, no. 2, pp. 62-80, Dec. 2007.

[241] C. R. Simovski, "On electromagnetic characterization and homogenization of nanostructured metamaterials," *Journal of Optics*, vol. 13001, 2011.

[242] J. Zhou, T. Koschny, M. Kafesaki, and C. M. Soukoulis, "Negative refractive index response of weakly and strongly coupled optical metamaterials," *Physical Review B (Condensed Matter and Materials Physics)*, vol. 80, no. 3, p. 035109, Jul. 2009.

[243] A. Andryieuski, C. Menzel, C. Rockstuhl, R. Malureanu, and A. V. Lavrinenko, "The split cube in a cage: bulk negative-index material for infrared applications," *Journal of Optics A: Pure and Applied Optics*, vol. 11, no. 11, p. 114010, Nov. 2009.

[244] C. Rockstuhl et al., "Bulk properties of metamaterials," *Proceedings of SPIE*, vol. 6987, p. 69871O-69871O-10, 2008.

[245] J. F. Wang, S. B. Qu, Z. Xu, Z. T. Fu, H. Ma, and Y. M. Yang, "A broad-band three-dimensional isotropic left-handed metamaterial," *Journal of Physics D: Applied Physics*, vol. 42, no. 15, p. 155413, Aug. 2009.

[246] V. Lucarini, *Kramers-Kronig relations in optical materials research*, vol. 110. Springer Verlag, 2005.

[247] S. A. Tretyakov, I. Nefedov, A. Sihvola, S. Maslovski, and C. Simovski, "Waves and Energy in Chiral Nihility," *Journal of Electromagnetic Waves and Applications*, vol. 17, pp. 695-706, May. 2003.

[248] J. B. Pendry, "A chiral route to negative refraction.," *Science (New York, N.Y.)*, vol. 306, no. 5700, pp. 1353-5, Nov. 2004.

[249] A. Andryieuski, R. Malureanu, and A. V. Lavrinenko, "Wave propagation retrieval method for chiral metamaterials.," *Optics Express*, vol. 18, no. 15, pp. 15498-503, Jul. 2010.

[250] A. I. Akhiezer, I. A. Akhiezer, R. V. Polovin, A. G. Sitenko, and K. N. Stepanov, *Plasma electrodynamics.*, Internatio., vol. 1. Pergamon Press, 1975, p. 414.

[251] J. Dong, J. Zhou, T. Koschny, and C. Soukoulis, "Bi-layer cross chiral structure with strong optical activity and negative refractive index.," *Optics Express*, vol. 17, no. 16, pp. 14172-9, Aug. 2009.

[252] X. Xiong et al., "Construction of a chiral metamaterial with a U-shaped resonator assembly," *Physical Review B*, vol. 81, no. 7, p. 075119, Feb. 2010.

[253] A. Andryieuski, S. Ha, A. A. Sukhorukov, Y. S. Kivshar, and A. V. Lavrinenko, "Bloch-mode analysis for unambiguous retrieval of metamaterial effective parameters," *Arxiv preprint arXiv:1011.2669*, pp. 1-10, 2010.

[254] P. Yeh, *Optical waves in layered media*, vol. 95. Wiley Online Library, 1988.

[255] J. D. Joannopoulos, *Photonic crystals: molding the flow of light*. Princeton Univ Pr, 2008.

[256] P. S. J. Russell, T. A. Birks, and F. D. Lloyd-Lucas, "Confined Electrons and Photons." Plenum, New York, 1995.

[257] N. A. Mortensen and M. Yan, "On the unambiguous determination of effective optical properties of periodic metamaterials: a one-dimensional case study," *Journal of the European Optical Society: Rapid Publications*, 2010.

[258] S. Ha, A. A. Sukhorukov, K. B. Dossou, L. C. Botten, C. M. de Sterke, and Y. S. Kivshar, "Bloch-mode extraction from near-field data in periodic waveguides.," *Optics Letters*, vol. 34, no. 24, pp. 3776-8, Dec. 2009.

[259] A. A. Sukhorukov, S. Ha, I. V. Shadrivov, D. a Powell, and Y. S. Kivshar, "Dispersion extraction with near-field measurements in periodic waveguides," *Optics Express*, vol. 17, no. 5, p. 3716, Feb. 2009.

[260] A. Andryieuski, C. Menzel, C. Rockstuhl, R. Malureanu, F. Lederer, and A. Lavrinenko, "Homogenization of resonant chiral metamaterials," *Physical Review B*, vol. 82, no. 23, p. 235107, 2010.

[261] E. D. Palik and G. Ghosh, *Handbook of optical constants of solids*. Academic press, 1998.

[262] P. A. Belov, E. A. Yankovskaya, I. V. Melchakova, and C. R. Simovski, "Studying the possibility of extracting material parameters from reflection and transmission coefficients of plane wave for multilayer metamaterials based on metal nanogrids," *Optics and Spectroscopy*, vol. 109, no. 1, pp. 85-96, Jul. 2010.

[263] C. Menzel, T. Paul, C. Rockstuhl, T. Pertsch, S. Tretyakov, and F. Lederer, "Validity of effective material parameters for optical fishnet metamaterials," *Physical Review B*, p. 035320, 2010.

[264] C. Menzel, C. Rockstuhl, R. Iliew, and F. Lederer, "High symmetry versus optical isotropy of a negative-index metamaterial," *Physical Review B*, vol. 81, no. 19, p. 195123, May. 2010.

[265] S. Lal, S. E. Clare, and N. J. Halas, "Therapy: Impending Clinical Impact," *Accounts of Chemical Research*, vol. 41, no. 12, 2008.

[266] A. Campion and P. Kambhampati, "Surface-Enhanced Raman Scattering," *Chemical Society Reviews*, vol. 27, pp. 241-250, Jan. 1998.

[267] T. Scheibel, R. Parthasarathy, G. Sawicki, X.-M. Lin, H. Jaeger, and S. L. Lindquist, "Conducting nanowires built by controlled self-assembly of amyloid fibers and selective metal deposition.," *Proceedings of the National Academy of Sciences of the United States of America*, vol. 100, no. 8, pp. 4527-32, Apr. 2003.

[268] A. Boltasseva, "Plasmonic components fabrication via nanoimprint," *Journal of Optics A: Pure and Applied Optics*, vol. 11, no. 11, p. 114001, Nov. 2009.

[269] S. Maruo, O. Nakamura, and S. Kawata, "Three-dimensional microfabrication with two-photon-absorbed photopolymerization.," *Optics Letters*, vol. 22, no. 2, pp. 132-4, Jan. 1997.

[270] M. Deubel, M. Wegener, and S. John, "3D–2D–3D photonic crystal heterostructures fabricated by direct laser writing," *Optics Letters*, vol. 31, no. 6, pp. 805-807, 2006.

[271] J. Serbin, A. Ovsianikov, and B. Chichkov, "Fabrication of woodpile structures by two-photon polymerization and investigation of their optical properties.," *Optics Express*, vol. 12, no. 21, pp. 5221-8, Oct. 2004.

[272] N. Grossman, A. Ovsianikov, A. Petrov, M. Eich, and B. Chichkov, "Investigation of optical properties of circular spiral photonic crystals.," *Optics Express*, vol. 15, no. 20, pp. 13236-43, Oct. 2007.

[273] D. O. Güney, T. Koschny, and C. M. Soukoulis, "Intra-connected three-dimensionally isotropic bulk negative index photonic metamaterial.," *Optics Express*, vol. 18, no. 12, pp. 12348-53, Jun. 2010.

[274] J. K. Gansel et al., "Gold Helix Photonic Metamaterial as," *Science*, vol. 1513, 2009.

[275] Y. Shacham-diamand, A. Inberg, Y. Sverdlov, V. Bogush, and N. Croitoru, "Electroless processes for micro- and nanoelectronics," *Electrochimica Acta*, vol. 48, pp. 2987-2996, 2003.

[276] D. Chen et al., "A general method for synthesis continuous silver nanoshells on dielectric colloids," *Thin Solid Films*, vol. 516, no. 18, pp. 6371-6376, Jul. 2008.

[277] K. Kim, H. B. Lee, H. K. Park, and K. S. Shin, "Easy deposition of Ag onto polystyrene beads for developing surface-enhanced-Raman-scattering-based molecular sensors.," *Journal of colloid and interface science*, vol. 318, no. 2, pp. 195-201, Feb. 2008.

[278] Y. Kobayashi, V. Salgueiriño-Maceira, and L. M. Liz-Marzán, "Deposition of Silver Nanoparticles on Silica Spheres by Pretreatment Steps in Electroless Plating," *Chemistry of Materials*, vol. 13, no. 5, pp. 1630-1633, May. 2001.

[279] G. Ling, J. He, and L. Huang, "Size control of silver nanoparticles deposited on silica dielectric spheres by electroless plating technique," *Journal of Materials Science*, vol. 39, no. 8, pp. 2955-2957, Apr. 2004.

[280] S. Demoustier-Champagne and M. Delvaux, "Preparation of polymeric and metallic nanostructures using a template-based

deposition method," *Materials Science and Engineering: C*, vol. 15, no. 1-2, pp. 269-271, Aug. 2001.

[281] M. Kostowskyj, R. Gilliam, D. Kirk, and S. Thorpe, "Silver nanowire catalysts for alkaline fuel cells," *International Journal of Hydrogen Energy*, vol. 33, no. 20, pp. 5773-5778, Oct. 2008.

[282] V. P. Menon and C. R. Martin, "Fabrication and Evaluation of Nanoelectrode Ensembles," *Plating*, vol. 67, no. 13, pp. 1920- 1928, 1995.

[283] D. Zhang, L. Qi, J. Yang, J. Ma, H. Cheng, and L. Huang, "Wet Chemical Synthesis of Silver Nanowire Thin Films at Ambient Temperature," *Chemistry of Materials*, vol. 16, no. 5, pp. 872-876, Mar. 2004.

[284] F. Formanek, N. Takeyasu, T. Tanaka, K. Chiyoda, A. Ishikawa, and S. Kawata, "Selective electroless plating to fabricate complex three-dimensional metallic micro/nanostructures," *Applied Physics Letters*, vol. 88, no. 8, p. 083110, 2006.

[285] L. Lu, A. Kobayashi, K. Tawa, and Y. Ozaki, "Silver Nanoplates with Special Shapes□: Controlled Synthesis and Their Surface Plasmon Resonance and Surface-Enhanced Raman Scattering Properties," *Synthesis*, no. 4, pp. 4894-4901, 2006.

[286] J. Zhang, P. Zhan, H. Liu, Z. Wang, and N. Ming, "A facile colloidal templating method to monodisperse hollow Ag and Ag/Au submicrometer spheres," *Materials Letters*, vol. 60, no. 2, pp. 280-283, Jan. 2006.

[287] Y.-S. Chen, A. Tal, S. M. Kuebler, and C. Florida, "Route to Three-Dimensional Metallized Microstructures Using Cross-Linkable Epoxide SU-8," *Chemistry of Materials*, no. 19, pp. 3858-3860, 2007.

[288] H.-C. Koo, S. Y. Kim, S. K. Cho, and J. J. Kim, "Ag Seed-Layer Formation by Electroless Plating for Ultra-Large-Scale Integration Interconnection," *Journal of The Electrochemical Society*, vol. 155, no. 9, p. D558, 2008.

[289] A. Inberg, V. Bogush, N. Croitoru, V. Dubin, and Y. Shacham-Diamand, "Novel Highly Conductive Silver-Tungsten Thin Films Electroless Deposited from Benzoate Solution for Microelectronic Applications," *Journal of The Electrochemical Society*, vol. 150, no. 5, p. C285, 2003.

[290] A. Inberg, V. Bogush, N. Croitoru, and Y. Shacham-Diamand, "Electrochemical Study of the Mechanism of Ag(W) Electroless Deposition," *Journal of The Electrochemical Society*, vol. 154, no. 1, p. D1, 2007.

[291] A. Inberg, “Electroless and sputtered silver–tungsten thin films for microelectronics applications,” *Microelectronic Engineering*, vol. 65, no. 1-2, pp. 197-207, Jan. 2003.

[292] Y. Shacham-Diamand, A. Inberg, Y. Sverdlov, and N. Croitoru, “Electroless Silver and Silver with Tungsten Thin Films for Microelectronics and Microelectromechanical System Applications,” *Journal of The Electrochemical Society*, vol. 147, no. 9, p. 3345, 2000.

[293] A. Inberg, V. Bogush, N. Croitoru, and Y. Shacham-Diamand, “Electrochemical Study of the Mechanism of Ag(W) Electroless Deposition,” *Journal of The Electrochemical Society*, vol. 154, no. 1, p. D1, 2007.

[294] “Sigma Aldrich Co., http://www.sigmaaldrich.com/denmark.html.” [Online]. Available: http://www.sigmaaldrich.com/denmark.html.

[295] J.-S. Huang et al., “Atomically flat single-crystalline gold nanostructures for plasmonic nanocircuitry,” *Nat Commun*, vol. 1, p. 150, Dec. 2010.

[296] R. Malureanu et al., “Enhanced broadband optical transmission in metallized woodpiles,” *Applied Physics A*, vol. 103, no. 3, pp. 749-753, Dec. 2010.

[297] R. Malureanu, M. Zalkovskij, A. Andryieuski, and A. V. Lavrinenko, “Controlled Ag Electroless Deposition in Bulk Structures with Complex Three-Dimensional Profiles,” *Journal of The Electrochemical Society*, vol. 157, no. 12, p. K284, 2010.

[298] S. Kawata, H. B. Sun, T. Tanaka, and K. Takada, “Finer features for functional microdevices.,” *Nature*, vol. 412, no. 6848, pp. 697-8, Aug. 2001.

[299] M. Deubel, G. von Freymann, M. Wegener, S. Pereira, K. Busch, and C. M. Soukoulis, “Direct laser writing of three-dimensional photonic-crystal templates for telecommunications.,” *Nature materials*, vol. 3, no. 7, pp. 444-7, Jul. 2004.

[300] R. W. Furness, *The practice of plating on plastics*. Draper (Teddington), 1968.

[301] S. Y. Lin et al., “A three-dimensional photonic crystal operating at infrared wavelengths,” *Nature*, vol. 24, no. 1997, pp. 1997-1999, 1998.

[302] M. Decker et al., “Strong optical activity from twisted-cross photonic metamaterials.,” *Optics Letters*, vol. 34, no. 16, pp. 2501-3, Aug. 2009.

[303] E. Plum, V. a Fedotov, a S. Schwanecke, N. I. Zheludev, and Y. Chen, "Giant optical gyrotropy due to electromagnetic coupling," *Applied Physics Letters*, vol. 90, no. 22, p. 223113, 2007.

[304] A. V. Rogacheva, V. A. Fedotov, A. S. Schwanecke, and N. I. Zheludev, "Giant Gyrotropy due to Electromagnetic-Field Coupling in a Bilayered Chiral Structure," *Physical Review Letters*, vol. 97, no. 17, p. 177401, Oct. 2006.

[305] M. Decker, M. W. Klein, M. Wegener, and S. Linden, "Circular dichroism of planar chiral magnetic metamaterials.," *Optics Letters*, vol. 32, no. 7, pp. 856-8, Apr. 2007.

[306] J. K. Gansel et al., "Gold Helix Photonic Metamaterial as Broadband Circular Polarizer," *Science*, vol. 325, no. 5947, pp. 1513-1515, Sep. 2009.

[307] J. Zhou, J. Dong, B. Wang, T. Koschny, M. Kafesaki, and C. Soukoulis, "Negative refractive index due to chirality," *Physical Review B*, vol. 79, no. 12, p. 121104, Mar. 2009.

[308] B. Wang, J. Zhou, T. Koschny, and C. M. Soukoulis, "Nonplanar chiral metamaterials with negative index," *Applied Physics Letters*, vol. 94, no. 15, p. 151112, 2009.

[309] S. Zhang, Y.-S. Park, J. Li, X. Lu, W. Zhang, and X. Zhang, "Negative Refractive Index in Chiral Metamaterials," *Physical Review Letters*, vol. 102, no. 2, p. 023901, Jan. 2009.

[310] M. C. K. Wiltshire, J. B. Pendry, and J. V. Hajnal, "Chiral Swiss rolls show a negative refractive index," *Journal of Physics: Condensed Matter*, vol. 21, no. 29, p. 292201, Jul. 2009.

[311] C. Menzel, C. Rockstuhl, T. Paul, and F. Lederer, "Retrieving effective parameters for quasiplanar chiral metamaterials," *Applied Physics Letters*, vol. 93, no. 23, pp. 233103-233106, Dec. 2008.

[312] N. Liu and H. Giessen, "Three-dimensional optical metamaterials asmodel systems for longitudinal and transversemagnetic coupling," *Optics Express*, vol. 16, no. 26, pp. 21233-21238, Dec. 2008.

[313] I. Sersic, M. Frimmer, E. Verhagen, and A. F. Koenderink, "Electric and Magnetic Dipole Coupling in Near-Infrared Split-Ring Metamaterial Arrays," *Physical Review Letters*, vol. 103, no. 21, p. 213902, Nov. 2009.

[314] K. Aydin, I. M. Pryce, and H. a Atwater, "Symmetry breaking and strong coupling in planar optical metamaterials.," *Optics express*, vol. 18, no. 13, pp. 13407-17, Jun. 2010.

[315] E. Shamonina and L. Solymar, “Properties of magnetically coupled metamaterial elements,” *Journal of Magnetism and Magnetic Materials*, vol. 300, no. 1, pp. 38-43, May. 2006.

[316] H. Liu, Y. M. Liu, T. Li, S. M. Wang, S. N. Zhu, and X. Zhang, “Coupled magnetic plasmons in metamaterials,” *physica status solidi (b)*, vol. 246, no. 7, pp. 1397-1406, 2009.

[317] Z. Li, H. Caglayan, E. Colak, J. Zhou, C. M. Soukoulis, and E. Ozbay, “Coupling effect between two adjacent chiral structure layers.,” *Optics Express*, vol. 18, no. 6, pp. 5375-83, Mar. 2010.

[318] M. Decker, R. Zhao, C. M. Soukoulis, S. Linden, and M. Wegener, “Twisted split-ring-resonator photonic metamaterial with huge optical activity.,” *Optics Letters*, vol. 35, no. 10, pp. 1593-5, May. 2010.

[319] S. Guenneau and F. Zolla, “Homogenization of 3D finite chiral photonic crystals,” *Physica B: Condensed Matter*, vol. 394, no. 2, pp. 145-147, May. 2007.

[320] K. J. Boller, A. Imamoglu, and S. E. Harris, “Observation of Electromagnetically Induced Transparency,” *Physical Review*, vol. 66, no. 20, pp. 2593-2596, 1991.

[321] X. Xiong et al., “Switching the electric and magnetic responses in a metamaterial,” *Physical Review B*, vol. 80, no. 20, p. 201105, Nov. 2009.

[322] L. Brillouin, *Wave propagation in periodic structures*. Dover Pubns, 2003.

[323] A. B. Movchan, C. G. Poulton, L. C. Botten, N. A. Nicorovici, and R. C. McPhedran, “Noncommuting Limits in Electromagnetic Scattering: Asymptotic Analysis for an Array of Highly Conducting Inclusions,” *SIAM Journal on Applied Mathematics*, vol. 61, no. 5, pp. 1706-1730, Jan. 2001.

[324] X.-X. Liu and A. Alù, “Limitations and potentials of metamaterial lenses,” *Journal of Nanophotonics*, vol. 5, no. 1, p. 053509, 2011.

[325] C. Balanis, “Antenna theory: analysis and design,” 2005.

[326] H. Yagi, “Beam transmission of ultra short waves,” *Proceedings of the Institute of Radio Engineers*, vol. 16, no. 6, pp. 715-740, 1928.

[327] A. D. Rakic, A. B. Djurisic, J. M. Elazar, and M. L. Majewski, “Optical properties of metallic films for vertical-cavity optoelectronic devices.,” *Applied optics*, vol. 37, no. 22, pp. 5271-83, Aug. 1998.

[328] M. Gu, P. Bai, and E.-ping Li, “Enhancing the Reception of Propagating Surface Plasmons Using a Nanoantenna,” *IEEE Photonics Technology Letters*, vol. 22, no. 4, pp. 2009-2011, 2010.